Developments In Increased Energy Density Lithium Batteries and Renewable Energy Storage

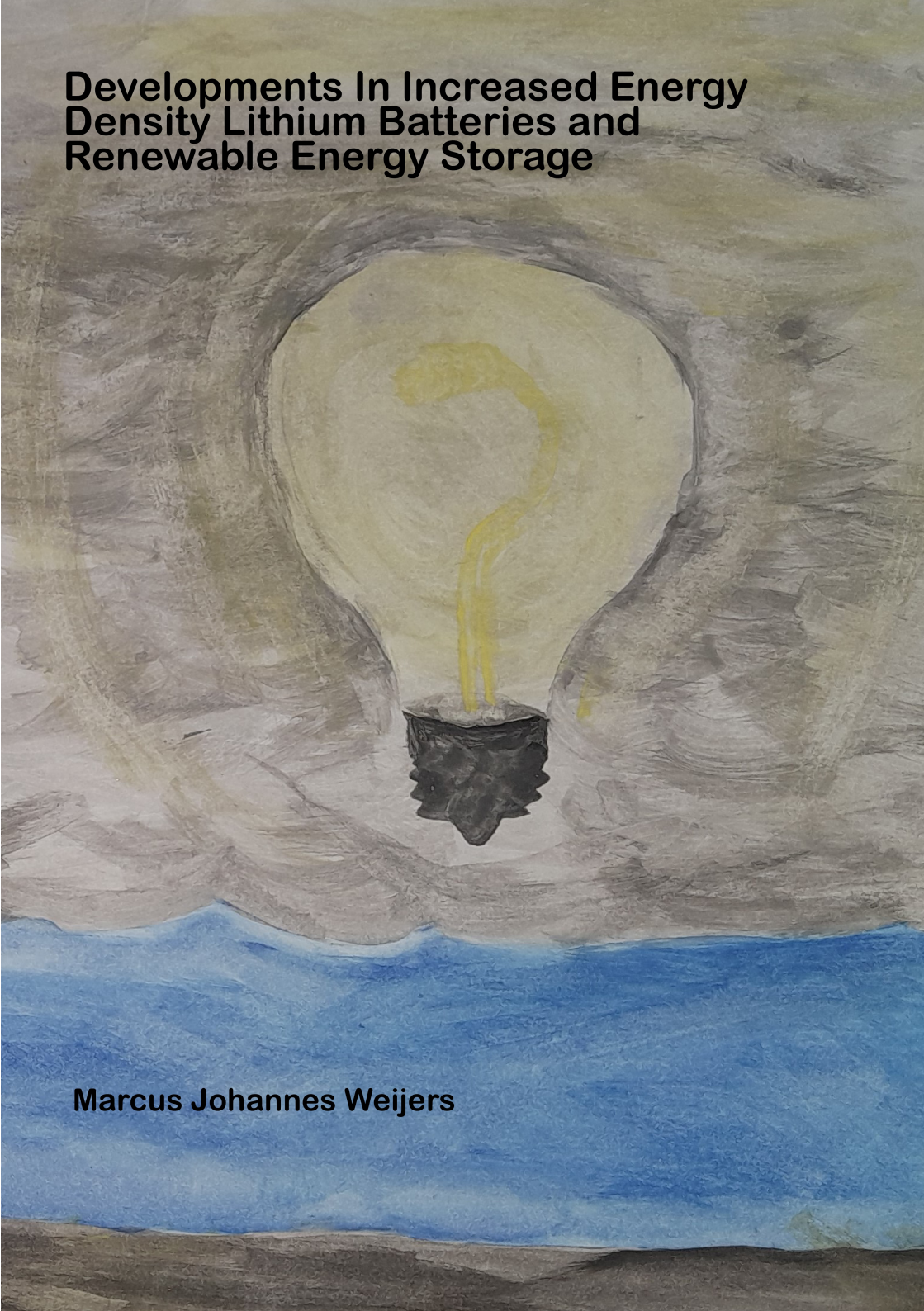

Marcus Johannes Weijers

DEVELOPMENTS IN INCREASED ENERGY DENSITY LITHIUM BATTERIES AND RENEWABLE ENERGY STORAGE

Dissertation

for the purpose of obtaining the degree of doctor

at Delft University of Technology

by the authority of the Rector Magnificus, Prof.dr.ir. T.H.J.J. van der Hagen,

chair of the Board for Doctorates

to be defended publicly on

Tuesday 24, June 2025

At 15:00 o'clock

By

Marcus Johannes WEIJERS

Master of Science in Life Science and Technology, Delft University of Technology, The Netherlands

born in Noordwijkerhout, the Netherlands

This dissertation has been approved by the promotors.

Composition of the doctoral committee:

Rector Magnificus,	chairperson
Prof. dr. F.M. Mulder	Delft University of Technology, promotor
Prof. dr. ir. M. Wagemaker	Delft University of Technology, promotor

Independent members:

Prof. dr. A.J. Houtepen	Delft University of Technology
Prof. dr. ir. M.A. van den Broek	Delft University of Technology
Dr.ir.drs. L.J. Bannenberg	Delft University of Technology
Prof. dr. P.M. Vereecken	Katholieke Universiteit Leuven, Belgium
Prof.dr.ir. M. Huijben	University of Twente

This doctoral research has been carried out in the Materials for Energy Conversion and Storage (MECS) group, Department of Chemical Engineering, Faculty of Applied Sciences, Delft University of Technology, the Netherlands. This research was funded by the European Union's Horizon 2020 research and innovation programme named SOLiDIFY under grant agreement No 875557.

Front cover artwork by: Marcus Johannes Weijers

ISBN 978-94-6518-080-9

An electronic version of this dissertation is available at

http://repository.tudelft.nl

Normal science, the puzzle solving activity we just have examined, is a highly cumulative enterprise, eminently successful in its aim, the steady extension of the scope and precision of scientific knowledge.

Thomas S. Kuhn - The structure of scientific revolutions

CONTENTS

LIST OF ABBREVATIONS

Abbrevation:	Meaning:
[x,y]PYR	x-propyl-y-methylpyrrolidinium
AGG	Aggregates
AM	Active material
BET	Brunauer–Emmett–Teller (model)
BMP	1-butyl-1-methylpyrrolidinium
BPP	Bloembergen-Purcell-Pound (model)
BSPP	British standard piping parallel (thread)
BTAB/BTATFSI	(1-Butyl)trimethylammonium bromide/ (1-Butyl)trimethylammonium bis((trifluoromethylsulfonyl)imide
CAPEX	Capital Expenses
CB	Carbon black
CBD	Carbon binder domain
CC/CV	Constant current/constante voltage
CE	Coulombic efficiency
CEI	Cathode/electrolyte interface
CF	Capacity Factor
CIP	Contact ion pairs
CMC	Carboxymethyl cellulose
C-rate	Charge rate
CTAC or HDTAC	(1-Hexadecyl)Trimethylammonium chloride or Cetrimoniumchloride
CV	Cyclic voltammetry
DAC	Direct Air Capture
DC	Direct current
DMSO	Dimethylsulfoxide
DSC	Differential scanning calorimetry
DTD	1,3,2-Dioxathiolane 2,2 Dioxide
EBC	European biochar certificate
EC measurements	Electrochemical measurements
EC/EMC/DMC/DEC	Ethylene carbonate/ethyl methyl carbonate/dimethyl carbonate/di-ethyl carbonate
EDS	Energy dispersive spectroscopy
EIS	Electrochemical impedance spectroscopy
EMI	1-ethyl-3-methylimidazolium
EPI	Ethanol induced phase inversion
EV	Electric Vehicle(s)
Fe	Iron
FEC	Fluoroethylene carbonate
FIB	Focused ion beam
FSI	bis((fluorosulfonyl)imide
FT	Fischer-Tropsch (reaction)
FWHM	Full width at half maximum
GITT	Galvanostatic intermittant titration technique
HB	Haber Bosch (reaction)
HCl	Hydrochloric acid
HF	Hydrofluoric acid
HHV/LHV	Higher heating value/Lower heating value
HTC	Hydrothermal carbonization
HTL	Hydrothermal liquefaction
HVDC	High voltage direct current
HVT	High vacuum treatments
ICE	Initial coulombic efficiency
IHBFBSR	Indirectly heated bubling fluidized bed steam reformer
IL	Ionic liquid
ILE	Ionic liquid electrolyte

LCOE	Levelized cost of energy/electricity
LFP	Lithium iron phosphate
Li	Lithium
LIB	Lithium ion battery
LiBOB	Lithium bis(oxalato)borate
LiOH	Lithium hydroxide
LiPF6	Lithium hexafluorophosphate
LiSt	Lithium stearate
LNMO	Lithium nickel manganese oxide
LNO	Lithium nickel oxide
MAS	Magic angle spinning (NMR)
MIP	Mercury intrusion porosimetry
Na	Sodium
nano-SCE	Nanostructured solid composite electrolyte
NCA	Nickel cobalt aluminium oxide
NDP	Neutron depth profiling
Ni	Nickel
NMCxyz	Nickel manganese cobalt oxides $Ni_{0.x}Mn_{0.y}Co_{0.z}O_2$
NMP	N-methyl-2-pyrrolidone
NMR	Nuclear magnetic resonance spectroscopy
NOESY	Nuclear Overhauser effect spectroscopy
OPEX	Operational expenses
P2D	Pseudo-2-dimensional model
P2X	Power to products
PAA	Polyacrylic acid
PAH	Poly-aromatic hydrocarbons
PDADMA	Poly(diallyldimethyl)ammonium
PEM	Proton exchange membrane
PES	Polythethersulfone
PFAS	Poly/Perfluorinatedalkyl substances
PFG	Pulse field gradient (NMR)
PGME	1-methoxy-2-propanol
PIL	Polymerized ionic liquids
PITT	Potentiostatic intermittant titration technique
PP	Polypropylene
PV	Photovoltaic cell (or solar cell)
PVDF	Polyvinylene difluoride
SBR	Sytrene butadiene rubber
SEI	Solid/electrolyte interface layer
SEM	Scanning electron microscopy
SHE	Standard hydrogen electrode
Sol-gel	Silica gel
SSIP	Solvent-separated ion pairs
TEOS	Tetra-ethylorthosilicate
TFSI	Bis((trifluoromethylsulfonyl)imide
VC	Vinylene carbonate
XPS	X-ray photoelectron spectroscopy

1. INTRODUCTION

The thesis in front of you contains part of the project result of the H2020 project 'SOLiDIFY' on solid state lithium ion batteries. This project aims to develop a battery architecture with high energy density using scalable liquid processed solid state chemistry. In addition the author contributed to the master Sustainable Energy Technology curriculum in the form of an energy system model building exercise. The outcome of this model building is presented first, introducing the role of energy storage technologies, including battery technologies. The research on lithium battery architectures is presented after that.

ENERGY USE IN EUROPE AND THE REQUIREMENT OF ENERGY STORAGE

The governmental pledges are clear (Paris agreement), the deadline is set (2050) and the race has started. Which technologies are going to win the competition of providing suitable renewable replacements for the usage of fossil fuels? There is fierce competition in multiple disciplines. One needs to first generate energy, be able to store it and finally convert it to the form in which the utility needs it (Figure 1). To date the methods of generating renewable energy provide highly time dependent production peaks. During night times only the wind generates some energy and during daytime an enormous amount of energy is generated from solar irradiance. As one does not have full control over the time at which the energy is generated, the storage of energy has become a major concern. In the field of stationary energy storage there are quite some candidates in the running: (Redox flow) batteries, hydropower, hydrogen, ammonia, e-fuels, and several other upcoming technologies are options which have their individual benefits and drawbacks. In **chapter 1** an optimization of using these options is sought to forecast a relatively probable winner, by estimating the economic impact of replacing all fossil fuels with renewables for generation of energy, complemented with various storage technologies to supply the different energy demands.

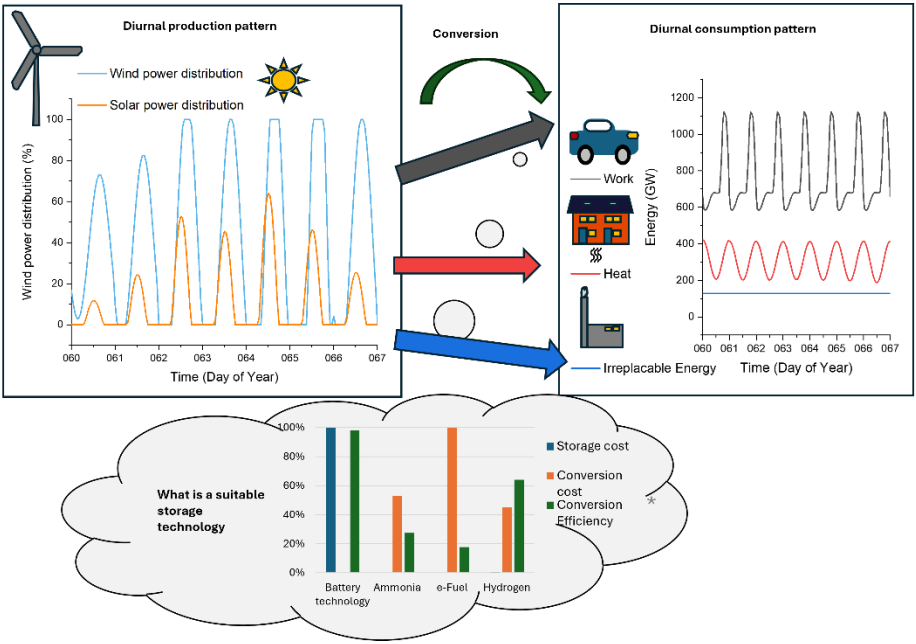

Figure 1: The diurnal nature and type of renewable energy production does not directly meet the demands of our current energy consumption behavior. Several scenario's of energy conversion and storage are modelled to tie the production and consumption. The cost associated with storage and conversion and the efficiency of the conversion create several cost effective scenario's for a completely renewable energy system.

HIGH ENERGY DENSITY BATTERIES FOR SUSTAINABLE ELECTRIFICATION OF TRANSPORT

On the energy consumption side, in the transport sector a big transition to renewable fuels is already ongoing. Often forgotten, replacement of gasoline to ethanol in commodity fuels and usage of biodiesel are currently stimulated by government programs, to lower net carbon dioxide (CO_2) exhaust in the mobility sector without replacing engines. Energy crops, the source of these fuels, are however not a viable replacement as they require too much fertile land, which is also used for food production (**chapter 1**). The big transition therefore has to emerge from either replacing gasoline and diesel by e-fuel (electricity and CO_2 derived fuel), or replacing the fuel engines themselves to either electric or hydrogen powered engines. Most prominent is currently the development of full electric vehicles (EV). Powered by high energy density lithium ion batteries the main advantage is the high roundtrip energy

efficiency of these batteries and their long cycle life which could enable e.g. 500 km times 700 cycles equaling 350000 km lifetime of an EV. The downside of current electric vehicle (EV) batteries is, however, that they demand significant amounts of materials resources. On the anode side of the lithium ion battery (LIB) graphite is used which is derived from mineral coals or oil. The cathode side and the electric connections (current collectors) consist of non-replaceable minerals Nickel, Cobalt, Manganese and Lithium (in $NiMnCoO_2$, or NMC cathode active material), Copper and Aluminium (in the current collectors). Some of these minerals are already scarce and most of them will require additional mining and high purification during manufacturing EV for the global transport sector. On top of that the battery separator and electrolytes are oil derived and the binder and lithium salt contain fluorine to stabilize the electrochemistry, but which makes the resulting battery a potentially poly/perfluoralkyl substances (PFAS) and hydrogen fluoride polluting candidate during manufacturing and recycling.

There is vast research going on to address these problems to make these batteries more energy dense with lower (inactive) materials inventories. Higher energy density will also reduce EV weight and therefore increase overall efficiency. Suitable replacements of the current EV battery standard -being the NMC and lithium iron phosphate (LFP) cathodes versus a silicon-graphite anode architecture- are however scarcely reaching the market. As EV prices generally are not competitive yet compared to fuel vehicles, EV customers typically demand the highest possible performance, and lower performances for driving range are less demanded in the current market. The market, which is increasingly competitive, therefore drives investigation in high TRL architectures which are relatively conservative in choice of chemistry and manufacturing method. With this approach, where developments can be dropped-into existing manufacturing methods, these manufacturing assets can be retained, and therefore previous investments maintained.

In this framework of battery architecture research and optimization, still significant improvement and insight can be gained (**chapter 2 - 4**). In order to reach higher energy and power densities one aims to minimize the supporting non-energy carrying or inactive materials in existing battery architectures. The scientific approach is to investigate the fundamental limits of the materials and the electrode and electrode-electrolyte interface morphology used to maximize their potential within an designed architecture.

Amongst the ideas for minimization of the non-energy carrying 'inactive' parts three options are assessed in this thesis. The most sensible way in making the battery more energy rich is by making the electrodes thicker compared to the current collectors and separators (**chapter 2**, see figure 2 for the proposed SOLiDIFY design). Here the fundamental challenge is to maintain acceptable charging times for EV use. An interesting trade-off between the amount of ions reacting on the internal porous electrode surface (equating to local current density) and the required overpotential driving the rate of replenishment of these ions through the separator surface and entering into the porous network of the electrode.

A second challenge is to replace the graphite anode by lithium metal, giving a potential tenfold increase in charge density at the anode. Here battery operation and manufacturing to date face unresolved challenges. The uncontrolled growth of lithium dendrites during battery charging cause short-circuit safety risks. In addition the presence of lithium metal during battery assembly makes manufacturing costly. The research field in lithium metal anode stabilization is vast. Here the approach of using surfactants in liquid electrolytes as plating moderator, starting with bare copper at the battery anode is reported (**chapter 5**). Such plating moderators could function as an anode stabilizer which reduce the safety risk during operation and would allow battery manufacturing without using lithium metal being present during the processing.

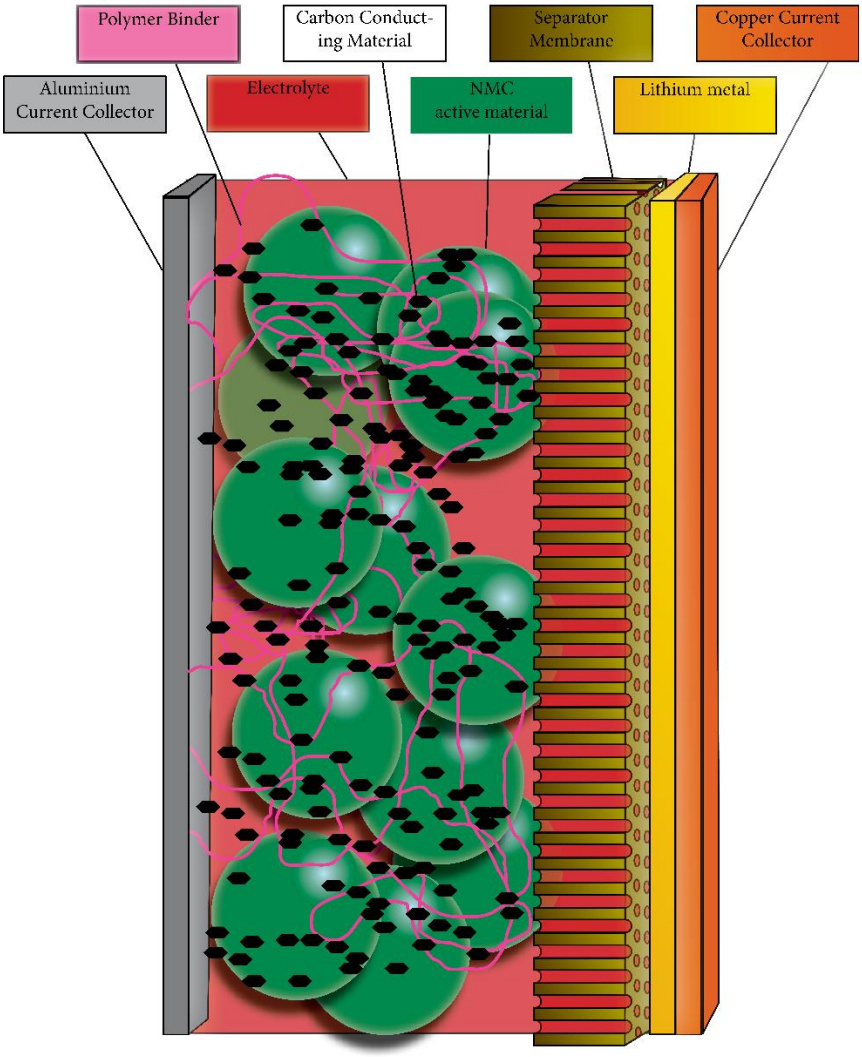

Figure 2: Lithium metal anode – NMC cathode battery architecture as finalized within the SOLiDIFY project: the porous 'trenched' electrode and a separator membrane are impregnated with the liquid electrolyte precursor, after which the electrolyte solidifies. The assembly is subsequently contacted with a lithium metal anode.

The third option which is investigated to increase energy density is battery cell stacking. The inactive material use would go down by making the separators thinner, and stacking the electrodes in such way that cell components are forming a serial network (bipolar stacking). For bipolar stacking a solid state electrolyte may be advantageous to prevent ion contacting between the positive and negative side of the current collector stack which would shortcut the serial connection. Two suitable solid state electrolytes are investigated. The first is a solgel derived solid state electrolyte in which liquid is retained in a porous structure of silica gel (sol-gel) (**chapter 3**). The second is a polymer gel mixed with ionic liquids (**chapter 4**). Both studies investigate the ionic dynamics of these (semi-)solid materials, as the ease of transferring ions through such materials is one of the bottlenecks for using such materials. By investigating the fundamental mechanisms of conductance in electrolytes and porous structures an addition to the fundamental understanding of materials is sought, which would hold for alternative but similar chemistries as well.

CONSIDERATIONS FOR THE CHOICE OF CHEMISTRY

Next to the SOLiDIFY project also other aspects are investigated related to alternatives for some existing LIB components that may be more sustainable. The use of fluorine in batteries is challenged by a completely fluorine free battery which shows performance data well enough for many battery applications (like commodity EV) (**chapter 6**). A quality assessment of a bio-derived graphite anode and conducting additive is conducted, both for Li and the more abundant Na ion battery electrode (**chapter 7**).

The feasibility of using certain battery chemistries at scale may stimulate to prevent mineral depletion and ecological damage. Such directions may provide feasible options during the transition from non-replaceable fossil fuel use in 2050.

After a general introduction on the functioning of batteries in general the subsequent chapters in this work are approached as separate works. The scope has always been to publish and therefor a paper format is chosen to report the findings. The benefit is that one can easily find the details on the individual works in the chapter itself. Every chapter contains a short preface and a small note section for additional context.

PART 1: ENERGY MODELLING

2. TRANSITION TO NET ZERO CARBON EMISSION ECONOMY: COST ANALYSIS OF ALTERNATIVE SCENARIO'S IN THE EUROPEAN ENERGY MARKET

The content of this chapter is in the process of submission to a scientific journal.

Transition to net zero carbon emission economy: Cost analysis of alternative scenario's in the European energy market

ABSTRACT

The necessary investment scale for completely transferring our energy system to sustainable resources seems enormous, and therefore requires a clear policy on which investors can rely. Here practical scenario's for completely renewable energy systems (including solar, wind and biomass) are drawn by comparing current technologies for generation, conversion and storage in terms of energy efficiency and price indications. For this a model is made which uses empirical data and compares the energy generation/consumption mismatch amplitude and frequency of occurrence, to predict a cost effective solution for Europe's energy use. A number of generation and use sites is modelled, representative of the main orders of magnitude of the relevant aspects. As the model is made available, further detailed modelling is facilitated. Results are that wind and solar energy combined with short-term electricity storage is predicted to be most cost efficient to buffer daily demand fluctuations. In addition, the most cost effective scenario primarily uses generation of ammonia by using solar energy for buffering seasonal generation/consumption mismatch. e-Fuels (liquid hydrocarbons from Fischer-Tropsch processing) from wind energy, are used to continuously provide hydrocarbons for chemicals. Using current technology costs the energy cost per EU capita would almost double. However, the very significant necessary scaleup of generation and conversion assets to meet EU goals by 2050 is that large, that the economies of scale may be expected to lower unit costs. When such economy of scale effect is accounted for, this lowers the eventual asset pricings. By 2050 one may therefor obtain an affordable energy cost while realising a green energy economy and maintaining current energy using activity levels. Affordable also in relation to the downscaling of fossil asset use, while fossil exploration and production costs may rise.

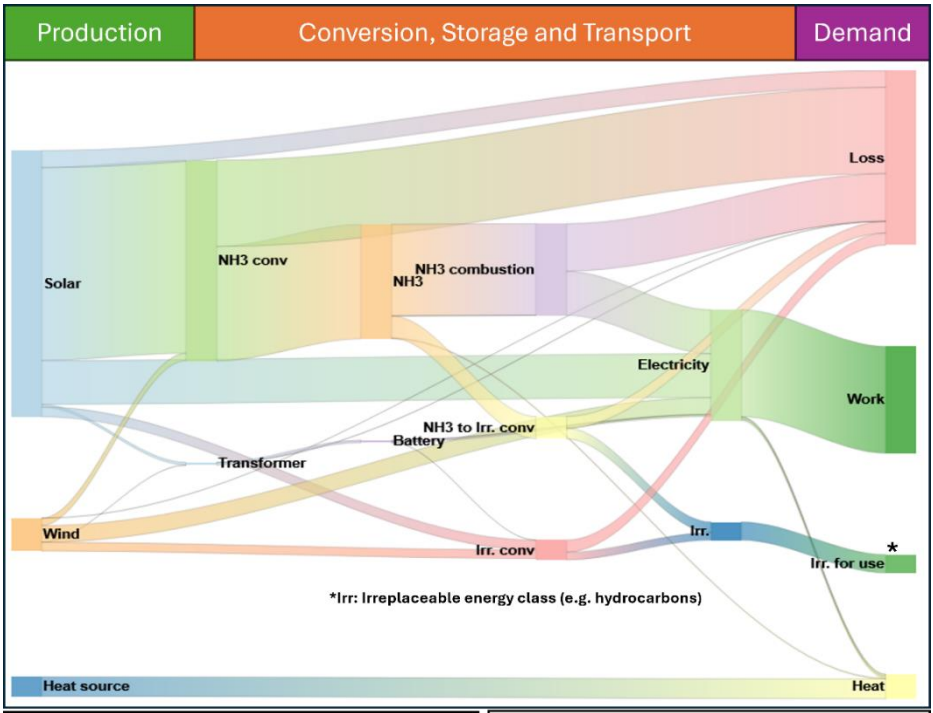
Production
Conversion, Storage and Transport
Demand
Solar
Wind
NH3 conv
NH3
NH3 combustion
Transformer
Battery
NH3 to Irr. conv
Irr. conv
Electricity
Loss
Work
Irr.
Irr. for use
*
*Irr: Irreplaceable energy class (e.g. hydrocarbons)
Heat source
Heat

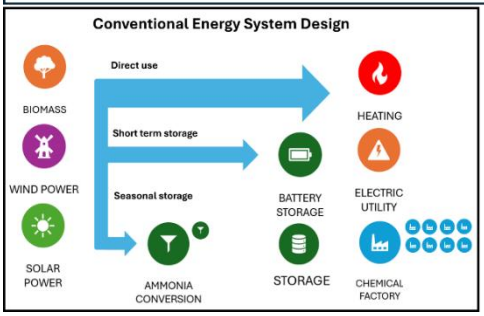
Conventional Energy System Design
BIOMASS
WIND POWER
SOLAR POWER
Direct use
Short term storage
Seasonal storage
AMMONIA CONVERSION
BATTERY STORAGE
STORAGE
HEATING
ELECTRIC UTILITY
CHEMICAL FACTORY

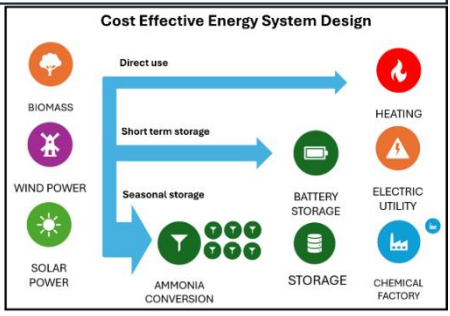
Cost Effective Energy System Design
BIOMASS
WIND POWER
SOLAR POWER
Direct use
Short term storage
Seasonal storage
AMMONIA CONVERSION
BATTERY STORAGE
STORAGE
HEATING
ELECTRIC UTILITY
CHEMICAL FACTORY

Transition to net zero carbon emission economy: Cost analysis of alternative scenario's in the European energy market

INTRODUCTION

The ambition to migrate from non-renewables to suitable replacements is agreed upon by most countries during the past UN Climate Change Conferences and other meetings. The European union has set out a target to cut carbon emissions by 55% in 2030 and become carbon neutral by 2050.[1] The US had set the same target to become carbon neutral (2050)[2] and other major industrial nations likely will follow, like China (in 2060)[3] and India (in 2070)[4]. Translation of this political ambition to implementation is one of the biggest technological challenges of the 21st century.

The daily and seasonal energy mismatch[5] can be identified as an emerging problem as supply from renewable sources increases. The energy production scale will necessarily overshoot average energy demand to make up for low production hours, and moderation using coal and gas fuelled electricity generation needs to be phased out as well. A wide amount of scenario's can be drawn to evaluate which investments are necessary to change our energy system into a fully renewable one. As a tool there are several models available which simulate energy system scenario's.[6,7] In e.g. Pickering et al.[8] a large number of options are studied. However, the technical potentials of the generation methods solar PV and wind need to be assessed as well to come to an energy system that fits in the land availability and socially acceptance within the EU (see e.g. SI 1.2 on the allowable energy harvest of wind parks). For drawing conclusions on scenario's, one needs to model the necessary scales of energy production, storage and conversion assets to be installed when a complete migration to suitable energy replacements is realized. The model type for such scenario development, called 'Optimization energy model', is selected.[9] In such model a complete energy system optimization is carried out to find the minimum energy cost while it satisfies the complete energy demand throughout the year as constraint, and where other constraints on the methods for generation of energy can also be included.

In this paper Europe's energy system is chosen, as Europe has stated clear goals to become completely sustainable in 2050. Also, to feed such model empirical data on energy consumption is necessary as starting point, as well as the consumption pattern of a typical Western European citizen. Both facets are studied prior to this work. For example, in a previous approach a pan European – North Africa copper-plate electricity grid was assumed [5]. Here Europe is considered as a closed system, so without imports, and the consequence of such approach can be discussed. The scenario

discussed first showcases the unconstrained model energy production, after which constraints are added which tie with current ambitions stated by the EU, like incorporating the projected installed capacity of windpower and restricting the use of biomass to practically attainable levels (indicated here as fuel crops). This paper also discusses the cost implications of a completely sustainable energy system in the case where society maintains using green fuel combustion engines. The scenario's shown are only a limited set of the possible ones, showcasing the ease of using the freely available model to make such projections. Also extension to wider regions with their generation and use characteristics can be made. The chosen scenario's, however, highlight the urgent need to draw a clear strategy choices to meet the 2050 deadline.

METHODS

The model calculates the annual investment costs to maintain an energy network. An overview of the model layout is shown in **Figure 1**. To provide input for the model, empirical data from two databases is used. The net energy production and consumption depends on the local weather and climate. Therefore meteorogical data from ECA&D[10] is used to provide input to predict local daily solar and wind production, and energy consumption patterns (**SI Ch 2.1**). The database contains data with quarter hour resolution of which the last reported year is taken. Averaging is not used to prevent smoothening of weather patterns, which might provide shortage of energy in the short (hour/day/night) or somewhat longer term (dunkelflaute scenario). Meteorogical data is directly translated to diurnal power output (%) from producers as such. The annual energy use in individual EU countries is reported by Eurostat in the year 2022.[11] This data discerns various fuel types used in various sectors like household, industry and agriculture. These sectors and fuel types are used to scale the appropriate fuel consumption patterns like heat utility, electric utility or feedstock materials. The various fuel types currently used in the European mostly fossil market data will not be directly comparable to the (electric/biomass) output of the future green producing sites. The following two paragraphs highlight the necessary calculations which link input data to a common unit descriptor.

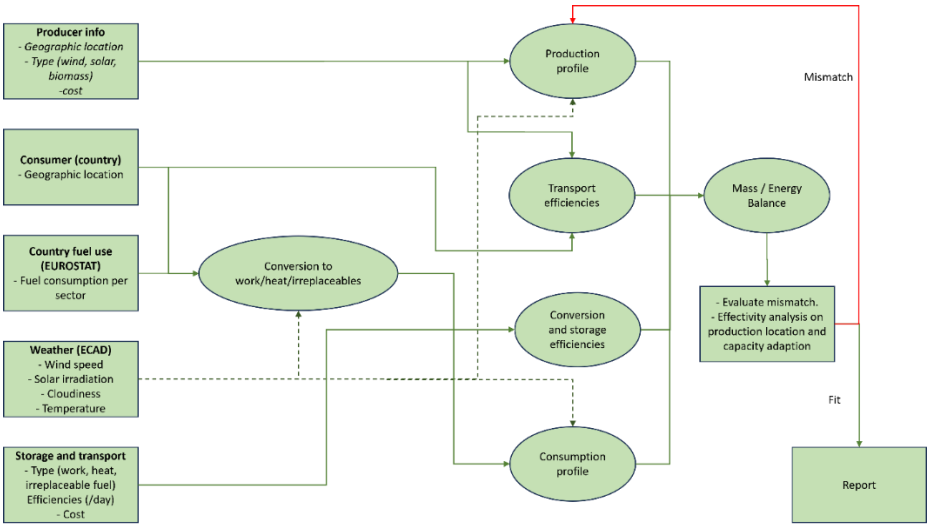

Figure 1 Model outline. Data is obtained from three databases and converted to a common unit descriptor. Consumption and production profiles in time for the whole year are subsequently fed to a mass/energy balance solver. The mismatch is also a pattern in time and place. The storage pattern results from compensating the mismatch. After this the most effective production site is scaled and this is iterated until a complete match is obtained.

The range of available fuels in our energy system have a common energy unit (kWh). The possible energy efficiency of fuel use varies however a lot. As an example one can imagine the usage of electric power in heat pumps ($\eta = 4 - 6$, by extracting heat from surroundings depending on air-source or ground-source[12]) is much more efficient than gas powered heating ($\eta < 1$). Added that the amount of reported fuel types in the database is quite broad, this would potentially make comparing fuel types complex. There is however a common descriptor in energy system simulation which incorporates the quality of the energy. This energy quality needed to meet the wanted utility is known as exergy.[13]

Only four utility classes are necessary in the exergy framework for energy mismatch modelling. Apart from biomass the common inputs from solar and wind sources is electricity. The highest exergy classes include heavy machinery and industrial heating, in which high power output and a large range of (high) temperatures are necessary. Suitable energy carriers range from high caloric combustion fuels like biodiesel,

synthetic (e-)fuels to electricity. The middle exergy class include consumers appliances, heating, ventilation, air-conditioning and transportation. The lowest exergy class include low temperature heating (< 40 °C). A fourth class not directly recognized in the exergy classification, but necessary to include in energy models are hydrocarbons or other energetic compounds (like chars, cokes, sulfur) which are used as raw material in the chemical industry for manufacturing paints, plastics, fine chemicals, lubricants, batteries and many more commodities. This exergy class is called 'irreplaceables', because the specific energy carrier itself is necessary as input for industrial consumers. A more elaborate discussion on the exergy classes can be found in SI 1.3.

The model approach is to vary the scale of production facilities to meet current energy consumption habits in their respective exergy classes. The analysis of cost effectiveness of all 'Producer – Storage – Transport – Consumer' route possibilities is performed based on production and consumption patterns. The appropriate route is subsequently allocated starting from the most cost effective option down to less cost effective ones. For instance, initially the model typically fits usage of wind energy combined with direct use, or a few hours of battery storage, and ties this to a 'work'-exergy-class consumer 365 times per year. After allocation of these routes the (less frequent) remaining energy need by this consumer may fall below a threshold usage frequency at which the route through battery storage is cost effective. This then in this example may cause solar energy combined with long term storage to be selected as more cost effective to satisfy the residual need of energy for this consumer. The storage facility scaling is thus a mere result of the cost effectiveness analysis and subsequent allocation. The model results in an energy balance throughout the year for each storage facility and transport line, which then yields the necessary storage capacity by integrating the energy balance over time. The least cost effective route will be allocated last, giving insight in the problematic periods and exergy classes during a year, as they are solved during the last few iterations.

Cost effectiveness calculations of conversion and transport are performed using cost estimates and energy conversion factors of some known scalable technologies [**SI Table S2**]. A known short term storage utility (like (EV)-battery type storage) and a few promising long term storage utilities (liquid hydrogen, ammonia, e-Fuels and heat storage) are incorporated, together with storage of biomass as (e)fuels. e-Fuels is a term used for suitable liquid storage fuels derived from either biomass or the Fischer-Tropsch process which is valuable for use as energy source and chemical feedstock.

First the energy efficiencies η of all possible consumption to production routes (spatial and temporal) are calculated using Eq. 2. Here consumer *C* may acquire energy $E_{c,t2}$ [kWh] at time t_2 from producer *P* after multiplication of energy efficiency values η [%] for conversion *conv*, storage *S* for period $dt=t_2-t_1$ and transport *T* over distance *dx*. References for efficiencies of storage, conversion and transport are summarized in [**SI Table S2**]. A final conversion from transport exergy to desired consumption exergy class $t \rightarrow c$ may also be included. For directly used energy, $dt=0$, and $\eta_{S,dt} = 1$.

$$E_{p,t1} * \eta_{conv-p\rightarrow s} * \eta_{S,dt} * \eta_{conv-s\rightarrow t} * \eta_{T,dx} * \eta_{conv-t\rightarrow c} = E_{c,t2}$$

Eq. 1

$$\eta_{route,consumer} \left[\frac{kWh\ received}{kWh\ produced}\right] = \frac{E_{c,t2}}{E_{p,t1}} = \prod_i \eta_i$$

Eq. 2

Then the associated cost of storage, conversion and transport is calculated including the energy loss term using the energy efficiencies (Eq. 3). For every unit operation an annual price per rated kW(h)/year is made based on CAPEX, OPEX and depreciation (**SI Table S2**). The effectiveness of using the unit operation during that year is however depending on the frequency of usage (for storage and conversion units) or location (production units). A challenge in cost efficiency calculation is incorporating the different units *i* for production, conversion and transport [Euro/kW installed/year] and storage [Euro/kWh installed/year]. The cost efficiency calculation is therefore approached using a projected annual 'route' usage frequency *f* to arrive at a projected capacity factor *CF.* The *CF* projection is done by evaluating the (mis)match frequency between a producer and a consumer using a Fourier Transform method [**SI Ch. 2.5**]. Energy losses of every previous processing step are accounted for by multiplying with conversion efficiencies η_j of units j upstream to arrive at unit i $cost_{i,route}$ specifically for the estimated frequency and energy which needs to be converted/stored/transported. All the utility costs are summed and divided by the total route efficiency $\eta_{total,route}$ which is the product of all conversion and storage efficiencies, yielding the projected consumer energy cost per year (Eq. 3).

$$cost_{route,consumer}\left[\frac{euro}{kWh\ received * year}\right] = \frac{\sum_i cost_{i,route}}{\eta_{total,route}} = \frac{\sum_i (cost_{unit,i} * 1/CF_{unit,i} * \prod_{j=1}^{i-1} \eta_j)}{\prod_i \eta_i}$$

Eq. 3

The resulting cost remains merely an indication: it projects the cost of providing energy from a specific producer to a specific consumer, incorporating a possible storage time interval in an isolated scenario (**Figure 2**). The model does not include combined use of production, conversion and storage facilities as it does not perform repeated (mis)match frequency estimation after allocating energy routes. This might lead to cases which underestimate the cost of overpopulated matching frequencies, causing energy overproduction to fulfil the calculated frequency prediction instead of combined usage of assets. This approach however serves well as the best guess for appropriate allocation of the most cost effective routes. Further discussion concerning the chosen nodes can be found in SI 1.1.

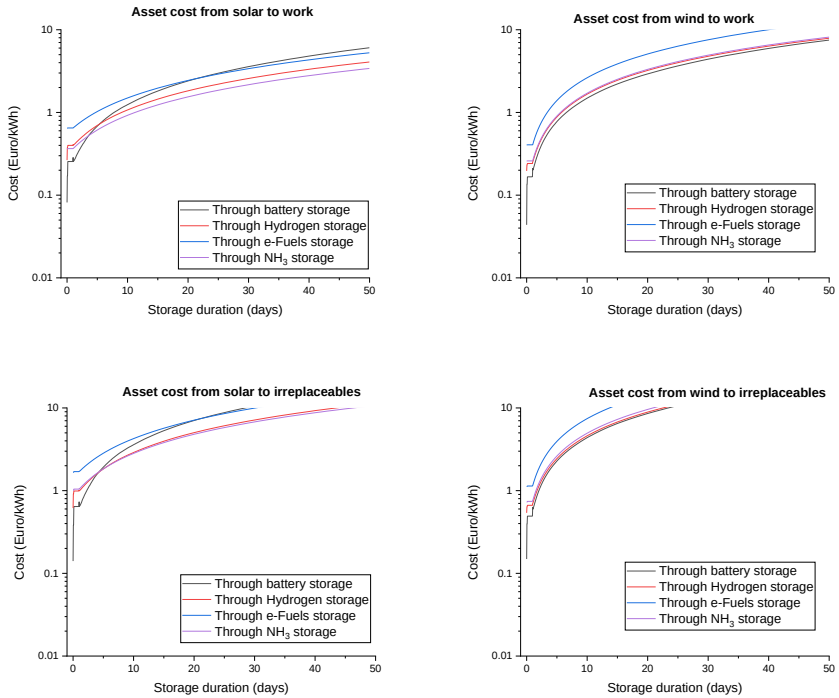

Figure 2 Estimated cost of providing solar (left) and wind (right) energy to work (top) and irreplaceables (bottom) exergy classes. Frequency analysis of production/consumption mismatch adjusts the estimated frequency the asset is used. Majority of the cost is associated with conversion and storage (Storage duration of 0 days to >0 shows a jump). Typically battery storage is preferred for short duration storage (<5 few days). Depending on the mismatch frequency and cost of energy production assets, battery storage or NH_3 storage are shown to be most cost effective. Only for moderate storage durations (5 – 10 days) e-Fuels from solar for consumption as irreplaceable exergy class appears to be cost competitive. Asset costs from wind to irreplaceable exergy class with a short term storage period are lower compared to solar, due to an improved utility percentage for these assets as diurnal production and consumption patterns show a better match.

After calculating all the possible routes their energy efficiency and cost effectiveness the routes are allocated starting from the most cost efficient one to the least cost efficient one. The excess or deficit energy from the production or consumption is stored on the energy balance of that producer/consumer node for the next iteration. The net amount of energy allocated by using storage, conversion and transport assets is stored as well. The energy distribution is carried out using conventional energy balance calculations on the hourly consumption and production energy patterns using the route energy efficiencies.

Production site capacities are defined as the optimization variables in a constrained solver (Matlab *fmincon*[14]), which uses parallel processing to solve the cost minimization problem. Here minimizing cost $COST_{total}$ *[euro/year]* of maintaining all assets for the duration of a year is set as objective function (Eq. 4), with producer (*p*), consumer (*c*), storage (*s*) and transport (*t*) costs. A completely satisfied consumer residual energy $\sum E_{c,residual} = 0$ is added as a constraint (overproduction and therefore curtailment at zero additional cost is allowed). This calculation results in a complete diurnal solution which shows the minimum investment scenario based on *a priori* utility estimation.

$$\min\left(\sum COST_{total}\ [\frac{euro}{year}]\right) = \min\left(\sum COST_p + \sum COST_c + \sum COST_s + \sum COST_t\right)$$

Eq. 4

The interest of the scenario's depicted in **Table 1** lies in predicting the costs of energy after replacing all fossil energy sources by renewables.

Boundaries and exclusion exercises in the modelling

Wind power is allowed to scale freely in the first two scenario's, and is restricted to a maximum installed level deemed accetable for the European Commission in view of land-use in the other scenario's[15]. The maximum usable wind power is set to 600 GW rated capacity, which, with an estimated 50 GWh on sea (prognosis 2030) would require an areal occupation of 5% throughout Europe (using 1 MW/km^2 areal energy density).

The solar power scales unlimited to reach the total demand. Biomass is restricted to a feasible amount per year in line with the magnitudes of sustainable biomass use discussed in various publications.[16,17] More strict consideration of the effective emission factors as highlighted in [18] would point towards additional carbon sequestration requirements when limiting biomass to zero emission solutions. Nuclear power is omitted in view of the anticipated high cost compared to sun and wind[19] and the uncertainty of costs of the required nuclear fuel breeding, recycling, and waste treatment infrastructure. In addition it will also require similar electricity input power storage infrastructure to sell its electricity in a market competing with other renewables; a power level of 20% of the installed nuclear capacity may be necessary.[20]

Insight in the marginal costs of the 'irreplaceable' exergy class (renewably produced chemical feedstocks) is obtained when omitting the current demand for hydrocarbons. Also scenarios are defined which use biomass as an energy source rather than as irreplaceables source, to see if biomass can play a role as replacement of fossil derived fuels. Models without electrification of the transport sector give an insight the impact of such choice. The model is designed in such a way that nodes, technologies, and prices can be easily adjusted. By making the code available the authors encourage to develop similar variations of relevant models.

Table 1 Short description of model scenario's evaluated in this paper.

Scenario	Short description
Wind, Solar and Biomass	Unrestricted production capacity scaling, incorporating wind, solar and biomass production types, using all short and long term storage options to fulfill the need of energy for work, heat and irreplacable exergy classes in Europe.
Wind, Solar and Biomass, without Hydrocarbons demand	Unrestricted production capacity scaling, incorporating wind, solar and biomass production types, using all short and long term storage options to fulfill the need of energy for work and heat exergy classes, without irreplaceable exergy classes in Europe to estimate only the necessary fuel use for energy purposes.
Solar and Biomass, Restricted Wind	Restricted capacity scaling incorporating a limited amount of wind energy production to mimic EC 2050 goals and unlimited solar and biomass production, using all short and long term storage options to fulfill the need of energy for work, heat and irreplacable exergy classes in Europe
Solar and Biomass, Restricted Wind,	Restricted capacity scaling incorporating a limited amount of wind energy production to mimic EC 2050 goals and unlimited solar and

Without Hydrocarbons demand	biomass production, using all short and long term options to fulfill the need of energy for work and heat exergy classes, without irreplacable exergy classes in Europe to estimate only the necessary fuel use for energy purposes.
Solar and Biomass, Restricted Wind, Without Hydrocarbons demand, Scaled	Restricted capacity scaling incorporating a limited amount of wind energy production to mimic EC 2050 goals and unlimited solar and biomass production, using all short and long term options to fulfill the need of energy for work and heat exergy classes, without irreplacable exergy classes in Europe to estimate only the necessary fuel use for energy purposes. Using pricing of estimated final scale of production, conversion and storage facilities.
Solar and Biomass, Restricted Wind, only NH_3 storage	Restricted capacity scaling incorporating a limited amount of wind energy production to mimic EC 2050 goals and unlimited solar and biomass production, using short term storage and long term NH_3 storage options to fulfill the need of energy for work, heat and irreplacable exergy classes in Europe
Solar and Biomass, Restricted Wind, only NH_3 storage, Scaled	Restricted capacity scaling incorporating a limited amount of wind energy production to mimic EC 2050 goals and unlimited solar and biomass production, using short term storage and long term NH_3 storage options to fulfill the need of energy for work, heat and irreplacable exergy classes in Europe using pricing of estimated final scale of production, conversion and storage facilities.
Transport not electrified. Restricted wind	Restricted capacity scaling incorporating a limited amount of wind energy production to mimic EC 2050 goals and unlimited solar and biomass production, using all short and long term storage options to fulfill the need of energy for work, heat and irreplacable exergy classes in Europe in the scenario that electrification of the transport sector is not implemented.
Transport not electrified. Restricted wind, all electric	Restricted capacity scaling incorporating a limited amount of wind energy production to mimic EC 2050 goals and unlimited solar production, using all short and long term storage options to fulfill the need of energy for work, heat and irreplacable exergy classes in Europe in the scenario that electrification of the transport sector is not implemented.
Transport not electrified. Restricted wind, only NH_3 storage	Restricted capacity scaling incorporating a limited amount of wind energy production to mimic EC 2050 goals and unlimited solar and biomass production, using short term storage and long term NH_3 storage options to fulfill the need of energy for work, heat and irreplacable exergy classes in Europe in the scenario that electrification of the transport sector is not implemented.

RESULTS

The representation of fuel consumption in their exergy class (**Figure 3**) implies that effective energy use becomes 76% of our current 2022 consumption, i.e. less energy is required to reach the same overall functionalities. The cause of this reduction is primarily the transition from fuel combustion engines in the transport sector to 'work' exergy. The work exergy of electric transport from battery to wheel is much higher (85%) while the fuel combustion to wheel has efficiencies that are generally low (weighted averaging for 15% and 31% of gasoline and diesel efficiencies respectively[21,22] yields η=23%). However, in the model, if one would choose the scenario to convert e-Fuels to work for this purpose that would reverse this potential reduction (so in case one would power the EV with electricity generated from burning an eFuel in a gas fired powerplant). Utilisation of the efficiency gain therefore depends on the actual production of sufficient electricity for the EV during their charging periods, and which type of storage is required for safeguarding that electricity availability throughout the year. Similarly there is also a great potential energy use reduction possible by using electric heat pumps, as energy necessary for heat is a major fraction of the total energy consumption (18% of total). Essentially low caloric heat can be generated by extracting heat from air or (underground stored) water using electricity with above unity efficiencies, or high coefficients of performance (up to 3 or 6 respectively for air and ground sourced). Note, however, that here too the electricity has to be available during heat demand, which may still partly come from stored energy, especially when considering space heating in winter. Finally, the exergy classification shows that only 12% of Europe's current energy need is used as irreplaceable exergy in the form of mainly hydrocarbon feedstocks. Still this amount of hydrocarbons is higher than the amount that may be provided by harvesting biomass energy crops.[5,23] Perhaps surprisingly the non-biomass routes in all scenarios appear lower cost than the biomass route, in part because the non-biomass route has to be installed anyway to come to sufficient production levelof irreplaceables. This is in line with Carus et al.[17] stating that 80% of future carbon demand has to come from other solutions than biomass.

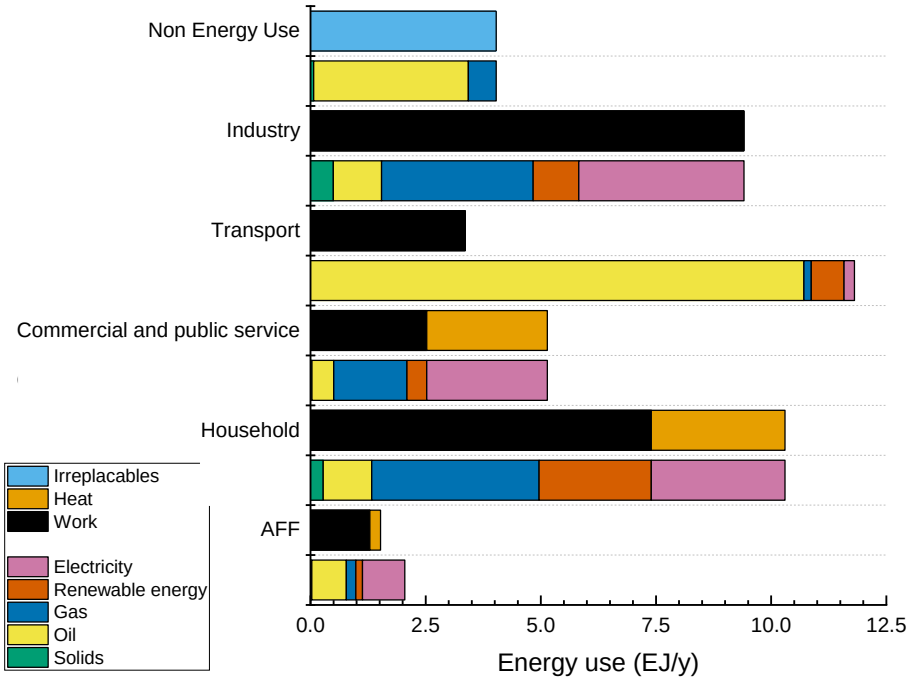

Figure 3 Per sector the exergy content (top bar) of the 2022 energy use (lower bar) of Europe is shown. (2022, Eurostat). AFF stands for Agriculture, Fishery and Forestry. In transport the exergy is much lower than the mainly fossil energy use. which identifies a major potential for minimization of the total demand of energy when high exergy technology (electrified transport) is adopted. Heat also offers a potential reduction of necessary energy production as it can be harvested with efficiencies higher than unity using heat pumps. Industrial fuel types are typically used for work or to maintain temperatures above 40 degrees Celsius, also categorized as work exergy. The industrial non energy use of fossil fuel is chemical feedstock use.

Figure 4 shows the model 3 output for selected days for an all-electric, wind restricted scenario (the necessity for wind restriction coming from space limitations is discussed further). The results can be divided in model input consumption patterns (**Figure 4**C), the meteorological influences on production (**Figure 4**A, B) resulting in the output-scaled production and storage patterns (**Figure 4**D and E/F respectively). The distribution of energy in the different scenario's is shown with Sankey diagrams which are included in SI Ch. 4. From calculations using empirical wind and cloudiness data, typical daily fluctuations are observed at production regions (**Figure 4**A and B respectively).

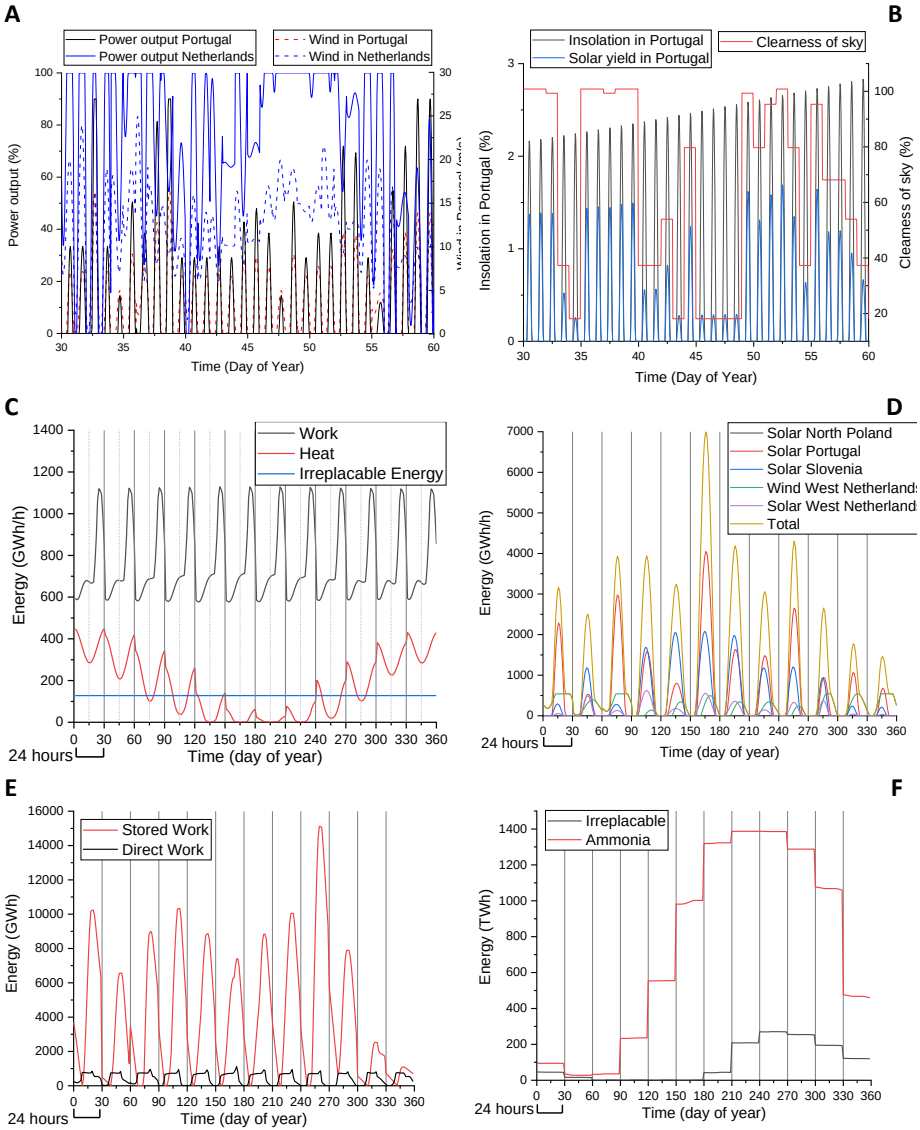

Figure 4. Overview of diurnal model output at various levels. Model output of scenario 'restricted wind' is shown. Top: Empirical meteorological data (ECA&D, 2021/2022)[15] is converted to power output of local production sites. Period of the year is shown for Wind with its weather dependent variation (A) and Solar with its clearness of sky dependent output (B) energy production. Middle: Average European demand expressed in exergy classification throughout a year (C), hourly production of renewable energy sources

during 24h on the selected days indicated (D). Note the much higher vertical scale in the production compared to the demand. Bottom: Storage hourly demand and direct delivered work necessary to fit the demand in C (E) and long term energy storage filling factor (F). On a day only a part of the necessary production (~1 TW) can be directly used compared to the necessary short term storage (~15 TWh per day) due to the lower generation at night, and long term storage (similar order, ~400 TWh/30 days increase during summer periods). Overall capacity requirement for long term storage corresponds to a max filling in August/September of about ~1400 TWh. X-axis of C, D, E and F indicate a 24 hour period on day 30 of the year from 0 to 1, 24 hour period on day 60 from 1 to 2, etc.

The model scenario's described in **Table 1** show differences in the necessary scale of production, conversion and storage (**Figure 5**). Two representative Sankey diagrams are shown in **Figure 6** for the scenario 1 and 7 highlighting the large losses associated with conversion to long term storage fuels. Solar PV, wind and heat are the renewable energy inputs here, where low temperature heat is driven by electric heat pumps and high T heat is under work exergy. Scenario 1 shows possibly the most energy efficient scenario, at large because it has no limitations on generation of wind power which matches the energy use pattern better than solar power. Scenario 7 is less energy efficient overall, but obeys space limits on the windpower and therefore is more socially acceptable; it has more solar power and associated long term storage needs and conversion losses as well as curtailment. Nevertheless both models can supply the required energy for the different exergy classes 24/365.

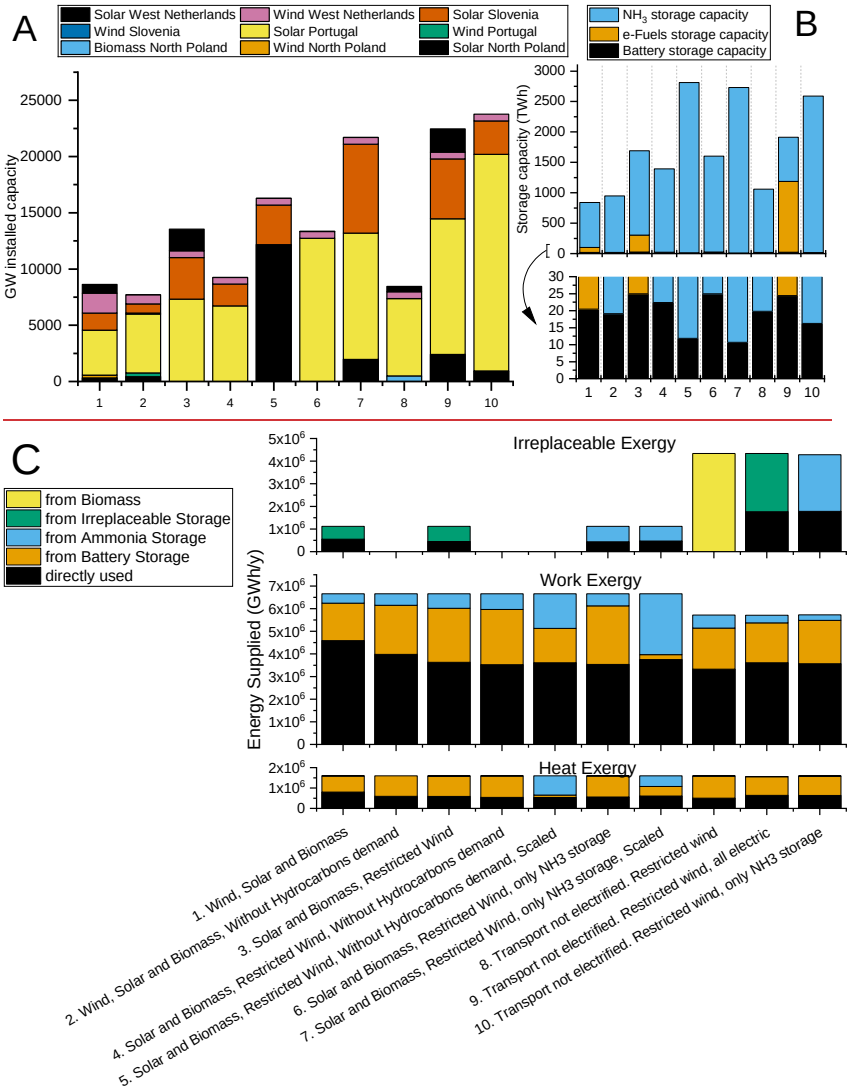

Figure 5 A) Energy systems implementation and storage capacities and energy supply for different exergy forms in selected models. A) Capacity of energy production assets. B) storage assets in various cases as discussed in the text for a completely renewable EU energy system. C) The annual energy supplied to satisfy the demand from production facilities per exergy class, either directly or through temporary storage. Depending on the (numbered) scenario a preference can be observed for direct supply, battery storage or ammonia storage solutions.

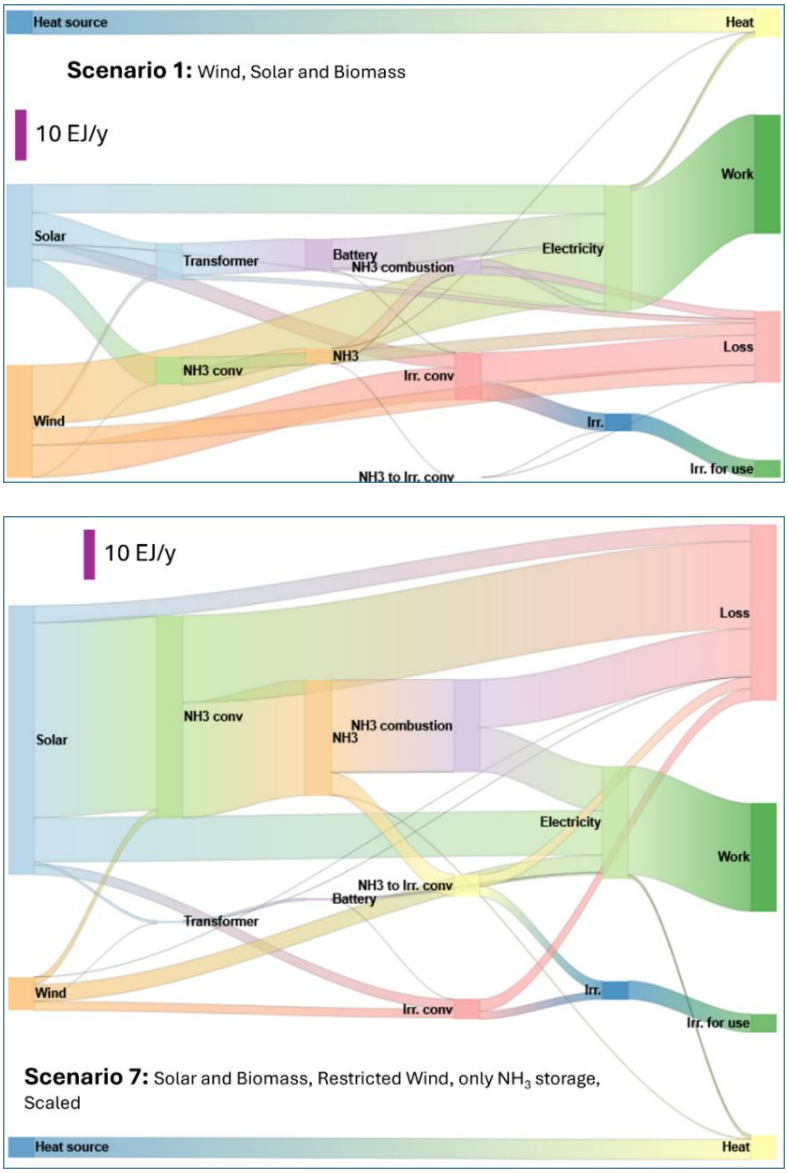

Figure 6. Sankey diagram for scenario 1 and 7. The different generation amounts, their utilization in different exergy classes Work, Heat, Irreplaceables, and the losses incurred in the process either as direct curtailment or losses from storage, conversions, and transport of energy. Biomass sourced as fuel crops is included as model input energy source. Cost effectiveness of this specific source is however predicted to be lower than other energy production assets combined with storage.

The associated costs for maintaining the energy system is shown in **Figure 7**. Each scenario result is described in a separate headings in SI 1.6. To show the impact for individual citizens the annual energy cost breakdown is expressed in cost per capita (**Figure 7A**). Also a net projected energy cost is calculated (LCOE, **Figure 7B**) The model itself uses a discount rate of 0% as it aims to show the lowest annual investment costs to maintain the energy system. **Figure 7B** however shows the LCOE with a discount rate of 12% (usage of interest rate and inflation in LCOE is discussed in SI 1.4). The LCOE is limited to production, conversion, transport, and storage assets, with generated and utilized energy in the denominator. Curtailment results in less energy used per installed capacity and therefore higher LCOE. Generally the LCOE of energy production assets don't vary much. The utilization of conversion and storage assets however change depending on the scenario's. Interestingly what can be observed is that in the case of a restricted wind scenario with both ammonia and e-Fuel storage options, both electricity to fuel conversion asset types show a high LCOE (0.78 and 1.20 €/kWh respectively). When using only ammonia as storage carrier the direct production of ammonia from electricity becomes less efficient while e-Fuel conversion from ammonia as hydrogen feedstock is utilized more effectively at higher capacity factor, resulting in a change to 0.25 €/kWh and 0.04 €/kWh respectively. Also the battery costs are relatively high (0.16 to 0.42 €/kWh). In scenario's 3 and 9 the e-Fuels conversion and ammonia conversion assets show a high LCOE respectively. In both cases the model underutilizes these assets by allocating only a small fraction of (solar) generated energy for long term storage due to a bad frequency fit between peak production to it's consumer. In the case of scenario 3 this is tied to limited utility of e-Fuels conversion for continuous supply to irreplaceables class. In the case of scenario 9 this is the result of limited use of ammonia when energy necessary for transport is defined as irreplaceables exergy class at the cost of work exergy. This highlights the LCOE should be appreciated as a representation of the expected price fluctuation during a year while serving a specific function (as short or long term storage carrier, or conversion for e-Fuels to continuously serve the irreplaceables demand in scenario 6). The price itself does not show if various assets are utilized effectively to achieve the lowest overall cost.

The long and short term storage appear to determine the overall total energy costs, while wind and solar contribute less costs. One could hypothesize that lower costs should be reached by building more sun and wind as the LCOE of these assets are an

order lower compared to storage and conversion assets. However, this does not appear in the optimization, as the boundary condition poses that energy should be available to supply the instantaneous demand always to provide an energy secure system. Therefore the dispatchable (costly) stored energy has to be available at sufficient scale anyway in all cases; blackouts cannot occur. Such is in line with the observed 'dunkel flaute' occurring in November-December 2024 leading to extreme electricity prices in Western Europe.

An iteration implementing cost adjustments according to the economy of scale factorization of *Way et. al*.[25] at *final* scale (alkaline) electrolyser costs are 20% of the current price, reducing the cost for conversion of electricity to e-Fuel and ammonia (53%) as well (see SI 1.5 for discussion on cost implications for scaling for various assets). Also PV cost is reduced to 20% of the current price and wind power prices are reduced to 50%. The resulting cost reduction using ammonia as storage carrier amounts to 29% compared to the same scenario without scale factors included (**Figure 7A**, case 'Solar and Biomass, Restricted Wind, only NH3 storage, Scaled'). Compared to our current energy cost the scaled renewable energy system is 77% more expensive in the model, but would make the energy market completely independent of fossil derived fuels and energy. It therefore would prevent the costs associated with more climate change effects, and also would prevent the possibly increasing costs for fossil fuel exploration and use. When applying cost scaling factors to the scenario in which irreplaceables are not taken into account, the energy cost will be only 27% more expensive to our current energy cost, illustrating the impact of irreplaceables on the energy costs (**Figure 7**, case 'Solar and Biomass, Restricted Wind, Without Hydrocarbons, Scaled').

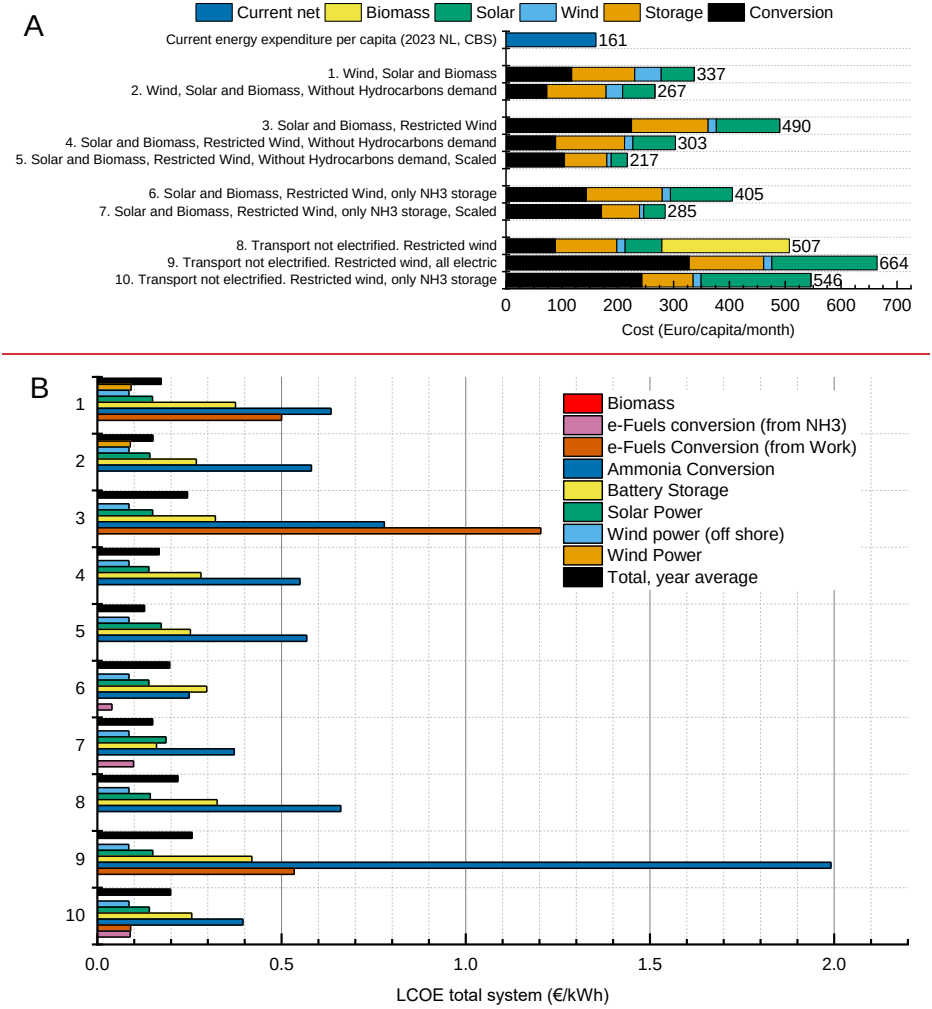

Figure 7. Cost estimations in various scenario's. A) Projected monthly cost per capita of completely renewable energy scenario's taken (Energy use data of 2022).[11] Cost buildup is showing the production types, storage and conversion cost. Marginal costs for producing hydrocarbons as feedstock chemicals can be compared by comparing 'without hydrocarbons demand' scenario's with the ones including the irreplaceable exergy class. For comparison the monthly energy expenditure for a Dutch citizen in January 2023 is shown (including transport, electricity and heat costs without temporary cost reductions).[24] To obtain the total costs per year in Europe, multiply with the population of 448 million EU inhabitants and 12 months. B) Levelized cost of electricity contributions of individual assets in the energy system. Total

projects the annual investment necessary to effectively supply all energy demand. Individual assets are calculated using their effective annual energy throughput as relative weights into the total. Note that biomass has no contribution to the sLCOE as it is not chosen for the electricity supply.

DISCUSSION AND CONCLUSION

A model is developed to create an understanding of the possible strategies for solving the complete replacement of non-renewable fuels in our energy system, creating a stable future energy system based on renewables only. The rather complex energy landscape containing various energy carrier types is simplified to create clarity on the scale and diurnal and seasonal nature of our current energy and feedstock consumption behaviour. For this simplification, conversion to more general exergy classes was necessary, which then allowed comparison of potential technology investment scenarios for storage, conversion and transport solutions. As a result the model offers insight in the necessary investment per capita or per generated energy amount, to replace the current non-renewable fuels. In all scenario's the cost of storage and conversion exceed the cost of generation. This is partially the result of relatively low learning rates and cost reductions of the currently still limited upscaling of the technologies involved. In a fully upscaled situation, however, the costs would come down, as indicated in the 'Scaled' scenario's, but not fully reach the current fossil cost level. In a future more depleted of fossil fuels, however, also the fossil system costs may increase as depletion makes costs of their discovery and exploration rather go up, which is not modelled here. One should also realise that the green energy system then includes energy independence from fossil fuels and their suppliers, a way out of the global warming fossil CO_2 emissions, and a potential reduction of high climate mitigation costs.

For the optimal system one observes that short-term frequently cycled, and long-term annually cycled storage options are required. The LCOE costs of those may be anticipated to be rather similar as otherwise it would be more affordable to build out either one to guarantee security of supply, which stops as soon as it becomes equally expensive as the other option. In line with that we observe similar LCOE resulting for battery and ammonia fuel costs in most scenario's.

REFERENCES

(1) European commission. State of the Union 2030 Climate Target Plan. *23-12-2022*.

(2) Fam, A.; Fam, S. Review of the US 2050 Long Term Strategy to Reach Net Zero Carbon Emissions. *Energy Reports* **2024**, *12*, 845–860. https://doi.org/10.1016/j.egyr.2024.06.031.

(3) Zhao, X.; Ma, X.; Chen, B.; Shang, Y.; Song, M. Challenges toward Carbon Neutrality in China: Strategies and Countermeasures. *Resources, Conservation and Recycling* **2022**, *176*, 105959. https://doi.org/10.1016/j.resconrec.2021.105959.

(4) Das, N.; Murshed, M.; Rej, S.; Bandyopadhyay, A.; Hossain, Md. E.; Mahmood, H.; Dagar, V.; Bera, P. Can Clean Energy Adoption and International Trade Contribute to the Achievement of India's 2070 Carbon Neutrality Agenda? Evidence Using Quantile ARDL Measures. *International Journal of Sustainable Development & World Ecology* **2023**, *30* (3), 262–277. https://doi.org/10.1080/13504509.2022.2139780.

(5) Mulder, F. M. Implications of Diurnal and Seasonal Variations in Renewable Energy Generation for Large Scale Energy Storage. *Journal of Renewable and Sustainable Energy* **2014**, *6* (3), 033105. https://doi.org/10.1063/1.4874845.

(6) Wang, X. L.; Xu, R. Q.; Zhang, J. H.; Wen, F. S.; Liu, C. Q. Optimal Capacity Allocation and Economic Evaluation of Hybrid Energy Storage in a Wind–Photovoltaic Power System. *Journal of Renewable and Sustainable Energy* **2023**, *15* (6), 064101. https://doi.org/10.1063/5.0165774.

(7) Yu, Q.; Gao, S.; Sun, G.; Qin, R. Optimization of Wind and Solar Energy Storage System Capacity Configuration Based on the Parzen Window Estimation Method. *Journal of Renewable and Sustainable Energy* **2023**, *15* (6), 064103. https://doi.org/10.1063/5.0172720.

(8) Pickering, B.; Lombardi, F.; Pfenninger, S. Diversity of Options to Eliminate Fossil Fuels and Reach Carbon Neutrality across the Entire European Energy System. *Joule* **2022**, *6* (6), 1253–1276. https://doi.org/10.1016/j.joule.2022.05.009.

(9) Laha, P.; Chakraborty, B. Energy Model – A Tool for Preventing Energy Dysfunction. *Renewable and Sustainable Energy Reviews* **2017**, *73*, 95–114. https://doi.org/10.1016/j.rser.2017.01.106.

(10) Klein Tank, A. M. G.; Wijngaard, J. B.; Können, G. P.; Böhm, R.; Demarée, G.; Gocheva, A.; Mileta, M.; Pashiardis, S.; Hejkrlik, L.; Kern-Hansen, C.; Heino, R.; Bessemoulin, P.; Müller-Westermeier, G.; Tzanakou, M.; Szalai, S.; Pálsdóttir, T.; Fitzgerald, D.; Rubin, S.; Capaldo, M.; Maugeri, M.; Leitass, A.; Bukantis, A.; Aberfeld, R.; van Engelen, A. F. V.; Forland, E.; Mietus, M.; Coelho, F.; Mares,

C.; Razuvaev, V.; Nieplova, E.; Cegnar, T.; Antonio López, J.; Dahlström, B.; Moberg, A.; Kirchhofer, W.; Ceylan, A.; Pachaliuk, O.; Alexander, L. V.; Petrovic, P. Daily Dataset of 20th-Century Surface Air Temperature and Precipitation Series for the European Climate Assessment: EUROPEAN TEMPERATURE AND PRECIPITATION SERIES. *Int. J. Climatol.* **2002**, *22* (12), 1441–1453. https://doi.org/10.1002/joc.773.

(11) *eurostat*. www.Ec.europa.eu/eurostat.

(12) Ruhnau, O.; Hirth, L.; Praktiknjo, A. Time Series of Heat Demand and Heat Pump Efficiency for Energy System Modeling. *Sci Data* **2019**, *6* (1), 189. https://doi.org/10.1038/s41597-019-0199-y.

(13) Woudstra, N. *Exergy: The Quality of Energy*; Delft University of Technology, 2019.

(14) MATLAB Version: 9.7.01190202 (R2019b), 2019. https://www.mathworks.com.

(15) 2050: Facilitating 50% Wind Energy. *EWEA* **2011**, 11.

(16) Lopez, G.; Keiner, D.; Fasihi, M.; Koiranen, T.; Breyer, C. From Fossil to Green Chemicals: Sustainable Pathways and New Carbon Feedstocks for the Global Chemical Industry. *Energy Environ. Sci.* **2023**, *16* (7), 2879–2909. https://doi.org/10.1039/D3EE00478C.

(17) Carus, M.; Porc, O.; vom Berg, C.; Kempen, M.; Schier, F.; Tandetzki, J. Is There Enough Biomass to Defossilise the Chemicals and Derived Materials Sector by 2050. *Nova- Institut GmbH, Hurth, Germany* **2025**.

(18) Daioglou, V.; Doelman, J. C.; Stehfest, E.; Müller, C.; Wicke, B.; Faaij, A.; Van Vuuren, D. P. Greenhouse Gas Emission Curves for Advanced Biofuel Supply Chains. *Nature Clim Change* **2017**, *7* (12), 920–924. https://doi.org/10.1038/s41558-017-0006-8.

(19) Plummer, D. Power Play: The Economics Of Nuclear Vs. Renewables. *Forbes* **2025**.

(20) Morilhat, P.; Feutry, S.; Le Maitre, C.; Favennec, J. M. Nuclear Power Plant Flexibility at EDF. *HAL* **2019**.

(21) Albatayneh, A.; Assaf, M. N.; Alterman, D.; Jaradat, M. Comparison of the Overall Energy Efficiency for Internal Combustion Engine Vehicles and Electric Vehicles. *Environmental and Climate Technologies* **2020**, *24* (1), 669–680. https://doi.org/10.2478/rtuect-2020-0041.

(22) Atabani, A. E.; Badruddin, I. A.; Mekhilef, S.; Silitonga, A. S. A Review on Global Fuel Economy Standards, Labels and Technologies in the Transportation Sector. *Renewable and Sustainable Energy Reviews* **2011**, *15* (9), 4586–4610. https://doi.org/10.1016/j.rser.2011.07.092.

(23) Turner, J. A. A Realizable Renewable Energy Future. *Science* **1999**, *285* (5428), 687–689. https://doi.org/10.1126/science.285.5428.687.

(24) CBS. *De energierekening januari 2024*. https://www.cbs.nl/nl-nl/longread/diversen/2024/de-energierekening-januari-2024.

(25) Way, R.; Ives, M. C.; Mealy, P.; Farmer, J. D. Empirically Grounded Technology Forecasts and the Energy Transition. *Joule* **2022**, *6* (9), 2057–2082. https://doi.org/10.1016/j.joule.2022.08.009.

(26) Wang, R. R.; Zhao, Y. Q.; Babich, A.; Senk, D.; Fan, X. Y. Hydrogen Direct Reduction (H-DR) in Steel Industry—An Overview of Challenges and Opportunities. *Journal of Cleaner Production* **2021**, *329*, 129797. https://doi.org/10.1016/j.jclepro.2021.129797.

(27) Dewulf, J.; Van Langenhove, H.; Muys, B.; Bruers, S.; Bakshi, B. R.; Grubb, G. F.; Paulus, D. M.; Sciubba, E. Exergy: Its Potential and Limitations in Environmental Science and Technology. *Environ. Sci. Technol.* **2008**, *42* (7), 2221–2232. https://doi.org/10.1021/es071719a.

(28) Delft High Performance Computing Centre (DHPC), DelftBlue Supercomputer (Phase 2), 2024. https://www.tudelft.nl/dhpc/ark:/44463/DelftBluePhase2.

(29) Tröndle, T.; Pfenninger, S.; Lilliestam, J. Home-Made or Imported: On the Possibility for Renewable Electricity Autarky on All Scales in Europe. *Energy Strategy Reviews* **2019**, *26*, 100388. https://doi.org/10.1016/j.esr.2019.100388.

(30) Miller, L. M.; Brunsell, N. A.; Mechem, D. B.; Gans, F.; Monaghan, A. J.; Vautard, R.; Keith, D. W.; Kleidon, A. Two Methods for Estimating Limits to Large-Scale Wind Power Generation. *Proc. Natl. Acad. Sci. U.S.A.* **2015**, *112* (36), 11169–11174. https://doi.org/10.1073/pnas.1408251112.

(31) Fraile, D.; Vandenberghe, A.; Ivan, K. Getting Fit for 55 and Set for 2050. *ETIP wind, WindEurope* **2021**.

(32) Sailor, D. J.; Lu, L. A Top–down Methodology for Developing Diurnal and Seasonal Anthropogenic Heating Profiles for Urban Areas. *Atmospheric Environment* **2004**, *38* (17), 2737–2748. https://doi.org/10.1016/j.atmosenv.2004.01.034.

(33) Short, W.; Packey, D. J.; Holt, T. *A Manual for the Economic Evaluation of Energy Efficiency and Renewable Energy Technologies*; NREL/TP--462-5173, 35391; 1995; p NREL/TP--462-5173, 35391. https://doi.org/10.2172/35391.

(34) Lai, C. S.; Jia, Y.; Xu, Z.; Lai, L. L.; Li, X.; Cao, J.; McCulloch, M. D. Levelized Cost of Electricity for Photovoltaic/Biogas Power Plant Hybrid System with Electrical Energy Storage Degradation Costs. *Energy Conversion and Management* **2017**, *153*, 34–47. https://doi.org/10.1016/j.enconman.2017.09.076.

(35) Steinbach, J.; Staniaszek, D. Discount Rates in Energy System Analysis. *BPIE* 20.

(36) Acevedo Arenas, A. C. Y.; Muñoz Maldonado, Y. A.; Petit Suárez, J. F.; Morales Sánchez, D. H.; Ramírez Contreras, D. F. Towards a Standardized LCOE Calculation for Informed Decision-Making in Energy Policy and Investment:

Application to the Colombian Context. *IJEEP* **2024**, *14* (6), 523–541. https://doi.org/10.32479/ijeep.16280.

(37) Loewen, J. LCOE Is an Undiscounted Metric That Distorts Comparative Analyses of Energy Costs. *The Electricity Journal* **2019**, *32* (6), 40–42. https://doi.org/10.1016/j.tej.2019.05.019.

(38) Kuckshinrichs, W. LCOE: A Useful and Valid Indicator—Replica to James Loewen and Adam Szymanski. *Energies* **2021**, *14* (2), 406. https://doi.org/10.3390/en14020406.

(39) Minke, C.; Suermann, M.; Bensmann, B.; Hanke-Rauschenbach, R. Is Iridium Demand a Potential Bottleneck in the Realization of Large-Scale PEM Water Electrolysis? *International Journal of Hydrogen Energy* **2021**, *46* (46), 23581–23590. https://doi.org/10.1016/j.ijhydene.2021.04.174.

(40) Alia, S. M.; Stariha, S.; Borup, R. L. Electrolyzer Durability at Low Catalyst Loading and with Dynamic Operation. *J. Electrochem. Soc.* **2019**, *166* (15), F1164–F1172. https://doi.org/10.1149/2.0231915jes.

(41) Kojima, H.; Nagasawa, K.; Todoroki, N.; Ito, Y.; Matsui, T.; Nakajima, R. Influence of Renewable Energy Power Fluctuations on Water Electrolysis for Green Hydrogen Production. *International Journal of Hydrogen Energy* **2023**, *48* (12), 4572–4593. https://doi.org/10.1016/j.ijhydene.2022.11.018.

(42) Mulder, F. M.; Weninger, B. M. H.; Middelkoop, J.; Ooms, F. G. B.; Schreuders, H. Efficient Electricity Storage with a Battolyser, an Integrated Ni–Fe Battery and Electrolyser. *Energy Environ. Sci.* **2017**, *10* (3), 756–764. https://doi.org/10.1039/C6EE02923J.

(43) Möller-Gulland, R.; Mulder, F. M. 3D Nickel Electrodes for Hybrid Battery and Electrolysis Devices. *Cell Reports Physical Science* **2024**, *5* (11), 102286. https://doi.org/10.1016/j.xcrp.2024.102286.

(44) Sims, R. E. H.; Hastings, A.; Schlamadinger, B.; Taylor, G.; Smith, P. Energy Crops: Current Status and Future Prospects. *Global Change Biology* **2006**, *12* (11), 2054–2076. https://doi.org/10.1111/j.1365-2486.2006.01163.x.

(45) European Commission. Directorate General for Energy.; Fraunhofer Institute for Systems and Innovation Research. *METIS 3, Study S5: The Impact of Industry Transition on a CO2 Neutral European Energy System.*; Publications Office: LU, 2023.

(46) Erdemir, D.; Dincer, I. A Perspective on the Use of Ammonia as a Clean Fuel: Challenges and Solutions. *Intl J of Energy Research* **2021**, *45* (4), 4827–4834. https://doi.org/10.1002/er.6232.

(47) Verhoeven, G.; van der Holst, B.; Sharma, S.; Kok, K. A Co-Simulation Framework Design to Assess the Effectiveness of Flexibility Activation Mechanisms on Congestion in Dutch Distribution Networks. In *2022 Open Source Modelling and Simulation of Energy Systems (OSMSES)*; IEEE: Aachen,

Germany, 2022; pp 1–6. https://doi.org/10.1109/OSMSES54027.2022.9769151.

(48) Wallington, T. J.; Woody, M.; Lewis, G. M.; Keoleian, G. A.; Adler, E. J.; Martins, J. R. R. A.; Collette, M. D. Green Hydrogen Pathways, Energy Efficiencies, and Intensities for Ground, Air, and Marine Transportation. *Joule* **2024**, *8* (8), 2190–2207. https://doi.org/10.1016/j.joule.2024.07.012.

(49) Martin, J.; Golab, A.; Durakovic, G.; Zwickl-Bernhard, S.; Auer, H.; Neumann, A. Modeling Cost-Optimal Fuel Choices for Truck, Ship, and Airplane Fleets: The Impact of Sustainability Commitments. *Energy* **2024**, *308*, 132882. https://doi.org/10.1016/j.energy.2024.132882.

(50) Masters, G. M. *Renewable and Efficient Electric Power Systems*; John Wiley & Sons: Hoboken, NJ, 2004.

(51) Milborrow, D. J. Technical Issues in Windfarms and Supporting Activities within the International Energy Agency (IEA). *Journal of Wind Engineering and Industrial Aerodynamics* **1988**, *27* (1–3), 309–318. https://doi.org/10.1016/0167-6105(88)90045-1.

(52) Lu, X.; McElroy, M. B.; Kiviluoma, J. Global Potential for Wind-Generated Electricity. *Proc. Natl. Acad. Sci. U.S.A.* **2009**, *106* (27), 10933–10938. https://doi.org/10.1073/pnas.0904101106.

(53) Hakawati, R.; Smyth, B. M.; McCullough, G.; De Rosa, F.; Rooney, D. What Is the Most Energy Efficient Route for Biogas Utilization: Heat, Electricity or Transport? *Applied Energy* **2017**, *206*, 1076–1087. https://doi.org/10.1016/j.apenergy.2017.08.068.

(54) Sedaghat, A.; Hassanzadeh, A.; Jamali, J.; Mostafaeipour, A.; Chen, W.-H. Determination of Rated Wind Speed for Maximum Annual Energy Production of Variable Speed Wind Turbines. *Applied Energy* **2017**, *205*, 781–789. https://doi.org/10.1016/j.apenergy.2017.08.079.

(55) Kostić, R.; Mikulović, J. The Empirical Models for Estimating Solar Insolation in Serbia by Using Meteorological Data on Cloudiness. *Renewable Energy* **2017**, *114*, 1281–1293. https://doi.org/10.1016/j.renene.2017.08.013.

(56) Hager, T. J.; Morawicki, R. Energy Consumption during Cooking in the Residential Sector of Developed Nations: A Review. *Food Policy* **2013**, *40*, 54–63. https://doi.org/10.1016/j.foodpol.2013.02.003.

(57) Gerbens-Leenes, P. W. Energy for Freshwater Supply, Use and Disposal in the Netherlands: A Case Study of Dutch Households. *International Journal of Water Resources Development* **2016**, *32* (3), 398–411. https://doi.org/10.1080/07900627.2015.1127216.

(58) Chakraborty, D.; Bunch, D. S.; Lee, J. H.; Tal, G. Demand Drivers for Charging Infrastructure-Charging Behavior of Plug-in Electric Vehicle Commuters.

Transportation Research Part D: Transport and Environment **2019**, *76*, 255–272. https://doi.org/10.1016/j.trd.2019.09.015.

(59) Schey, S.; Scoffield, D.; Smart, J. A First Look at the Impact of Electric Vehicle Charging on the Electric Grid in The EV Project. *WEVJ* **2012**, *5* (3), 667–678. https://doi.org/10.3390/wevj5030667.

(60) Wadhwa, C. L. *Electrical Power Systems*, 2nd ed.; J. Wiley: New York, 1991.

(61) European Commission. Joint Research Centre. Institute for Energy and Transport. *HVDC Submarine Power Cables in the World: State of the Art Knowledge.*; Publications Office: LU, 2015.

(62) Martin, J.; Neumann, A.; Ødegård, A. Renewable Hydrogen and Synthetic Fuels versus Fossil Fuels for Trucking, Shipping and Aviation: A Holistic Cost Model. *Renewable and Sustainable Energy Reviews* **2023**, *186*, 113637. https://doi.org/10.1016/j.rser.2023.113637.

(63) Becker, W. L.; Braun, R. J.; Penev, M.; Melaina, M. Production of Fischer–Tropsch Liquid Fuels from High Temperature Solid Oxide Co-Electrolysis Units. *Energy* **2012**, *47* (1), 99–115. https://doi.org/10.1016/j.energy.2012.08.047.

(64) Ueckerdt, F.; Bauer, C.; Dirnaichner, A.; Everall, J.; Sacchi, R.; Luderer, G. Potential and Risks of Hydrogen-Based e-Fuels in Climate Change Mitigation. *Nat. Clim. Chang.* **2021**, *11* (5), 384–393. https://doi.org/10.1038/s41558-021-01032-7.

(65) Poullikkas, A. An Overview of Current and Future Sustainable Gas Turbine Technologies. *Renewable and Sustainable Energy Reviews* **2005**, *9* (5), 409–443. https://doi.org/10.1016/j.rser.2004.05.009.

(66) Harvey, S. P.; Knoche, K. F.; Richter, H. J. Reduction of Combustion Irreversibility in a Gas Turbine Power Plant Through Off-Gas Recycling. *Journal of Engineering for Gas Turbines and Power* **1995**, *117* (1), 24–30. https://doi.org/10.1115/1.2812776.

(67) Pashchenko, D.; Mustafin, R.; Karpilov, I. Thermochemical Recuperation by Steam Methane Reforming as an Efficient Alternative to Steam Injection in the Gas Turbines. *Energy* **2022**, *258*, 124913. https://doi.org/10.1016/j.energy.2022.124913.

(68) Steilen, M.; Jörissen, L. Hydrogen Conversion into Electricity and Thermal Energy by Fuel Cells. In *Electrochemical Energy Storage for Renewable Sources and Grid Balancing*; Elsevier, 2015; pp 143–158. https://doi.org/10.1016/B978-0-444-62616-5.00010-3.

(69) Smith, C.; Hill, A. K.; Torrente-Murciano, L. Current and Future Role of Haber–Bosch Ammonia in a Carbon-Free Energy Landscape. *Energy Environ. Sci.* **2020**, *13* (2), 331–344. https://doi.org/10.1039/C9EE02873K.

(70) Mostafa, M.; Antonicelli, C.; Varela, C.; Barletta, D.; Zondervan, E. Capturing CO2 from the Atmosphere: Design and Analysis of a Large-Scale DAC Facility.

Carbon Capture Science & Technology **2022**, *4*, 100060. https://doi.org/10.1016/j.ccst.2022.100060.

(71) Rouwenhorst, K. H. R.; Van der Ham, A. G. J.; Lefferts, L. Beyond Haber-Bosch: The Renaissance of the Claude Process. *International Journal of Hydrogen Energy* **2021**, *46* (41), 21566–21579. https://doi.org/10.1016/j.ijhydene.2021.04.014.

(72) milieu centraal. Volledig Elektrische Warmtepomp. *https://www.milieucentraal.nl/energie-besparen/duurzaam-verwarmen-en-koelen/volledige-warmtepomp/*.

(73) Aregawi, B. H.; Atiku, F. A.; Pirouzfar, V.; Su, C.-H.; Wang, F.-M. Evaluating the Optimal Capacity for the Implementation of Fluidized Catalytic Cracking in the Refinery by the Technical and Economic Analysis. *Pet. Chem.* **2021**, *61* (7), 729–738. https://doi.org/10.1134/S096554412107001X.

(74) Kleen, G.; Gibbons, W.; Fornaciari, J. DOE Hydrogen Program Record 23002, 2023. https://www.hydrogen.energy.gov/docs/hydrogenprogramlibraries/pdfs/23002-hd-fuel-cell-system-cost-2022.pdf?Status=Master.

(75) Hank, C.; Sternberg, A.; Köppel, N.; Holst, M.; Smolinka, T.; Schaadt, A.; Hebling, C.; Henning, H.-M. Energy Efficiency and Economic Assessment of Imported Energy Carriers Based on Renewable Electricity. *Sustainable Energy Fuels* **2020**, *4* (5), 2256–2273. https://doi.org/10.1039/D0SE00067A.

(76) Makhloufi, C.; Kezibri, N. Large-Scale Decomposition of Green Ammonia for Pure Hydrogen Production. *International Journal of Hydrogen Energy* **2021**, *46* (70), 34777–34787. https://doi.org/10.1016/j.ijhydene.2021.07.188.

SUPPORTING INFORMATION

1. *INTRODUCTION OF MODEL*

A complete renewable energy systems needs a large investment in assets. The scale of the investment needed is very likely to change the market economy with respect to the costs of these assets:

- The material availability and subsequent raw material cost progression upon scaling is often still unknown and may depend on several learning curves for e.g. mining, ore processing and purification, manufacturing of goods.
- The projected technology advancement, potential investors decisions and policy change is unknown. The resulting market and/or behavioural change

would give sub-optimal results if only a restricted set of technologies is chosen.

- As an alternative to energy storage there is also demand side management as a possibility for a limited amount of applications and magnitude in energy use. But this necessarily calls for investment into upscaling of these demand responding assets to keep the same product or service output volumes. E.g. if one has aluminium production only during 25% of the hours in a year one requires 1/0.25 = 4 times the production capacity to produce the same volume of aluminium.
- The definition of (non)'renewable', 'sustainable', 'green' may be obvious for the source of the energy, for manufacturing assets (e.g. processing method, mineral use, ecological impact) the definition is less clear. Energy or energy intensive feedstock technologies may still have additional costs if converted to completely renewable sources. An example is the usage of green power and hydrogen instead of using fossil derived fuels for steel production, which will modify the process and assets.[26]

Therefore a cost projection for the scenario development in the European energy market runs into a representativeness problem. Still such extrapolation of an energy system remains useful to project the necessary investment scales for generation, storage and transport of energy in a completely renewable energy system. The model results may show grave market implications or policy requirements. Therefore the model is analyzed and adjusted several times using an iterative approach to add additional constraints to follow up on relatively more realistic and cost effective scenario's.

A second risk is that complexity of energy systems obfuscate the solution. For this reason a set of descriptors is introduced through the exergy concept,[27] which guide the optimization and analysis of the model results. The fuels are classified by their purpose (heat, work, irreplaceable) instead of their type. As purpose class 'heat' and 'work' are quite common. Irreplaceable is used to position the use of hydrocarbons as chemical commodity in our energy landscape (which cannot be replaced by electrification). As both fuels and these hydrocarbons are derived from crude oil in refineries, their purpose class needs to be defined as well to allow an estimation on the energy need to provide for these commodities. The classification prevents creating mass balances for all available fuel types ranging from charcoal, natural gas to municipal waste with the same end use. For conversion and storage of sustainable

fuels a representative, scalable technology is chosen. Such technology has published unit pricing and depreciation to allow an economic analysis. Finally the consumption behavior is also described per fuel exergy class described above. With such simplified descriptors for producers, converters, storages, transport and consumers one can draw feasible scenario's quickly, while it is still relatively straightforward to convert the fuel class to a range of suitable fuels for economic evaluation.

The following method is thus executed: empirical fuel consumption data is converted to time dependent energy consumption for individual countries. Using local empirical weather data (including sunless and windless days) a time dependent hourly energy generation at selected locations is simulated. Consumer and producer locations are indicated as nodes. Consumer nodes in this paper are individual European countries with published fuel statistics. Producer nodes in this paper are various locations known for good solar and/or wind farming, having a wide spread across the consuming countries. Such wide spread makes that the weather and time zone is varying to an extent, spreading the instantaneous solar generation and weather as well (locations chosen as example are: Netherlands, Spain, Poland and Slovenia, but this can be increased if need be at the cost of computational time). As wind farming may need additional locations with lower yield as well, there might be an overestimation of the capacity factor. The percentage of utility for the wind farms which are scaled in this model are 37+/-1%. Energy conversion and storage is assumed to be near the production area (limiting grid costs). The model calculates the cost effectiveness of every energy transport route (meaning, the highest utility per euro invested, irrespective of distance and time). The route effectiveness approach results in expected trends like the necessity for high frequency use and low energy losses when batteries are used as storage asset. It also discerns the effectiveness of less obvious trends, like the choice between storage solutions with higher energy losses at the benefit of lower investment costs for long-term (seasonal) storage. Then iteratively energy transport is allocated between energy production site and consumption site, until the energy consumption is fully satisfied.

Optimization of the production capacities is carried out by feeding the model to a non-linear solver to find the minimum cost in this non-linear constrained parameter set. This method also allows overproduction and curtailment, should it be a cost effective method to satisfy the consumption pattern. For optimization a parallel computing task

is defined for the DelftBlue supercomputer, using 15 processing cores simultaneously.[28] Finally the model shows the projected minimum annual cost for a complete sustainable energy system.

1.1 Variables defined a priori

To moderate the calculation demand two important variables were set *a priori*. The production locations are chosen in this model. The locations chosen have either a known high yield (offshore wind in the Netherlands and Portugal, or solar in Portugal) or an expected advantage in diurnal timing (solar and wind in Slovenia and North Poland). The diurnal consumption patterns of all participating countries are individually calculated based on their local weather around the capital, taking into account the local time zones and subsequently summed to a single node. The location of these work, heat and irreplaceables nodes are chosen to be a central point in Europe to ease the demand in calculating routing combinations. The amount of options for routing (having a unique efficiency and cost effectiveness) is: time Intervals* Producers*Consumers, which give $7.57*10^6$ possible iterations with 32 countries (365 * 24 hours per year* 9 producers* 3 exergy types * 32 countries) and $2.4*10^5$ iterations with a centralized consumption pattern. The time dependence of the energy demand is incorporated by summation of the individual country consumption pattern. The accuracy of transport efficiency is however sacrificed and large differences in heat demand during cold periods (which would be spatially defined) are averaged. However, the European climate more often shows a common cold and hot period which would give a simultaneuous demand. An overestimation of energy loss due to transport distance is also to be expected, as in reality the majority of energy production and consumptions would take place between shorter distances. By this approach typically about 65 iterations are necessary to get a full match between 9 production sites and 1 consuming site with 5 fuel storage types and 3 types of exergy.

1.2 Power density of solar PV and wind

With regards to the optimum in wind energy generated per area and cost, the Pickering study appears to base the installed capacity density for wind power on Tröndle et al,[29] with a number of 8 to 15 MW installed wind capacity per km^2 on- and offshore. However, Miller et al. studied the yield of wind power as a function of the installed power density and came to a significant saturation of the observed yield in MW_e / km^2 already at an installed capacity of 7 MW/km^2.[30] Therefore the free scaling above 8 MW/km^2 in wind appears unlikely to yield a benefit in the electricity

harvested, as the capacity factor will be excessively low due to the reduction of the wind speed for turbines spaced relatively too close together. We here also present several models, where we either allow free scaling of capacity of wind and solar PV, or we come to a more restricted wind implementation, in line with the socially acceptable density of installed wind power as projected by the European Wind Agency.[31]

1.3 EXERGY CLASSES

In this paper several exergy classes are mentioned, of which the irreplaceable exergy class is one which is not mentioned often in literature. For an adequate processing step similar to current practice in oil refinement, manufacturing of alkanes through Fischer-Tropsch processing is used as benchmark fuel of the 'irreplaceable' exergy type. The Fischer-Tropsch process after purification yields various liquid fuels including alkanes similar to oil, which function as chemical feedstock for many types of applications. Such oils can be used as storage fuel as well. Note that this choice means that no fossil sources are used for producing such chemicals.

The highest and middle exergy class both imply direct usage of electrical energy and therefore three classes are defined in the model, named 'work' (highest and middle exergy), 'heat' (lowest exergy) and 'irreplaceable' (chemical feedstocks, and carbon based transport fuels). The fuel consumption per country reported in the database of Eurostat is converted to exergy class depending on the reported sector and fuel type by using common energy efficiency numbers [**SI Table 3**]. Only the transport sector is subjected to additional conversion. Here a conversion number of energy 'to wheel' is estimated, which follows the 'work' exergy definition. The consumer type dictates also the exergy class of specific fuel groups. For example, in households the current reported natural gas is typed as heat exergy. Industrial natural gas consumption is assumed to also play a role in the work exergy class for turbines and high caloric combustion, and is therefore typed as the higher quality exergy 'work'. The future models then use different realisations to provide the required exergy types. For example, although heat from industrial waste heat are potentially a significant source of heat energy for some area's in Europe and might even originate from some of the conversion processes used, it however may not be applicable in every area. Heat pumps and/or combustion of fuels however are so widely used that it may be considered conventional in Europe.

The consumption pattern of the three exergy classes are subsequently forecast. In short: An electrical consumption pattern general in Western countries is used.[5,32] In addition HVAC usage and electric vehicle charging is forecast by using local temperature and user charging habits respectively [**SI Ch 2.1.2**]. As stated in the introduction, a separate scenario is modelled in which the transport sector uses irreplaceable exergy rather than work, to investigate the implications in the energy model of *not* performing electrification of the transport sector. The diurnal industrial fuel consumption pattern is kept constant as the capacity factor of the energy demanding industry is assumed to be 1 to maximize utility of the assets (the fraction of actual production versus the plants theoretical capacity). This implies there is limited to no additional demand side management of industries assumed when large scale energy storage and conversion is available. The simple rationale for that is that industrial factories are costly enterprises that are running in shifts to make best use of the facilities. Taking out some of the shifts to lower energy demand at convenient times is often not possible because of the inflexible process, and/or simply because then one requires to increase the capacity of the factory to increase production in other hours when energy is available. The latter would mean increasing the factory by a factor 1/(renewable energies capacity factor), which equals a factor 2-5 depending on more wind or solar use to still produce the same output in products. In general reported 'non-fuel use' classes in the Eurostat source data are defined as irreplaceable exergy. As this involves chemical feedstock used in industry that runs 24/7 throughout the year, this is set out to be constant during the year with the same argument as general industrial energy use. In this way a consumption pattern for every exergy class for every country in Europe is defined.

1.4 LCOE AND SLCOE

For the energy system costs the levelized cost of used energy (LCOE) is a metric which allows comparison of the economic costs of selected asset utilization.[33,34] Often the LCOE is expressed as the summation of annual cash flow which is reduced by the discount rate, divided by the annual energy yield reduced by the same discount rate (*d*=12% is used[35], using an inflation rate *i* of 3% and an interest rate *r* of 9% (and d = i+r). All other prices are indicated in SI 2.4):

$$LCOE = \frac{\sum_{t=1}^{n} \frac{I_t + M_t + F_t}{(1+i+r)^{t-1}}}{\sum_{t=1}^{n} \frac{E_t}{(1+i+r)^{t-1}}}$$

Eq. 5

Here the year discounted investment costs I, maintenance costs M and consumables and utilities costs F are in the numerator, and discounted delivered energy in year t is in the denominator. As E_t notes the energy delivered this excludes curtailed energy, i.e. LCOE increases with increasing curtailment. The 'annual renewal cost' (d=0%, Figure S 1 top) is the cost used to calculate the cost efficiencies. There are however a number of approaches to calculate the levelized costs of energy technologies for comparative purposes. These methods take into account a discount rate to come to a net present value.[36,37] The definition also has been objective of discussion[37,38] where the assumptions on what or what not should be discounted plays a role. Essentially a future cost and a future revenue in year n should be discounted by a factor $(1+d)^{-n}$ to correct for a present-day value of this cost or revenue. The argument for that is that one could have invested the same numerical amount of $Y_{cost\ or\ revenue}$ Euros or dollars today and then have the compiled interest $(1+d)^n$ increase this number to a larger value $Y_{cost\ or\ revenue}(1+d)^n$. Therefore a future cost or revenue represents today a value $Y_{cost\ or\ revenue}(1+d)^n(1+d)^{-n} = Y_{cost\ or\ revenue}$. In an often used definition of LCOE above both the costs and the revenues are therefore discounted. Here we would like to note, however, that this approach assumes that the basic notion of LCOE is an expression in terms of Euro per energy unit: Eu/MWh. That implies that the moment at which the conversion of MWh to Eu takes place is also relevant, i.e. the way the associated costs are modelled in time.

If at day 0 all associated costs and revenues are known and defined by contract, so the MWh and the Euro amounts are given, one should perform the discounting both in the costs and the revenues. However, if one or the other is not bound by contract another situation occurs because the energy value itself expressed in MWh may not change with regular inflation; in year *n* the energy yield is still measured in MWh, not in $MWh(1+i)^n$, while Eu_n numbers of Eu in year *n* do decrease according to a discount rate: $Eu_n = Eu_0(1+i)^{-n}$. In other words, fixing the price of a MWh in year *n* fixes it in already discounted Eu_n, so the revenue of conversion of MWh to Eu_n in year *n* becomes $MWh = (1+r)^n Eu_n$ assuming that the intrinsic functionality of a MWh is the same in year *n* and investors would like to see their interest rate *r*. One could look at it as a non-inflationary value of a MWh, equalling 3.6×10^9J, in year *0* or in year *n*, of which the amount of Eu is established in year *0* or *n*. Here we argue the investment should be

discounted using an interest rate and expected inflation y. However, the expected revenue from energy should be subjected to interest rate only, shown in Eq. 6.

$$LCOE = \frac{\sum_{t=1}^{n} \frac{I_t + M_t + F_t}{(1+r+y)^{t-1}}}{\sum_{t=1}^{n} \frac{E_t}{(1+r)^{t-1}}}$$

Eq. 6

This leads to more attractive (and in our opinion more representative) expected cost of long term storage assets (Figure S 1, bottom). The levelized cost of energy expressed in the main text (Figure 7) uses a discount rate of 12%. A decrease in LCOE for long term storage and conversion assets is observed without inflation on energy, as they generally process large quantities of energy during their lifetime, making them relatively cheap.

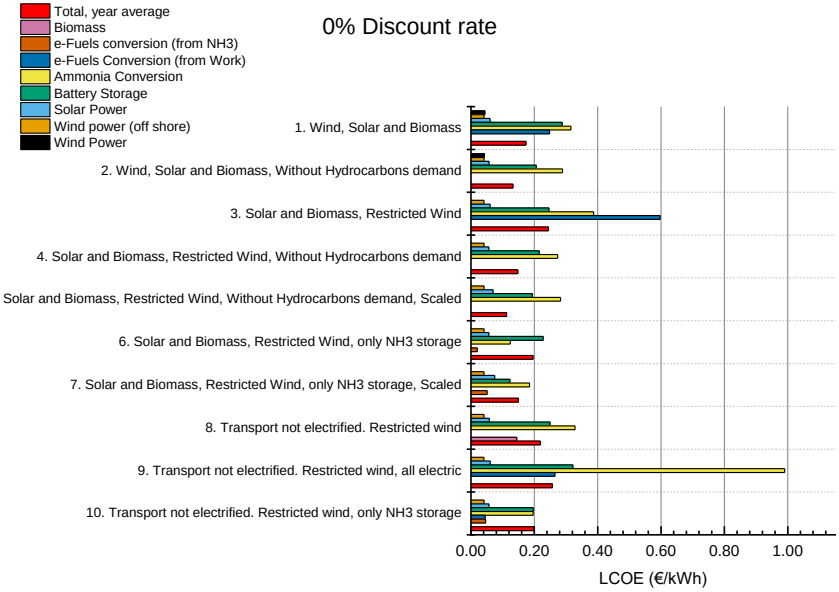

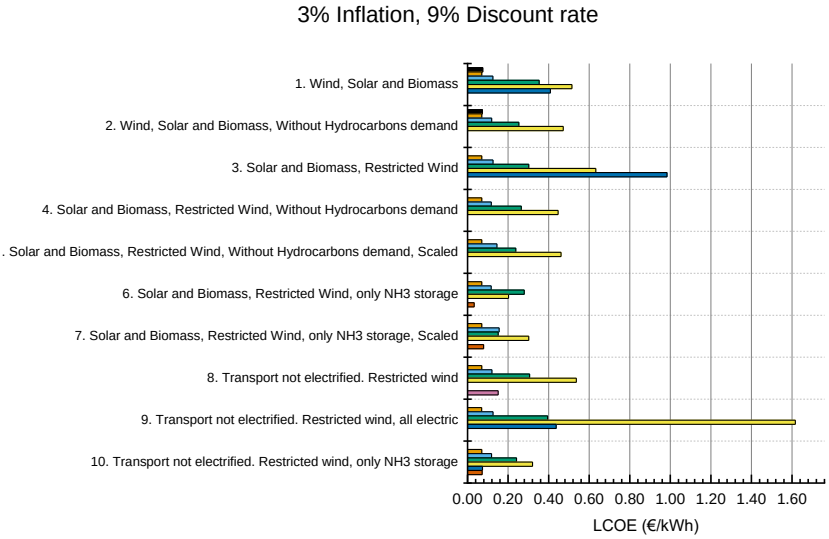

Figure S 1 Top: LCOE without discount rate. Bottom: LCOE with inflation and discount rate separate. The rationale for this is that revenue obtained from energy through the day ahead market would not be subjected to inflation as it is revenue obtained from the day ahead market in the future year.

USE OF LCOE AS GRADIENT FUNCTION

The total LCOE could itself be formulated as a gradient objective for minimization functions of cost effectiveness to mimic market drive. Outliers in the LCOE calculation often indicate a bad fit of producer/consumer match patterns and conversion and storage assets. During the calculation of the LCOE in scenario 7 an apparent battery cost of € 0.78 /kWh stood out as other scenario's never exceeded € 0.26 /kWh for battery storage. A close look at the battery storage usage duration and frequency showed that the estimated usage frequency was estimated far higher than the actual usage frequency (**Figure S 2**). A local optimum was causing the battery storage frequency to be allocated while additional solar production combined with ammonia conversion and storage would reduce the net cost of the spikes caused by these short demand periods by 7%, leading to a sLCOE of € 0.106 /kWh and a marginal increase of solar and ammonia storage and conversion sLCOE.

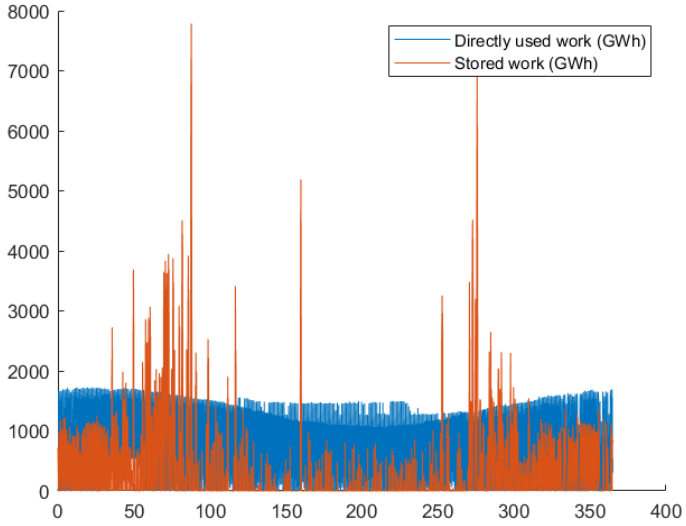

Figure S 2 Initial frequency estimation of battery storage in scenario 7 (stored work (GWh)) shows a frequent utilization below 1125 GWh storage. However, the model allocates a few infrequent storage durations as well, making the total energy processed per capacity of battery lower than necessary.

1.5 Further factors implemented in the selected model and its scenario's

Cost estimations of selected scenario's

The cost estimations used as model input depend on learning curves for the different technologies. The learning curve that is effective for a certain energy technology can be approached in an empirical manner for the relevant energy technologies.[25] In general, the increased manufactured and installed base of a technology leads to price reductions of the technology. This can result in costs reducing continuously upon transitioning to a renewables based system, under the condition that no fundamental 'floor' in certain cost aspects is reached. Then cost reductions result from larger manufacturing capacities of the equipment, the scale of the units built, improving production knowledge, innovations in the product, scale up and associated learnings in the supply chain and realising factories to produce factories. According to [25] there are no fundamental causes for the existence of a floor given in the energy technologies considered. However, if one would think of some fundamentals that can lead to a floor this may be e.g. required materials not being available on sufficient scale to be able to build the technology. For instance the necessary use of iridium in PEM electrolysers requires sufficient amount of IrO_2 to be available.[39] Then the upscaling of mining may lead to lower grade ores being processed, which makes that the production means themselves may still profit from reduced prices per ton of ore processed but the yield does not increase. A second reason for a floor in the production cost of renewable technologies can be the maximum scale that is reached upon full implementation; what is actually required based on the energy supply and demand? Such a floor does not show up in the cost scaling equation as such, but just means that the ultimate built scale is limited. A third reason for a floor may be safety, social acceptance and available space requirements. In this case the technology itself could become lower costs, but the outside 'battery limits' costs still cause that energy cost cannot further reduce.

Next to the asset costs also the energy efficiency of a route is important: if two technologies have similar costs and learning curve, it makes sense that the more energy efficient solution still leads to lower costs after upscaling. That is because the actual scale of deployment scales with 1/efficiency.

To extend on how the availability of materials may play a role one can look at the economy of scaling of P2X, as shown by Way et al.[25] It is presented as not as effective compared to batteries, wind and solar, as it is based on observed and anticipated trends for PEM electrolysers. The reason to choose PEM may be its higher flexibility compared to alkaline electrolysers. However, PEM intrinsically requires use of IrO_2 as positive electrode catalyst and Pt at the negative electrode, which will likely result in materials availability limitations when scaling to the TW scale. Especially Ir is a rare element where the world supply is low.[39] Reducing the amount of Ir inside a PEM electrolyser is not feasible in view of lifetime issues associated with catalyst dissolution and intermittent operation.[40] Increased PEM use may therefore cause a price rise of these catalyst, rather than a reducing price by scaling up, as the materials availability and prospects for alternatives is too limited. Alkaline electrolysis, however, can work without noble metal catalysts, but also suffers from performance degradation upon variable load.[41] However, there are no intrinsic materials shortages there as mostly Ni and Fe compounds are used as active catalysts. Also concepts geared towards long term intermittent operation are in development,[4243] which indicates that there is no fundamental scarce resource or functionality reason that leads to stalling of innovation, and therefore the upscaling should still lead to cost reduction benefits. As the materials type inventory, the processing from materials to devices, as well as the energy density (space requirement kW/m^2 of systems) is similar as building battery systems, one may expect a cost scaling behavior that is similar to what is seen for battery systems. We therefore here select a similar cost scaling for P2X, using alkaline technologies, as for battery technologies from the work of Way et al.[25]

THE ROLE OF ENERGY CROPS, BIOMASS

Biomass has many varieties, has applications in multiple exergy classes and therefore has a wide price range depending on the quality and allowable end-use. Here, a bulk agricultural manufactured type of biomass like rapeseed oil or palm oil is taken with associated cost necessary to compete with other agricultural markets. The high cost associated with such biomass, as it competes with food and feedstock prices does not pose a cost effective use in energy applications. Only when the transport sector is not electrified, the use of such biomass becomes cost effective. In this scenario, however, the estimated required European biomass production capacity of 501 GWy exceeds the projected annual global energy crop yield by sevenfold (~70 GWy).[44] Rather, for irreplaceable hydrocarbons for chemicals, the Fischer Tropsch process combined with hydrogen electrolysis and direct air capture offers a more suitable replacement for

such production scale. Authors realize this is a gross oversimplification of the complete biomass market, just as waste streams at the end of lifetime also allow production of a limited fraction of the necessary energy with relatively high cost effectiveness due to lower prices. However, when using such bio-waste, which is a derivative of food production, the amounts remain low compared with energy market amounts. It however shows that the biomass production scale necessary to fulfil a large fraction of the energy demand from a complete sector is not feasible. This has been noted before in [5] and references therein.

A combination of mostly wind power and liquid storage fuels for seasonal storage offers the most cost effective scenario. Here ammonia as seasonal storage fuel shows the highest cost efficiency. In the most cost effective scenario found, the scale at which wind power would be necessary to fit the demand of energy best is found to be unrealistic, as generally support for wind farms in populated area's is rather poor and the area availability near the more windy shore is limited. As an alternative, solar energy generation coupled with liquid fuel storage (amounting to 888 L ammonia storage per EU citizen) poses a possible alternative when combined with 25 TWh of short term storage (amounting to 54 kWh battery storage per EU citizen). The major difference in this solution is that a relatively large fraction of the energy is obtained from solar power and therefore not produced at the time it is consumed (but mostly on midday hours and during the summer months). Such scenario leads to more storage on a seasonal scale, and also more day/night storage (22% compared to unrestricted wind availability). Generation of hydrocarbons for chemical feedstock is provided by direct generation and using energy from ammonia, as e-Fuel generation assets are most expensive and therefore need the highest capacity factor which is provided by continuous supply via long term storage non-carbon fuels.

Surprisingly the most cost effective scenario with a non-electrified transport sector uses liquid ammonia as long term storage carrier as well. A similar argument for the electrified e-fuels production, being: a sustained capacity factor for e-Fuel generation assets, is applicable with a higher e-Fuel demand when ammonia is used as hydrogen storage and fuel. But the scenario is relatively expensive, with an additional cost of 26% compared to an electrified transport sector.

THE SUPPLY OF HYDROCARBONS TO THE CHEMICAL SECTOR

The model shows that, without including hydrocarbons consumption in a wind restricted scenario, the cost of conversion drops more than for unrestricted wind generation scenario's. The cause of this steeper drop is the seasonal dependence of solar yield, resulting in a severe under-utilisation of e-Fuels plants compared to the better seasonal match with a wind profile in the unrestricted scenario. This is evidenced by the negligible change of cost in the *unrestricted wind* scenario when only ammonia is available as storage fuel, as wind power ensures a good match of wind power and e-Fuel generation throughout the year already. In the restricted case this leads to a steep drop in costs as well, as the estimated capacity factor for e-Fuel conversion turns out to be much lower if combined with solar power. The relatively high costs associated with sourcing the CO_2 as feedstock plays a role here, as it needs a high capacity factor to gain sufficient return on investment. The high investment cost in e-Fuel generation plants is therefore a potential cause for stress on the energy market, as it could lead to non-affordable energy bills for the consumer during the winter season when energy is scarce, and such plants may buy electricity for high prices to ensure continued carbon based e-Fuel production. This would also impact the amount of stored electricity, hydrogen and ammonia, to realise the continued production during night-time and winter periods.

Direct production of e-Fuels from solar is therefore not advised. Direct production of e-Fuels is naturally tied to wind power by the model due to a high match in capacity factor, which leads to a cost effective outcome. However, wind energy is not abundant enough to fulfil the need without electrification of our fossil fuel use for energy. Solar energy creates a larger 'surplus' market as it generates more frequent and shorter peak production periods (with relatively low energy cost). While other consumers can benefit from these moments, e-Fuels plants cannot afford such downtime due to their operational cost and depreciation. In this case also importing fuel from other regions like deserts will also not result in lower costs by definition, because there are not much electricity users there that can pay for the base load of electricity that can be directly used. For such regions all costs therefore have to be carried by fuel production.

When ammonia is used as storage fuel carrier, the generation and usage is decoupled, and obtaining energy from other regions will become also an option. However, for energy that is used as electricity in Europe one needs to produce then 3 times more electricity in such region with relatively low capacity factors, convert, store, transport, and reconvert the energy back to electricity. In such cases it is hard to currently

compete with low cost surplus EU electricity available during most of the year, when also long distance fuel transport needs to be added to the production costs.[45] During the winter season ammonia storage fuel will however be needed to generate sufficient energy, which poses a potential market for such investments.

For energy consumers, the use of non-carbonaceous fuels in the expensive time of the year can be offset by increased energy efficiency using heat pumps and electrical transport. An affordable scenario for consumers' daily energy use throughout the year can be developed, with a steep market incentive to drive more efficient electrically on direct electricity or indirect electricity from stored non carbon liquid fuels. This drives the market to electrified utilities and EV, stabilised by short and carbon free long term storage. The strategy will also result in pricing increase of consumables like plastics, fine chemicals and lubricants, not so much because of energy costs but because of their dependence on captured CO_2 and manufacturing and maintenance cost for generation.

AMMONIA AS LARGE SCALE HYDROGEN STORAGE

Using carbon free ammonia as energy carrier is a technologically feasible option, as conversion through the Haber Bosch process using abundant N_2 from air occurs at a scale of 180 million tons annually (which has a ~4 EJ = 1125TWh HHV). Using ammonia as long term energy storage potentially reduces the cost compared to e-Fuels: e-Fuels as defined here contain carbon and therefore require CO_2 capture which is a more energy intensive process than N_2 purification, as concentrations of CO_2 are low compared to abundant N_2. Therefore the route via NH_3 yields a net higher energy efficiency for long term energy storage applications, especially when reconverted to electricity. Also liquid ammonia has the same benefit of e-Fuels being a liquid carrier for cheap storage and transport. The energy density of liquid ammonia is smaller than for liquid hydrocarbons, but still much larger than gaseous hydrogen.

The above modelling exercise also appears to indicate that ammonia as long term energy storage may be advisable. However, it is a poisonous substance with a low limit in exposure. Such factor will be important in the social acceptance of its use. However, today it is one of the largest chemical processes in industry. The indicated 450 TWh of long term stored ammonia corresponds to 72 million tonne on an European scale. For a world scale a multiple of that would be required, which is in fact not such a dramatic

increase of todays ammonia use. Still one should not underestimate that this storage fuel is in a liquid pure form, and not further processed to solid non-volatile fertiliser compounds, as is done with most ammonia to date. A second concern is that with large scale combustion of ammonia, exhaust of N_2O, a strong greenhouse gas, needs to be prevented with solutions like catalytic reduction or using dedicated combustion systems.[46] Also NO_2 , NO and NH_3 need to be catalytically converted to reduce these unwanted potential acid rain and/or nitrification emissions. Such de-NOx is currently mature as it is also utilised routinely at fossil powerplants and (large) diesel engines that can also produce NO_x.

Concerns about the scale up of solar energy production

Next to limited space for wind power, a second concern of the areal requirement to place solar panels and direct air capture (DAC) is less severe. A projected area spanning 12.600 km^2 of solar is needed for Europe (with 0.23 kW/m^2 rated capacity). Such an area has to be provided by installed solar on rooftops and solar parks combined. Decentralized solar energy production poses a challenge as transport of energy to conversion locations become costly. Already in 2023 the electricity grid in the Netherlands experienced net congestion, an occurrence which was predicted in 2022.[47] The installed solar capacity in that year amounted to (only) 19.6 GW. Instead of a decentralized generation by solar, investment in solar farms directly combined with conversion plants for long term storage would create a more viable solution as it would centralize the energy production, conversion and storage altogether. An added benefit is that such plants do not need to be attached to the electric grid for the peak capacity, but only for the usable capacity that can be used directly locally as electricity during peak production.

Concerns regarding the shift in transport sector assets

Recent publications[48,49] indicate the EV routes to be most energy efficient starting from the input of green electricity in the mode of transport. Our work here indicates, however, that notwithstanding such energy efficiency considerations in the transport application, there still is the overall system integration aspect that should also be taken into account. In other words, if EV electricity comes in part from the long term stored fuel or short term battery storage before it is charged into the EV, these costs should also be taken into account as well. This is where the current work then points into the direction that costs become distributed differently at system level: it is not the one directional feed of always available green electricity into EV route, but rather a multi

directional feed -with its associated costs and efficiencies- which needs to be implemented to fullfill the energy demand continuously. In a follow-up study one can model utilization of ammonia fuel directly for the relevant sectors in the energy system framework presented.

IMPLICATIONS OF EUROPE'S ENERGY TRANSITION

The energy cost can be compared to current net energy expense of an average (Dutch) household with 2.2 persons on average.[24] The energy cost in January 2023 was estimated to a monthly cost of 354 euro. A household spends yearly 3280 euro on household energy and 984 euro on gasoline (measured every 5 years). The fraction of fuel cost for consumables, like food and materials is harder to estimate and therefore left out. Using current pricing of available technologies this cost will increase to 420 to 552 euro per month for the average household (with an electric car). Here the price per capita of '*Solar and Biomass, Restricted Wind, Without Hydrocarbons demand*', *scaled* and *not scaled* are taken as example respectively, as they illustrate what an electrified energy bill would look like. The marginal household cost for consumption of goods containing hydrocarbons will rise. This will create a higher price for many chemical derivatives like plastics, lubricants, synthetic rubbers which are used for construction and industrial purposes as well. As in the end the consumer pays, this will trickle down to an additional 139 to 180 euro per month for such products. This highlights an affordable and completely sustainable scenario without fossil carbon based energy is within reach, which would adequately value goods for the (energetic) effort needed to make them. Given the required scale for production and the scale of reconversion storage fuels our society needs a clear migration pathway and investment strategy to come to such energy system.

The availability of data is key to enable discussing complete scenarios for solving the migration to a renewable energy system. Looking into various options illustrates what would be logical solutions, at what scale the energy system needs to shift and what are challenges to achieve such shift. With this work we provide a scenario-flexible modelling tool to predict such drastic changes in scenario's and we pose a few potentially viable solutions for achieving a completely renewable energy system in Europe. The model has shown to perform well in optimization of single short and long term storage solutions simultaneously. However, when multiple storage solutions are

fed, an adjustment on the capacity factor must be performed during solving the mass balance.

1.6 SCENARIO DESCRIPTIONS

Scenario 1: Wind, Solar and Biomass

The base model which utilizes wind, solar and biomass shows an investment is needed in a minimum of six production locations for the spread of energy production to meet the diurnal consumption pattern of Europe (**Figure 4**A, case 1 'wind, solar and biomass'). Of all production, the majority is covered by wind power near the shore of the Netherlands, as it meets the diurnal nature of the consumption pattern and reaches a high yield. The base model has no limit on the wind power capacity that can be installed, although it is noted that unlimited wind scaling is not realistic and the required capacity near the shore of the Netherlands is not feasible. Therefore below the case with a limited wind power capacity is also investigated.

Interestingly however, here without limitations the model chooses for high amounts of wind power as its production pattern matches better with the use patterns (**Figure 4**C). Still long and short term storage is expected for providing energy in periods with low production. An investment of 20 TWh short term storage capacity is necessary.

Interestingly due to energy efficiency and cost factors in this case, seasonal energy storage that compensates seasonal overproduction and seasonal demand variation for the work exergy class is solved by synthetic ammonia fuel storage (**Figure 3**C, scenario 1). Only for shorter duration surplus of specifically wind energy e-Fuel storage is used, to provide for the irreplaceable exergy energy class of which industrial consumers need a continuous supply (**Figure S 3**).

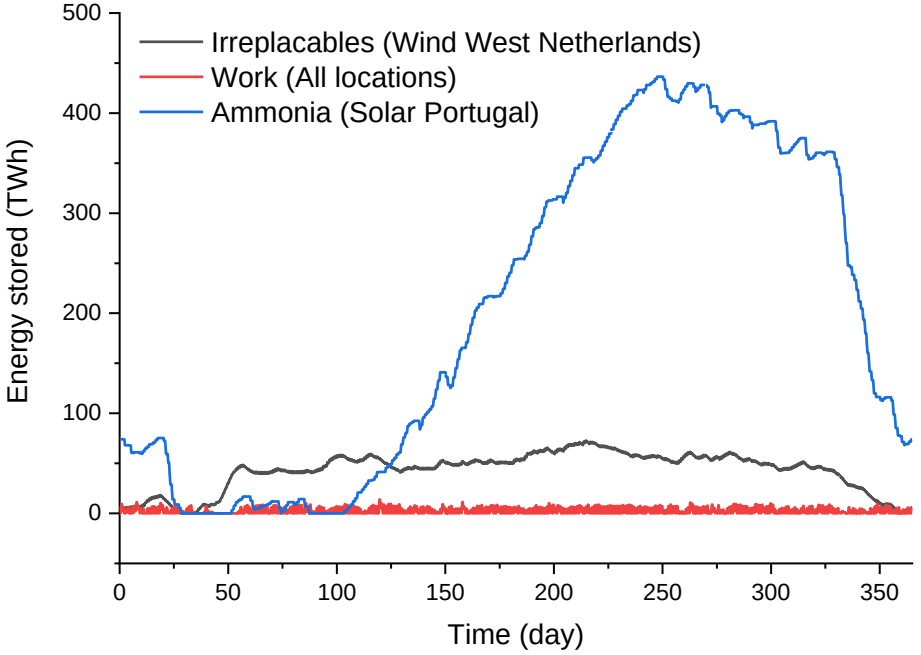

Figure S 3 Year-round storage at three sites in the base case scenario 1 'Wind, Solar and Biomass'. Stored energy indicated as 'Work' indicates short term battery storage. Aggregated over the year the energy throughput through the Work storage exceeds long term storage magnitude (2013 TW h) as short term storage is cycled full/empty many times during the 365 days in a year. The storage capacity of Ammonia and e-Fuels from solar power in Portugal and the Netherlands are most significant compared to other production locations.

Perhaps surprisingly the biomass route does not come back in the model optimisation, although it is enabled. The reason is relatively high costs as is discussed in section 1.6 below. The realisation of carbon containing irreplaceables is done via e-Fuel storage facilities, which are scaled as well and can operate continuously thanks to windpower availability and short term storage. In this case it is therefore not made continuous via a route with ammonia hydrogen storage, as this seems less energy efficient. In this regard direct e-Fuels production offer a more suitable source for the need of irreplaceable carbon based exergy, as they consist of very similar hydrocarbon streams and are utilized as such in this scenario. This is however not necessarily the case as the model tries to find an optimum based on 'a priori' frequency estimation, overestimating the true capacity factors of e-Fuel production facilities. To highlight

this, an iteration is carried out in which e-Fuels and hydrogen storage is left out, leaving only ammonia storage as long term storage candidate. The iteration result shows an additional cost of 4% using the same production capacities for wind and solar as the base case, with similar energy matching performance. After rescaling the production facilities this difference is only 0.4% additional cost. In the last case the model solves the energy mismatch by predominantly wind power (3.1 TW instead of 2.0 TW) with a smaller role for solar power (0.6 TW instead of 1.5 TW) to maximize direct e-Fuel production by wind power further to reduce the demand for reconversion of ammonia to e-Fuel.

In the cost comparison between scenario's shown in **Figure 7A**, the optimized market distribution using current day pricing for assets would yield 71% additional cost compared to current energy market pricing (**Figure 7A**, case *Wind, Solar and Biomass* versus *Current energy expenditure per capita*).

Scenario 2: Wind, Solar, Biomass, without demand of hydrocarbons

To investigate the effect on cost on specifically the energy sector a modified base case scenario is assumed in the model, in which the irreplaceable exergy class is left out, artificially assuming there is no need for such form of energy containing irreplaceables. The result of the optimisation then shows that long term storage need for work exergy in the form of ammonia remains to have a pivotal role in creating an affordable scenario in which the required exergy is always available. In this scenario carbon containing e-Fuels storage is not implemented. Without having irreplaceable energy need by the end users e-Fuels appear not cost effective. As the transport sector is put in the 'work' exergy class this scenario only uses 10% of the total energy to provide for a fully electrified transport sector. This is remarkable because the transport sector is often thought as the major consumer of energy in the current fossil carbon powered situation. In terms of costs this scenario shows that an optimized market would yield only 31% additional cost compared to current energy market pricing **(Figure 7A,** case 2 '*Without hydrocarbons demand*'). This scenario evidences that energy demand for manufacturing hydrocarbons for chemicals, as is in reality required of course, increases the cost drastically.

Scenario 3: Solar and Biomass, restricted Wind

The drawback of unrestricted capacity scaling is that instead of storage solutions the daily work and irreplaceables consumption is mostly met by using 2 to 3 TW wind power. However, the European Commission has stated goals for the projected scale of sustainable energy in which the installed capacity of wind power amounts to 500 GW in 2030 (1/3 of the electricity demand, COM/2023/669) and at least 600 GW by 2050 (40% of the electricity demand).[15] In 2021 the achievable wind capacity by 2050 was increased to 855 GW installed capacity by the European wind association WindEurope.[31] However, no new policy to achieve such target has been implemented. Therefore the wind capacities are restricted to 600 GW installed capacity offshore wind in further scenario's, to create scenario's which tie the projected capacities in line with current EU policy, mimicking a blend of on- and offshore wind towards 855 GW installed capacity. Note that such limitation of installed wind capacity is related to the space available with good wind conditions and social acceptance around potential wind turbine locations. In line with empirically observations[50,51] Lu et al. [52] calculate using 2.5 MW rated wind mills in large arrays an installed capacity of 7 MW/km^2 still yields a high capacity factor (>90% of theoretical), while above that capacity the achievable power density (in MW_e/km^2) rapidly saturates and the capacity factor decreases therefore rapidly as well. Moreover, onshore wind power, according to Miller et al.[30] would only yield about 1 MW/km^2 electrical energy averaged, with an installed capacity of 5 MW/km^2. The 600 GW wind capacity installed, assuming an allowable power density of 7 MW/km^2 would already use 2% of the EU land area while it has limited yield. The 600 GW assumed in the model is based on offshore wind, where the windspeeds are higher and therefore one can anticipate an average electrical energy yield of 3.2 MW/km^2 to be feasible. The electrical yield coming from 600 GW installed capacity offshore is equivalent to 1.35 TW installed capacity onshore or a mix of 54% onshore and 46% offshore wind with a total installed capacity of 855 GW wind power (as planned by the European Union to date).

One could expect that with a limitation in year-round energy availability of wind energy the cost effectiveness of energy crops will dominate the long term storage market. Instead, biomass plays no role in the restricted wind scenario's (**Figure 4**E and F), because they are costly compared to other producers and have a comparatively low conversion efficiency. In the wind restricted scenario the energy production requires an installed power of 2.9 TW Solar combined with the limited 0.6 TW of Wind power to meet demand (**Figure 5A** case *'Solar and Biomass, restricted Wind'*). This scenario

includes an investment in 26 TWh of short term storage, as Solar meets the diurnal consumer needs to a lesser extent compared to Wind production. Such capacities can be achieved using redox flow type batteries with sufficient power capabilities to be (dis)charged within up to ten hours and/or grid batteries which include abundant chemistry like lithium/sodium based batteries, aqueous Ni/Fe or Fe/air type of batteries.

Similar to the *Wind, Solar and Biomass* scenario, the model scales e-Fuel and ammonia storage based on the 'a priori' frequency estimation. The model scales both technologies at certain production facilities, which result in lower actual frequencies. Here, because long term storage has a key role in energy supply, investment in only one of the storage technology is investigated. The cost effect of using only e-Fuels as long storage fuel results in 3% additional cost compared to investing in both long term storage technologies. Surprisingly, the cost effect of using only ammonia as long term storage fuel results in 20% *lower* cost compared to investing in both long term storage technologies. The additional solar capacity needed to compensate the losses for reconversion of ammonia amount to 2%. This highlights the key role that ammonia storage could play for realistic cost effective and secured sustainable energy supply.

One can see that in the '*restricted Wind'* scenario's with a (realistic) limitation of wind power conversion and storage has a bigger contribution to the total *cost* compared to the base case *(***Figure 7*A*** case '*Solar and biomass, restricted wind*' versus '*Solar, wind and biomass'*). Essentially this is due to the stronger dependence on solar power, which has a stronger day/night and seasonal dependence opposite to the seasonal demand of energy, and therefore leads to a poorer direct-use match with the demand throughout the year.

Scenario 4: Solar and Biomass, restricted Wind. Without hydrocarbons demand.

Similar to the unrestricted scenario, in the *'Without hydrocarbons demand'* scenario also the space limitation on installed wind power can be taken into account by limiting wind to 0.6 TW installed power. The usage of hydrocarbons for chemicals weighs heavy on the net annual energy price for electrified scenario's. The restricted scenario without an irreplaceables exergy class shows that the installed capacity (2.6 TWh) for wind and heat is reduced compared to the installed capacity in the base case with restricted wind (3.5 TWh) (73%, **Figure 5** case *'Solar and Biomass, restricted Wind. Without hydrocarbons demand,'*). The marginal cost of irreplaceables on the total

energy price is however 65% for restricted scenario's instead of 31% for unrestricted scenario's (**Figure 7,** comparison '*restricted Wind*' scenario's *with* and *without hydrocarbons demand* versus comparison '*Wind, Solar and Biomass*' scenario's *with* and *without hydrocarbons demand*). The major cause of such an increase is the allocation of wind energy for providing the irreplaceables energy class (because the wind provides more continuous supply). This causes a steep increase in the need of seasonal storage for work and heat exergy classes from solar, which otherwise would be provided (partially) from short term storage capacity provided by wind power. Also the amount of wind energy is not sufficient to provide for the irreplaceable exergy consumers, causing the necessity of large seasonal storage of e-Fuel as well (**Figure 5B**). e-Fuel generation tied to solar energy generation result in low utility factors, making it a relatively expensive solution. This result shows the need to further minimize hydrocarbon derived products, as energy generation is not the most expensive but rather continuous demand of hydrocarbons for chemical products itself is costly (which requires CO_2 capture for feedstock as well).

Scenario 5: Solar and Biomass, restricted Wind. Without hydrocarbons demand. Scaled.

This is the same scenario as 4, but with an assumption for the learning curves of the generation and storage assets involved. As indicated in the main text the implemented cost adjustments are according to the economy of scale factorization of *Way et. al*.[25] At the *final* scale (alkaline) electrolyser costs become then 20% of the current price, reducing conversion of electricity to e-Fuel and ammonia (53%) as. Also PV cost is reduced to 20% of the current price and wind power prices are reduced to 50%. The resulting cost reduction using ammonia as storage carrier amounts to 24% compared to the same scenario without scale factors included. The obtained cost factors are implemented in the LCOE and sLCOE as discussed in SI 1.5.

Scenario 6: Solar and Biomass, restricted Wind, only NH_3 storage.

In this scenario the hydrocarbon e-Fuels are on purpose assumed to be produced from directly produced hydrogen feedstock which is stabilised by using stored ammonia. In that way the eFuels and irreplaceables can be produced with high capacity factor, requiring less eFuel assets. The result is another minimum cost system that can be found in the minimisation routine, which was not found when starting from both eFuel

and NH_3 storage at equal preference. This illustrates that initial choices determine what the model finds as minimum cost solutions.

Scenario 7: Solar and Biomass, restricted Wind, only NH_3 storage. Scaled.

Same scenario as above, but now with an additional cost scaling performed similarly to scenario 5 above. Since in this case the ammonia infrastructure is already larger cost benefits from upscaling the sector can again be anticipated.

Scenario 8: Transport sector not electrified. Restricted wind.

More extremes in the possible choices for future energy systems can be studied within the model. A scenario is made to describe what would happen if the transport sector is not electrified, but remains closer to our current transport sector that still depends heavily on fossil derived fuels. This would elucidate the contrast with an electrified case. In this scenario the transport sector doesn't shift to more efficient use of energy by electrification, but remains an 'irreplaceable' exergy class in the form of using carbon containing petrol fuel. Having a restricted amount of wind energy, solar power would need to be increased, but this is a poor replacement of wind when considering the consumption pattern (**Figure 4**, middle). Such leads to inefficient use of the costly eFuel assets, with low capacity factors. Therefore the choice was made to calculate how biomass energy crops would need to be scaled up to produce the fuel for transport. The projected annual energy from biomass then becomes 502 GWy, which is far above a feasible energy output for landfill (~70 GWy globally[44]). It also leads to relatively high costs. Although it is not a feasible scenario, it is listed as illustration in **Figure 7**.

Scenario 9: Transport sector not electrified. Restricted wind, all electric.

As the above scenario 8 this handles a hydrocarbon e-Fuel based transport sector, but now the hydrocarbons are produced via CO_2 capture and reaction with hydrogen, ultimately from using green electricity. In that way no large amount of biomass is required. However, now the need for an increase in installed solar capacity from 2.9 to 4.8 TW (**Figure 5**, scenario *'Transport sector not electrified. Restricted wind, all electric'*). This also results in a net energy price increase of 31% with respect to the scenario in which the transport sector is electrified (**Figure 7A**, scenario *'Transport*

sector not electrified. Restricted wind, all electric'). In this case the conversion to hydrocarbons from electricity amounts to 63% of the total energy cost.

Scenario 10: Transport sector not electrified. Restricted wind, only NH_3 storage.

Similar to previous cases with irreplaceables consumption, giving the model a single long term storage solution shows a benefit due to improved capacity factors for energy conversion plants. The net cost is 22% lower when choosing for ammonia as long term storage carrier. An additional solar capacity of 9% (5.2 TW) is needed for this solution. Also when e-Fuel is the single long term storage carrier the cost is lowered by 18% with 24% additional solar capacity needed (6.0 TW). Still any solution of the scenario in which the transport sector remains (e)Fuel based is 26% more expensive compared to an electrified transport sector. The outcome of this scenario however also evidences that ammonia is a more reduced costs energy storage carrier for long term storage of energy, irrespective of electrification of the transport sector.

2. MODEL DESCRIPTION

The aim of the model is to show the ideal energy distribution based on a given consumption pattern. This method solves consumption demand based on the order of highest efficiency instead of using time dependent balancing functions, similar to Hakawati et. al.[53]. The benefit of this approach is that efficiency can be conveniently expressed in economic efficiency, energy loss efficiency or areal usage efficiency without changing the base structure of the model. Unmatched or highly inefficient consumption and production methods can be distilled from 'the bottom of the list'. Additionally the model generates the ideal case matching consumer and production patterns and fuel types unbiased. The drawback is that mass/energy balances are less intuitive as it includes some additional accounting. The basic structure of the energy balance is solving the equation:

$$E_{p,t1} * \eta_{conv-p\rightarrow s} * \eta_{s,dt} * \eta_{conv-s\rightarrow t} * \eta_{t,dx} * \eta_{conv-t\rightarrow c} = E_{c,t2}$$

In which E_P is the produced energy at some time *t1*, η is the efficiency of conversion (conv) from producer (*p*), storage (*s*), transport (*t*) and consumer (*c*) and the storage efficiency over *dt (s,dt)* to finally provide the energy demand E_c at some other time *t2*.

2.1 Production and consumption profiles Ep and Ec

2.1.1 Producers

Diurnal energy producer and consumer profiles are obtained by converting empirical data to energy functions. Time and position dependent production data from solar panels and wind farms use the day average cloud and wind strength data obtained from the nearest location available via ECA&D[10] to determine output for the selected nodes. For future use the model facilitates easy incorporation of existing wind and solar data readily available, by providing scalable vector $E_{p,\theta,\varphi,t} = Q_{p,\theta,\varphi} * \eta_{\theta,\varphi,t}$ in which $Q_{p,\theta,\varphi}$ is the rated power of the production facility and $\eta_{\theta,\varphi,t}$ the time dependant efficiency vector depending on the local climate.

Wind

Wind energy efficiency calculation is based on a ramping efficiency from an offset windspeed P_{min}[Bft] until an optimal P_{opt}[Bft] efficiency. Higher windspeed yield equal efficiency until too high windspeeds P_{max} [Bft].[54] The efficiency is subsequently multiplied with the rated capacity of the wind park to yield the time dependent energy output. subsequently modelled using equations:

$$\eta_{\theta,\varphi,t} = \begin{cases} 0 & \{P_{min} > P_w \; or \; P_w > P_{max}[10]\} \\ \dfrac{P_{w,t} - P_{min}[2]}{P_{opt}[6] - P_{min}[2]} * \eta_{max} & \{P_{min} < P_w < P_{opt}\} \\ \eta_{max} & \{P_{opt} < P_w < P_{max}\} \end{cases}$$

Solar

Solar panel efficiency calculation is based on the insolation equation of FM Mulder.[5] Empirical local cloudiness data for a node is incorporated using equation:

$$\eta_{\theta,\varphi,t,c} = \eta_{\theta,\varphi,t}(I_{Diff} + I_{Dir})/I_{max}$$

Here diffusive and direct irradiation I_{Diff} and I_{Dir} are calculated using the adjusted ASHRAE Clear Day model depending on their lattitude/longtitude θ/τ, time t and cloudiness c .[55]

$$I_{Dir} = I_{max} * \left(0.77{K_T}^2 - 0.106K_T + 1\right) * \sin(\beta)$$

$$I_{Diff} = I_{max} * \left(-1.12{K_T}^2 + 0.836K_T + 1\right) * (0.095 + 0.04\sin(\frac{360}{365} * (n - 100))$$

In which I_{max}, I_{Dir} and I_{Diff} are the lambert-beer irradiation, direct irradiation and diffusive radiation respectively and β the inclination angel with respect to the sun. Factor K_T is the normalized cloudiness obtained from empirical wheather data and n is the ordinal number of the day in the year. The polynomial is a generalization of an empirical adjustment proposed by Kostić and Mikulović for the Serbia region representative of an in-land region with moderate temperatures.[55]

2.1.2 Consumers

Electricity usage except heating and transport is based on the equation of Mulder[5], which in turn was modelled based on US data.[32] The polynomial equation is normalized and factorized by population density at each node.

Heating

Household, office and agricultural heating by electric heat pumps is probably the most effective and cheap way in which energy can be saved. Good prediction of the energy used for heating is therefore key. Time and position dependent consumption profiles of (household) heating is a complex parameter set in which temperature, wind speed, goodness of insulation plays a role. The empirical data available is limited and the most trustworthy indicators are the annual national gas use and typical energy consumption values for cooking and warm water use. Therefore this model uses a combined modelling and empirical approach to predict heat consumption behavior. To estimate the gas fraction used for heating the net natural gas usage of the Netherlands during a year in which electricity was barely used for cooking, hygiene and heating is taken (1980, 413 PJ, 14.15 million people *p*). The gas fraction used for cooking one daily warm meal and warm water are estimated per capita (0.9 GJ/year/capita[56] and 9.9 GJ/year/capita[57] respectively). The residual energy (413 – 152.8 PJ = 260.2 PJ for household heating is assumed to be on at days in which the average temperature difference dT=T-18 ^{o}C is below 0. The temperature 18^{o}C is the nominal minimal in-house temperature. Temperature data from 1980 is taken and from this the insulation factor is derived solving:

$$Q_{heating} = \sum_{t=0}^{365} -k * p * dT_{t,T<18}$$

The natural gas usage of households in 2021 is only 8% higher while the increase in population is 24%. This can be explained by the cooler temperature in 1980. The formula reasonably estimates the gas usage in 2021: the k value found for 1980 amounts to 0.00567 PJ/million persons/Celcius difference which predicts 278.7 PJ gas used for heating in 2021, which is 7% higher. Including cooking and warm water energy (189.5 PJ) would predict a 13% increase in gas consumption. Improved insulation and a shift in cooking and heating methods are thought to be the prime contributors, but cannot be clearly attributed. In 2021 the shift from household boilers to electric types is not widespread and therefore the difference is contributed to improved insulation in the model. The most conservative case in potential energy saving is therefore assumed by lowering the insulation constant k to 0.00522 PJ/million person/Celsius difference. This could be enhanced by improving insulation, utilization of stored heat and/or efficient use of heat pumps. Heat pumps are included in the model as converters from work to heat. The daily use is subsequently derived by fractionating the year heating energy to the day energy by using the dT of that particular day. The periodic energy need on heating days is obtained by solving Q using temperature description:

$$T_t = T_{avg} + (T_{max} - T_{min})\cos\left((t - 0.5) * \pi\right)$$

Electric vehicles including hydrogen electric vehicles

Contrary to gasoline powered vehicles the EV consumption profiles are highly infrastructure dependent. The periods outside traffic hours will effectively lead to high grid usage. Charging can be facilitated from home or at the office shifting the load by approximately half a day.[58] Charging can occur smart (availability/pricing dependent) or linear. The EV battery can be used as storage equipment or not. Here we argue that office charging and installing a secondary battery at home situated PV's is the best solution:

- Energy efficiency perspective: The peak capacity of EV charging ties with the peak capacity of energy available for wind and solar energy.
- Capital expenditure perspective: An EV battery is designed for the highest charge density which is not necessary for installation near PV electric storage. A battery suitable for PV energy storage can be a lot cheaper as more chemistry options are available compared to EV batteries.
- Safety perspective: Risks during charging are mitigated from suburban areas

However, this is not the current practice of EV charging. Therefore energy demand for the two cases (house and office charging) are options in the model, using the charge rate definition. House charging is assumed throughout the main text:

$$E_t = \begin{cases} \frac{Q_{EV}}{t_c} \left\{ \frac{18}{24} < t_h < \frac{24+9}{24} \right\} \\ 0 \, \{other \; t\} \end{cases}$$

Here energy at time t is the electric vehicle capacity Q_{EV} divided by the charging time t_c in hour. The approach reflects the current empirical behaviour of home charging.[59] Note that the capacity Q_{EV} is modified from the current gasoline transport figure, by multiplying the annual energy input with the gas engine efficiency dividing it by the electric engine efficiency. Also note that the energy may come from stored energy; e.g. in winter a H_2 or eFuels fired gas turbine may provide the required electricity E_t as well.

2.2 Efficiency equations

The method of efficiency evaluation is described. First a certain storage loss function and a transport loss function is defined on which the evaluation is carried out. This part can be changed for differing types of storage and transport technologies respectively.

2.2.1 Storage and transport equations

Loss functions of a certain type of storage is defined as energy and time dependent. The change in stored energy X in carrier with c_1 [1/h] rate , without in or output is thus given by:

$$\frac{dE}{dt} = -c_1 E$$

Which gives

$$E = E_0 e^{-c_1 t}$$

And efficiency equation

$$\frac{E}{E_{t=0}} = (e^{-c_1})^t = {\eta_1}^t$$

Evaluation carried out for to- and back conversion for storage for all t:

$$S_{1,1}\begin{cases} {\eta_1}^t \\ \eta_{1,i,conv} * {\eta_i}^t * \eta_{i,1,conv} \end{cases}$$

Creating i matrices $S_{i,I}$ containing [t x (1+i)] efficiency fields.

Evaluation carried out including fuel type change:

$$S_{1,2}\begin{cases} \eta_{1,2,conv} * {\eta_1}^t \\ \eta_{1,2,conv}{\eta_2}^t \\ \eta_{1,3,conv} * {\eta_3}^t * \eta_{3,2,conv} \end{cases}$$

Creating i x j matrices $S_{i,j}$.

TRANSPORT OF FUELS

Similarly the transport function of a certain type of gas or liquid is defined as rate dependent as friction of flow in a tube is velocity dependent. For loss per unit of energy this becomes v/E = D. The function includes distance D:

$$X = X_0 e^{-c_1 D}$$

In which D is the calculated distance between two nodes. This leads to a similar equation as with storage

$$T_{1,2}\begin{cases} \eta_{1,2,conv} * {\eta_1}^D \\ \eta_{1,2,conv}{\eta_2}^D \\ \eta_{1,3,conv} * {\eta_3}^D * \eta_{3,2,conv} \end{cases}$$

For electric transmission line losses the calculation method could be taken from Wadhwa.[60] The net power transmitted over a real line however is unknown as nodes do not necessarily represent real trajectories. Therefore a base geometry of an electric field line is taken and the calculated value must be evaluated as the bare minimum loss of transporting via electricity.

Electric power is defined as:

$$P = I * U$$

In which power P [W] is the current I [A] multiplied by the voltage U [V]. The general equation of efficiency between sending and receiving ends read:

$$\eta = \frac{P_r}{P_s}$$

For simplicity short lines (< 80 km) and high voltage DC lines are assumed.

In short lines and high voltage DC lines, energy loss is dominated by resistive effects. The efficiency equation reads:

$$\eta_{short} = \frac{Out}{In} = \frac{P_r}{P_r + 3I^2R} = \frac{P_r}{P_r + 3\left(\frac{P_r}{U_r}\right)^2 R}$$

With resistance R [Ω] defined as

$$R[\Omega] = \rho \frac{D}{A}$$

For example aluminium resistivity ρ [3.2 μΩ*cm] and 25 cm^2 area A and length D, 400 kV power lines may be assumed. Similar to friction loss a linear dependance on length is observed, allowing the same frictional loss equation as other transport types.

Due to lumping of consumer production energies throughout Europe and positioning of the node in central Europe in the main text, uniform line losses of 3.5% / 1000 km,representative for 800 kV HVDC lines are taken.[61]

2.3 Evaluation of effective use

The energy demand $E_{c,t,i}$ of fuel type i at moment t is a given per consumer. The demand is resolved by evaluating all possible trajectories:

$$\max_{\eta} \begin{cases} j \begin{cases} S_{j,j} \rightarrow T_{j,i} \\ S_{j,i} \rightarrow T_{i,i} \\ S_{j,k} \rightarrow T_{k,i} \end{cases} \\ i \begin{cases} S_{i,i} \rightarrow T_{i,i} \\ S_{i,j} \rightarrow T_{j,i} \end{cases} \end{cases}$$

With S and T are matrices defined as in Efficiency equations. As a fuel type j≠i can have both efficient transport and storage properties, all i,j conversion need to evaluated in between transport and storage as well.

2.4 DISTRIBUTION OF ENERGY

The consumption profile $c_2(\psi_2,\theta_2,i)$ with fuel i at node location ψ_2,θ_2 are taken as example. Production profile $p_1(\psi_1,\theta_1,j)$ gives matrices

$\eta_{1,2} \begin{cases} S_{i,i} \rightarrow T_{i,i,\psi1,\theta1,\psi2,\theta2} \\ S_{i,j} \rightarrow T_{j,i,\psi1,\theta1,\psi2,\theta2} \end{cases}$ (single conversion) and

$\eta_{1,2} \begin{cases} S_{j,j} \rightarrow T_{j,i,\psi1,\theta1,\psi2,\theta2} \\ S_{j,i} \rightarrow T_{i,i,\psi1,\theta1,\psi2,\theta2} \\ S_{j,k} \rightarrow T_{k,i,\psi1,\theta1,\psi2,\theta2} \end{cases}$ (intermediate fuel)

The transport efficiencies are calculated by filling in the node distances. The time (storage) dependent efficiencies need to be calculated. For this a lookup table is made with span t = [0:(1/24):365] days. This results in a [S x t x T] matrix per consumer/producer combination.

A final total efficiency vector is defined of size (n*t) x (m*t) for n producer and m consumer nodes containing the net efficiency of storage/transport between E_c and E_p at every t. This is the main energy balance matrix which is used in the model. The choice of efficiency between producer and consumer is however not necessarily the maximum efficiency as the model is minimizing the cost (see cost calculation).

After calculating the maximum cost efficiency the energy efficiency matrix is made. Then, starting from the most cost efficient route $\eta_{1,2,dt}$ the model calculates the energy distribution by solving $E_{p1,t}\eta_{1,2,dt}=dE_{c2,t+dt}$ using the energy efficiency matrix. If $E_{p1,t}\eta_{1,2,dt}>E_{c2,t+dt}$ the residual energy produced, or if $E_{p1,t}\eta_{1,2,dt}< E_{c2,t+dt}$ the deficit in energy consumed is placed in vector E_p at t or E_c at t+dt respectively. The 'used' energy producer/consumer route $\eta_{1,2,dt}$ are closed by making the efficiency equal to 0. At the

end of an iteration the unmatched residual energies ends up in E_c (deficit case) or E_p (excess case).

2.5 COST CALCULATION

For finding the most cost effective route, the production cost and the cost associated with the conversion and storage need to be combined. The estimation of using energy conversion and storage facilities depend on their effective usage time. For comparing the cost effectiveness, the cost of production is combined with the routing cost. To get to the same units (€/kWh/y), initial conversion from producer (in €/kW/y installed) is multiplied by the maximum conversion of a producer divided by its annual output (kW installed / (kWh/y)).

$$cost_{init\ conv} = cost_{init\ conv,max} * \frac{P_{p1,max}}{Q_{p1}}$$

As the wind and solar energy production varies on the local weather, the mismatch between a certain producer and consumer is estimated by assessing the mismatch frequency. First producer and consumer patterns are normalized and subsequently subtracted. This results in a mismatch pattern which has a net zero sum. After calculating the consumption profile E_c [kWh/h] and production profile E_p [kWh/h] the mismatch profile is defined.

$$E_{mm} = \frac{E_p}{\sum E_p} - \frac{E_c}{\sum E_c}$$

The storage cost (€/kWh/y installed) and downstream conversion and transport cost is calculated by assessing the usage frequency. On the mismatch vector a fourier transform[1]* is carried out, giving the complex signal a:

$$a(f) = \sum_{dt=1}^{365*24} E_{mm}(t)(e^{\left(-\frac{2\pi i}{T}\right)})^{(t-1)(f-1)}$$

With frequencies:

[1]* Via mathworks https://nl.mathworks.com/help/matlab/ref/fft.html#buuutyt-6

$$f = \{0: 1/24: 365\}$$

The real part of the signal amplitude is obtained by taking the absolute value of the signal:

$$A(f) = \frac{|a(f)|}{T}$$

Then the probability the route is used at least used once during dt is obtained by probability distribution p_{dt} which is calculated using the signal amplitude

$$p_{dt} = \sum_{i=1/24}^{dt} a(\frac{1}{i})$$

Finally the estimated annual cost of the storage [€/kWh/y] utility s can be calculated based on such usage probability giving a real annual user frequency f_p:

$$cost_{s,dt} = \frac{dt}{365 * p_{dt}} * cost_s = 1/f_p * cost_s$$

With capping the frequencies above daily frequencies using:

$$dt(dt \leq 1) = 1$$

This approach yields a cost estimation which adequately estimates storage cost, but overestimates the cost of conversion and transport as this is not cumulative over time, but periodic. The spread of the consumption profile needs to be accounted for by an additional term.

Similar to the initial conversion, the spread of consumption is taken into account by evaluating the maximum energy demand $P_{c1,max}$ to the daily demand $Q_{c1,d}$, now combined with the user frequency and a demand period:

$$cost_{i,dt} = \frac{P_{c1,max}}{Q_{c1,d}} * 1/f_p * cost_i$$

In this equation cost depends on requested Power P_{c1} [kW/y], usage frequency f_p [times/year] and average energy demand Q_{c1} [kWh/day] respectively.

As one would expect the fourier approach shows that wind is a more suitable match for work demand compared to solar, as the amplitude of the daily wind/work mismatch frequency is higher compared to that of solar/work mismatch, giving a high cost effectiveness for short term storage.

3. Cost and Efficiency values used in model

3.1 Note on e-Fuel synthesis

E-fuel synthesis is a multistep process. First CO_2 is harvested from air using Direct Air Capture (DAC) or from another source like water purification or cement production. Hydrogen is harvested by splitting water in an electrolyser. Subsequently the CO_2 is subjected to the water gas shift reaction yielding CO in the reaction $H_2 + CO_2 \rightarrow H_2O + CO$. The final step is to synthesize alkanes using CO and H_2 in the Fischer-Tropsch (FT) reaction $(2n+1)\ H_2 + n\ CO \rightarrow C_nH_{n*2+2} + H_2O$. Starting from electricity, the electrolyser efficiency (64.2%), DAC energy (1.28 MWh/t CO_2) and FT efficiency and input (80%, 0.341 kg CO_2/kWh alkanes, 1.25 kWh H_2 /kWh alkanes) are used, yielding a net conversion efficiency of 37% kWh/kWh (for values and references see Table S2). Starting from H_2 the electrolysis step is omitted and full efficiency of H_2 to capture CO_2 is assumed, as the majority of DAC energy use is heating of the absorbing material to release the CO_2 (using H_2 combustion in that case). This yields a conversion efficiency of 57% kWh H_2 to kWh e-Fuels. Similarly, ammonia cracking efficiency in such facility is assumed to be 85% (94.8% is the limit, as this reaction is endothermic). As a result this yields a conversion efficiency of 48% kWh NH_3 to kWh e-Fuels.

The more complex hydrocarbon (e-fuel) synthesis investment costs are reported in several ways. The wide spread of the projected CAPEX becomes problematic when comparing storage of e-fuels with storage of hydrogen or ammonia. For e-fuel plants an estimated CAPEX of € 800/kW for a Fischer Tropsch based conversion plant was projected by Martin et. Al as part of their model published in 2023.[62] The input for this plant still required CO_2 (€ 600/t, same reference), hydrogen (€ 1100/kW, same reference) and electricity. An alternative calculation is performed by Becker[63] published in 2012 in which a full analysis of a e-Fuels plant is made, based on steam electrolysis. This resulted in an estimated € 1630 euro/kW installed capacity. Uekerdt et al[64] projected in 2021 a cost of € 400 euro/kW installed capacity excluding electrolysis. Comparing the three sources the estimation from Martin et. Al. seems adequate. The total annual cost from electricity to e-Fuels amounts to € 273/kW/y

installed capacity. The cost per year is assume a lifetime of 25 years and a OPEX of 3% of the capex per year. Here the hydrogen electrolysis is taken over from Martin et. al with a cost of € 77 /kW/y. The cost of hydrogen liquefaction from the same reference amounts to € 123 /kW/y resulting in a net cost of € 200 /kW/y for stored hydrogen. Compared to Haber Bosch (€ 169 /kW/y including electrolysis for ammonia) one only would expect e-Fuels to be competitive for irreplaceables exergy class.

3.2 Note on biomass and irreplaceable feedstock.

Caloric value and market price of agricultural biomass is taken. Ranges from 0.06 (rapeseed) – 0.35 (potatoes) €/kWh. E.g. for Energy of Potatoes the price of potatoes (~30 €/100 kg in 2024 European Energy Exchange) divided by its caloric value yields a value of 0.35 €/kWh. Similarly rapeseed yields 0.06 €/kWh. 0.3 €/kWh is subsequently ***chosen*** as majority of land used for energy crops need to ***compete*** with food prices.

E-fuels, also functioning as irreplaceable feedstock for the chemical industry, is defined as liquid alkanes typically derived using Fischer-Tropsch processing. For convenience, full utilization of the biomass its caloric value is assumed (e.g. by combining oil yield, the majority of the caloric value, and methanogenesis on residual biomass cuttings).

3.3 Note on fuel combustion

Price estimated on gas turbines, e.g. [65], with long lifetime (38 years) or average sized fuel combustion aggregates (Dutch market pricing in 2024: 255 €/kW/year, fully serviced), with shorter lifetime (20 years)). Efficiencies vary between 30-70% depending on off-gas heat recycling utility and steam injection.[66] Gas turbine efficiency with steam injection is used.[21,67]

3.4 TABLE WITH VALUES USED IN BASE MODEL

Table S2 Cost of production, conversion, storage and transport units per year, expected lifetime and efficiency of conversion, storage or transport. Values are expressed in installed output capacity, per kW (for conversion, generation) or kWh (storage) per year. # exergy: work, heat, irreplaceable (irr) or storage fuels hydrogen (H_2), ammonia (NH_3).

Name	From#	To#	CAPEX (€/kW)	OPEX (€/kW)	Yearly $cost_{unit}$ (€/kW(h)/y) unless specified otherwise)	Lifetime (years)	Efficiency	Description of technology
Per production type:								
PV	Solar	Work	1000		**50**	20		Complete photovoltaic system[68]
Wind turbine (on shore)	Wind	Work	1000	30	**70**	25		Projection for 2035.[62]
Wind turbine (off shore)	Wind	Work	2000	60	**140**	25		Projection for 2035.[62]
Biomass as continuous energy source	Biomass	Irr.	0.3 €/kWh * 8760 h / year		**2538.8**	NA		See note 3.2
Per storage fuel:								
Battery storage	Work	Work storage	151		**30**	5	99.8 %/day 95%	Prognosis Bloomberg 2022.*[2] Conversion efficiency: 60 mV overpotential on 1.2V system (vanadium flow cell) yields 95%.

*[2] https://about.bnef.com/blog/lithium-ion-battery-pack-prices-rise-for-first-time-to-an-average-of-151-kwh/

								Daily loss: Self-discharge of grid storage.[68]
HVDC line	Work	Transport efficiency			**2.5 €/kW /1000 km/y**		96.5% / 1000 km	Cost analysis for HVDC lines per 1000 km.* [3] Efficiency see 1.2.1
Electrolysis	Work	H_2	1100	2.5% of CAPEX	**77**	25	64.2%	Water Electrolysis price [62], Efficiency depends on type.[62,69]
e-Fuels synthesis	Work	Irr.	3385	~3.5 % of CAPEX	**273**	25	37%	Includes DAC[70], CO_2 conversion to CO (electric or water gas shift), Water electrolysis, Fischer Tropsch.[62,63] Cost: 3385 =800 Fischer Tropsch + 1855 Electrolyser + 730 DAC.
Haber Bosch (HB) from electricity	Work	NH_3	2224	3% and 5% of CAPEX	**169**	25 and 30	57%	Electrolysis and Haber Bosch.[62,69,71] Cost: 2224 =1229 electrolyser + 995 HB.
Heat pump	Work	Heat	1625	0	**81.3**	20	600%	Commercial heat pump.[72]
Heat storage	Heat	Heat storage			**0.02**		99.6%/ day	Seasonal heat storage (50% eff/180 days). Heat storage cost prediction by CE Delft.* [4] 50% heat retained after 180 days.
Heat transport		Transport efficiency			**7480 €/kW /1000 km/y**		15.9%	Given the hydrogen piping costs and an energetic density difference of

*[3] Analysing the costs of High Voltage Direct Current (HVDC) transmission (electrical-engineering-portal.com)

*[4] Kansen voor thermische opslagsystemen – CE Delft, August 2020, p72-80: cost of system € 4.60 – 16.75 /GJ/year.

								a factor 520. Efficiency: E.g. water (4.2 kJ/kg/K) with dTusage = 15 K gives 63 kJ/kg transported. Transport of 1 tonne/s, 63 MJ/h using 1 m diameter pipe gives 90 bar head pressure. Pump shaft power is 14.72 kW in this scenario and transport efficiency becomes 15.9%
Fuel storage	Irr.	Storage			**0.02**		100%	Nominal price to store crops is a few cents per bushel, which equates to at maximum one euro per tonne. Taking 600 kWh/tonne yield and a nominal storage period of 180 days gives marginal storage costs. Similar pricing for liquid fuel storage.
Truck transport		Transport			**3.8 €/kW/ 1000 km/y**		98.8%	Estimate for diesel truck transport. Calculation including investment price of a truck, fuel cost and salary. Efficiency: 20 T freight transported using a diesel fueled engine uses approximately 242 kg of diesel. Pipe transport

								would be 99.8%.
Haber Bosch		NH_3	995	5% of CAPEX	**82.9**	30	99%	Current Haber Bosch processing practice
Gas thermostat		Heat	64	0	**3.2**	20	100%	Commercial gas thermostat.
Gas turbine		Work	410	-	**10.8**	38	48%	See note 3.3
e-Fuels cracking		H_2			**44**		65%	Economic evaluation of Fluidized Catalytic cracking.[73]
Hydrogen storage	H_2	Storage	2.7		**0.135**	20	100%	45 kg Storage container of hydrogen.[68] Service life of 20 years. E.g. Martin et. Al. uses € 0.62 /kWh.[62]
Hydrogen liquifaction		Converter	1255 €/kW	2% of CAPEX	**67**	30	100%	Liquefaction of hydrogen.[62]
Hydrogen Pipe transport		Transport			**14.4 €/kW/ 1000 km/y**	30	99.8%	Price: Nordstream is taken as example. Investment price divided by length and energetic throughput. Negligible OPEX assumed. Pipe transport head drop assumed as energy loss. 250 mm diameter 400 bar piping with smooth (lined) inner surface, pressure head of 8 kBar/1000 km is necessary to transport of 252 kg/h, giving 32.76 GJ/h. Pump shaft power becomes 9 kW.

Gas turbine		Work	410	-	**10.8**	38	48%	See note 3.3
Fuel cell		Work			**140**		52%	Fuel cells: Based on a 276 kW PEM fuel cell interim target for heavy duty applications.[74]
e-Fuels from hydrogen		Irr.	2010	~3.5 % of CAPEX	**177**	25	57%	Based on e-Fuels synthesis without electrolysis for Fischer Tropsch.[62,63]
Haber Bosch		NH_3	995	5% of CAPEX	**82.9**	30	99%	Haber Bosch without an electrolyzer.[62,69,71]
Gas thermostat		Heat	64	0	**3.2**	20	100%	Commercial gas thermostat.
Ammonia storage	NH_3	Storage			**0.02**		100%	Same pricing for irr. (liquid) fuel storage is taken. E.g. ref [75] quotes CAPEX € 350 /tonne which amounts 0.06 €/kWh/y.
Ammonia conversion		Converter			**0**			No conversion costs included
Ammonia transport		Transport			**3.8 €/kW/ 1000 km/y**		98.8%	Estimate for diesel truck transport. Calculation including investment price of a truck, fuel cost and salary. Efficiency: 20 T freight transported using a diesel fueled engine uses approximately 242 kg of diesel. Pipe transport would be 99.8%.

Gas turbine		Work	410	-	**10.8**	38	48%	See note 3.3
e-Fuels from ammonia		Irr.	1530 (=800 Fischer Tropsch + 730 DAC)	3.5% and 7.4% of CAPEX	**143**	25	48%	Ammonia splitting, direct air capture and fischer tropsch processing. Efficiency: 48% (=85% (NH_3 cracking) * 57% (e-Fuel synthesis)
Ammonia splitting		H_2			**140**		85%	Cost for hydrogen fuel cell technology assumed with theoretic maximum conversion efficiency, cracking may offer cheaper and scalable solution.[76] Technology is not used in the scenario's mentioned in the main text.
Direct combustion		Heat	410	-	**10.8**	38	100%	Direct combustion. Commercial gas thermostat equivalent not likely. Turbine cost assumed, see note 3.3.

3.5 Fuel type conversion from database

Only transport sector is subjected to conversion from fuel values obtained by Eurostat.[11] Since electrification is expected to be fully implemented, here a conversion number to estimate the necessary energy 'to wheel' is estimated (23% combustion efficiency for the average engine, 85% for an electric vehicle). This value is divided by the electrified vehicle efficiency (85%) to deal with the losses of 'work' exergy from the grid during charging and driving.

Table 3 Conversion of fuel data to exergy classification

Sector	Fuel/Exergy class	Efficiency factor
Non energy use	Irreplaceables	1
Industry	Work	1
Transport	Work	Fully electrified: - On electricity 0.85/0.85, - on other 0.23/0.85 Non converted: - All irreplaceable
Commercial and public services	Electricity: work Other: heat	1
Household	Electricity: work Other: heat	1
Agriculture, fishery, forestry	Oil and electricity: work Solids and gas: heat	1

4. SANKEY DIAGRAMS COMPARING ENERGY DISTRIBUTION

Energy distribution in Europe to fullfill the complete energy demand in case of various investment scenario's. The scenario's are described in the main text, for convenience a table with a short description is added below. Diagrams are scaled relative to each other. 'Losses' include line loss, conversion losses as well as curtailment during peak production periods.

	Scenario	Short description
1	Wind, Solar and Biomass	Unrestricted production capacity scaling, incorporating wind, solar and biomass production types, using all short and long term storage options to fulfill the need of energy for work, heat and irreplacable exergy classes in Europe.
2	Wind, Solar and Biomass, without Hydrocarbons demand	Unrestricted production capacity scaling, incorporating wind, solar and biomass production types, using all short and long term storage options to fulfill the need of energy for work and heat exergy classes, without irreplaceable exergy classes in Europe to estimate only the necessary fuel use for energy purposes.
3	Solar and Biomass, Restricted Wind	Restricted capacity scaling incorporating a limited amount of wind energy production to mimic EC 2050 goals and unlimited solar and biomass production, using all short and long term storage options to fulfill the need of energy for work, heat and irreplaceable exergy classes in Europe

4	Solar and Biomass, Restricted Wind, Without Hydrocarbons demand	Restricted capacity scaling incorporating a limited amount of wind energy production to mimic EC 2050 goals and unlimited solar and biomass production, using all short and long term options to fulfill the need of energy for work and heat exergy classes, without irreplaceable exergy classes in Europe to estimate only the necessary fuel use for energy purposes.
5	Solar and Biomass, Restricted Wind, Without Hydrocarbons demand, Scaled	Restricted capacity scaling incorporating a limited amount of wind energy production to mimic EC 2050 goals and unlimited solar and biomass production, using all short and long term options to fulfill the need of energy for work and heat exergy classes, without irreplaceable exergy classes in Europe to estimate only the necessary fuel use for energy purposes. Using pricing of estimated final scale of production, conversion and storage facilities.
6	Solar and Biomass, Restricted Wind, only NH_3 storage	Restricted capacity scaling incorporating a limited amount of wind energy production to mimic EC 2050 goals and unlimited solar and biomass production, using short term storage and long term NH_3 storage options to fulfill the need of energy for work, heat and irreplaceable exergy classes in Europe
7	Solar and Biomass, Restricted Wind, only NH_3 storage, Scaled	Restricted capacity scaling incorporating a limited amount of wind energy production to mimic EC 2050 goals and unlimited solar and biomass production, using short term storage and long term NH_3 storage options to fulfill the need of energy for work, heat and irreplaceable exergy classes in Europe using pricing of estimated final scale of production, conversion and storage facilities.
8	Transport not electrified. Restricted wind	Restricted capacity scaling incorporating a limited amount of wind energy production to mimic EC 2050 goals and unrestricted solar and biomass production, using all short and long term storage options to fulfill the need of energy for work, heat and irreplacable exergy classes in Europe in the scenario that electrification of the transport sector is not implemented.
9	Transport not electrified. Restricted wind, all electric	Restricted capacity scaling incorporating a limited amount of wind energy production to mimic EC 2050 goals and unlimited solar production, using all short and long term storage options to fulfill the need of energy for work, heat and irreplacable exergy classes in Europe in the scenario that electrification of the transport sector is not implemented.
10	Transport not electrified. Restricted wind, only NH_3 storage	Restricted capacity scaling incorporating a limited amount of wind energy production to mimic EC 2050 goals and unlimited solar and biomass production, using short term storage and long term NH_3 storage options to fulfill the need of energy for work, heat and irreplacable exergy classes in Europe in the scenario that electrification of the transport sector is not implemented.

Transition to net zero carbon emission economy: Cost analysis of alternative scenario's in the European energy market

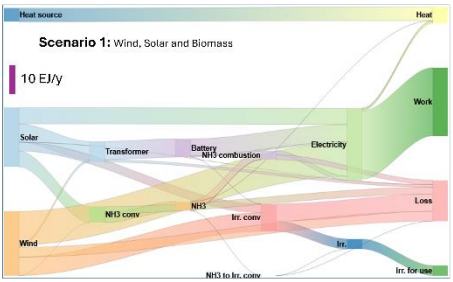

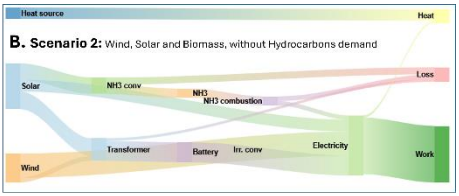

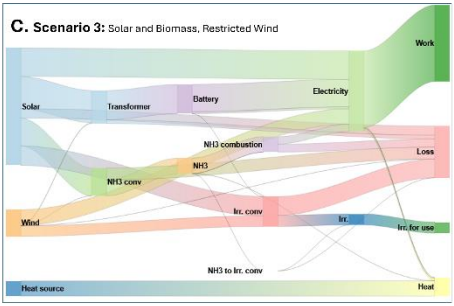

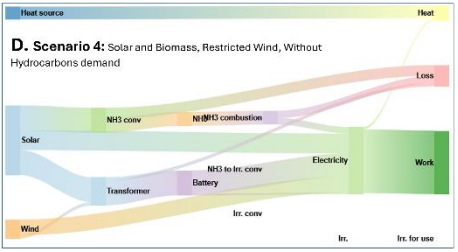

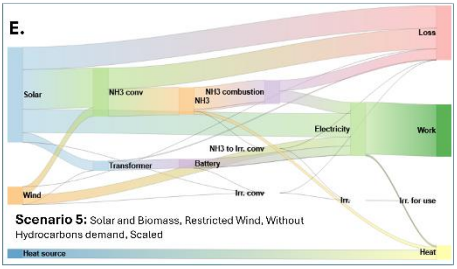

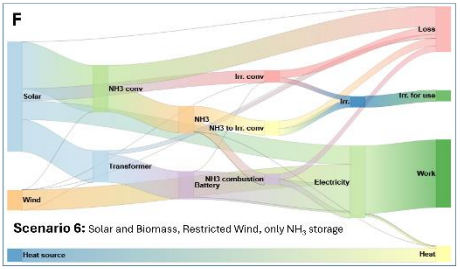

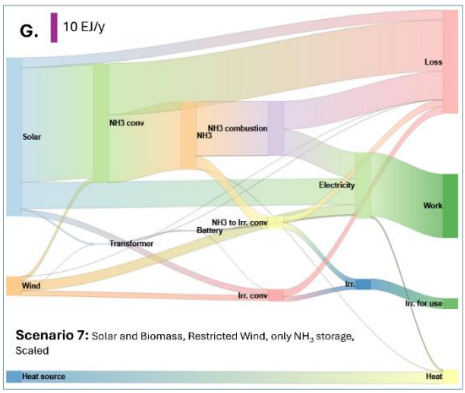

Scenario 7: Solar and Biomass, Restricted Wind, only NH_3 storage, Scaled

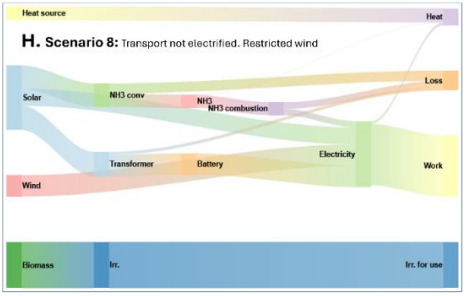

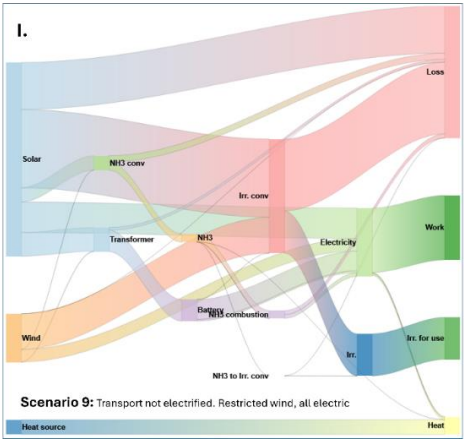

Scenario 9: Transport not electrified. Restricted wind, all electric

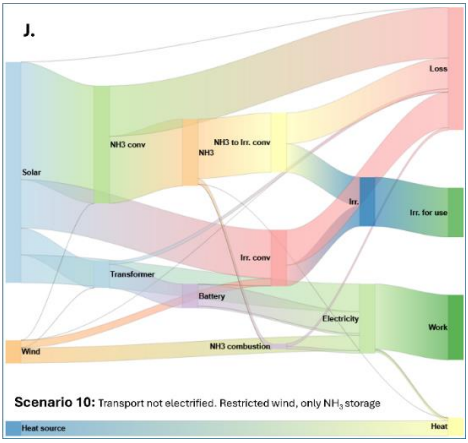

Scenario 10: Transport not electrified. Restricted wind, only NH_3 storage

PART 2: BATTERY TECHNOLOGY

A SHORT INTRODUCTION ON BATTERY CHEMISTRY

A very general description of battery function is outlined here to understand the following chapters. For more insight in redox principles, active materials for batteries and battery testing, please read [1]. On ionic conductivity, ionic double layers and ionic behaviour see [2]. On NMR principles for the solid state see [3].

REDOX CHEMISTRY

One can see a battery as a set of electrochemical reactions between which a series of transfer problems arise. A pair of chemical oxidation and reduction reactions is decoupled, by which electrons can be forced to flow via the outer electrical network to balance the positive ionic motion internally. For lithium ion batteries, upon discharging at the battery anode the active material is oxidized, donating an electron and leaving a positively charged lithium ion. The lithium ion needs to travel through several materials, such as the active material, electrolyte and separator, before it reaches the cathode in which a transition metal ion such as Ni or Fe is reduced upon arrival of Li^+ and an electron. The resistance which the lithium ion feels during transfer through the materials is expressed in terms of conductivity, relating the physical transfer process of diffusion to electrochemical units of current and potential. The transfer or lithium ion needs to pass through (bulk) materials and material interfaces. The energy necessary for transfer is expressed by evaluating the overpotential in Volts at a certain reaction rate, or current density.

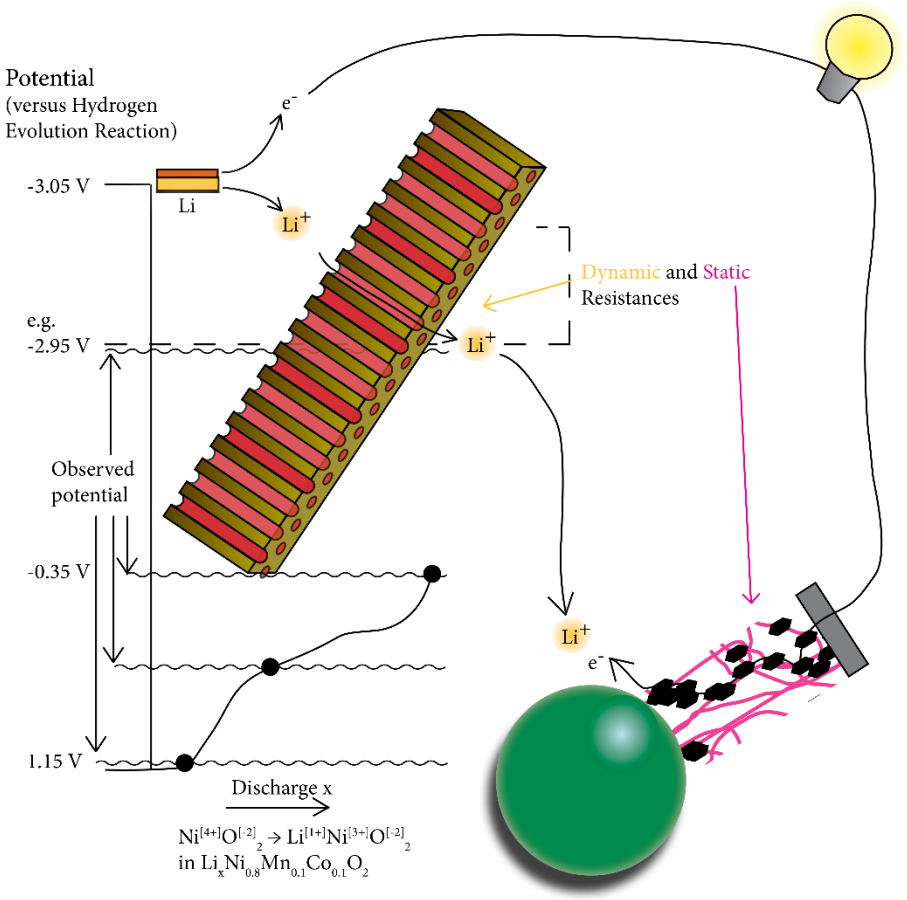

Graphical depiction of the relationship between redox reactions, internal resistances and energy obtained from the battery cell. The energy difference between the chemical states of the transition metals involved translate to an observed (usable) electrical potential. Resistances inside the battery depend on the reaction rate (current). Dynamic resistances are time dependant as well. Upon discharging the battery the potential of NMC changes, causing a gradual change in the observed potential.

Oxidation and reduction of lithium and transition metal ions is intended to occur for the active materials. However, the chemical potential of the materials, especially in their charged state, may result in additional redox side reactions, either assisted by one of the two half reactions or spontaneously. Side reactions may result in the formation of a solid product which is not able to react further because they are fully reduced or oxidized (at the anode and cathode respectively) and stable in contact with

the electrolyte, or they are not electron conductive and therefor leave a redox inactive interface. A thin, ionically conductive but non-reactive interface layer is desired. Dissolved or gaseous reaction products can however also form, as well as morphological changes of the surface can occur, which both can break the formed interface layer, enabling continued side reactivity on the exposed active material surface. Continued side reactivity may result in lithium depletion of active material, buildup of low ion conducting layer and/or depletion of electrolyte constituents. Stabilization of the active material solid/electrolyte interface layer (SEI) therefor plays a large role in battery research.

ION MIGRATION THROUGH MATERIALS

The transfer mechanism of lithium ions through the active materials, electrolyte and reaction products at the interfaces may vary, which result in characteristic conductive behavior. This leads to different characteristics in overpotential. For example, the active material and solid electrolyte phases may be crystalline, which make the diffusion mechanism dependent on the lithium ion concentration and the amount of positions (or 'holes') a lithium ion can move to and its spatial distribution of strength of binding at these positions and movement trajectories. For such 'hopping' type of diffusion, which is dominant in crystalline and polymer solid electrolytes, the binding strength of lithium ions to their surroundings influence the conductive motion of the lithium. As the lithium counterion is highly immobile, the conductivity of the electrolyte measured originates solely from lithium ion migration. The fraction of current originating from the transfer of redox active ions is expressed in terms of transference number, which in the case of solids is near unity. In a battery with solid electrolytes, the measured overpotential therefor is only the result of the mobility of lithium, giving a potential/current response invariant of time. For liquids however there may be variation in time. In the liquid phase, ion diffusion with such hopping transfer also occurs, but one can distinguish also movement of lithium ions which are associated with their counterions or taking part in a solvation shell. The migration of both positively and negatively charged ions happens. The migration may even be different than their independent state of charge would dictate, due to such solvation effects in the electric field. These migration effects give rise to ion concentration differences. Such concentration gradients then cause a chemical potential, as the liquid is not in equilibrium, which is known as cell polarization. As such buildup of concentration gradient is time dependent, cell polarization is giving a potential/current response which is time dependent. Low currents cause weak polarization after which

the concentration gradient becomes stagnant (and overpotential stable). When the rate of reaction however exceeds the rate of supply of lithium ions this may lead to concentration depletion of lithium ions during mass transport limited operation, which gives rise to a steep increase in overpotential and which may cause unwanted side reactivity because of the high overpotentials reached. The mechanism of ion hopping and solvated migration in ionic liquids, confined ionic liquids and polymerized ionic liquids with an added ionic liquid plasticiser is addressed in chapter 4 and 5.

ELECTRIC DOUBLE LAYER

Other than bulk transfer phenomena, lithium ion transfer through the electric double layer is a second effect causing an overpotential upon charge transport, i.e. an apparent ionic resistance contribution. At the charged surface (typically the active material), mobile ionic species form an ordering to compensate for the ionic charge of the surface, leading to a capacitive effect. Depending on the ionic species of the material contacting such surface, this may give rise to high resistances (e.g. by immobile charge carriers unable to compensate the charged layer, or low ionic concentrations). In this thesis the fundamental phenomena of charge transfer through the electric double layer is observed. As most electrolytes used in this thesis involve ionic liquids, typically the concentration of charge carriers is very high and the ions are also fairly mobile, which generally leads to low observed double layer resistances.

Modification of the electric double layer is however investigated as it addresses a major hurdle in enabling lithium metal battery architectures. The specific topic addressed is modification of the lithium metal plating process in liquid electrolytes. During the lithium plating process, the charged current collector surface pulls a lithium ion to its surface to combine with an electron at the conducting surface, which thus nucleates on the surface as solid lithium metal. That solid is of metallic nature, which implies that it starts to serve as a nucleation site itself causing subsequent nucleation. As the distance between the charged surfaces is shortest between the nucleation site and the opposite site, lithium nucleates preferably perpendicular to the plane instead of along the plain. This leads to dendritic growth of lithium towards the other side of the battery and eventually short circuiting when reaching the macroscopic scale dimension through the separator thickness. This is fortunately only partially true. After initial nucleation lithium atoms appear to be highly mobile on the surface and prefer to reside at the most energetically favourable state. Fortunately this is the lattice state with as much ‘like’ neighbours as possible (so not at the sides), which statistically

would result in dense lithium formation if lithium atoms would be allowed the time to orient themselves. In practice, however, we would like to deposit lithium much faster than the duration of this dynamic process. Moreover, we would like to start from a copper current collector surface, where i.e. initially there is no lithium metal yet, and where the initially reduced lithium has different lattice dynamics to begin with. Modification of the initial surface to electrolyte interface which may influence the lithium nucleation sites is tested by using surfactants which can dynamically cover such locations in chapter 6.

CATHODE STRUCTURE OPTIMIZATION

When lithium metal anodes become an option for rechargeable batteries, one can store the highest theoretical gravimetric charge density (and probably also volumetric density) at the anode side for lithium type chemistries. Such a high charge density needs to be countered with at least the same quantity of charge carriers at the other side to make a balanced redox pair. Problematic for cell design is that cathode materials often are bad electron conductors (unlike lithium being a metal or carbon) which hinders the supply of electrons to the reactive site. Also they have an order of magnitude lower gravimetric capacity (100 - 200 mAh/g instead of 3860 mAh/g for lithium) and volumetric capacity (although they are typically much denser compared to lithium). Finally the diffusion rate of lithium in cathode materials may also be quite low. To address the poor ionic conductivity the material is made into a powder which minimizes the distance from the outer surface of the particle to the particle core. The outer surface is contacted with electrolyte (which is typically a good ionic conductor). To address the electric conductivity additional carbon needs to be added as 'electron highways' through the electrode to guide electrons from the site at which the electronic current comes in (the 'current collector', typically an aluminium foil for cathodes), to the surface of these particles. Then finally this assembly has to be made as thick as possible to provide a suitable quantity of charge carriers to pair with the lithium counter electrode. As the ionic current is flowing from active material surface to active material surface, the flux of ions reacting at the lithium metal side needs to be equal to the flux reacting at the cathode side. Ion transfer through the electrode pores may however limit the allowable reaction rate, especially deeper in a thick cathode structure, as the pore structure creates longer and more narrow high tortuosity ionic pathways. This leads to more rapid concentration depletion during insufficient influx of ions, leading to polarization. Chapter 3 addresses the optimization of such pore structure, to minimize the ionic pathway length to allow sufficient ion flux

deeper in the cathode structure to minimize polarization in the electrode. In addition the advantageous pore structure enables the adequate liquid state impregnation of the electrolyte into the cathode.

CHOICE OF BATTERY CHEMISTRY

Finally this thesis addresses some issues regarding the renewability of storage solutions. As pointed out in the preface, the nature of the chemicals and manufacturing processes used in current lithium ion batteries are worrisome in regards to their persistence, toxicity and renewability. The characteristics of battery materials which allow their high performance at such extremely high and low electrochemical potentials as occurring in lithium ion batteries are partially causing the problem of persistence. The chemical potential between the anode and cathode side of the battery give rise to the need for extremely stable materials. Materials which typically show low redox activity are often chemically inert and therefore hard to break down. It appears, however, to be possible to select chemistry which shows these highly stable characteristics but which is also using building blocks that are abundant in nature, so nature is adjusted to its exposure. A good example in this regard are the borate type materials. Upon oxidation, one is left with borate molecules which are abundant in nature, lithium carbonate and carbon dioxide. This beats oxidation products containing fluorine as it produces highly acidic HF during recycling steps.[1] That said, the natural degradation process of the LiBOB electrolyte salt itself is not investigated here, but an effort has been made to show its usage may replace the usage of persistent PFAS containing molecules and highly fluorinated molecules in lithium batteries with good performance (Chapter 7).

Enabling lithium metal would be the best scenario to maximize the volumetric energy density of batteries. However, batteries with graphite anode and $LiNi_{0.5}Mn_{0.3}Co_{0.2}O_2$ cathode have shown performance which would translate to driving 1.6 million kilometers in an electric vehicle.[5] Such batteries do not have the highest energy density, but may prove to be essential to electrify the transport market globally. In that regard the source of graphite for lithium anodes must be considered which may preferably originate from a renewable source. The usage of biomass seems to be the only source for graphite which may not result in a net emission of CO_2 in the atmosphere. Biomass is however a scarce carbon source also used in food, feed and for construction. In Chapter 8 we address utilization of graphitized carbonaceous char

from syngas gasifiers for the use of lithium anodes which would make maximum use out of biomass from wood chips.

Finally, the choice of cathode active material is the last consideration to address in the framework of lithium (or similar) battery chemistries. Here classes of cathode materials (oxides, phosphates) typically have transition metals which vary in their oxidation state to allow the uptake of lithium. A separate thesis can be addressed on the choice of transition metal ratio's in intercalating oxides, or the mechanism of phase transition in phosphates. One concern however with all current cathode class materials is that at least one of their components is scarce due to mining from geospecific locations (Cobalt), reserves (Phosphate [5] *, Nickel, Lithium) or environmental damage (Lithium, Cobalt, Nickel). In that regard one may want to diverge to develop sodium batteries. These batteries show lower gravimetric and volumetric capacity, but have reported highly renewable choices for their chemistry and show extremely good performance as well (like $Na_2Fe(SO_4)_2$ with 15000 cycles at 3C with 77% retained capacity). [6] The fundamental insights of ionic motion in electrolytes, usage of dielectric surface modifiers and consideration for using carbonaceous biomass and fluorine-free chemistries from this thesis may be taken into account just as well for sodium battery development, to arrive at battery design which fits the scope of a more climate friendly energy carrier.

[5]* U.S. Geological Survey, Mineral Commodity Summaries, January 2024

References

(1) *Advanced Batteries*; Springer US: Boston, MA, 2009. https://doi.org/10.1007/978-0-387-76424-5.

(2) Bockris, J. O.; Reddy, A. K. N.; Bockris, J. O. *Ionics*, 2. ed.; Modern electrochemistry / John O'M. Bockris and Amulya K. N. Reddy; Plenum Press: New York, NY, 1998.

(3) *Solid State NMR*; Chan, J. C. C., Ed.; Topics in Current Chemistry; Springer Berlin Heidelberg: Berlin, Heidelberg, 2012; Vol. 306. https://doi.org/10.1007/978-3-642-24803-0.

(4) Jiang, J.; Dahn, J. R. Comparison of the Thermal Stability of Lithiated Graphite in LiBOB EC/DEC and in LiPF[Sub 6] EC/DEC. *Electrochem. Solid-State Lett.* **2003**, *6* (9), A180. https://doi.org/10.1149/1.1592911.

(5) Harlow, J. E.; Ma, X.; Li, J.; Logan, E.; Liu, Y.; Zhang, N.; Ma, L.; Glazier, S. L.; Cormier, M. M. E.; Genovese, M.; Buteau, S.; Cameron, A.; Stark, J. E.; Dahn, J. R. A Wide Range of Testing Results on an Excellent Lithium-Ion Cell Chemistry to Be Used as Benchmarks for New Battery Technologies. *J. Electrochem. Soc.* **2019**, *166* (13), A3031–A3044. https://doi.org/10.1149/2.0981913jes.

(6) Zheng, Z.; Wang, Y.; Zhang, Y.; Li, X.; Zhang, Y.; He, Y.-S.; Che, H.; Li, L.; Ma, Z.-F. Sodium Iron Sulfate Cathodes with Ultra-Long Cycle-Life and High Safety for Sodium-Ion Batteries. *Nano Energy* **2024**, *128*, 109907. https://doi.org/10.1016/j.nanoen.2024.109907.

3.1 A PHASE INVERSION STRATEGY FOR LOW-TORTUOSITY AND ULTRAHIGH-MASS-LOADING NICKEL-RICH LAYERED OXIDE ELECTRODES

The content of chapter 3.1 has been published in Cell Reports Physical Science in 2024, Volume 5, Issue 6, 101972 in which Mark Weijers was one of the two first authors with equal contribution. https://doi.org/10.1016/j.xcrp.2024.101972

A phase inversion strategy for low-tortuosity and ultrahigh-mass-loading nickel-rich layered oxide electrodes

ABSTRACT

Increasing the electrode thickness, thereby reducing the proportion of inactive cell components is one way to achieve higher energy density Li-ion batteries. This, however, results in higher electronic and ionic overpotentials and/or mechanical failure induced by binder migration. Here, we report Ethanol-induced phase inversion (EPI) as an effective method for making high-mass loading Nickel-rich layered oxide (NMC811) electrodes. The EPI electrodes significantly outperform their conventionally processed counterparts with similar loading (35 mg/cm^2) and porosity (30%) in Li/NMC half cells (131.7 mAh/g vs 56.7 mAh/g) at 1C (7 mA/cm^2) discharge. The binder structure induced by the nonsolvent improves the pore connectivity and results in lower tortuosity factors. The rapid solvent removal reduces the binder migration during drying, enabling ultrahigh active mass loadings up to 60 mg/cm2 (12 mAh/cm^2). Further, the excellent compatibility of the phase inversion process with current roll-to-roll coating setups makes this a processing technique with high industrial feasibility.

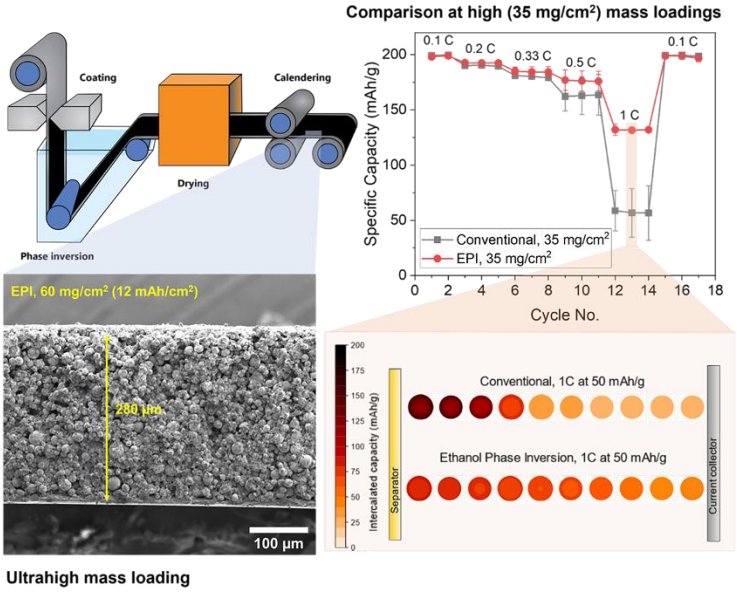

INTRODUCTION

Increasing the energy density of Lithium-ion batteries is a widely researched area today, thanks to the ever-increasing demand for higher driving ranges in electric cars[1] and a push for increased adoption of batteries in heavy-duty vehicles such as commercial aircraft.[2,3] A significant part of this research is dedicated to the development of high energy density electrodes.[4] From a materials perspective, while a transition to Li metal or Si anodes (from Graphite) would significantly boost the pack level energy densities, Ni-rich layered oxides such as $LiNi_{0.8}Mn_{0.1}Co_{0.1}O_2$ (hereafter referred to as NMC811) remain the active material of choice on the cathode side, owing to a combination of factors such as high specific capacity, high intercalation voltages vs Li (3.6-4.3V) and good electronic/ionic conductivities. A way to further enhance the cell and pack energy density in terms of electrode architecture, particularly for the cathodes, is increasing the electrode thickness, thereby increasing the active mass loading and reducing the proportion of inactive components (current collectors, casing, etc.).[5]

Increasing the thickness of battery electrodes, however, comes with its own set of technical challenges that can impact the power density and the cycle life of these electrodes. An increase in electrode thickness would increase the path length for the electronic transport through the percolation network (consisting mainly of carbon additives) and the ionic transport through the electrolyte-filled porous network.[5] While the former issue can be addressed using 1D and 2D long-range conductive additives,[6,7] ion concentration polarization is generally considered the bigger challenge for thick electrodes, especially when moderate to high charge/discharge rates are desired.[5,8,9]

Ion transport through a porous network is influenced by its porosity and tortuosity factor, which in turn affect the Macmullin number, i.e., the ratio of bulk ionic conductivity to effective ionic conductivity of the electrolyte in the porous network.[10] In thick slurry cast electrodes, binder migration towards the separator side, induced by a relatively stronger association of the binder (typically PVDF) with the solvent (typically NMP) than with the active material, is also reported.[11,12] Binder migration in electrodes would typically result in an unfavorable Carbon-binder domain (CBD) and porosity distribution across the depth of the electrode, resulting in higher tortuosity factors.[13] While calendering is an essential step in battery electrode processing, necessary to improve electrical and mechanical contacts, this often negatively affects

the electrode tortuosity,[14] particularly in the case of thick electrodes with a nonhomogeneous CBD distribution. Further, the binder migration can also negatively affect the overall mechanical strength of the electrode and its adhesion to the current collector. With the successive electrode volume changes induced over extended cycling periods, both these factors can aggravate contact loss and capacity fade.[15]

Many efforts in the recent past have already focused on developing electrodes with lower tortuosities. The various approaches tried in this regard include freeze casting,[16,17] magnetic alignment,[18–20] laser etching,[21] mold templating[22], and reactive templating[23] among others. However, many of these techniques also result in high electrode porosities and face challenges in terms of scalability. High electrode porosities can be undesirable in the context of volumetric energy density, and it is therefore necessary to develop techniques that can induce lower tortuosities at standard electrode porosities (25-30%).[24] It is also important to consider the costs involved and the compatibility of the electrode casting technique with the current industrial roll-to-roll processing for battery electrodes.[25]

Nonsolvent-induced phase inversion/separation (also known as NIPS/Immersion precipitation), a well-known technique in the membrane processing industry,[26–28] is another such technique that has been used to make high-performance battery electrodes. When the polymer-based (either pure or inorganic/polymer mix) coating is contacted with a binder nonsolvent, liquid-liquid demixing in the metastable region results in a Polymer-rich phase (polymer backbone) and a polymer-lean phase (pores).[27,29] Different nonsolvents under different process conditions (temperature, dilution, presence of additives, etc.) result in different demixing rates, which consequently affect the pore connectivity and the pore size distribution.[29,30] In addition to being used for making battery separators, fuel cell electrodes, and flow battery electrodes,[30,31] phase inversion has already been used to produce high-performance Sulfur/Carbon,[32,33] $Li_4Ti_5O_{12}$,[34] $LiFePO_4$[34,35] and Silicon[36] electrodes for Li-ion batteries, typically using water as the binder nonsolvent. However, to our knowledge, the technique has not yet been applied to state-of-the-art but water-sensitive Ni-rich layered oxide materials (Ni-rich NMC, NCA, LNO, etc.), where a move towards higher mass-loading architectures is of significant interest to enable cell-level specific energies of 500 Wh/kg and higher.[4]

In this work, we report high-mass loading, high-rate performance Ni-rich NMC811 electrodes prepared using a novel ethanol-induced phase inversion method. The origin of the improved rate performance for the phase inversion-based electrodes with high active mass loadings (35 mg/cm^2 and higher) is elucidated using a combination of techniques (porosimetry, FIB-SEM, P2D modeling, symmetric cell EIS, solid-state NMR). The altered carbon binder domain structure for the phase inversion electrodes is shown to significantly reduce the tortuosity factor. Further, stable long-term cycling of the phase inversion electrodes is also observed for these high loadings, demonstrating the potential of phase inversion as a scalable, effective technique to obtain high mass-loading Ni-rich layered oxide electrodes.

METHODS

ELECTRODE MANUFACTURING

NMC811 electrodes were made with a 92:4:3:1 mass ratio of active material (AM) : binder: carbon black: graphite using a dry and wet mixing step. First, NMC811 (Umicore) AM was mixed with the conductive additive Carbon black C45 (Imerys) in a mortar, followed by the addition and mixing of KS4 Graphite (Imerys) and Solef 5130 (Solvay) PVDF respectively. NMP (Sigma Aldrich) was added to this mixture in a 1:14 PVDF:NMP mass ratio, and subsequently, the suspension was mixed using a high-shear top stirrer (IKA Microstar 7.5) for 1 hour at 1000 RPM to create a homogeneous slurry. The obtained slurry was cast on aluminum foil using a doctor blade. To obtain freestanding electrodes for the purpose of tensile strength and mercury intrusion porosimetry measurements, the slurry was cast on clean glass plates. Immediately after casting, the sheet was either immersed in a bath of ethanol (96%, VWR) for 60-300 seconds (Ethanol phase inversion, EPI) or was not subjected to an immersion treatment (Conventional). The electrode sheets were dried in two steps. NMP/nonsolvent was evaporated in an oven at 70 °C for an hour, and subsequently, the electrode sheets were dried in a vacuum oven at 60 °C for 24 hours. Finally, the electrodes were calendered to 30% apparent porosity using a calender press (MTI). Details on the porosity estimation are provided in the Supplementary Information (**Table S2, Table S3**).

ELECTRODE CHARACTERIZATION

Electrode porosity and pore size distribution of freestanding NMC811 electrodes were tested using mercury intrusion porosimetry (Autopore 9500, Micromeritics). Approximately 1 gram of freestanding electrode sample was loaded in strips of 3x1 cm

in a 15 mL penetrometer with the surface perpendicular to the entry side of the mercury. The stem volume of 0.39 mL was utilized between 40 - 88% during pressurization between 3.7 kPa and 210 MPa. Rheometry was performed on the slurries using a 40 mm Peltier plate with 0° cone angle and 500 µm gap width on a Discovery HR10 rheometer (TA Instruments). The shear rate was varied between 0.01 and 10/s.

Scanning electron microscopy (SEM) pictures were taken using a JEOL JSM-IT700HR FE-SEM setup either in scattering electron imaging (Acc. Voltage: 1- 5 kV) or Backscattered electron imaging (Acc. voltage: 5 kV) mode. Focused Ion Beam SEM (FIB-SEM) images were taken using a Helios G4 CX. Ion milling times were referenced to 0.8 times the silicon etching duration for a specific depth. The ion beam was set to 30 kV with 65 nA beam strength.

Solid-state MAS NMR measurements were carried out on a Bruker Avance 500 Spectrometer. NMC811 electrodes coated on Al foil were scraped off and packed into 1.9 mm rotors. ^{19}F NMR (Larmor frequency: 475 MHz) was carried out at 32 kHz spinning speeds. A zgbs (background subtraction) protocol was used with a recycle delay of 2 seconds. All spectra were processed and fitted using Mestrenova 14 software.

The tensile strength measurements were performed on a ZwickRoell 10 kN universal testing machine. For these measurements, freestanding electrodes were calendered between two Ni foils to a porosity of 30% and cut according to ASTMD412 type F,[66] with the target test area being about 6x50 mm. The tensile force test was performed at a speed of 1 mm/min.

Electrochemical characterization

Coin cells (CR2032) were assembled to study the rate performance of the NMC811 electrodes in a half-cell configuration. NMC811 electrodes were punched as 12.7 mm discs and assembled versus a 250 um Lithium disc (Tobmachine) in an Argon-filled glove box. One Celgard 2400 and one Whatman separator (Grade Gf/C) each were used, with 110 µl of 1 M $LiPF_6$ in 3:7 EC:EMC (vol%) electrolyte (LP57, ELyte) per cell. After 24 hours of rest, the cells underwent two formation cycles at C/10 on a MACCOR 3400 galvanostat. Rate performance tests were then carried out on the Maccor 3400 at 20 °C.

Long term cycling performance of the NMC811 electrodes was also tested in a half-cell configuration (vs. Li) similarly, except that the electrolyte used was changed to 1 M $LiPF_6$ + 0.1 M LiDFOB + 0.1 M LiTFSI + 0.1 M LiFSI + 0.1 M $LiNO_3$ in EC:DMC (1:1 wt%) + 5 wt% FEC (1.4 M HE) for the sake of improved long-term stability with the Li metal anode at high plating and stripping currents. The 1.4 M HE electrolyte was prepared as described elsewhere.[63] The long-term cycling was carried out at 20 °C. Following the formation cycles at C/10, the protocol used was as follows: first 2 cycles at C/10 charge-discharge, followed by 50 cycles at C/4 charge and 1C discharge, and the protocol repeats every 52 cycles.

Electrochemical impedance spectroscopy (EIS) was performed on a potentiostat (Metrohm Autolab) after the formation cycles. First, a voltage hold (until I < 0.01C) at 3.7 V was carried out. A frequency range from 500 kHz to 100 mHz was used. The analysis and fitting of the spectra was carried out using Zview (Scribner). Tortuosity factors were measured for these electrodes based on the symmetric cell method often applied to Li-ion battery electrodes.[49,67] A non-intercalating electrolyte, 25 mM $TBAClO_4$ in EC:DEC (1:1 vol%), is used along with fully intercalated NMC811 electrodes of interest to achieve the desired blocking conditions for ion flow. Both the electrodes had mass loadings around 7.5 mAh/cm^2 and were calendered to an apparent porosity of 30%.

P2D Modelling

Simulations were carried out using the open-source software MPET[68], which uses a standard pseudo-2-dimensional (P2D) model. [60,69] The parameters (**Table S7**) were obtained as follows: the electrolyte parameters for the Stefan-Maxwell model[70] were obtained from the work of Nyman et. al.[71] the dependence on the concentration of the reaction resistivity and the solid-state diffusivity were taken from the fitting of McClelland et. al.[72]; electrical conductivity, thickness, porosity and particle size distribution were taken from measured values; the rest of the parameters, such as the tortuosity factor were estimated by minimization of the weighted mean square error. The details of the model can be found in the supplementary information.

Results

Optimization of the phase inversion process for Ni-rich layered oxides

Through the solvent/antisolvent screening for electrode slurries with PVDF as the binder, NMP and DMSO solvents were considered. DMSO is considered a green

alternative to the conventionally used NMP[37,38] and is also typically miscible with the nonsolvent of PVDF/NMP. Miscibility of solvent and nonsolvent is necessary to ingress the nonsolvent in the cathode slurry. As opposed to previously investigated battery active materials (such as LFP) where water has often been used as the binder nonsolvent for making phase inversion-based electrodes,[34,35] options for suitable nonsolvents can be more limited for Ni-rich layered oxide materials such as NMC811. NMC811 is alkaline in nature as it exchanges lithium ions with protons in a protic nonsolvent medium such as water. This Li^+ leaching, leading to the formation of LiOH and Li_2CO_3, and the resulting alkaline environment (pH >12) subsequently results in corrosion of both the aluminum current collector and the native alumina layer on its surface.[39,40] Also, water phase inversion showed delamination of the electrode from the aluminum current collector after about 15 seconds, making the manufacturing process more error-prone.

The solubility parameters calculated based on the Hansen solubility index[41,42] (see **Note S1** and **Table S1**) indicate that alcohols are suitable nonsolvents for PVDF. The alcohol hydroxyl group generally has a higher pKa (15.9)[43] compared to the NMC alkalinity measured in an aqueous environment, [39] where relatively more acidic nonsolvents would form lithium salts upon contact. Among alcohols, ethanol was selected owing to its relatively higher abundance, safety, and non-solubility with PVDF. The low enthalpy of evaporation of ethanol, its low viscosity, and ease of separation with NMP and DMSO solvents by extractive distillation[44] or membrane filtration [45] make it a suitable nonsolvent. Also, no delamination from the Al current collector was observed after extended periods of nonsolvent contact.

Further, the choice of dilution decides the viscosity of the slurry and the proximity of the active material particles in the solution during precipitation. The viscosity of DMSO shows a higher dilution dependence and a high temperature dependence (**Note S2** and **Figure S1**). NMP slurries show only a slight viscosity difference upon dilution, and only for low dilutions (1:10 PVDF:NMP), a significant temperature dependence is observed. With a 1:10 m:m PVDF:solvent ratio, the electrode height and pore distribution were uneven. Such high viscosities may also not be applicable using conventional slot dye coating processing. A sufficiently low dilution of 1:12 or ideally 1:14 m:m PVDF:NMP showed the best distribution in pores (Figure S1). Dilutions up to 1:20 m:m were tried, and too high dilutions led to a non-binding precipitation. NMP is chosen as the solvent

for the rest of this work, as the slurry viscosity shows a smaller temperature and dilutiocon dependence, which improves the repeatability of the experiments.

Changes to the electrode structure upon phase inversion and the effect of calendering

The phase inversion processing of NMC811 electrodes resulted in changes to both the CBD microstructure and the CBD distribution across the depth of the electrode in comparison to the conventional electrodes. Cross-section FIB-SEM images show channel structures throughout the uncalendered ethanol phase inversion-based (EPI) electrodes (**Figure 1**c), and no significant binder migration is observed (SI, **Figure S2**c). Further, ethanol phase inversion also causes macropores (pores in the micron range) throughout the cathode material (**Figure 1**c). Such macropores are not observed in the conventional electrodes. In conventional electrodes, a thick CBD layer is observed on the electrode surface (**Figure S2**a), and the CBD interconnects the particles with a porous microstructure (**Figure 1**a). For the EPI electrodes, the rapid precipitation of PVDF upon nonsolvent contact prevents binder migration by causing a rapid polymer-rich phase precipitation, creating a more evenly distributed CB structure throughout the electrode and negligible binder migration.

The immersion time (or solvent/nonsolvent exchange time) optimization also plays a crucial role in the effectiveness of the phase inversion process in generating the intended binder microstructure, as exchange times lesser than the binder precipitation time could result in partial/complete reversal of the binder structure generation, making the phase inversion processing ineffective.[46] Here, setting the immersion time to 5 minutes resulted in a good overall balance in terms of phase inversion/precipitation completeness, electrode adhesion, and overall processing time, resulting in binder microstructures observed in Figure 1a (cross-section) and **Figure S2**c (top view). With lower exchange times (1 min), while the binder migration is still reduced in comparison to the conventional electrode (**Figure S2**a), the CBD still had a porous microstructure similar to the conventional electrodes (**Figure S2**b), suggesting an incomplete binder precipitation during phase inversion.

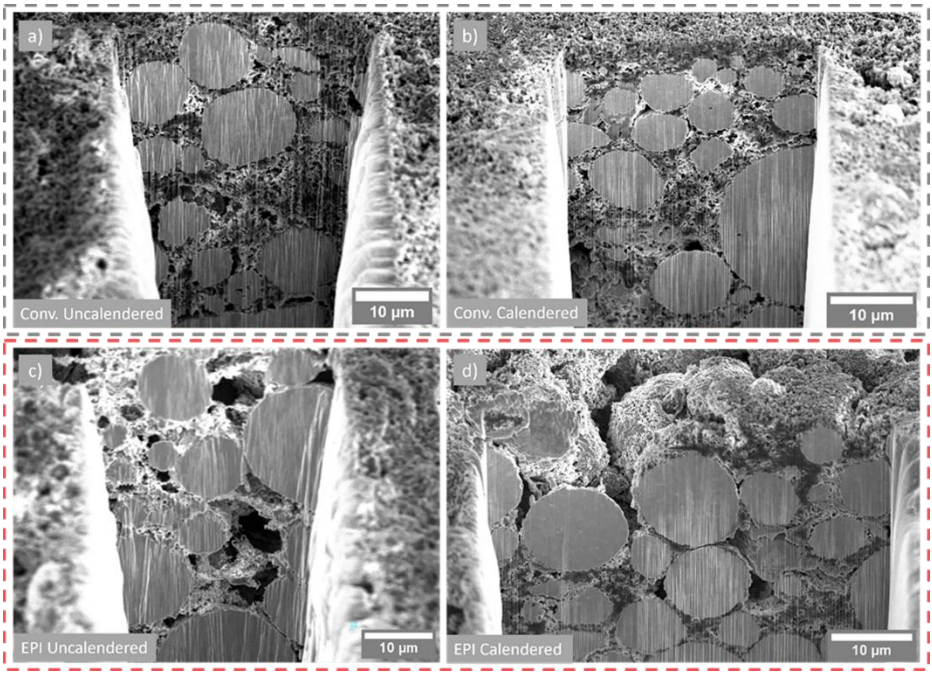

Figure 1. Cross-section FIB-SEM of NMC811 Electrodes: a) Conventional uncalendered, b) Conventional calendered, c) EPI uncalendered, d) EPI calendered. While the conventional electrodes show a high degree of intra-CBD microporosity before and after calendering (a,b), uncalendered EPI electrodes show a channeled structure with macropores (c). These macropores are retained to some extent with calendering while the CBD microstructure densifies (d). The length of the scale bars indicates 10 µm.

For the EPI electrodes, calendering yields an evenly distributed electrode structure, and the macropores between the active material and the CBD phase are partly retained after calendering (Figure 1d, Figure S3). The CBD microstructure becomes denser after calendering for the EPI electrodes, while the conventional electrodes retain a porous CBD microstructure (Figure 1b, **Figure S3**).

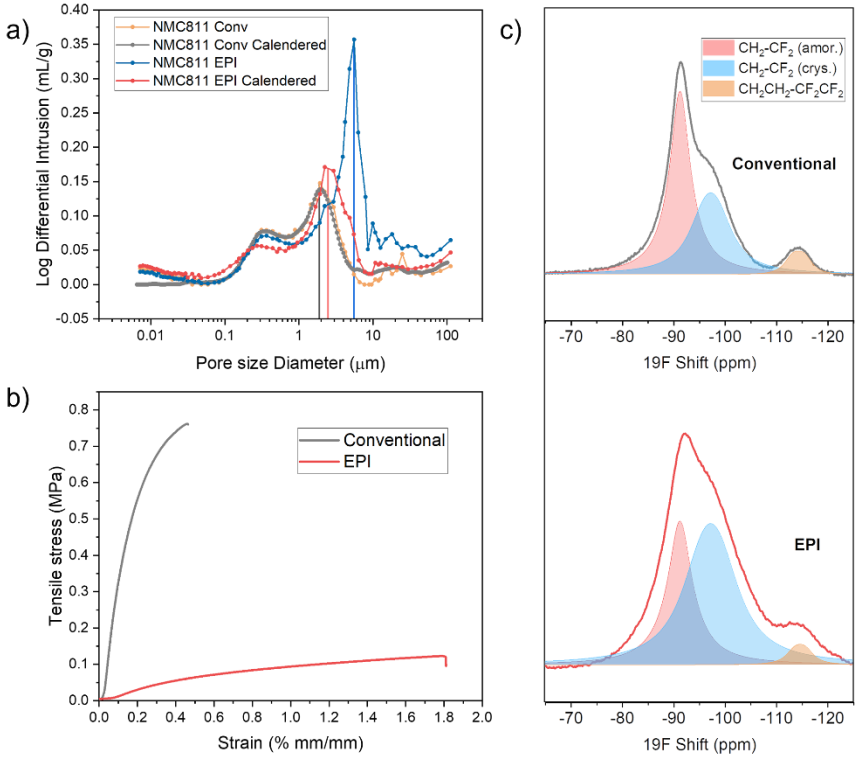

Figure 2. Characterization of NMC811 electrodes: a) Pore size distribution obtained by MIP of conventional and EPI electrodes before and after calendering. b) Tensile stress-strain curves for 35 mg/cm^2, 30% porosity freestanding Conventional and EPI electrodes. c) ^{19}F NMR spectra at 32 kHz spinning speed for NMC811 Electrodes (4 wt% PVDF) with the conventional drying method (top) and the EPI method (bottom), showing the differences in the amorphous/crystalline CH_2-CF_2 fractions for the two methods.

Further, a significant change to the pore size distribution in the electrodes because of phase inversion is observed by Mercury Intrusion Porosimetry (MIP). MIP shows the preferred liquid pathway in the porous structure as a function of applied pressure. Cathode structures before and after calendering (more details on the target porosity estimation in **Note S3**) were subjected to MIP to map the changes to the pore size distribution in the CBD phase upon calendering. A cutoff of 10 microns was chosen, as pores above this diameter were never observed with microscopy, and mercury intrusion commences first between the cathode sheets. Mercury intrusion

porosimetry shows a shift in the macropore (pore sizes >1 µm) size from 1.8 µm for calendered conventional electrodes towards 2.6 µm for calendered EPI electrodes (indicated with lines in **Figure 2**a). The CBD phase with micropores (pore sizes of 0.1 to 0.8 µm) is also smaller in the EPI electrodes. This corroborates well with the FIB-SEM. The EPI pore size distribution thus shows a lowered CBD porosity and increased macropores, which is beneficial for achieving lower tortuosities in thicker electrodes without affecting the net porosity.

Ethanol-based phase inversion in NMC811 electrodes also results in a change in the degree of crystallinity of PVDF, and this is clearly observed with the ^{19}F MAS NMR measurements (Figure 2c, d). For both the samples, three environments are observed at -91.2 ppm, 97 ppm, and -114.3 ppm, and these have been previously attributed to the amorphous CH_2-CF_2 component in PVDF, the crystalline CH_2-CF_2 component and the defect environment (CH_2-CH_2 and CF_2-CF_2 units instead of alternating CH_2-CF_2) respectively.[47] Clearly, a greater extent of the crystalline environment is observed for the electrode that underwent Ethanol phase inversion. These results agree well with the FIB-SEM and porosimetry observations that indicate lesser intra-CBD micropores and a denser CBD structure.

The changes to the CBD microstructure and distribution upon ethanol phase inversion were also found to affect the mechanical properties of the EPI NMC811 electrode. In general, for electrodes with 35 mg/cm^2 active mass loading and 30% apparent porosity, the EPI electrodes displayed better flexibility (higher Strain tolerance until fracture), i.e., 1.8% in the case of EPI as compared to 0.5% for the conventional electrode (**Figure 2**b). This could be relevant for roll-to-roll processing of these electrodes and for the application of these electrodes in non-planar cell architectures in which higher electrode flexibility is desired. Further, EPI electrodes at these loadings showed a more uniform adhesion to the Al current collector along the length of the electrode (uniform peeling force) than the conventional electrode (**Note S4** and **Figure S5**) at these loadings. These favorable properties for the EPI electrodes enable robust-crack-free electrodes at ultrahigh mass loadings of up to 60 mg/cm^2 (280 µm at 30% porosity), while conventional electrodes with a similar loading showed several cracks on the surface. (**Figure S4**).

DIFFERENCES IN ELECTROCHEMICAL RATE PERFORMANCE

The observed changes to the CBD microstructure in the EPI electrodes are expected to influence the tortuosity of the pore network and the surface coverage (by CBD) of the NMC particles, thereby the Li^+ charge transfer resistance. The tortuosity factor of NMC electrodes has previously been observed to be a major bottleneck, particularly at high discharge (Lithiation) rates,[14] while any differences in Li^+ charge transfer area would influence both the charge and the discharge rates. In this regard, the NMC811 electrodes were tested for their rate performance under both varying charge and discharge conditions at active mass loadings of 35 mg/cm^2 (7 mAh/cm^2) and apparent porosities of ~30%.

For the varying discharge rate tests, the electrodes were tested up to 1C, with C/10 being the constant charge rate (**Figure 3**a). For discharge rates up to C/3, not much difference is observed for the discharge capacities. However, higher discharge capacities are observed for the EPI electrode starting from C/2. At 1C, a clear difference in the discharge capacities is observed for the EPI electrodes (131.7 mAh/g vs. 56.7 mAh/g for EPI and Conv. respectively at cycle 14). From the discharge voltage traces for the two electrodes at 1C (**Figure 3**b), it can be observed that the ohmic drop during the initial stage of discharge is nearly the same after charging at C/10. During discharge, however, the slope of the discharge curve is lower for the EPI electrode, indicating a lower ionic resistance across the porous electrode network for the EPI electrodes.

In the case of varying charge rate tests (with C/10 constant discharge rate) shown in Figure 3c, while the discharge capacities remain similar for C/10, higher discharge capacities are observed at C/5 and higher charge rates for the EPI electrodes. At C/2, the EPI electrode shows a discharge capacity of 142 mAh/g as opposed to 88 mAh/g for the conventional electrode. A comparison of the charge/discharge curves of the two electrodes at C/2 charging is shown in **Figure 3**d. Again, while the ohmic polarization observed for the EPI electrodes is similar to that of the conventional electrodes, a lower slope is observed for the charging curve, corresponding to a higher charge capacity, which could be attributed to higher effective ion migration along the porous electrode network, influenced by the tortuosity factor and/or the porosity, which in this case lowers the Macmullin number.

A phase inversion strategy for low-tortuosity and ultrahigh-mass-loading nickel-rich layered oxide electrodes

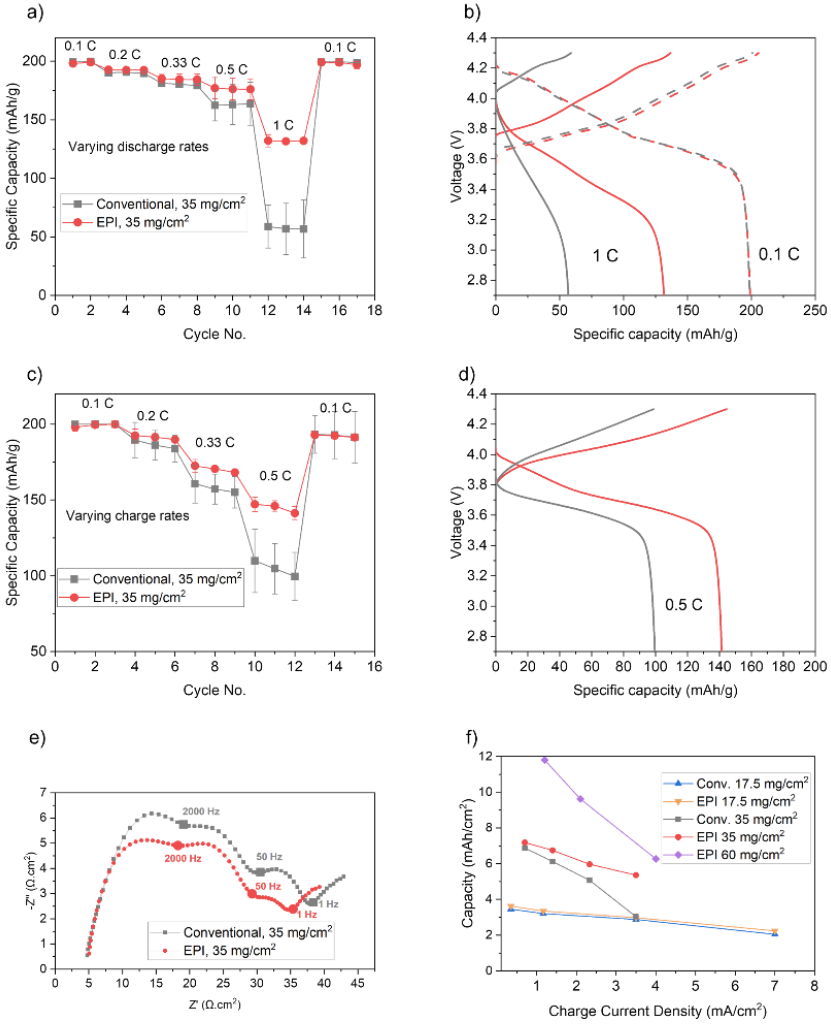

Figure 3. Electrochemical rate performance comparison: a) Rate performances of 35 mg/cm² NMC811 electrodes in Li half cells at varying discharge rates and a constant C/10 charge rate. b) The voltage traces of Figure a, cycle 13 for both electrodes. c) Rate performances of 35 mg/cm² NMC811 electrodes in Li half cells at varying charge rates and a constant C/10 discharge rate. d) The voltage traces of figure c, cycle 11 for both electrodes. e) EIS Nyquist plots at 3.7 V for the conventional and EPI based Li/LP57/NMC811 cells. f) Overview of the specific (discharge) capacities for NMC811 electrodes obtained at varying charge rates and mass loadings. Error bars in Figures 3a and 3c indicate the standard deviation from the mean of a duplicate experiment.

Electrochemical impedance spectroscopy (EIS) performed on the 35 mg/cm^2 half cells at 3.7 V after the formation cycles also sheds light on the differences in the impedance contributions for the two electrodes (**Figure 3**e, see **Note S5** for equivalent circuit shown in **Figure S6** and fit values in **Table S4**). The curved features occurring between 500k – 2kHz, 2 kHz- 50 Hz and 50 Hz – 1 Hz have been attributed to the total electronic resistance R_{elec} of the electrodes (including the contact resistance between the NMC811 electrode film and Al current collector), the Li SEI film resistance R_{SEI} and the charge transfer resistance at the cathode-electrolyte interface R_{CT} respectively (based on time constants typically reported for these components[48]).

Both the electrodes are observed to have similar electronic resistance values perpendicular to the plane (R_{elec}), with the value for the EPI cell being slightly lower (12.0 Ω.cm^2) compared to the conventional cell (13.1 Ω.cm^2). The electronic resistance obtained with EIS is in line with through-plane DC electronic resistances for the electrodes measured in an ion-blocking setup (18.2 Ω.cm^2 and 18.4 Ω.cm^2 for EPI and conventional electrodes respectively; further details can be found in **Note S6** and **Table S5**). Further, the R_{CT} value for the EPI electrode is observed to be lower (5.50 Ω.cm^2) compared to the conventional cell (7.79 Ω.cm^2). R_{CT} can depend on several factors, such as the active material, the state of charge, and the available surface area for charge transfer. In this case, the lower R_{CT} in the case of the EPI electrode could be explained by the enhanced surface area for Li^+ exchange, caused by a lower CBD coverage of the active material surface and/or the improved electrolyte uptake in its pore network resulting in a better active surface utilization.

Further, **Figure 3**f provides an overview of the discharge capacities at different charging currents for NMC811 electrodes at different active mass loadings (17.5 – 60 mg/cm^2). It can be observed that while the rate performance of both the conventional and the EPI electrodes are similar for 17.5 mg/cm^2 (3.5 mAh/cm^2), a clear improvement in discharge capacities is observed for the electrodes at 35 mg/cm^2 (7 mAh/cm^2), particularly at higher charge rates. EPI electrodes with ultra-high mass loadings of 60 mg/cm^2 (12 mAh/cm^2) also show a remarkable discharge capacity of 9.62 mAh/cm^2 (160.3 mAh/g) capacity at charge current densities of ~2.1 mAh/cm^2, whereas the conventional electrodes cast at these loadings did not show enough mechanical integrity to be tested in coin cells.

DIFFERENCES IN THE TORTUOSITY FACTOR

The symmetric cell EIS (eSCM) measurements for the two electrodes also reveal differences in the ionic resistance contributions from the porous network and the CBD, and thereby, the electrode tortuosity factor. **Figures 4**a and b show the Nyquist plots obtained for the conventional and EPI electrodes.

Both plots show three features, i.e., two curved features in the high-mid frequency region and a sloping line in the mid-low frequency region. Similar feature(s) have been observed previously for porous Li-ion electrodes, and their physicochemical interpretation has been subject to wide debate. Some possible reasons for such a feature include electrical contact resistance, [49,50] uneven CBD distribution through the depth of the electrode resulting in a depth-wise difference in the ionic resistance,[13,51] and the intrinsic porosity/electrolyte uptake of the CBD.[52]

In this case, the high-frequency feature (up to 6250 Hz) is attributed to the electronic (contact) resistance of the electrode. The second (mid-frequency) curved feature (6250 – 125 Hz) is attributed to the impedances coming from the carbon binder domain (CBD). The magnitude of this feature is observed to be higher for the EPI electrode than for the conventional one. A possible origin of this feature here could be the non-homogenous distribution of the CBD phase along the depth of the electrode, which is known to occur for thick electrodes with drying. While a migrated binder layer was indeed observed for the Conventional electrodes with the FIB-SEM, a nonuniform distribution of the CBD was not observable for the EPI electrodes at mass loadings of 7-7.5 mAh/cm^2 (**Figure 1**a).

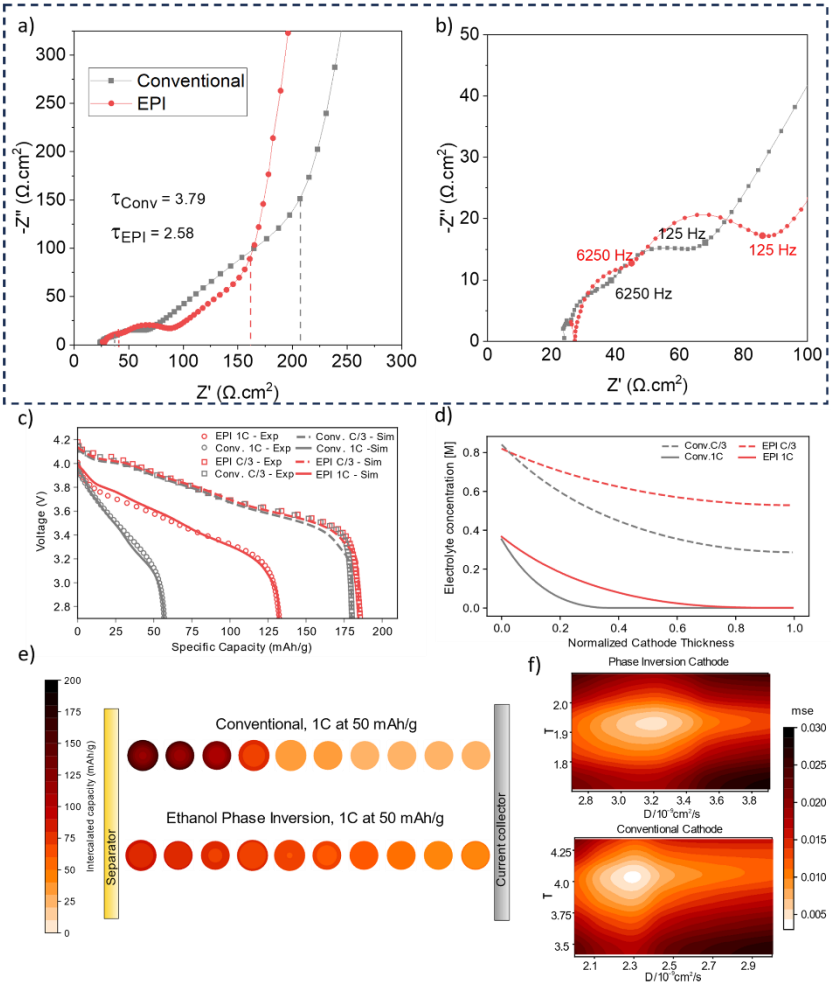

Figure 4. Tortuosity factor measurements: a) EIS Nyquist plots for the NMC811 symmetric coin cells with 25mM $TBAClO_4$ in EC:DEC electrolyte. The drop-down values indicate the real axis length considered for the R_{ion} calculations b) The zoomed inset of the high-to-mid frequency region for the NMC811 symmetric cells. c) Comparison between the experimental and the simulated voltage curves. d) Electrolyte concentration along the cathode at 25% DOD. e) Particle concentrations, expressed in terms of capacity delivered during discharge, along the cathode at 25% DOD for conventional and EPI electrodes. f) Mean square error landscape for varying diffusivities (D) and tortuosity factor (τ) for conventional and EPI electrodes.

When it comes to the CBD structure, however, the FIB-SEM (**Figure 1**c) reveals a more dense CBD structure in terms of microporosity for the EPI electrodes. This observation is also supported by the MIP results (**Figure 2**a) that show a lower pore size distribution in the 10-200 nm range (typically corresponding to intra-CBD pores) and also the 19F ssNMR results (**Figure 2**c, d) that show a more crystalline PVDF structure produced by the EPI process. This results in a lower surface area offered by the CBD phase for the EPI electrodes, explaining the higher real axis value for the second curved feature.

Finally, the sloping line feature occurring at medium to low frequencies denotes the resistance to ion migration through the long-range (macro)porous network along the electrode, and here, the value of ionic resistance appears to be lower for the EPI electrode.

The tortuosity factors are estimated by approximating the sum of the real axis (x-axis) lengths of the sloping line and the mid-frequency curve to be $R_{ion}/3$, where R_{ion} is the total ionic resistance of the two electrodes in the symmetric cell.[13,49] This value is then used to calculate the tortuosity factors (further details can be found in **Note S7**, **Table S6**). The EPI electrode displays a lower tortuosity factor of 2.58 compared to a value of 3.79 for the conventional electrode.

The rate performance and the difference in obtainable tortuosity factors for Ethanol phase inversion can be further compared to conventional processing through porous electrode modeling.[53–60]. The physical constants of the model were found by fitting the unknown parameters, such as effective diffusivity, exchange current density, Li metal charge transfer resistance, and tortuosity factor, to match the experimental voltage curves. The result is shown in **Figure 4**c-f.

The effect of the most sensitive parameters (effective diffusivity D and tortuosity factor τ) on the mean square error (mse) between the simulated and the experimental voltage curve (**Figure 4**f) clarifies the importance of tortuosity factor in the correct fitting of the experimental results, revealing the best fit for the conventional and the phase-inversion to have tortuosity factors of 4.05 and 1.92, respectively.

Despite the intrinsic assumption underlying the P2D model,[61,62] which considers every particle in an ideal electrolyte bath, the relation between the fitted tortuosity factor is in line with the results of the EIS (**Figure 4**a), showing the effect of the phase inversion

on the performance. Moreover, an optimal fit (**Figure 4**c) is achieved by decreasing the effective diffusivity and the exchange current densities of the conventional electrode compared to the EPI electrode, obtaining values of 2.28 10^{-9} cm^2/s and 3.19 10^{-9} cm^2/s for the effective diffusivities and 2.48 A/m^2 and 3.5 A/m^2 for the exchange current densities, respectively (see **Note S8**). This result, coming from the unbounded parameter estimation, aligns well with the (cathode) charge transfer resistance calculated from the EIS.

Finally, the validated model shows the effect of the microstructural changes on the Li^+ concentration in the electrolyte along the cathode (**Figure 4**d), also capturing the consequences in terms of Li concentration in the particles (**Figure 4**e). This result underlines the advantages of phase inversion in reducing CBD inhomogeneities and the tortuosity factor in thick electrodes.

LONG-TERM CYCLING PERFORMANCE

A comparison of the long-term electrochemical performances of the conventional and EPI NMC811 electrodes at high active mass loadings of 7 mAh/cm^2 (35 mg/cm^2) is shown in **Figure 5**. In this case, Li foil (250 µm) was again selected as the anode due to the unavailability of other suitable candidates that can deliver these high capacities without undergoing performance limitations of their own. The electrolyte was changed to a high-entropy electrolyte, i.e. 1 M $LiPF_6$ + 0.1 M LiDFOB + 0.1 M LiTFSI + 0.1 M LiFSI + 0.1 M $LiNO_3$ in EC:DMC (1:1 wt%) + 5 wt% FEC (hereafter referred to as 1.4 M HE electrolyte) salt electrolyte previously reported by Wang et. al.[63], as high-entropy multi salt electrolytes were shown to enable uniform Li plating/stripping at high current densities and capacities.[63,64]

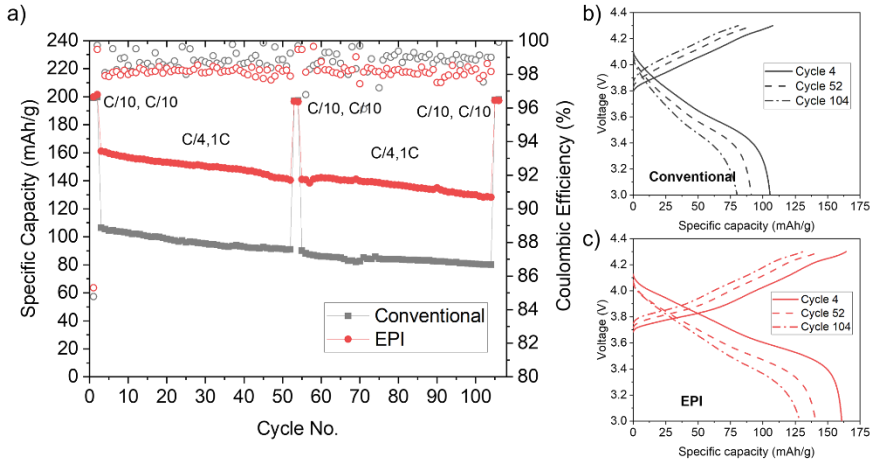

Figure 5. Long-term cycling comparison: a) Discharge capacities and coulombic efficiencies in Li/NMC811 half cells with 35 mg/cm² (7 mAh/cm²) active mass loading and 1.4 M HE electrolyte cycled at 20 °C. b) Voltage traces for the Conventional Li/NMC811 cells at 10, 52, and 104 cycles. c) Voltage traces for the EPI Li/NMC811 cells at 4, 52, and 104 cycles (C/4 C, 1C D).

Here, a clear improvement in the discharge capacity at 1C is observed for the EPI NMC811 electrode for over 100 cycles (**Figure 5**a). A gradual capacity fade is observed for both electrodes over the high cycling rates, and such capacity fade is typically observed due to the increase of polarization at the Li interface, due to the buildup of dead Lithium and/or gradual salt consumption at these high plating/stripping rates.[65] This phenomenon contributes to the increase of ohmic polarization during charge, going from cycle 4 to 104 for both electrodes (**Figure 5**b, c). However, the original capacities are observed to be nearly retained for both electrodes at low rates (0.1 C) after the 100 cycles. Remarkably, the EPI electrodes show a capacity retention of 98.65% (197.3 mAh/g) even after cycling with significantly higher discharge capacities compared to the conventional electrodes for over 100 cycles.

Discussion

Ethanol phase inversion (EPI) processing on casted NMC811 slurries causes rapid precipitation of the Carbon binder domain (CBD). As the nonsolvent enters, the low miscibility of the binder with the solvent/nonsolvent phase results in the formation of a polymer-rich phase in the solution and subsequent precipitation of the binder. The

solvent/nonsolvent phase penetrates throughout the electrode, solidifying the constituents of the final electrode.

As a result, phase inversion processing, of which a simplified depiction is shown in **Figure 6**a during roll-to-roll processing, shows a substantial change in the CBD phase (**Figure 6**c bottom left), as shown with FIB-SEM, Mercury intrusion porosimetry, and solid-state NMR as well. The rapid precipitation of the binder with ethanol phase inversion results in electrodes with a higher degree of (connected) macropores but a lower degree of micropores, even after calendering (**Figure 6**c bottom right). The reduction in the degree of microporosity for the EPI electrodes was also further confirmed by ^{19}F NMR, which shows a higher degree of PVDF crystallinity, increasing the overall volumetric density of the PVDF binder. The FIB-SEM also reveals a reduction in the degree of binder migration for the EPI NMC811 electrodes.

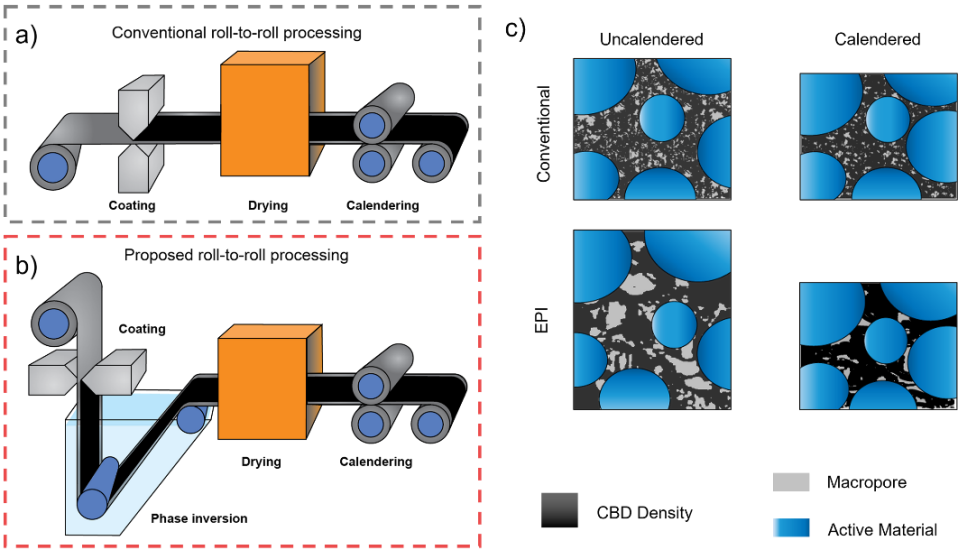

Figure 6. Differences between Conventional and EPI processes: a) Schematic procedure of the current roll-to-roll process based on conventional drying b) Schematic procedure of the proposed roll-to-roll process based on phase inversion c) Electrode microstructures obtained before and after calendering for the conventional and ethanol phase inversion processes.

The EPI electrodes show an improved flexibility, essential for roll-to-roll processing thick electrode architectures. The structure maintains its integrity during calendering

and results in electrodes with improved rate performances at both high charge and discharge rates.

The eSCM (EIS) using a non-intercalating electrolyte showed a significant decrease in tortuosity factor for the EPI electrodes. The lower tortuosity results in a higher charge capacity at high charge rates, but the capacity gain is more evident during high discharge. During fast discharge, Li^+ concentration depletion due to insufficient influx in a tortuous pore network causes uneven charge distribution across the depth of the electrode and a rapid (concentration) overpotential buildup. In this regard, a lower tortuosity of the pore network is beneficial for maintaining sufficient ion flux deeper in the cathode. The effect of tortuosity is shown using the P2D model, and the computed tortuosity factors nearly match the experimental values for both conventional and phase inversion electrodes.

The EPI electrodes consistently maintain a higher discharge capacity over 100+ cycles during long-term cycling tests of high mass loading (35 mg/cm^2). While both EPI and conventional electrodes show the same gradual capacity fade mechanism at high discharge rates (1C, 7 mA/cm^2) originating from the increase in impedance from the Li metal anode, the EPI electrode shows an excellent capacity retention of 98.65%.

An estimate of the cell level volumetric and weight density of batteries fitted with double-sided EPI electrodes shown in this work are 1210 Wh/L and 503 Wh/kg, respectively without casing. Here, the calculation assumes a zero-excess lithium configuration and Celgard separators filled with conventional liquid electrolyte (see **Note S9, Table S8**). For lithium excess architectures, using twice the lithium inventory needed for the rated capacity, the energy density will slightly lower to 1054 Wh/L and 487 Wh/kg. These values highlight the benefit of high mass loadings enabled by Ethanol phase inversion, as the inactive components in a cell lower from 43% to 37% of the total cell when going from 4 to 7 mAh/cm^2.

To implement phase inversion processing in current industrial practice, the conventional roll-to-roll electrode manufacturing setup would need an additional nonsolvent processing step. As typical solvents are replaced with more volatile and/or benign nonsolvents, introducing phase inversion would lower the energy investment of subsequent drying and ease solvent recovery. In this work and previous works,[30-36] it is shown that phase inversion processing is compatible with a wide range of

materials and compositions. Finally, the available literature on membrane processing using phase inversion steps allows a steep learning curve in a roll-to-roll setup.

In summary, we have developed a new Ethanol-based phase inversion (EPI) strategy for making ultrahigh-loading, high-performance electrodes out of Ni-rich layered oxide materials. We show high active mass loading (35 mg/cm^2) EPI NMC811 electrodes which outperform conventional NMC811 electrodes during fast charge (50% improvement at 0.5C) and discharge (120% improvement at 1C) at similar porosities (~30%). Unlike conventional electrodes, EPI electrodes can be made ultrathick (60 mg/cm^2, 12 mAh/cm^2) without having delamination or cracking issues. The EPI electrodes show a higher gravimetric capacity and similar capacity retention as the conventional electrodes on extensive cycling, which indicates that the processing does not adversely affect the cathode active material. The improved rate performance originates from the lower tortuosity of the electrode. With the addition of a phase inversion processing step in conventional battery manufacturing processes, it is possible to increase the rate performance of battery electrodes at high mass loadings, and this presents a viable path toward future batteries with both high energy and power densities.

REFERENCES

[1] A. Masias, J. Marcicki, W.A. Paxton, Opportunities and Challenges of Lithium Ion Batteries in Automotive Applications, ACS Energy Lett. 6 (2021) 621–630. https://doi.org/10.1021/acsenergylett.0c02584.

[2] V. Viswanathan, A.H. Epstein, Y.-M. Chiang, E. Takeuchi, M. Bradley, J. Langford, M. Winter, The challenges and opportunities of battery-powered flight, Nature. 601 (2022) 519–525. https://doi.org/10.1038/s41586-021-04139-1.

[3] A. Bills, S. Sripad, W.L. Fredericks, M. Singh, V. Viswanathan, Performance Metrics Required of Next-Generation Batteries to Electrify Commercial Aircraft, ACS Energy Lett. 5 (2020) 663–668. https://doi.org/10.1021/acsenergylett.9b02574.

[4] J. Liu, Z. Bao, Y. Cui, E.J. Dufek, J.B. Goodenough, P. Khalifah, Q. Li, B.Y. Liaw, P. Liu, A. Manthiram, Y.S. Meng, V.R. Subramanian, M.F. Toney, V.V. Viswanathan, M.S. Whittingham, J. Xiao, W. Xu, J. Yang, X.-Q. Yang, J.-G. Zhang, Pathways for practical high-energy long-cycling lithium metal batteries, Nat. Energy. 4 (2019) 180–186. https://doi.org/10.1038/s41560-019-0338-x.

[5] Y. Kuang, C. Chen, D. Kirsch, L. Hu, Thick Electrode Batteries: Principles, Opportunities, and Challenges, Adv. Energy Mater. 9 (2019) 1901457. https://doi.org/10.1002/aenm.201901457.

[6] S.-H. Park, P.J. King, R. Tian, C.S. Boland, J. Coelho, C. (John) Zhang, P. McBean, N. McEvoy, M.P. Kremer, D. Daly, J.N. Coleman, V. Nicolosi, High areal capacity battery electrodes enabled by segregated nanotube networks, Nat. Energy. 4 (2019) 560–567. https://doi.org/10.1038/s41560-019-0398-y.

[7] W. Yao, M. Chouchane, W. Li, S. Bai, Z. Liu, L. Li, A.X. Chen, B. Sayahpour, R. Shimizu, G. Raghavendran, M.A. Schroeder, Y.-T. Chen, D.H.S. Tan, B. Sreenarayanan, C.K. Waters, A. Sichler, B. Gould, D.J. Kountz, D.J. Lipomi, M. Zhang, Y.S. Meng, A 5 V-class cobalt-free battery cathode with high loading enabled by dry coating, Energy Environ. Sci. 16 (2023) 1620–1630. https://doi.org/10.1039/D2EE03840D.

[8] H. Gao, Q. Wu, Y. Hu, J.P. Zheng, K. Amine, Z. Chen, Revealing the Rate-Limiting Li-Ion Diffusion Pathway in Ultrathick Electrodes for Li-Ion Batteries, J. Phys. Chem. Lett. 9 (2018) 5100–5104. https://doi.org/10.1021/acs.jpclett.8b02229.

[9] M. Weiss, R. Ruess, J. Kasnatscheew, Y. Levartovsky, N.R. Levy, P. Minnmann, L. Stolz, T. Waldmann, M. Wohlfahrt-Mehrens, D. Aurbach, M. Winter, Y. Ein-Eli, J. Janek, Fast Charging of Lithium-Ion Batteries: A Review of Materials Aspects, Adv. Energy Mater. 11 (2021) 2101126. https://doi.org/10.1002/aenm.202101126.

[10] B. Tjaden, D.J.L. Brett, P.R. Shearing, Tortuosity in electrochemical devices: a review of calculation approaches, Int. Mater. Rev. 63 (2018) 47–67. https://doi.org/10.1080/09506608.2016.1249995.

[11] L.S. Kremer, A. Hoffmann, T. Danner, S. Hein, B. Prifling, D. Westhoff, C. Dreer, A. Latz, V. Schmidt, M. Wohlfahrt-Mehrens, Manufacturing Process for Improved Ultra-Thick Cathodes in High-Energy Lithium-Ion Batteries, Energy Technol. 8 (2020) 1900167. https://doi.org/10.1002/ente.201900167.

[12] S. Jaiser, M. Müller, M. Baunach, W. Bauer, P. Scharfer, W. Schabel, Investigation of film solidification and binder migration during drying of Li-Ion battery anodes, J. Power Sources. 318 (2016) 210–219. https://doi.org/10.1016/j.jpowsour.2016.04.018.

[13] T.-T. Nguyen, A. Demortière, B. Fleutot, B. Delobel, C. Delacourt, S.J. Cooper, The electrode tortuosity factor: why the conventional tortuosity factor is not well suited for quantifying transport in porous Li-ion battery electrodes and what to use instead, Npj Comput. Mater. 6 (2020) 1–12. https://doi.org/10.1038/s41524-020-00386-4.

[14] X. Lu, S.R. Daemi, A. Bertei, M.D.R. Kok, K.B. O'Regan, L. Rasha, J. Park, G. Hinds, E. Kendrick, D.J.L. Brett, P.R. Shearing, Microstructural Evolution of Battery Electrodes During Calendering, Joule. 4 (2020) 2746–2768. https://doi.org/10.1016/j.joule.2020.10.010.

[15] R. Xu, Y. Yang, F. Yin, P. Liu, P. Cloetens, Y. Liu, F. Lin, K. Zhao, Heterogeneous damage in Li-ion batteries: Experimental analysis and theoretical modeling, J. Mech. Phys. Solids. 129 (2019) 160–183. https://doi.org/10.1016/j.jmps.2019.05.003.

[16] C. Huang, C.L.A. Leung, P. Leung, P.S. Grant, A Solid-State Battery Cathode with a Polymer Composite Electrolyte and Low Tortuosity Microstructure by Directional Freezing and Polymerization, Adv. Energy Mater. 11 (2021) 2002387. https://doi.org/10.1002/aenm.202002387.

[17] B. Delattre, R. Amin, J. Sander, J.D. Coninck, A.P. Tomsia, Y.-M. Chiang, Impact of Pore Tortuosity on Electrode Kinetics in Lithium Battery Electrodes: Study in Directionally Freeze-Cast LiNi0.8Co0.15Al0.05O2 (NCA), J. Electrochem. Soc. 165 (2018) A388. https://doi.org/10.1149/2.1321802jes.

[18] J. Billaud, F. Bouville, T. Magrini, C. Villevieille, A.R. Studart, Magnetically aligned graphite electrodes for high-rate performance Li-ion batteries, Nat. Energy. 1 (2016) 1–6. https://doi.org/10.1038/nenergy.2016.97.

[19] L. Li, R.M. Erb, J. Wang, J. Wang, Y.-M. Chiang, Fabrication of Low-Tortuosity Ultrahigh-Area-Capacity Battery Electrodes through Magnetic Alignment of Emulsion-Based Slurries, Adv. Energy Mater. 9 (2019) 1802472. https://doi.org/10.1002/aenm.201802472.

[20] J.S. Sander, R.M. Erb, L. Li, A. Gurijala, Y.-M. Chiang, High-performance battery electrodes via magnetic templating, Nat. Energy. 1 (2016) 1–7. https://doi.org/10.1038/nenergy.2016.99.

[21] K.-H. Chen, M.J. Namkoong, V. Goel, C. Yang, S. Kazemiabnavi, S.M. Mortuza, E. Kazyak, J. Mazumder, K. Thornton, J. Sakamoto, N.P. Dasgupta, Efficient fast-charging of lithium-ion batteries enabled by laser-patterned three-dimensional graphite anode architectures, J. Power Sources. 471 (2020) 228475. https://doi.org/10.1016/j.jpowsour.2020.228475.

[22] D.P. Singh, A. George, R.V. Kumar, J.E. ten Elshof, M. Wagemaker, Nanostructured TiO2 Anatase Micropatterned Three-Dimensional Electrodes for High-Performance Li-Ion Batteries, J. Phys. Chem. C. 117 (2013) 19809–19815. https://doi.org/10.1021/jp3118659.

[23] D.P. Singh, F.M. Mulder, A.M. Abdelkader, M. Wagemaker, Facile Micro Templating LiFePO4 Electrodes for High Performance Li-Ion Batteries, Adv. Energy Mater. 3 (2013) 572–578. https://doi.org/10.1002/aenm.201200704.

[24] A.M. Boyce, D.J. Cumming, C. Huang, S.P. Zankowski, P.S. Grant, D.J.L. Brett, P.R. Shearing, Design of Scalable, Next-Generation Thick Electrodes: Opportunities and Challenges, ACS Nano. 15 (2021) 18624–18632. https://doi.org/10.1021/acsnano.1c09687.

[25] A. Kwade, W. Haselrieder, R. Leithoff, A. Modlinger, F. Dietrich, K. Droeder, Current status and challenges for automotive battery production technologies, Nat. Energy. 3 (2018) 290–300. https://doi.org/10.1038/s41560-018-0130-3.

[26] B.F.K. Kingsbury, K. Li, A morphological study of ceramic hollow fibre membranes, J. Membr. Sci. 328 (2009) 134–140. https://doi.org/10.1016/j.memsci.2008.11.050.

[27] P. van de Witte, P.J. Dijkstra, J.W.A. van den Berg, J. Feijen, Phase separation processes in polymer solutions in relation to membrane formation, J. Membr. Sci. 117 (1996) 1–31. https://doi.org/10.1016/0376-7388(96)00088-9.

[28] M. Lee, B. Wang, Z. Wu, K. Li, Formation of micro-channels in ceramic membranes – Spatial structure, simulation, and potential use in water treatment, J. Membr. Sci. 483 (2015) 1–14. https://doi.org/10.1016/j.memsci.2015.02.023.

[29] A.K. Hołda, I.F.J. Vankelecom, Understanding and guiding the phase inversion process for synthesis of solvent resistant nanofiltration membranes, J. Appl. Polym. Sci. 132 (2015). https://doi.org/10.1002/app.42130.

[30] R.R. Jacquemond, C.T.-C. Wan, Y.-M. Chiang, Z. Borneman, F.R. Brushett, K. Nijmeijer, A. Forner-Cuenca, Microstructural engineering of high-power redox flow battery electrodes via nonsolvent induced phase separation, Cell Rep. Phys. Sci. 3 (2022) 100943. https://doi.org/10.1016/j.xcrp.2022.100943.

[31] C.T.-C. Wan, R.R. Jacquemond, Y.-M. Chiang, K. Nijmeijer, F.R. Brushett, A. Forner-Cuenca, Nonsolvent Induced Phase Separation Enables Designer Redox Flow Battery Electrodes, Adv. Mater. 33 (2021) 2006716. https://doi.org/10.1002/adma.202006716.

[32] X. Yang, Y. Chen, M. Wang, H. Zhang, X. Li, H. Zhang, Phase Inversion: A Universal Method to Create High-Performance Porous Electrodes for Nanoparticle-

Based Energy Storage Devices, Adv. Funct. Mater. 26 (2016) 8427–8434. https://doi.org/10.1002/adfm.201604229.

[33] W. Wahyudi, Z. Cao, P. Kumar, M. Li, Y. Wu, M.N. Hedhili, T.D. Anthopoulos, L. Cavallo, L.-J. Li, J. Ming, Phase Inversion Strategy to Flexible Freestanding Electrode: Critical Coupling of Binders and Electrolytes for High Performance Li–S Battery, Adv. Funct. Mater. 28 (2018) 1802244. https://doi.org/10.1002/adfm.201802244.

[34] P.-P.R.M.L. Harks, C.B. Robledo, C. George, C. Wang, T. van Dijk, L. Sturkenboom, E.D.W. Roesink, F.M. Mulder, Immersion precipitation route towards high performance thick and flexible electrodes for Li-ion batteries, J. Power Sources. 441 (2019) 227200. https://doi.org/10.1016/j.jpowsour.2019.227200.

[35] J. Wu, Z. Ju, X. Zhang, C. Quilty, K.J. Takeuchi, D.C. Bock, A.C. Marschilok, E.S. Takeuchi, G. Yu, Ultrahigh-Capacity and Scalable Architected Battery Electrodes via Tortuosity Modulation, ACS Nano. 15 (2021) 19109–19118. https://doi.org/10.1021/acsnano.1c06491.

[36] N.P. Jimenez, M.P. Balogh, I.C. Halalay, High Porosity Single-Phase Silicon Negative Electrode Made with Phase-Inversion, J. Electrochem. Soc. 168 (2021) 040507. https://doi.org/10.1149/1945-7111/abe3f1.

[37] N. Evenepoel, S. Wen, M. Tilahun Tsehaye, B. Van der Bruggen, Potential of DMSO as greener solvent for PES ultra- and nanofiltration membrane preparation, J. Appl. Polym. Sci. 135 (2018) 46494. https://doi.org/10.1002/app.46494.

[38] M. Wang, X. Dong, I.C. Escobar, Y.-T. Cheng, Lithium Ion Battery Electrodes Made Using Dimethyl Sulfoxide (DMSO)—A Green Solvent, ACS Sustain. Chem. Eng. 8 (2020) 11046–11051. https://doi.org/10.1021/acssuschemeng.0c02884.

[39] S.Y. Li, B.C. Church, Effect of aqueous-based cathode slurry pH and immersion time on corrosion of aluminum current collector in lithium-ion batteries, Mater. Corros. 67 (2016) 978–987. https://doi.org/10.1002/maco.201608843.

[40] D. Bresser, D. Buchholz, A. Moretti, A. Varzi, S. Passerini, Alternative binders for sustainable electrochemical energy storage – the transition to aqueous electrode

processing and bio-derived polymers, Energy Environ. Sci. 11 (2018) 3096–3127. https://doi.org/10.1039/C8EE00640G.

[41] C.M. Hansen, Hansen Solubility Parameters: A User's Handbook, Second Edition, 2nd ed., CRC Press, Boca Raton, 2007. https://doi.org/10.1201/9781420006834.

[42] A. Bottino, G. Capannelli, S. Munari, A. Turturro, Solubility parameters of poly(vinylidene fluoride), J. Polym. Sci. Part B Polym. Phys. 26 (1988) 785–794. https://doi.org/10.1002/polb.1988.090260405.

[43] PubChem, Ethanol, (n.d.). https://pubchem.ncbi.nlm.nih.gov/compound/702 (accessed August 25, 2023).

[44] S. Yuan, C. Zou, H. Yin, Z. Chen, W. Yang, Study on the separation of binary azeotropic mixtures by continuous extractive distillation, Chem. Eng. Res. Des. 93 (2015) 113–119. https://doi.org/10.1016/j.cherd.2014.05.005.

[45] J. Chau, K.K. Sirkar, Organic solvent mixture separation during reverse osmosis and nanofiltration by a perfluorodioxole copolymer membrane, J. Membr. Sci. 618 (2021) 118663. https://doi.org/10.1016/j.memsci.2020.118663.

[46] B. Wang, Z. Lai, Finger-like voids induced by viscous fingering during phase inversion of alumina/PES/NMP suspensions, J. Membr. Sci. 405–406 (2012) 275–283. https://doi.org/10.1016/j.memsci.2012.03.020.

[47] T. Montina, P. Wormald, P. Hazendonk, 13C Solid-State NMR of the Mobile Phase of Poly(vinylidene fluoride), Macromolecules. 45 (2012) 6002–6007. https://doi.org/10.1021/ma3013477.

[48] J. Moškon, J. Žuntar, S.D. Talian, R. Dominko, M. Gaberšček, A Powerful Transmission Line Model for Analysis of Impedance of Insertion Battery Cells: A Case Study on the NMC-Li System, J. Electrochem. Soc. 167 (2020) 140539. https://doi.org/10.1149/1945-7111/abc769.

[49] J. Landesfeind, J. Hattendorff, A. Ehrl, W.A. Wall, H.A. Gasteiger, Tortuosity Determination of Battery Electrodes and Separators by Impedance Spectroscopy, J. Electrochem. Soc. 163 (2016) A1373. https://doi.org/10.1149/2.1141607jes.

[50] F. Pouraghajan, H. Knight, M. Wray, B. Mazzeo, R. Subbaraman, J. Christensen, D. Wheeler, Quantifying Tortuosity of Porous Li-Ion Battery Electrodes: Comparing Polarization-Interrupt and Blocking-Electrolyte Methods, J. Electrochem. Soc. 165 (2018) A2644. https://doi.org/10.1149/2.0611811jes.

[51] R. Morasch, J. Landesfeind, B. Suthar, H.A. Gasteiger, Detection of Binder Gradients Using Impedance Spectroscopy and Their Influence on the Tortuosity of Li-Ion Battery Graphite Electrodes, J. Electrochem. Soc. 165 (2018) A3459. https://doi.org/10.1149/2.1021814jes.

[52] A. Shodiev, E.N. Primo, M. Chouchane, T. Lombardo, A.C. Ngandjong, A. Rucci, A.A. Franco, 4D-resolved physical model for Electrochemical Impedance Spectroscopy of Li(Ni1-x-yMnxCoy)O2-based cathodes in symmetric cells: Consequences in tortuosity calculations, J. Power Sources. 454 (2020) 227871. https://doi.org/10.1016/j.jpowsour.2020.227871.

[53] M. Doyle, T.F. Fuller, J. Newman, Modeling of Galvanostatic Charge and Discharge of the Lithium/Polymer/Insertion Cell, J. Electrochem. Soc. 140 (1993) 1526–1533. https://doi.org/10.1149/1.2221597.

[54] T.F. Fuller, M. Doyle, J. Newman, Simulation and Optimization of the Dual Lithium Ion Insertion Cell, J. Electrochem. Soc. 141 (1994) 1–10. https://doi.org/10.1149/1.2054684.

[55] T.R. Ferguson, M.Z. Bazant, Nonequilibrium Thermodynamics of Porous Electrodes, J. Electrochem. Soc. 159 (2012) A1967–A1985. https://doi.org/10.1149/2.048212jes.

[56] A. Vasileiadis, N.J.J. de Klerk, R.B. Smith, S. Ganapathy, P.P.R.M.L. Harks, M.Z. Bazant, M. Wagemaker, Toward Optimal Performance and In-Depth Understanding of Spinel $Li_4Ti_5O_{12}$ Electrodes through Phase Field Modeling, Adv. Funct. Mater. 28 (2018) 1705992. https://doi.org/10.1002/adfm.201705992.

[57] P. Ombrini, M.Z. Bazant, M. Wagemaker, A. Vasileiadis, Thermodynamics of multi-sublattice battery active materials: from an extended regular solution theory to a phase-field model of LiMnyFe1-yPO4, Npj Comput. Mater. 9 (2023) 148. https://doi.org/10.1038/s41524-023-01109-1.

[58] T.K. Schwietert, P. Ombrini, L.S. Ootes, L. Oostrum, V. Azizi, D. Cogswell, J. Zhu, M.Z. Bazant, M. Wagemaker, A. Vasileiadis, Phase-Field Computational Framework for Addressing Challenges in Solid-State Batteries, PRX Energy. 2 (2023) 033014. https://doi.org/10.1103/PRXEnergy.2.033014.

[59] G. Galuppini, M.D. Berliner, D.A. Cogswell, D. Zhuang, M.Z. Bazant, R.D. Braatz, Nonlinear identifiability analysis of Multiphase Porous Electrode Theory-based battery models: A Lithium Iron Phosphate case study, J. Power Sources. 573 (2023) 233009. https://doi.org/10.1016/j.jpowsour.2023.233009.

[60] V. Sulzer, S.G. Marquis, R. Timms, M. Robinson, S.J. Chapman, Python Battery Mathematical Modelling (PyBaMM), 9 (2021) 14. https://doi.org/10.5334/jors.309.

[61] M. Andersson, M. Streb, J.Y. Ko, V. Löfqvist Klass, M. Klett, H. Ekström, M. Johansson, G. Lindbergh, Parametrization of physics-based battery models from input–output data: A review of methodology and current research, J. Power Sources. 521 (2022) 230859. https://doi.org/10.1016/j.jpowsour.2021.230859.

[62] A.A. Wang, S.E.J. O'Kane, F. Brosa Planella, J.L. Houx, K. O'Regan, M. Zyskin, J. Edge, C.W. Monroe, S.J. Cooper, D.A. Howey, E. Kendrick, J.M. Foster, Review of parameterisation and a novel database (LiionDB) for continuum Li-ion battery models, Prog. Energy. 4 (2022) 032004. https://doi.org/10.1088/2516-1083/ac692c.

[63] Q. Wang, C. Zhao, Z. Yao, J. Wang, F. Wu, S.G.H. Kumar, S. Ganapathy, S. Eustace, X. Bai, B. Li, J. Lu, M. Wagemaker, Entropy-Driven Liquid Electrolytes for Lithium Batteries, Advanced Materials 35 (2023) 2210677. https://doi.org/10.1002/adma.202210677..

[64] Q. Wang, C. Zhao, J. Wang, Z. Yao, S. Wang, S.G.H. Kumar, S. Ganapathy, S. Eustace, X. Bai, B. Li, M. Wagemaker, High entropy liquid electrolytes for lithium batteries, Nat Commun 14 (2023) 440. https://doi.org/10.1038/s41467-023-36075-1..

[65] A.J. Louli, A. Eldesoky, R. Weber, M. Genovese, M. Coon, J. deGooyer, Z. Deng, R.T. White, J. Lee, T. Rodgers, R. Petibon, S. Hy, S.J.H. Cheng, J.R. Dahn, Diagnosing and correcting anode-free cell failure via electrolyte and morphological analysis, Nat. Energy. (2020) 1–10. https://doi.org/10.1038/s41560-020-0668-8.

[66] Standard Test Methods for Vulcanized Rubber and Thermoplastic Elastomers—Tension, (n.d.). https://www.astm.org/d0412-16r21.html (accessed August 22, 2023).

[67] N. Ogihara, S. Kawauchi, C. Okuda, Y. Itou, Y. Takeuchi, Y. Ukyo, Theoretical and Experimental Analysis of Porous Electrodes for Lithium-Ion Batteries by Electrochemical Impedance Spectroscopy Using a Symmetric Cell, J. Electrochem. Soc. 159 (2012) A1034. https://doi.org/10.1149/2.057207jes.

[68] R.B. Smith, M.Z. Bazant, Multiphase Porous Electrode Theory, J. Electrochem. Soc. 164 (2017) E3291. https://doi.org/10.1149/2.0171711jes.

[69] M. Doyle, T.F. Fuller, J. Newman, Modeling of Galvanostatic Charge and Discharge of the Lithium/Polymer/Insertion Cell, J. Electrochem. Soc. 140 (1993) 1526. https://doi.org/10.1149/1.2221597.

[70] B. Balu, A.S. Khair, Role of Stefan–Maxwell fluxes in the dynamics of concentrated electrolytes, Soft Matter. 14 (2018) 8267–8275. https://doi.org/10.1039/C8SM01222A.

[71] A. Nyman, M. Behm, G. Lindbergh, Electrochemical characterisation and modelling of the mass transport phenomena in LiPF6–EC–EMC electrolyte, Electrochimica Acta. 53 (2008) 6356–6365. https://doi.org/10.1016/j.electacta.2008.04.023.

[72] I. McClelland, S.G. Booth, N.N. Anthonisamy, L.A. Middlemiss, G.E. Pérez, E.J. Cussen, P.J. Baker, S.A. Cussen, Direct Observation of Dynamic Lithium Diffusion Behavior in Nickel-Rich, $LiNi_{0.8}Mn_{0.1}Co_{0.1}O_2$ (NMC811) Cathodes Using *Operando* Muon Spectroscopy, Chem. Mater. 35 (2023) 4149–4158. https://doi.org/10.1021/acs.chemmater.2c03834.

[73] R. Jung, M. Metzger, F. Maglia, C. Stinner, H.A. Gasteiger, Oxygen Release and Its Effect on the Cycling Stability of LiNixMnyCozO2 (NMC) Cathode Materials for Li-Ion Batteries, J. Electrochem. Soc. 164 (2017) A1361. https://doi.org/10.1149/2.0021707jes.

[74] R.J. Good, R.Sh. Mikhail, The contact angle in mercury intrusion porosimetry, Powder Technol. 29 (1981) 53–62. https://doi.org/10.1016/0032-5910(81)85004-8.

[75] Standard Test Method for Peel Resistance of Adhesives (T-Peel Test), (n.d.). https://www.astm.org/d1876-08r15e01.html (accessed August 10, 2023).

SUPPORTING INFORMATION

NOTE S1 HANSEN SOLUBILITY PARAMETERS FOR COMMON SOLVENTS/NON-SOLVENTS AND THEIR SOLUBILITY WITH PVDF

Hansen Solubility parameters, developed by Charles Hansen, provide a measure of the relative solubility of two materials. Each material is defined by three Hansen parameters (typically measured in MPa), i.e., δ_d corresponds to intermolecular dispersion forces, δ_p corresponds to intermolecular dipolar forces, and δ_h corresponds to intermolecular hydrogen bond forces.

The relative solubility between the parameters is then given by the parameters Ra, the distance between the Hansen parameters of the two materials in the 3D Hansen space, which is calculated as:

$$(Ra)^2 = 4(\delta_{d2} - \delta_{d1})^2 + (\delta_{p2} - \delta_{p1})^2 + (\delta_{h2} - \delta_{h1})^2$$

The Hansen solubility parameters for commonly used solvents are obtained from the Hansen Solubility Parameters Handbook,[S1] while the solubility parameters of PVDF are obtained from the work of Bottino et. al.[S2]

Table S1. Hansen solubility parameters for commonly used solvents, non-solvents, and PVDF

Compound	δ_d (MPa)	δ_p (MPa)	δ_h (MPa)	Ra (solubility parameter) with PVDF
PVDF	17.2	12.5	9.2	0
N, N-dimethylacetamide (DMAc)	16.8	11.5	10.2	1.62
N, N-dimethylformamide (DMF)	17.4	13.7	11.3	2.45
N-methyl-2-pyrrolidone (NMP)	18	12.3	7.2	2.57
Acetone	15.5	10.4	7	4.56

Dimethylsulfoxide (DMSO)	18.4	16.4	10.2	4.69
Tetrahydrofuran (THF)	16.8	5.7	8	6.95
Acetic acid	14.5	8	13.5	8.24
Propylene- 1,2-carbonate (PC)	20	18	4.1	9.36
1-Butanol	16	5.7	15.8	9.77
1-Propanol	16	6.8	17.4	10.27
Ethanol	15.8	8.8	19.4	11.21
Methanol	15.1	12.3	22.3	13.76
Ethylene glycol	17	11	26	16.87
Glycerol	17.4	12.1	29.3	20.11
Water	15.5	16	42.3	33.46

NOTE S2 VISCOSITY EFFECTS ON PHASE INVERSION PROCESSING

The cathode slurry solvent-to-binder ratio is an adjustable parameter that changes cathode structures significantly during phase inversion. High viscosity slurries with 1:10 PVDF:Solvent ratio yield uneven pore and height distributions (Figure S1, top left). A solvent ratio of 1:12 yields targeted pore diameters of a few micrometers (Figure S1, top left), which serve as ion channels to the deeper layers of the electrode. Higher dilutions barely show structural change, which can be explained by the minor change in the viscosity of the slurry above the 1:12 binder-to-solvent ratio (Figure S1, bottom left). DMSO shows a more significant temperature dependence than NMP-based slurries (Figure S1, bottom right). NMP is chosen as the solvent for subsequent slurry processing to prevent this large temperature-induced effect.

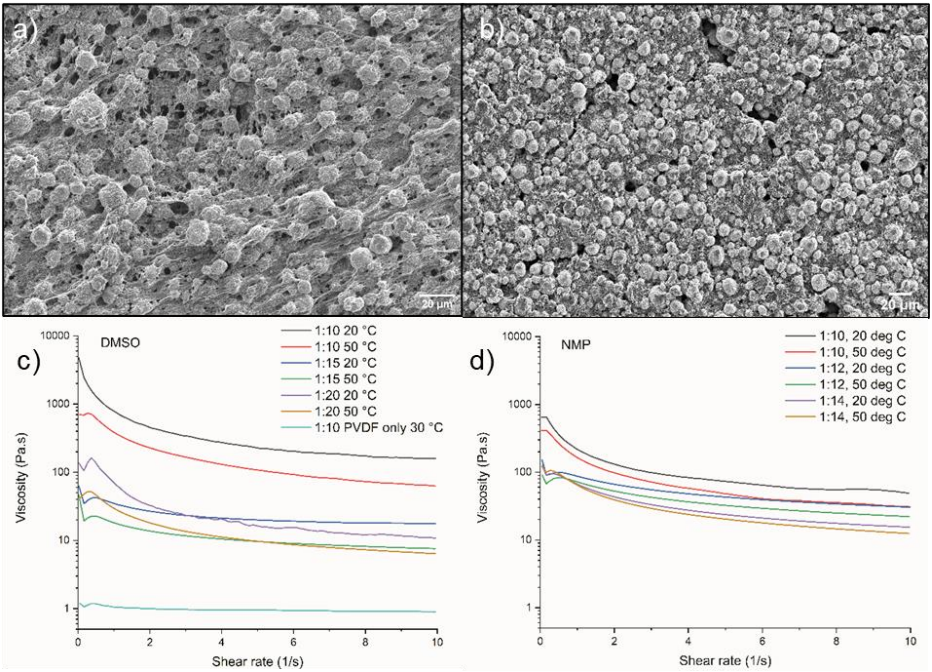

Figure S1. Influence of viscosity on phase inversion processing. The low solvent-to-binder ratio (1:10 PVDF:DMSO) causes uneven pore distributions (a) during the phase inversion processing compared to processing using a higher solvent-to-binder ratio (1:12 PVDF:DMSO, b). This can be explained by the viscosity change of DMSO, which has a high temperature and binder/solvent ratio dependence (c). For NMP, this dependence is much lower (d).

Electrode Characterization: Additional Scanning Electron Microscopy (SEM) Images

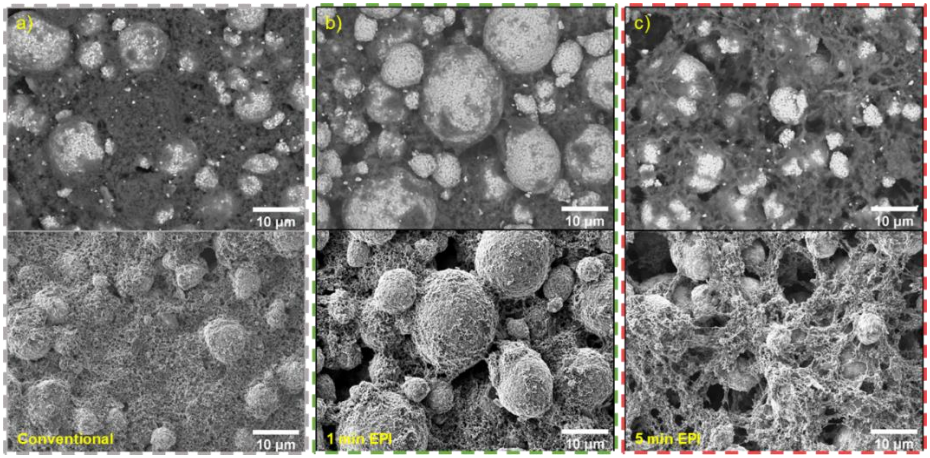

Figure S2. Top view SEM images (Backscattered electron mode on top, secondary electron incidence mode below) of uncalendered NMC811 electrodes: a) conventional, b) phase inversion (1 min exchange), c) phase inversion (5 min exchange) electrodes

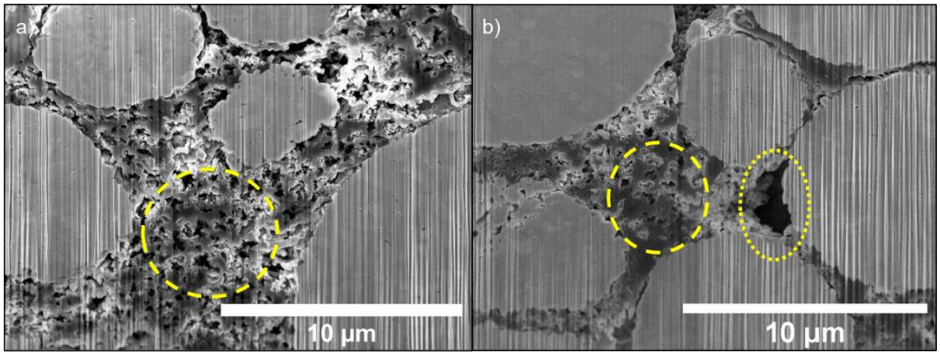

Figure S3. Zoomed cross-section FIB-SEM of CBD structures after calendering: a) conventional electrodes, b) EPI electrodes. The dashed ellipse indicates CBD with micropores, and the dotted ellipse indicates macropores.

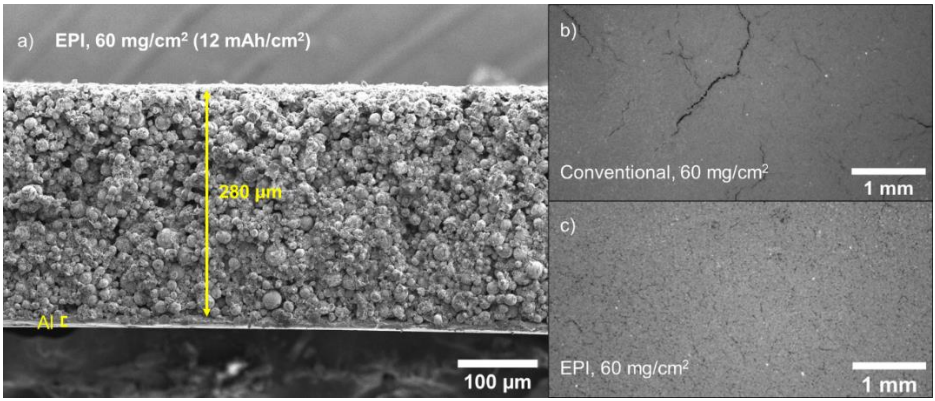

Figure S4. NMC811 electrodes at ultrahigh mass loadings: a) Cross-section SEM of EPI NMC811 electrode with active mass loading of 60 mg/cm² and 30% porosity. b) Top view optical micrograph of 60 mg/cm² Conventional NMC811 electrode (30% porosity) c) Top view optical micrograph of 60 mg/cm² EPI NMC811 electrode (30% porosity)

NOTE S3 POROSITY CALCULATION AND MIP POROSITY MEASUREMENTS

For apparent porosity, the cathode volume is first calculated from thickness measurements by multiplying a representative area A_{cat} with thickness d_{cat}. Volume fractions of the cathode body are calculated by dividing the mass fractions $x_{m,x}$ with the components' individual densities ρ_x, summation, and multiplication with the weighed cathode mass. Dividing the cathode body mass with the cathode volume then gives the volume fraction of the body, of which the porosity is calculated by subtracting 1 minus this value.

$$d_{cat} = \frac{M_{cat}}{A_{cat}}\left(\frac{x_{m,AM}}{\rho_{AM}} + \frac{x_{m,CB}}{\rho_{CB}} + \frac{x_{m,PVDF}}{\rho_{PVDF}} + \frac{x_{m,KS4}}{\rho_{KS4}}\right)/(1-\varepsilon) = {d_{cat,body}}\Big/{(1-\varepsilon)}$$

While the particle density typically used in apparent porosity calculations for NMC/NCA electrodes is the secondary particle density (3.75 kg/dm³ in this case), the intrusion of mercury at high pressures can also provide it access to the void volume between the primary crystallites of these particles, typically not accessible to the electrolyte on assembly using these electrodes. Therefore, the single crystallite particle density of 4.8 kg/dm³ has been considered for estimating the cathode body volume fraction used in the case of MIP.[S3]

The mercury extrusion volume provides a measure of the amount of mercury expelled from the microporous structure because of the high surface tension (contact angles near 180°)[S4]. With this volume, the fraction of fine structural porosity can be estimated. On calendered cathodes, the extrusion volume fraction yields 28% porosity for conventional cathodes and 31% for EPI cathodes. In comparison, the apparent porosities, as measured by comparing the areal mass loading and the cathode thickness, were 29% and 31% respectively. With the EPI uncalendered sample, the apparent porosity of 46%, however, exceeds the MIP extrusion porosity of 18% as the droplet size of mercury becomes smaller than the size of the macropores (>15 µm at 0.1 MPa) and the mercury is not expelled as a result.

Table S2. Densities of NMC811 electrode components

Compound	Density (kg/dm^3)
NMC811 (crystallographic density)	4.8
NMC811 (secondary particle density)	3.75
PVDF	1.78
Carbon (used for KS4 and CB)	1.9

Table S3. Apparent porosities and Microporosities of freestanding NMC811 electrodes calculated from Mercury intrusion porosimetry

Electrode	Extrusion volume (mL/g)	Loading (mg/cm^2)	Measured Thickness (µm)	Mass / body volume of cathode (mg/mm^3)	Body Volume cathode (mm^3/cm^2)	Total Volume cathode (mm^3/cm^2)	Apparent porosity (mm/mm)	Micro-porosity (mm/mm)
Conventional calendered	0.09	53.41	175.33	0.24	12.55	17.53	0.28	0.29
Conventional uncalendered	0.09	53.41	178.20	0.24	12.55	17.82	0.30	0.27
EPI calendered	0.11	47.54	163.00	0.24	11.17	14.90	0.31	0.31
EPI mild calendered	0.15	47.54	174.20	0.24	11.17	17.42	0.36	0.40
EPI uncalendered	0.08	47.54	200.00	0.24	11.17	20.00	0.44	0.18

NOTE S4 ADHESION STRENGTH MEASUREMENTS

Similar to the tensile strength measurements, the t-peel adhesion strength measurements were performed on the ZwickRoell 10 kN universal testing machine. For the adhesion strength measurement, the electrodes were cut into strips of 100x15 mm. A 3M VHB double-sided tape was applied onto the strips, with about 20 mm of the tape/electrode remaining unbound. These strips were placed under ~1 kg steel blocks overnight to ensure good adhesion. The peel test was performed similar to ASTM D1876-08.[S5] The unbound part of the tape/electrode was used to clamp the sample onto the test setup in a t-position, with a 20 mm gap between the clamps. A 100N loadcell (Zwick) was connected to the setup. The tape was peeled off from the electrode at a constant speed of 200 mm/min.

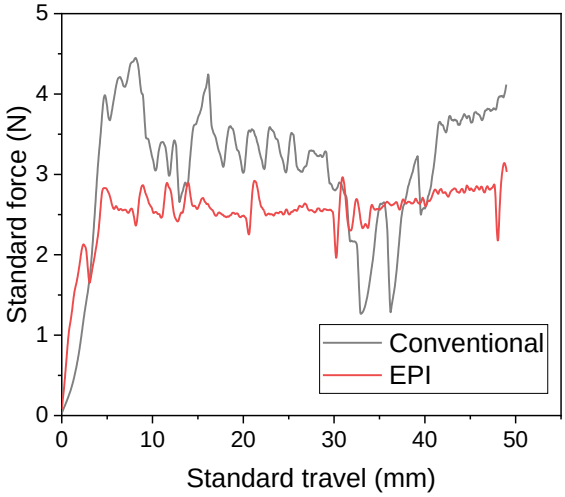

Figure S5. Peel off force vs. travel distance for 35 mg/cm² active mass loading NMC811 electrodes on Al current collector.

With the T-peel adhesion strength measurements, it was observed that while the EPI electrodes with active mass loading of 35 mg/cm^2 and 30% porosity) peeled off from the current collector at a nearly constant force, the conventional electrode peeled off at highly varying forces, highlighting uneven adhesion of the electrode to the current collector at these thicknesses.

Note S5 Electrochemical Impedance Spectroscopy for Li/LP57 electrolyte/NMC811 cells

The equivalent circuit used in fitting the EIS spectra is displayed in Figure 3e, and the corresponding resistance values are shown below:

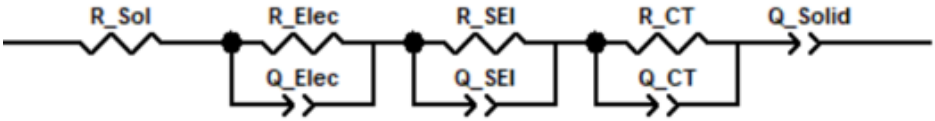

Figure S6. The equivalent circuit used for fitting the EIS data.

Table S4. Fitted R values for the EIS spectra shown in Figure 3e

Component	Conventional	EPI
Electrolyte Resistance, R_Sol (Ω.cm^2)	4.51	4.76
Electronic Resistance (overall), R_Elec (Ω.cm^2)	13.07	12.03
Li-SEI Resistance, R_SEI (Ω.cm^2)	11.48	12.46
Cathode charge transfer Resistance, R_CT (Ω.cm^2)	7.79	5.5

NOTE S6 DC ELECTRONIC RESISTANCE OF ELECTRODES

The through-plane (two-point) electronic conductivity was measured by pressing the electrode(s) between two stainless steel metal plates (**Table S5**)**.** To mitigate contact resistance due to surface roughness, the electrodes were subjected to gold sputtering (~ 10 nm). Gold sputtering indeed leads to a lower measured electronic resistance. This, however, may be a combined effect of gold plating on the electrode surface and on the material at the pore entrance. Therefore, the electronic resistance values for the non-gold-plated electrodes are reported in the main text.

Table S5. DC electronic resistance of electrodes perpendicular to the plane

Component	Conventional	EPI
Non gold plated [Ω.cm^2]	18.42	18.16
Gold plated [Ω.cm^2]	11.11	6.11

NOTE S7 ELECTROCHEMICAL TORTUOSITY FACTOR MEASUREMENTS

Electrochemical tortuosity factors were calculated according to the following equation:[S6]

$$\tau = \frac{\varepsilon . R . A . \kappa}{2 . d}$$

The terms and their corresponding values for the conventional and EPI electrodes are provided in the table below.

Table S6. Details of the electrochemical tortuosity factor calculations for the EIS plots shown in Figure 4a

Property	Conventional	EPI
Avg. Thickness, d (μm)	170	173
Avg. weight (mg)	55	56
Electrode (geometric) area, A (cm^2)	1.27	
Avg. porosity, ε	0.302	0.3015
Electrolyte conductivity, κ (mS/cm)	0.77	
Ionic Resistance (Ω.cm^2), R.A	512.48	357.28
Tortuosity factor, τ	3.79	2.58

NOTE S8 DETAILS OF THE P2D MODEL

The P2D model (also known as the Doyle-Fuller-Newman model[S7,S8]) uses volume averaging to simulate a complete porous electrode. A set of particles is set along the simulation axes such that they react with the surrounding electrolyte depending on the local electrolyte potential. The electrolyte transport is simulated considering the porosity and the tortuosity factor as parameters that, respectively, multiply and divide the electrolyte conductivity and diffusivity. These models can be used to optimize the battery (dis)charge protocols or obtain information about the limiting factors of specific morphologies or materials. The computational efficiency of P2D models allows broad parameter estimation, such that variables like diffusivity, charge-transfer resistance, and tortuosity factor can be subjected to sensitivity analysis by fitting voltage curves at different rates.

The P2D model [S7,S8] was implemented in the open-source software MPET, [S9] the complete set of porous electrode equations is shown by Smith et. al.,[S9] we here summarize the tailored NMC811 model developed for this study. The particles were considered spherical and homogenous, following then the Fick's law of diffusion:

$$\frac{\mathrm{dc}}{\mathrm{dt}} = \nabla \cdot (\mathrm{D(c)} \nabla \mathrm{c})$$

Where c is the Li concentration normalized to the maximum Li concentration, and $\mathrm{D(c)}$ is a concentration-dependent diffusivity.

The reaction rate was modeled using the Butler-Volmer equation with a concentration-dependent exchange current density $\mathrm{k_0(c)}$:

$$\mathrm{j} = \mathrm{k_0(c)}\ \mathrm{c_{elyte}^{0.5}} \left(\mathrm{e}^{\frac{1\ e\eta}{2 k_B T}} - \mathrm{e}^{-\frac{1\ e\eta}{2 k_B T}} \right)$$

Where $\mathrm{c_{elyte}}$ is the electrolyte concentration at the particle-electrolyte interface, η is the reaction overpotential, $\mathrm{k_B}$ is the Boltzmann constant, T is the temperature, and e is the electron charge.

Both diffusivities and exchange current density are given in literature[S10] as relative values, since the absolute values can change depending on exposed surface area and particle shape. The model is then considering

$$D(c) = D_0 \, f_D(c)$$

And

$$k_0(c) = k_0^* \, f_{k_0}(c)$$

And fitting the experiments by changing the pre-factors. The values of the fitted parameters for the simulations are listed in **Table S7**.

The single discharge mean square error was calculated considering the square of the difference between the experimental and the simulated voltages, V_{exp} and V_{sim} in the collected N data points p. The total mean square error (MSE) for the various C-rates was calculated by summing them and multiplying for the square root of the Crae in order to increase the weight of the higher rates, which contain more physical information about the transport limitations.

$$MSE = \sum_{C_{rate}} \left\{ \left[\sum_{p} \frac{\left(V_{exp}(p) - V_{sim}(p) \right)^2}{N} \right] \sqrt{C_{rate}} \right\}$$

To further clarify the parameter estimation, a summary of the effect of varying tortuosity factor and diffusivity on the simulated voltage curves is reported in Figure S7.

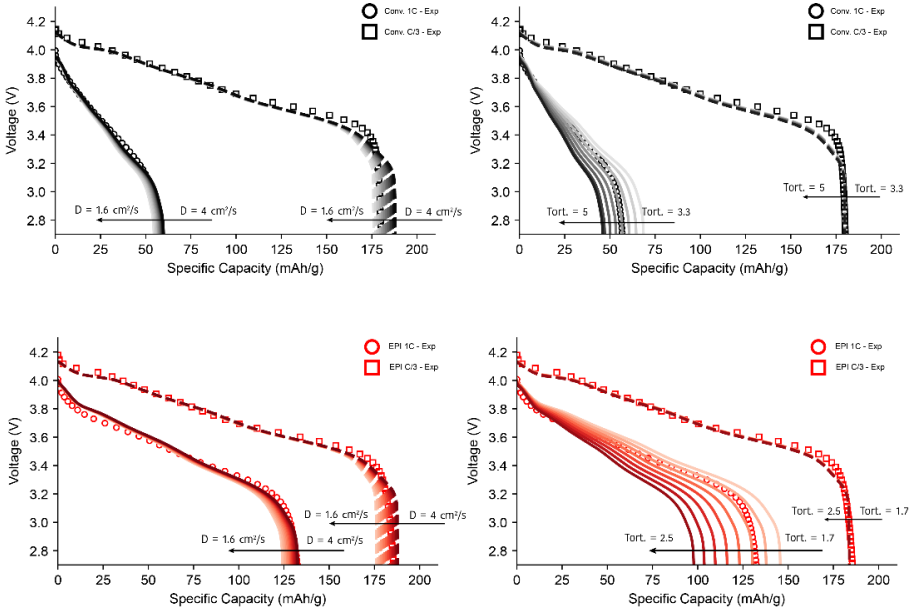

Figure S7. Comparison of simulated and experimental voltage curves at different tortuosity and diffusivities.

The simulated voltage curves show a non-linear effect of the variation of diffusivity and tortuosity factor. The change in diffusivity has a limited impact on the 1C curve since the main bottleneck for this rate is the electrolyte conductivity, which shows an increased sensitivity for the tortuosity factor. On the contrary, the diffusivity presents a greater effect on the utilized capacity of the C/3 discharge, since the transport overpotential for this rate is not the main driver of the capacity losses, while the low diffusivity at high Li concentrations contributes greatly to the final drop of the voltage curve.

Table S7. P2D Simulation parameters

Parameter name	Value	Unit of measure	Origin
Particle Diffusion coefficient function, $f_D(c)$	10^ $(-66631.56\,c^9 + 317224.13\,c^8 + - 647127.91\,c^7 + 740625.61\,c^6 + - 522889.49\,c^5 + 235652.79\,c^4 + - 67638.171\,c^3 + 11887.013\,c^2 + - 1155.894\,c + 37.601)$	-	[72]
Particle Diffusion coefficient pre-factor conventional, D_0	2.28 10^{-9}	$cm^2\ s^{-1}$	Fitted
Particle Diffusion coefficient pre-factor EPI, D_0	3.19 10^{-9}		Fitted
Exchange current density function, $f_{k_0}(c)$	$87.15\,c^5 - 445.05\,c^4 + 815.43\,c^3 - 669.95\,c^2 + 236.09\,c - 23.67$	-	[72]
Exchange current density pre-factor conventional, k_0^*	2.48	$A\ m^{-2}$	Fitted
Exchange current density pre-factor EPI, k_0^*	3.5	$A\ m^{-2}$	Fitted
OCV	$(-0.8090\,c + 4.4875 - 0.0428\,\tanh(18.5138\,(c - 0.5542)) \pm 17.7326\,\tanh(15.7890\,(c - 0.3117)) + 17.5842\,\tanh(15.9308\,(c - 0.3120)))$		[72]
Particle size	11.5	μm	Measured

Electrolyte conductivity	9.48 (for electrolyte concentration of 1 M)	mS/cm	[71]
Li metal\\Li^+ exchange current density	2.056	A m^{-2}	Fitted
Electronic conductivity	1	mS cm^{-1}	Measured
Number of simulated particles	20	-	
Starting stoichiometry	$Li_{0.26}Ni_{0.8}Mn_{0.1}Co_{0.1}O_2$	-	Measured
Cathode Thickness EPI	152	μm	Measured
Cathode Thickness Conv	147	μm	Measured
Cathode porosity EPI	0.316	-	Measured
Cathode porosity Conv	0.2976	-	Measured

LONG TERM CYCLING REPRODUCIBILITY

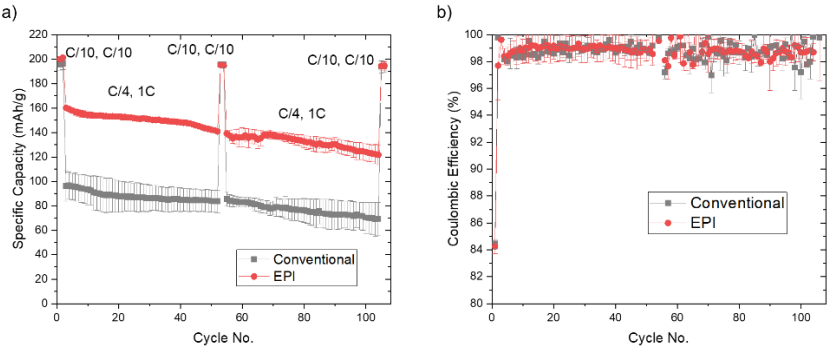

Figure S8. Long-term cycling reproducibility: a) Discharge capacity reproducibility and b) Coulombic efficiency reproducibility for Li/NMC811 half cells with 35 -37.5 mg/cm² (7-7.5 mAh/cm²) active mass loading and 1.4 M HE electrolyte cycled at 20 °C. Error bars indicate standard deviation.

NOTE S9 ELECTRODE ENERGY DENSITY CALCULATION

The electrode energy density calculations are performed using the values listed in **Table S8**.

Table S8. Electrode parameters used for energy density calculations

Name	Unit	Value
Key design parameters:		
Areal capacity	mAh/cm^2	7
Porosity	%	30
Body fraction	%	70
Active material fraction in body	%	92
Densities:		
Density of cathode body	g/cm^3	3.46
Density of anode body	g/cm^3	0.543
Density of electrolyte	g/cm^3	1.22
Density of current collector	g/cm^3	2.7 (Al), 8.96 (Cu)
Electrochemical Performance parameters:		

Average discharge potential	V	3.8
Charge density of AM	mAh/g	208 (NMC811) 3862 (Li)
Electrolyte conductivity	S/cm	0.01
Thicknesses		
Separator	µm	25
Current collector	µm	10
Cathode (calculated)	µm	151
Anode (calculated)	µm	33.4 (zero excess)
Cell (calculated)	µm	219.4
Projected cell architecture and performance (calculated)		
Volumetric fraction cathode	%	69
Volumetric fraction anode	%	15
Net vol. charge density	mAh/cm^3	319
Volumetric energy density	Wh/L	1210
Density of battery cell	g/cm^3	2.41
Gravimetric energy density	Wh/kg	503

REFERENCES:

[S1] C.M. Hansen, Hansen Solubility Parameters: A User's Handbook, Second Edition, 2nd ed., CRC Press, Boca Raton, 2007. https://doi.org/10.1201/9781420006834.

[S2] A. Bottino, G. Capannelli, S. Munari, A. Turturro, Solubility parameters of poly(vinylidene fluoride), J. Polym. Sci. Part B Polym. Phys. 26 (1988) 785–794. https://doi.org/10.1002/polb.1988.090260405.

[S3] R. Jung, M. Metzger, F. Maglia, C. Stinner, H.A. Gasteiger, Oxygen Release and Its Effect on the Cycling Stability of LiNixMnyCozO2 (NMC) Cathode Materials for Li-Ion Batteries, J. Electrochem. Soc. 164 (2017) A1361. https://doi.org/10.1149/2.0021707jes.

[S4] R.J. Good, R.Sh. Mikhail, The contact angle in mercury intrusion porosimetry, Powder Technol. 29 (1981) 53–62. https://doi.org/10.1016/0032-5910(81)85004-8.

[S5] Standard Test Method for Peel Resistance of Adhesives (T-Peel Test), (n.d.). https://www.astm.org/d1876-08r15e01.html (accessed August 10, 2023).

[S6] J. Landesfeind, J. Hattendorff, A. Ehrl, W.A. Wall, H.A. Gasteiger, Tortuosity Determination of Battery Electrodes and Separators by Impedance Spectroscopy, J. Electrochem. Soc. 163 (2016) A1373. https://doi.org/10.1149/2.1141607jes.

[S7] T.F. Fuller, M. Doyle, J. Newman, Simulation and Optimization of the Dual Lithium Ion Insertion Cell, J. Electrochem. Soc. 141 (1994) 1–10. https://doi.org/10.1149/1.2054684.

[S8] M. Doyle, T.F. Fuller, J. Newman, Modeling of Galvanostatic Charge and Discharge of the Lithium/Polymer/Insertion Cell, J. Electrochem. Soc. 140 (1993) 1526. https://doi.org/10.1149/1.2221597.

[S9] R.B. Smith, M.Z. Bazant, Multiphase Porous Electrode Theory, J. Electrochem. Soc. 164 (2017) E3291. https://doi.org/10.1149/2.0171711jes.

[S10] I. McClelland, S.G. Booth, N.N. Anthonisamy, L.A. Middlemiss, G.E. Pérez, E.J. Cussen, P.J. Baker, S.A. Cussen, Direct Observation of Dynamic Lithium Diffusion Behavior in Nickel-Rich, $LiNi_{0.8}Mn_{0.1}Co_{0.1}O_2$ (NMC811) Cathodes Using *Operando* Muon Spectroscopy, Chem. Mater. 35 (2023) 4149–4158. https://doi.org/10.1021/acs.chemmater.2c03834.

3.2 Lithiation distribution in porous cathodes, a Neutron Depth Profiling investigation.

Introduction

The lithiation rate distribution in cathodes is investigated using Neutron Depth Profiling (NDP). The technique uses the annihilation of neutrons with 6-lithium isotope to yield tritium atoms (an elaborate explanation and examples can be found on page 242 and 259 respectively). The location of the lithium atoms in the cathode indicate where the cathode active material is (de)lithiated during operation as the location of lithium isotopes is directly shown by this technique with LFP electrodes.[1] This technique therefor potentially shows the interplay between resistances originating from the electron conducting network and the ionic network. The charge rate distribution, as described by Chen et. al.[2] dictate that should the electronic network have low conductivity the lithiation occurs at the current collector side, the ionic network have low conductivity the lithiation occurs at the separator side. Should both be similarly conducting networks the current is distributed equally. Should a bad electronic network provide electrons at high resistances, the reaction is deemed to happen at the side of the current collector, the location from which the electrons are supplied and the NDP tritium particle detector acquires signal. Vice versa, the inflow of ions may be hindered by poor wetting and/or limited influx. This causes the lithiation reaction to occur at the separator side from which the ions originate.

Methods

Materials and methods

Electrodes were made as described by Karanth and Weijers et. al [3]. The slurry was casted using a doctor blade height of 200 µm. Three electrodes were tested with approximately the same charge density, NMC811 electrodes processed using ethanol phase inversion, a conventionally dried NMC811 electrode and a LNMO electrode with similar loading. They were calendared to the same porosity of 33% and subsequently punched to 34 x 34 mm squares including a bare aluminium tab for welding. The counter electrode consists of a 36 x 36 mm square graphite electrode with a nickel tab weld, with N/P of 1.2. A 40 x 40 mm Celgard 2400 separator and glass fibre separator was used. The electrodes were heat glued in a pouch at the tab side. In the aluminium current collector side of the pouch a circular hole was punched to enable tritium to exit, similar to the method by Verhallen et. al.[4] The current collector was heat glued

around this hole to prevent electrolyte to leak out. The heat glueing was performed for a limited period to prevent melting of the cathode binder material. Cells were dried in a vacuum oven at 60 °C overnight and filled with 1 M $LiPF_6$ 1:1 EC:EMC + 2% VC in a glove box. After a 24 hour rest period cells were formed by cycling the cells twice with 0.1C current density after which the pouch was degassed. After formation the cells were subjected to rate cycling in the NDP setup at 0.1C, 0.2C, 0.5C and 1C. After every charge and discharge a CV step follows to arrive at comparable degrees of lithiation in the next cycle. Higher discharge rates yield potentially steeper lithium concentration gradients in the electrode and therefor the 1C lithiation (discharge) cycle is compared.

The NDP measurements have resulted in three representative data sets compared to regular cathode (dis)charge performance in coin cells. On the battery side, during operation gas buildup, electrolyte leakage from the glue interfaces and subsequent failure were the most dominating mode of failure. During the period of my PhD a new heat glueing procedure and a new sample holder was developed which may overcome these modes of error. This subchapter shows that NDP can show rate distributions, without going into a full analysis of stopping powers, but by comparing the sample with only itself during various (dis)charge routines. The datasets to follow up on are mentioned in Supporting information Table 1.

Stopping power calculations

First an ab initio calculation is performed to assess to what depth the profiling shows signal. Stopping power calculations are performed on the basis of 92/4/4 wt% $LiNi_{0.8}Mn_{0.1}Co_{0.1}O_2$/PVDF/C with a density of 3.5 g/mL and 33% porosity. The electrolyte, 1M $LiPF_6$ in EC/EMC with a density of 1.3 g/mL is used. The mass density is calculated and subsequently the mass fractions are derived per volume. Finally the molar weights are taken to arrive at the stoichiometric distribution necessary to calculate the stopping powers from electron densities, using an ion stopping power calculation tool called SRIM.[5] From the ion stopping power one can estimate the residual energy of the tritium ion after traversing through matter by integrating the curve from its original ion energy till the energy measured at the NDP PIPS detector.

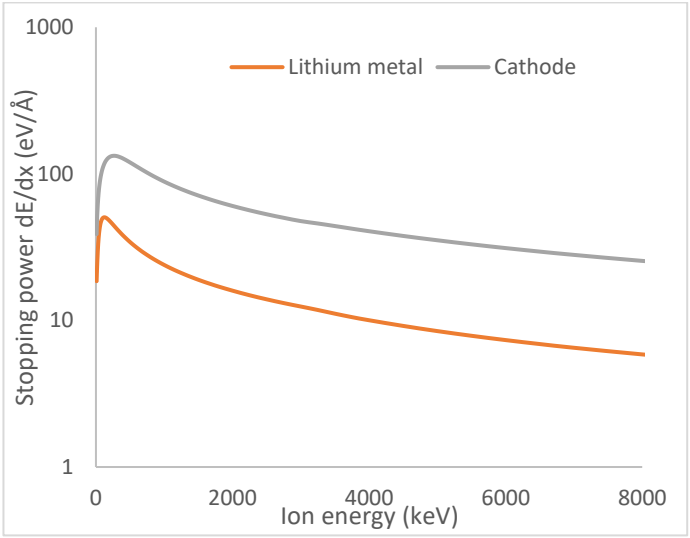

Figure 1 Stopping power of cathode material filled with electrolyte, compared to lithium metal stopping powers.

Compared to lithium the stopping power is significantly higher, due to higher mass numbers of the individual atoms (see page 259). The depth of the cathode which may be profiled is estimated to be 22 µm, as the initial tritium ion energy amounts to 2727 keV and at a certain threshold depth the aluminium current collector foil stops low energetic tritium completely.

Results

The NMC electrode containing 1.7 +/- 0.1 mAh/cm^2 yields a thickness of 40 micron, allowing 55% of the cathode lithiation process to be observed during discharging and delithiation during charging. A discrepancy between the observed lithiation of the active material would be expected during fast discharging, as the reaction rate at the active material surface may be higher than the allowable influx of ions in the porous network. As the observed depth amounts to 55% of the total one would expect a change of the slope of tritium counts as function of time. An increased initial slope indicates faster initial lithiation at the current collector side which correlates to a worse electronic conductivity compared to the ionic conductivity. At high rates, a deviation of the slope may occur near the limiting potential as the allowable influx cannot keep up the reaction rate at the current collector.

3.2 Lithiation distribution in porous cathodes, a Neutron Depth Profiling investigation.

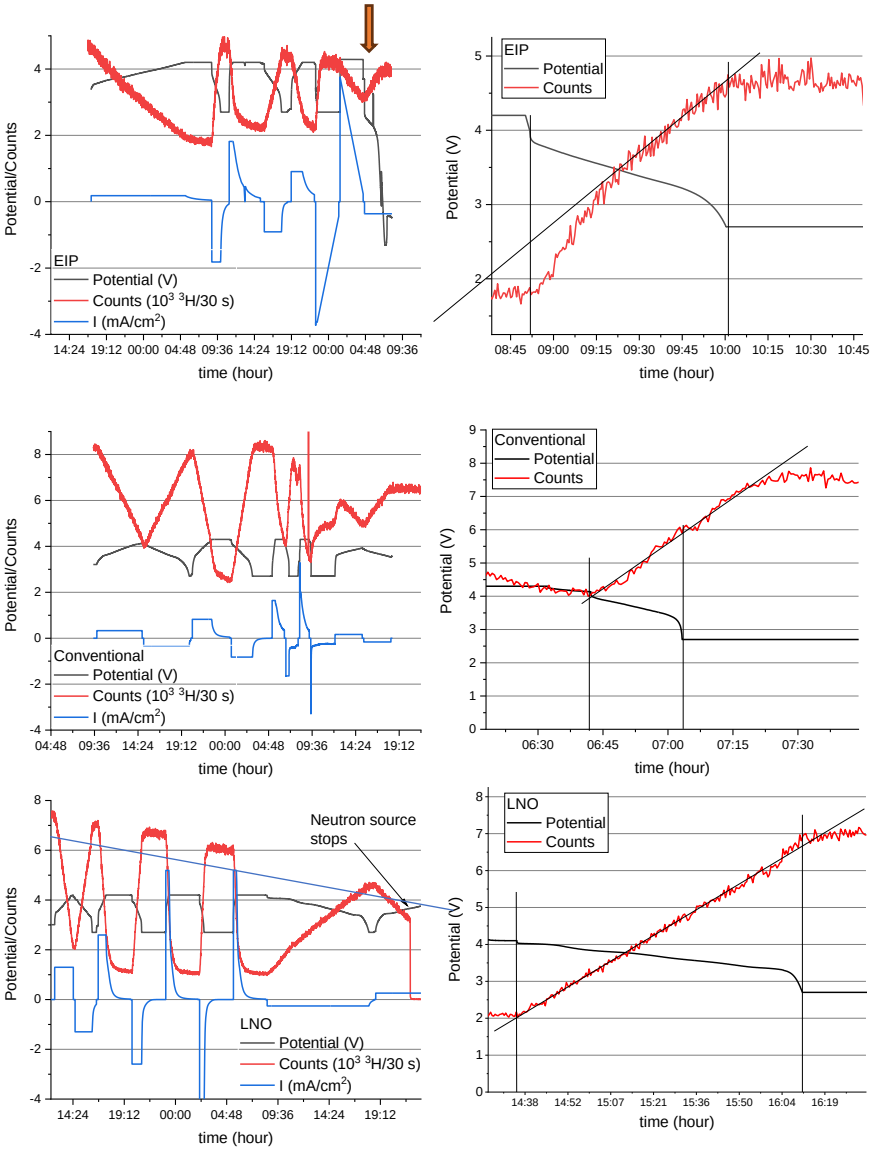

Figure 2 Potential trace and total detector count as function of time during an operando neutron depth profiling experiment. From top to bottom: NMC811 EIP, NMC811 Conventional and LNMO Conventional cathodes were lithiated during a discharge cycle at approximately 1C (right). The complete potential trace shows the reversibility of lithiation at the current collector side over time (left).

The complete potential trace, combined with the detector count rate shows the reversibility of lithiation during the onset of the test. For EIP (Figure 2, top left) the depth of delithiation initially achieved at 0.1C is not achieved during the subsequent CC/CV steps. During the onset of the test at 3C lithiation rate the potential limit causes an immediate switch to constant voltage step. During the constant current step the delithiation occurs only to a certain extent and compared to a previous 1C delithiation step at lower rates (orange arrow, Figure 2), indicating an internal short. The conventional cell fails in a similar manner during the 3C lithiation (Figure 2, middle). A second observation is that during the cycling net lithiation of LNMO is lower at higher discharge currents (Figure 2, bottom, red). The constant voltage step does not equalize this effect, while the net capacity transferred is the same for each step (29.8 +/- 0.4 mAh) after each cycle. This effect may be caused by uneven lithiation of the active material, with higher concentrations of lithium near the separator compared to the observed current collector side. More probable is an unknown effect causing a linear decrease in the count rate, because also during the rest periods a slight decrease in count rate is observed.

The results of a 1C discharge cycle is shown in Figure 2 on the right. Here for the EIP type NMC cathode a steep onset of count-rate, and therefor lithiation at the current collector, is observed. The slope however bends as the discharge continues, highlighting an unequal lithiation distribution along the depth of the electrode with higher initial reaction rates at the current collector. For the conventional cell this is not observed. Here the lithiation count gradually increases, highlighting a continuous influx of lithium at the current collector side. However, the total resistance of the electrode is high which gives rise to a large overpotential and subsequently during the CV step the lithiation rate gradually progresses in the same linear fashion. The LNO cathode shows best performance, a completely linear progression of tritium counts during lithiation indicating a completely uniform charge distribution. The estimated charge capacity however was slightly off and the C-rate therefor as well 0.66C. However, during 2C charging a similar trend was observed (Figure 3).

3.2 Lithiation distribution in porous cathodes, a Neutron Depth Profiling investigation.

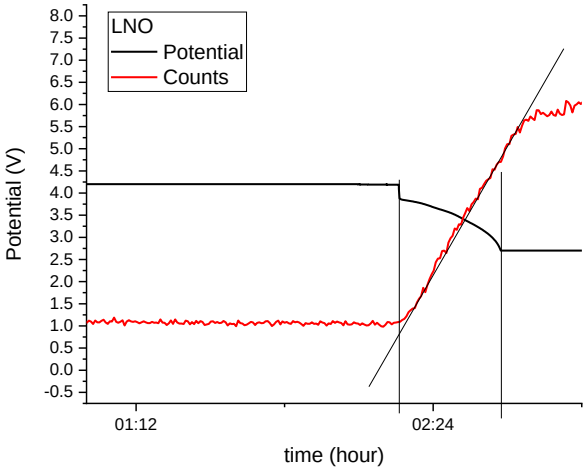

Figure 3 LNMO lithiation during discharge at 2C discharge rate.

DISCUSSION

The NDP experiments on cathodes show that is possible to provide insight in the lithiation reaction rate distribution in the porous network. There is a clear trend between potential, tritium count and outside behavior (like shorting). Also quite convincingly the datasets show that the delithiation rate does change in the observable range of the NDP. From the three datasets shown above one however cannot make a comparison between the cathode chemistries or manufacturing methods since the battery cell assembly procedure shows too much variability to ensure that the battery function is e.g. at least near the theoretical capacity and fully reversible (or comparable to other types of cells). Advisable is to only vary the side of the cell that is studied and use a commercial counter electrode to enhance consistency between tests. Also heat glueing should be iterated a few times before the actual sample is glued to ensure a good leak-tight weld. Degassing the pouch after formation is of utmost importance. The side of the rectangular pouch can be used to open up the pouch en reweld under vacuum. Finally, leakage in the end was the main reason for an experiment to fail halfway. Therefor to change the glued sample window method to a more robust method is advisable to prevent precious time loss on the NDP beamline.

REFERENCES

(1) Zhang, X.; Verhallen, T. W.; Labohm, F.; Wagemaker, M. Direct Observation of Li-Ion Transport in Electrodes under Nonequilibrium Conditions Using Neutron Depth Profiling. *Adv. Energy Mater.* **2015**, *5* (15), 1500498. https://doi.org/10.1002/aenm.201500498.

(2) Chen, Z.; Danilov, D. L.; Eichel, R.-A.; Notten, P. H. L. On the Reaction Rate Distribution in Porous Electrodes. *Electrochemistry Communications* **2020**, *121*, 106865. https://doi.org/10.1016/j.elecom.2020.106865.

(3) Karanth, P.; Weijers, M.; Ombrini, P.; Ripepi, D.; Ooms, F.; Mulder, F. M. A Phase Inversion Strategy for Low-Tortuosity and Ultrahigh-Mass-Loading Nickel-Rich Layered Oxide Electrodes. *Cell Reports Physical Science* **2024**, 101972. https://doi.org/10.1016/j.xcrp.2024.101972.

(4) Verhallen, T. W. *Neutron Depth Profiling: Following the Lithium Distribution in Rechargeable Batteries*; 2019.

(5) Ziegler, J. F.; Biersack, J. P. The Stopping and Range of Ions in Matter. In *Treatise on Heavy-Ion Science*; Bromley, D. A., Ed.; Springer US: Boston, MA, 1985; pp 93–129. https://doi.org/10.1007/978-1-4615-8103-1_3.

SUPPORTING INFORMATION

Table 1 Data sets of cathode experiments

Cycling data (Biologic)	NDP data set
MJW-20230913-LNOGr_3mAhcm2_cycling2_2_C01	MJW_230924_LNOGr_Cycling2
MJW-20230509-200Conv400Graph_Rate_Determination1_C01	MJW_20230509_200ConvGraph_Rate
MJW-20230904-200EIPCF-DRONE_EV_try1continued_C01	MJW_20230905_200EIPCF-DRONE_EV2
MJW-20230904-200EIPCF-DRONE_EV_try1continued22_C01	MJW_20230905_200EIPCF-DRONE_EV2

3.2 Lithiation distribution in porous cathodes, a Neutron Depth Profiling investigation.

4. Elucidation of Enhanced Lithium Conductivity in Nanoporous Ionogel Using Solid State NMR

The content of this chapter has been published in Advanced Materials Interfaces in 2023, Volume 10, 2201646 in which Mark Weijers is first author.

https://doi.org/10.1002/admi.202201646

Elucidation of Enhanced Lithium Conductivity in Nanoporous Ionogel Using Solid State NMR

Abstract

Nanostructured solid composite electrolyte or nano-SCE, which is composed of an ionic liquid, nanoporous silica, and residuals of immobilized precursor components, shows promising synergistic properties. The ionic conductivity of nano-SCE is in the range of 2–5 mS cm^{-1}, which exceeds the bulk ionic liquid conductivity at ambient temperature, while maintaining characteristics of a solid electrolyte such as having no leakage issues as the ionic liquid is confined, and lower flammability compared to conventional liquid electrolytes. In this study, the underlying mechanism of enhanced conductivity is investigated by using magic angle spinning NMR and NMR relaxometry analysis. Water, one of the volatile precursor molecules has shown to play a key role in the final conductivity and stability at the solid-electrolyte interface, as it enhances the temperature range in which the ionic liquid remains mobile. In line with previous studies, water with lowered mobility is found in the silicon matrix. The activation energies of lithium ion transfer probed by NMR relaxometry, however, do not change as function of water content. The increase in bulk mobility of lithium ions under ambient conditions compared to water-less nano-SCE is found to be the origin of the altered conductivity of this material.

Introduction

Solid composite electrolytes consisting of a porous polymer or silicon solid matrix, combined with an ionic liquid electrolyte (ILE) show promising characteristics in EV battery applications. By combining a morphology structuring compound with an ionic liquid, conductivities nearing conventional liquid electrolytes are achieved while non-flammability[1], bendability and strength characteristics of a solid electrolyte are maintained [2].

Hybrid electrolytes may have synergystic properties enhancing mechanical strenght, ionic conductivity and/or mechanical or thermal stability[3,4]. The of sol-gel processed ionogels form composites in situ, which is a different approach than physical mixture composites in e.g. [3–7]. Recently Sagara *et al.* found synergistic properties of the lithium-bis((fluorosulfonyl)imide/1-ethyl-3-methylimidazolium bis(fluorosulfonyl)imide (Li-FSI/EMI-FSI) and lithium-bis((trifluoromethylsulfonyl)imide 1-butyl-1-methylpyrrolidinium bis(trifluoromethylsulfonyl)imide (Li-TFSI/BMP-TFSI) ILEs combined with a silicon network in which the obtained gel showed better lithium ion conductivities than the

bulk ionic liquid.[8,9] In this work the ionogel shows similar rate performance compared to conventional liquid electrolyte $LiPF_6$ in EC:DMC in Li-LFP battery cells. Chen et al.[10] proposed that the origin of this behavior *i.e.* increase in lithium conductivity in nano-SCE is facilitated by the de-solvation of the lithium ions. In this work lithium-bis((trifluoromethyl)sulfonyl)imide / 1-ethyl-3-methylimidazolium bis(trifluoromethylsulfonyl)imide (Li-TFSI/EMI-TFSI) ILE is used (**Figure 1**). Previously it has been shown that porous silica networks show several mechanisms which lead to a change in the diffusivity of the various mobile species. Guyomard-Lack *et al.* show that lithium diffusivity is an interplay between surface and bulk associated lithium concentrations.[11] The two environments are further elucidated by Jayakody *et al.* who show two diffusion regimes by varying pore sizes, restrictive diffusion at the surface and long ranged diffusion in the bulk.[12] For nano-SCE comprising of SiO_2, ILE and water, the silanol hydroxyl bonds are thought to be (partially) covered by water molecules.[10] In this structure, the TFSI anion hydrogen bonds through their O=S=O group with these immobilized water molecules. The EMI cations would show increased affinity compared to lithium cations with the formed TFSI layer through hydrogen bonding. As a result, with the proper number of water molecules, an immobile 'glacial' layer is formed on the silicon backbone and charge layers emerge of which the layer next to water molecules consists predominantly of hydrogen bond making EMI cations. The charge layers form a dipole of which the TFSI associated to lithium is drawn, which leads to a lower net activation energy of lithium mobility. As this type of diffusion is dependent on the presence of a polymer backbone, this is called surface associated diffusion.

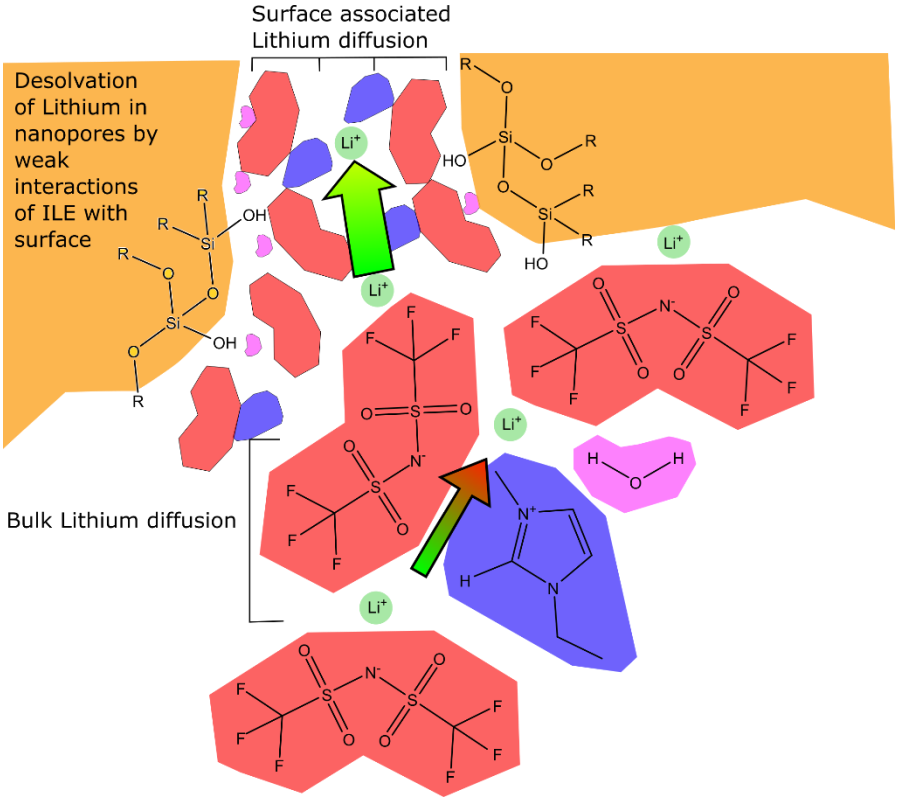

Figure 1. Interplay with silicon backbone surface and ILE. TFSI and EMI are thought to have preferred orientations towards the surface, facilitated with water. This causes the lithium ions to desolvate and become highly mobile.

In ILE polymer hybrid systems, both surface associated and bulk lithium diffusion can be expected as pore geometry and sizes vary in the network. Jayakody et al. describe a method to investigate surface and bulk associated lithium ions.[12] A necessary characteristic for the surface lithium ions is that its residence lifetime is longer than the translational correlation time in the bulk to enable distinguishing the two environments. Net conductivity can be expected to drop in polymer systems as steric effects of the polymer network create more tortuous diffusion pathways of the mobile species compared to bulk liquids. Surface associated diffusivity can however play a role in altering the mobility of specific molecular species, specifically Li^+.

In this study, NMR techniques are used to elucidate the structure/ion mobility relation of the nano-SCE components. The conductivity of lithium ions measured by electrochemical impedance spectroscopy (EIS) is compared to that obtained with static relaxometry using nano-SCE samples containing varying amounts of water. In this way the dependence of the concentration of the volatile components to the local and bulk energetics of various diffusional processes could be elucidated. A comprehensive method and complete derivation of the self-diffusion constant from relaxometry data is described in detail by *Uitz et al.*[13] and *McDowell et al.*[14] respectively, using a model introduced by Bloembergen, Purcell and Pound.[15] Considerations and equations for relaxometry fitting are included in the supporting information (SI).

METHODS

SYNTHESIS OF NANO-SCE

Nano-SCE is made in line with the synthesis method described by Chen et al.[10] except for the last drying steps, in which shorter and longer vacuum times are used. 0.33:1 mol mol^{-1} ratio Li-TFSI:EMI-TFSI (Solvionic, IL) is prepared in a glove box. Tetraethyl orthosilicate (>99%, Sigma Aldrich), 1-methoxy-2-propanol (99.5%, Sigma Aldrich), Deionized water or D_2O (99.9%, Sigma Aldrich) and IL are mixed in a ratio of 14:25:14:47 m/m%. After shaking the sample vigorously the liquid is poured over target material (porous cathode, current collector) or solidified in a glass vial. The mixture is solidified using >7 day room temperature (RT) polymerization at 44% rel. humidity. The gel is subsequently dried for 96 hours at 800 mBarA pressure. The structure is further dried at 200 mBarA for 72 hours. The dry nano-SCE sample without volatiles is obtained by drying the sample subsequently in 0.3 mBarA vacuum at 60 ^oC overnight. Semi-dry nano-SCE was obtained by sampling the container after 3.5 hours during HVT. In the D_2O-nano-SCE samples instead of deionized water, deuterated water was added in the initial precursor solution.

ELECTROCHEMICAL TESTING

EIS and galvanostatic tests were conducted using a vacuum clamp cell setup. A circular gel-sample holder was made by punching a ring with an inner diameter of 14 mm disc from a 0.80 mm thick sample cap. The gel sample was pressed in the ring shape, resulting in a 800 micron thick electrolyte disk. Lithium discs of 15.4 mm diameter were

used as electrodes. Electrochemical impedance spectroscopy was conducted using an Autolab PGSTAT302N potentiostat and a temperature programmable oven. Fitting of EIS data is performed using Zview. Cycling was performed using a MACCOR-4000 multichannel battery cell cycler in a climate controlled room.

NMR SPECTROSCOPY

For NMR testing a Bruker Ascend 500 (B_0 =11. 7 T) magnet equipped with a NEO console was used. The sample was filled in in an air tight 4 mm rotor zirconia rotor with a vespel cap and inserted in a 4 mm triple resonance MAS NMR probe (Bruker). For ^{7}Li (194.37 MHz), $\pi/2$ pulse lengths of 3.48-4.50 µs (143.88 W) corresponding to an RF field strengths of 71.8-55.5 kHz were utilized. T_1's and $T_{1\rho}$'s measurements were performed under static conditions in the temperature range of -70 to 105 ^{o}C. Low temperature measurements were conducted by forcing the VT gas flow through liquid nitrogen as coolant and subsequent heating to the appropriate temperature. T_1 measurements were performed using the saturation recovery experiment, while $T_{1\rho}$ measurements were performed at spin lock fields of 12.5 and 30 kHz in the temperature range of -70 to 105 ^{o}C. The recycle delay was adjusted each time based on T_1 to ensure complete relaxation after every measurement. Relaxation measurement fitting was performed using the Dynamics Center module from Bruker. Temperature dependent relaxation rate fitting was conducted using the OriginPro 2019 software after deconvolution of the spectra. To evaluate the chemical composition of the various environments in which lithium ions are present in the nano-SCE, MAS NMR measurements were performed on ^{1}H (ω_0=500.130 MHz, $\pi/2_1$=3.15 µs, 170 W, ω_1=79.4 kHz), ^{2}D (ω_0=76.773 MHz, $\pi/2$=4.87 µs, 350 W, ω_1=51.4 kHz) and ^{7}Li (ω_0=194.370 MHz, $\pi/2$=3.48 µs, 143.88 W, ω_1=71.8 kHz). All MAS NMR measurements were performed at a 1.5 kHz spinning rate except NOESY performed at 5 kHz. Peak deconvolution was performed using the MestreNova software.

SCANNING ELECTRON MICROSCOPY (SEM)

SEM measurements were carried out using a JEOL6010 on additionally dried samples in which also liquid ionic liquid traces that were not bound in the nano-SCE were removed to prevent SEM contamination. Samples containing ionic liquid were soaked in a surplus of acetone and incubated several days to allow complete mixing and

removal of any free ionic liquid not bound to the nano-SCE. The majority of the acetone was removed by careful pouring. The dilution, mixing and pouring off was repeated three times. The resulting material was subsequently dried overnight in a vacuum oven at 60 ^{o}C resulting in sand-like particles which were directly measured.

RESULTS

Nano-SCE is prepared by a one pot synthesis of liquid precursors. This may allow its penetration in porous materials like battery electrodes before polymerization.[8] During synthesis, a typical solvent supported, slightly alkaline, sol-gel formation process is taking place. Of the various possible polymerization rate coefficients for tetra-ethyl-orthosilicate polymerization intermediates, $Si(OCH3CH2OH)_X(OH)_Y(OSi)_Z$, to polymerize only three rates are determining in acid supported polymerization.[16] In slightly alkaline solutions however, after hydrolysis, the deprotonated silanol group is able to attack more acidic silanol groups which leads to increased branching compared to the acidic polymerization process.[17,18] The result is a flexible finely branched colloidal structured gel which can be dried to a more condensed sol-gel by removing the solvent 1-methoxy-2-propanol (PGME) and water using conventional drying.[19]

The acidity of the solution in this initial process is very sensitive. Modification of alkaline conditions by addition of lithium hydroxide to pH 11 did not result in successful gel formation, showing the delicate conditions in which polymerization takes place. In the confined structure, the majority of unbranched silane sites which are unavailable for condensation are hydrolyzed if the polymerization product is sufficiently diluted during the polymerization step.

After gel formation the volatile precursors are removed slowly to maintain structural integrity of the material. This process is monitored by weighing the sample after each drying step as shown in **Figure S20** for reference. After the initial polymerization process the extent of drying is 17%. Subsequent 800 mBarA and 200 mBarA drying steps yield 49% and 69% extent of drying. Further high vacuum treatments (HVT) at 0.3 mBarA and 60 ^{o}C yields 98%-100% extent of drying overnight, i.e. essentially complete removal of ethanol, water and PGME. Samples called nano-SCE were prepared without the HVT treatment. After 3.5 hours HVT a sample was taken called Semi-dry nano-SCE (Table 2 SI 13 for an overview).

The obtained nano-SCE gel has interesting mechanical characteristics. The sample is slightly bendable but it easily fractures upon puncturing with e.g. a spatula. Upon

fracturing, typically complete breakage of the material that is parallel with the spatula edge is observed. The parts do easily adhere together, but the material does not cure upon re-contacting. This indicates that the polymerization process has finished and only weak molecular interactions cause grain/grain adhesion, together with ionic liquid surface tension. The material is leakage free in normal circumstances. Centrifugation at 6000 rcf does not show phase separation of ionic liquid from the nano-SCE and the material shows stable performance after one year of storage in a glove box. The ionic liquid can however separate out of the nano-SCE after compressing as a sponge-like feature, which leads to formation of droplets observed after removing the compressed particles. After washing the gel with acetone extensively and subsequent drying in a vacuum oven, sand-like particles are obtained which show smooth fracturing planes as can be seen in the SEM image given in **Figure 2A**. Its surface structure shown in Figure 2B is rough, indicating that fracturing doesn't expose a clean facet.

A verification of the electrochemical characteristics is provided to ensure a similar material is made compared to other nano-SCE's reported previously.[8] Conductivities of the three SCE were measured using EIS in symmetric Li | SCE | Li cells. The resistance at the touchdown point at high frequencies of the Nyquist plot are taken as the electrolyte resistance at room temperature.[20] Conductivities are subsequently calculated using the pellet geometry detailed in the methods section. After EIS, samples were subjected to potentiostatic polarization of 80 mV for one hour and the

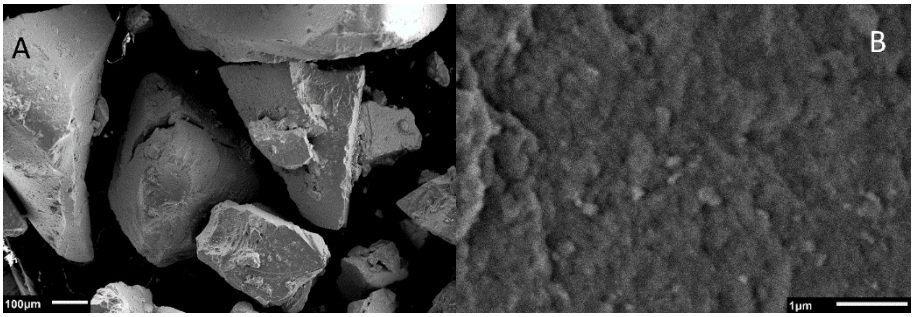

Figure 2 A) and B) SEM images of acetone-washed nano-SCE. After material fracturing, quite smooth surfaces are observed with small debris attached on the surfaces (left). A higher magnification shows roughness in the sub-micron scale (right).

EIS spectrum was re-measured. Obtained values before and after a few repeats of the polarization process are shown in **Figure 3A** (Some Nyquist plots are shown in the SI **Figure S8, Figure S9, Figure S10**).

Nano-SCE shows a high conductivity compared to the bulk ionic liquid, which is in line with the findings of Sagara *et al.*[10] However after potentiostatic polarization both a decrease in conductivity and a large increase in charge transfer resistance is measured, indicating the change of the bulk conductivity is in concert with SEI formation on the lithium surface (SI **Figure S8**). Nano-SCE was repeatedly subjected to galvanostatic polarization and the bulk conductivity subsequently measured kept decreasing, indicating that the presence of the initial volatile components in nano-SCE cause continuing side reactions.

The contribution of the volatile solvents to the stability was further tested by drying nano-SCE at 60 ^{o}C at 0.3 mBarA vacuum for an extended period removing the volatile components, yielding dry-nano-SCE. Dry-nano-SCE shows a reduced conductivity compared to the nano-SCE but unlike nano-SCE maintains the same conductivity before and after polarization testing. Remarkably, for dry-nano-SCE, the contact resistance decreased after 12 hours of extended polarization (SI **Figure S9**). The conductivity of dry nano-SCE is in line with the conductivities found by Sagara et al.[8] and remains relatively high compared to other polymer electrolytes which have conductivity ranges of $10^{-2} – 10^{0}$ mS cm^{-1}.[21]

The material stability is further tested with a galvanostatic cycling test. Symmetric Li-Li cells with ionic liquid EMI-TFSI and nano-SCE varieties are subjected to galvanostatic cycling for 70 days at 0.1 mA cm^{-2} (**Figure 3B**). Nano-SCE immediately shows high overpotentials indicating a high interfacial resistance. Semi-dry nano-SCE did not show stable cycling behavior (SI, **Figure S7**). In case of dry nano-SCE, the overpotential decreases from 80 mV to 60 mV over the first 20 days, indicating an improved charge transfer, probably originating from improved contact between the lithium metal and dry nano-SCE interface. The dry-nano-SCE shows stable potential profiles for the complete duration of cycling.

Electrochemically the dry-nano-SCE behaves like an electrolyte with limited charge carrier density. Upon increasing the current to 1 mA cm^{-2}, the voltage profile shows continuous polarization increase as seen from **Figure 3C**. Initially the potential seems to reach a plateau similar to lower currents, but then the potential starts to increase

rapidly over time indicating concentration depletion. Such polarization buildup requires lithium and counter ions to move and therefore one may view it as bulk liquid diffusion that is the dominant mode of diffusion for dry-nano-SCE.

The role of volatiles in the bulk conductance becomes apparent from temperature dependent EIS measurements. The bulk activation energy of lithium conductivity is determined using the temperature dependent impedance of the high frequency region in a symmetric cell. Semi-dry-nano-SCE was tested for this, as it contains some volatiles and shows enhanced conductivity of the material compared to dry-nano-SCE. First the sample is cooled down to -40 ^{o}C, then it is heated up to 70 ^{o}C and finally the sample is cooled to ambient temperatures. A glass fibre immersed with 0.33:1 mol:mol Li-TFSI:EMI-TFSI (ILE) is also tested in the same setup to compare activation energies. The static resistance value originating from the intercept in the Nyquist plot are converted to conductivities using Ohm's law and plotted in **Figure 3D**. A shallow slope is observed for the semi-dry nano-SCE above 30 ^{o}C corresponding to an activation energy of 51.5 meV (green, Figure 3D). Both the conductivity and temperature dependence are slightly lower than the ILE in this temperature region (red, Figure 3D, 179.5 meV). A change of slope can be observed in the temperature range between -26 and +30 ^{o}C. In here a semi-linear regime is observed which gives an estimated activation energy of 0.45 eV (blue, **Figure 3D**). At -40 ^{o}C a conductivity value is found which does not follow this trend (grey, **Figure 3D**). After heating to 70 ^{o}C however conductivities change in the low temperature region. A steeper slope corresponding to lower conductivities a higher activation energy of 0.74 eV is observed. This indicates that the volatile components are mobilized during heating to higher temperatures which allows them to migrate and react at the lithium interface during the experiment. The trend of the linear regime after heating extrapolates well to the -40 ^{o}C conductivity measured before heating, indicating that at this temperature, the volatiles did not play a significant role in the bulk conductivity in the first place. The presence of volatiles thus effectively lowers the bulk activation energy. This phenomenon is further explored with NMR to determine whether the lithium ion transfer mechanism itself changes, or if only the bulk mobility of all species are the cause of the overall lower activation energy.

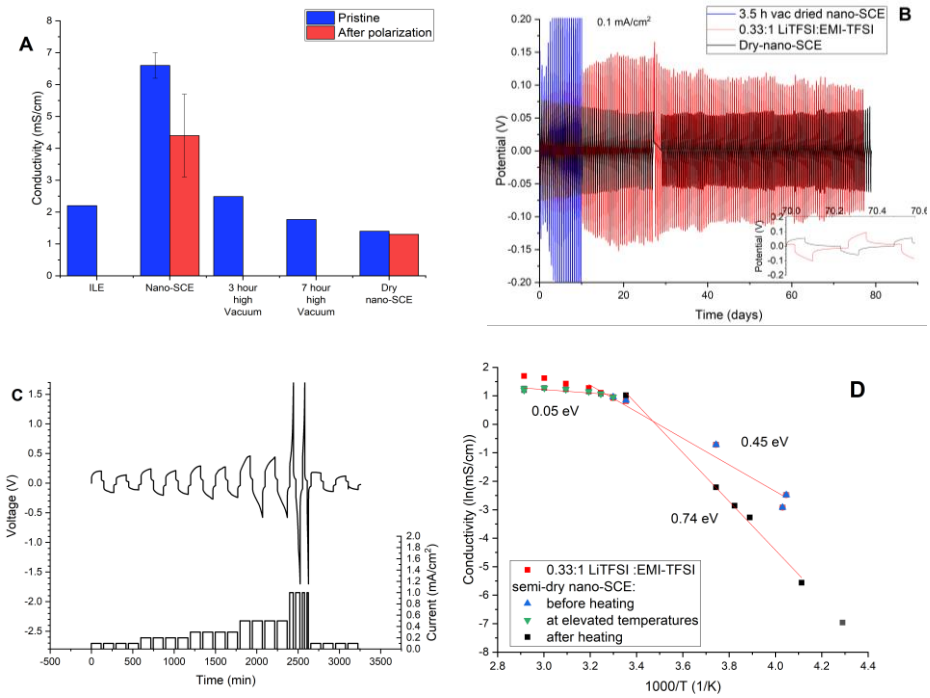

Figure 3. A) EIS derived conductivities of 0.33:1 LiTFSI:EMI-TFSI ILE and nano-SCE materials before and after polarization studies. The nano-SCE conductivity drops upon extended duration of drying. The error bars indicate different results by varying the potential window and duration of the polarization testing. B) Voltage profile during galvanostatic cycling at 0.1 mA cm-2 in Li|Electrolyte|Li cells of: 3.5 h vacuum dried nano-SCE (blue), dry-nano-SCE (black) and 4 glass fibre separators immersed with EMI-TFSI-based ILE (red). C) Voltage profile of dry-nano-SCE in Li|dry-nano-SCE|Li at galvanostatic cycling for 2 h with varying current densities. The cut-off potential of 1.7V is reached at a current of 1 mA/cm2. D) EIS derived conductivity of semi-dry nano-SCE and ILE as function of temperature. Red lines indicate estimated linear regions of semi-dry nano-SCE. Before heating to 70 °C (blue, green) and after heating to 70°C (black) show different characteristic slopes. At high temperatures bulk ILE 0.33:1 LiTFS:EMI-TFSI (red) is slightly higher compared to semi-dry nano-SCE (green).

Mobility of lithium ions and local activation energy barrier changes of lithium environments can be effectively probed by using NMR relaxometry techniques.[22] The ^{7}Li T_1 (ω_0=194.5 MHz) and $T_{1\rho}$ (ω_1=12.5 kHz) relaxation times are probed for the nano-SCE variants prepared with deuterated water between -90 and +100 °C. In **Figure 4**, the relaxation rates measured at various temperatures for nano-SCE, semi-dry nano-

SCE and dry nano-SCE are shown. For all samples a maximum relaxation rate can be observed in the data, but at different temperatures.

Upon drying towards dry nano-SCE an upward shift in temperature can be observed for the highest relaxation rate ($1/T_1$) at which the correlation time (time between jumps) is of the order of the larmor frequency *i.e.* $\tau_C \sim = 1/\omega_0$. This indicates that the lithium ion mobility is reduced by the absence of the mobile volatile liquid species and the correlation time peak is only obtained when the solid dry-nano-SCE is heated to 60 ^oC.

The shape of the nano-SCE $T_{1\rho}$ and T_1 relaxation rate/temperature curves around the peak maxima are symmetric. Also the dry nano-SCE $T_{1\rho}$ curve is symmetric. Such a symmetric peak in the Arrhenius plot implies dominant uncorrelated self-diffusive type motion as given in the framework of the BPP (Bloembergen- Purcell - Pound) model.

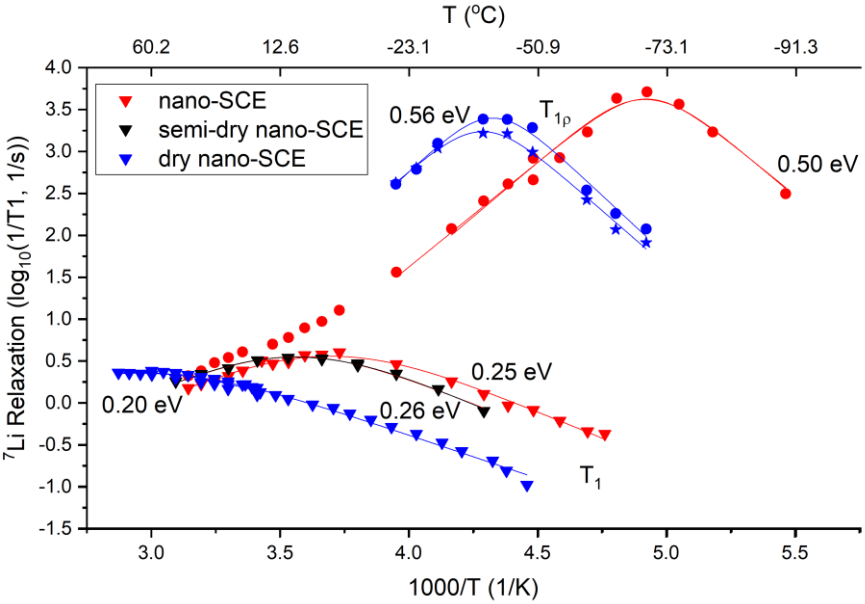

Figure 4. 7Li relaxation in nano-SCE using various probing frequencies. Lines show fit region around the peak relaxation rate. Fits of T1ρ 12.5 kHz (circles), T1ρ 30 kHz (stars) and T1 194.5 MHz (triangles) are fitted simultaneously.

For nano-SCE (red circles) the $1/T_{1\rho}$ shows a change in slope above 0 ^{o}C. The static ^{7}Li NMR spectrum around this temperature (**Figure 5**) shows a shift in dominant chemical environment, indicating the material surrounding the lithium changes around this temperature which is in line with the temperature dependent conductivities measured.

The redistribution of lithium over chemical environments or states will be the main reason for the change in relaxation rate for nano-SCE. The static ^{7}Li spectrum is resolved by fitting three peaks at temperatures above -20 ^{o}C and fitting two peaks below -20 ^{o}C (SI **Figure S14 and S15**). The three peaks at -0.74, -1.07 and -1.22 ppm at 16 ^{o}C are assigned to three environments according to their characteristics: pore confined/ surface associated (broad, chemically shielded), intermediate IL layering (relatively broad, less chemically shielded) and bulk mobile lithium (sharp, least chemically shielded) in line with the interpretation of Guyomard-Lack et. al. on lithium in an ionic liquid filled silica host.[23] The pore geometries present in the nano-SCE give a broad distribution of states for the confined lithium ions. For nano-SCE below – 6 ^{o}C the relatively sharp peak around -1.22 ppm broadens and the signal fraction attributed to this environment lowers significantly (**Figure 5**). The same temperature can be identified as the region at which the slope of the $T_{1\rho}$ relaxation time starts to diverge in **Figure 4**. The change in slope can therefore be attributed to the change in dominant lithium environment from mobile to surface associated state upon cooling.

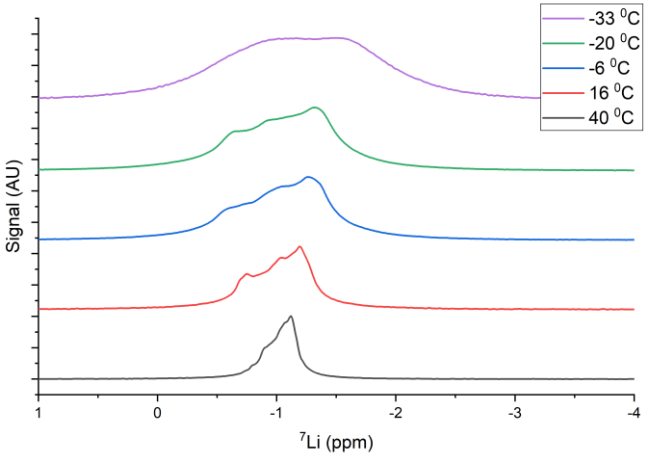

Figure 5. 7Li static NMR spectra of nano-SCE as function of temperature.

Elucidation of Enhanced Lithium Conductivity in Nanoporous Ionogel Using Solid State NMR

As the probing frequency of T_1 is high, T_1 relaxation probes fast processes (Larmor precession frequency, 194.5 MHz, ~ 4 nanosecond range) while $T_{1\rho}$ probes relatively slow, long range processes (spin-lock frequency of 10-30 kHz, tens of microsecond range). The interpretation of the motions in terms of activated Li ion hopping or ionic liquid reorientations can be addressed by determining activation barriers from the Arrhenius behavior in Figure 4, but solely in the region in which the material does not show changes in dominant environment.

The activation energies of lithium transfer in the low frequency/low temperature regime only shows minor changes upon drying. The relaxation rate function is fit around the peak maxima using BPP derived equations assuming one activation energy (SI 1).[14] These energies associated with each environments motion are summarized in SI 1 **Table S1** . For the dry-nano-SCE, only a slightly higher activation energy is found compared to the nano-SCE indicating the apparent activation energy is locally fairly similar. Interestingly an opposite change in activation energy is observed for the fast lithium ion transfer process probed by T_1 relaxation at higher temperatures. The activation energy decreases from 0.25 eV to 0.21 eV after drying. The rationale for such lower barrier for diffusion of Li may be the increased ion concentration which lowers the hopping distance. At these higher temperatures desolvation of lithium through preferred hydrogen bonding of the TFSI molecule with surface layers are expected to only play a small role. The changes in E_A are remarkably enough relatively small considering the small plasticizing solvent molecules are fully removed.

The temperatures at which the maximum relaxation rates occur shows a pronounced shift when volatiles are removed. Mobility of ions influenced by viscosity and mixing effects is thus thought to be the major contributor to apparent barriers in the lithium ion diffusion process. The temperature regions at which the presence of volatile solvent shows increased conductivity of the bulk material is in line with the temperature regions at which the activation energies of a long range lithium hops are lower.

An estimate of the conductivity by using the activation energy and characteristic hop time obtained from **Figure 4** curve fitting might elucidate which of the two environments play a dominant role in the bulk conductivity. Using Arrhenius **Equation S4** (Supporting information) a hopping time τ at a certain temperature is calculated.

The self-diffusion coefficient may then be estimated from concentration derived distance r by using **Equation 1**.

$$D = \frac{r^2}{6\tau} \quad (1)$$

The characteristic hop time is derived from the fit at the maximum relaxation rate condition, yielding diffusion coefficients in the order of 10^{-11} to 10^{-10} $m^2 s^{-1}$ This is of the same order as that obtained for the high temperature region of the ionogel system investigated by Jayakody.[12] The dry-nano-SCE shows this diffusivity around 50 - 70 ^oC, where similar diffusivities were also found by Jayakody et al. Strikingly, nano-SCE has the same order of diffusivity already at 4 ^oC, at which temperature typical ionogels normally show diffusivities around 10^{-12} $m^2 s^{-1}$. Using the Nernst-Einstein relationship (**Equation 2**),[24] an estimate of the conductivity is derived. Here AC conductivity σ_{AC} is derived as function of the lithium concentration c_{li+}, diffusion constant D, Faraday constant F, molar gas constant R and the temperature T.

$$\sigma_{AC} = \frac{c_{Li^+} D F^2}{RT} \quad (2)$$

With the diffusion coefficient estimates of T_1 and $T_{1\rho}$ of dry nano-SCE, room temperature conductivities of 1.12 mS cm^{-1} and 0.08 mS cm^{-1} were calculated respectively. The calculated conductivity from T_1 measurements is in fair agreement with the EIS study, indicating the mobile lithium/high temperature characteristics are the main contributor to the net conductivity. Similarly for the nano-SCE the conductivity derived from T_1 and $T_{1\rho}$ gives 6.78 mS cm^{-1} and 1.29 mS cm^{-1} respectively. It thus appears the fast transfer process probed by T_1 shows the temperature region and chemical environment resulting in conductive motion. The change in the dominant lithium environment upon cooling shows the shift of lithium from this conductive environment thus best explaining the higher apparent activation energy measured by temperature dependent EIS.

So far the chemical composition changes of nano-SCE with varying amounts of water has to our knowledge not been studied, while understanding the presence and mobility of the volatile molecules is key for the increased conduction mechanism. The molecular species present in the material are probed by magic angle spinning (MAS) NMR. The materials synthesis involves the following reaction steps: Ethyl groups of the TEOS molecule are hydrolyzed by available (deuterated) water. The hydroxyl group of

the silicate subsequently condenses with other partially hydrolyzed silicate groups leaving water, ethanol the solvent PGME and ionic liquid in the solution[18]. The resulting structure contains the ionic liquid, a polymerized silica network and water. PGME and ethanol remain from the synthesis and their amounts depend on the drying stage of the nano-SCE. These components can all be visualized by NMR spectroscopy.

The ^{1}H NMR spectrum of nano-SCE (**Figure 6A**, red) does not show an apparent narrow liquid water signature around 4-5 ppm, which is consistent with the notion of frozen surface layer of water in the structure as probed using IR spectroscopy proposed by Chen et al.[10]. To elucidate if water is present in the solid form, deuterated water is used to prepare the nano-SCE. The proton spectrum of this deuterated sample is compared to the original protonated sample as shown in black in **Figure 6A**. Peaks corresponding to EMI (~1.41, 3.81, 4.1, 7.31, 7.38 and 8.45 ppm)[25] and PGME (~1.15, 3.35 ppm) were resolved. In the deuterated sample no signature of water is resolved in the ^{1}H NMR spectrum and also a slight decrease in peak intensity at 8.47 ppm is observed. The ^{2}D MAS-NMR spectrum of the deuterated nano-SCE does show two broad peaks at 3.81 and 8.36 ppm (**Figure 6B**, red) indicating ^{2}D from the water has transferred partially to the central proton position on the imidazolium ring of the EMI molecule.

This prompted to probe the active exchange of the two deuterium environments. The peak at 8.36 ppm is associated with the highly polar single proton between the nitrogen groups in the imidazolium ring of the EMI molecule. The relative peak intensity of the proton peak at 8.36 ppm compared to other protons in the proton spectrum is lowered in the nano-SCE (**Figure 6A**, inset) indicating a fraction of the protons has exchanged with deuterium. With Nuclear Overhauser Effect Spectroscopy (NOESY, **Figure 6D**) is shown that the two environments are not having cross-peaks, indicating no active exchange in the material on the timescale of the exchange period. A control test was performed by mixing D_2O with ILE and on probing the ^{2}D environments, a peak around 8.36 was not observed. This indicates that the exchange process is not spontaneous but catalyzed by the environment during sol-gel formation. The central proton on the imidazolium ring is known to have strong affinity with the anions[26] and is reported to be a reactive site in acid-base reactions [27,28].

Comparison of signal broadening of the two deuterium environments (**Figure 6C**) shows that volatiles become immobile more rapidly compared to the ionic liquid. The 3.81 ppm ^{2}D peak is associated with the hydroxyl groups of the ethanol-D6 and residual D_2O of the polymerization process and possibly silanol groups[29]. The peak is very broad compared to the ionic liquid peak, an indication that they are much less mobile compared to the ionic liquid. The EMI associated peak FWHM shows less broadening from 0 to -20 ^{o}C, at which temperatures the hydroxyl associated signal shows dramatic broadening (**Figure 6C**, inset right).

A quantification of the amount of hydroxyl groups in the material can be made using the deuterium signal. In dry nano-SCE, a majority of the deuterated water is removed which is observed by the reduced peak at 3.85 ppm in the ^{2}D MAS NMR spectrum (**Figure 6B**, black). The dry-nano-SCE shows a dramatic decrease of peaks at 1.15 and 3.35 ppm in the ^{1}H spectrum which corresponds to the loss of PGME. Also a slight peak shift of the EMI associated peaks at 7.31, 7.38 and 8.45 ppm is apparent (SI, **Figure S18**). The peak shift indicates de-shielding of the three protons of the imidazolium ring upon drying. The EMI group becomes more polar in the environment with lowered amounts of solvent. A concentration estimate can be made by comparing the peak intensities of the relative loss in intensity of the 8.36 ppm proton peak of the EMI to the increase in peak in the deuterium spectrum. Of the original EMI ^{1}H 8.47:7.35 ppm signal ratio, 47% of the signal is lost in the ^{1}H spectrum in the nano-SCE prepared with deuterated water. This signal amounts to 25% deuterium signal in the deuterium spectrum in the nano-SCE. For dry nano-SCE this amounts to approximately 95% of the total peak area and increased broadening of the residual 5% of the signal indeed indicating immobilization of the water and other residuals with hydroxyl signatures upon extended drying. An indication of the solvation of mobile molecules is that nano-SCE has a ratio of 0.66 EMI cations per hydroxyl bond and for dry-nano-SCE this becomes 38 EMI cations per hydroxyl bond.

Cycled nano-SCE shows broader peaks in the ^{1}H spectrum, indicating lower mobility (SI **Figure S19**). The peak positions are maintained indicating the chemical composition of the ionic liquid is largely unaffected, although the peak around 3.42 ppm seems to indicate that some EMI has reacted to a dimer through the redox couple EMI-TFSI + Li → dim(EMI) + Li-TFSI. This is confirmed by a lower signal around 8.47 ppm, which cannot be caused by the proton-deuterium exchange as this sample was prepared using H_2O instead of D_2O .

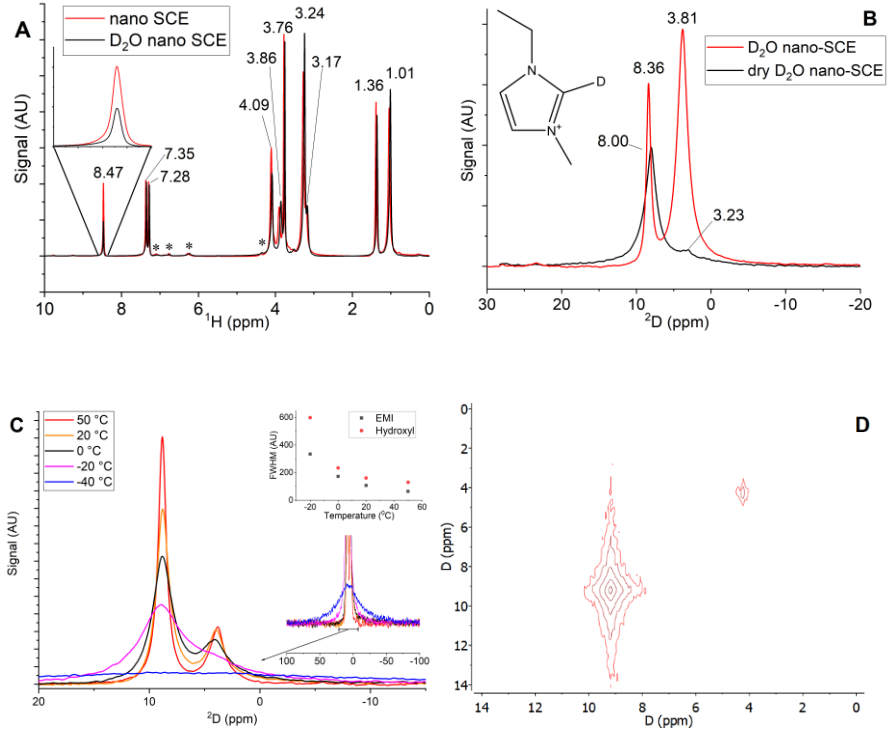

Figure 6 A) 1H MAS-NMR spectra of nano-SCE prepared with H2O (red) and D2O (black) at room temperature and 1.5 kHz spinning frequency. Inset: the signal change in the D2O derived nano-SCE indicates the proton in between the nitrogen groups in the EMI molecule has exchanged with deuterium. B) 2D MAS-NMR spectra at 1.5 kHz at room temperature of nano-SCE (red) and dry-nano-SCE (black) produced with D2O. C) Static 2D spectra as function of temperature. Semi-dry nano-SCE is measured at temperatures 50 °C (red), 20 °C (orange), 0 °C (black), -20 °C (maroon) and -40 °C (blue). Line broadening as a result of a change in mobility is most dramatic from -20 to -40 °C. D) 2D Exchange spectrum at 5 kHz at room temperature using Nuclear Overhauser Effect SpectroscopY (NOESY) of semi-dry nano-SCE using mixing times of 50 ms (blue).

Finally, ^{7}Li MAS NMR is utilized to ascertain the presence of different lithium ion environments that may explain the shift in signal shape. For the nano-SCE at temperatures above 4 °C, the ^{7}Li spectral peak at 1.5 kHz spinning rate shows an optimum spectral deconvolution with a single peak around -0.86 ppm (SI Figure S12). This indicates the differences between the chemical environments are not

distinguishable. Below 4 ^{o}C however two peaks can be distinguished and their intensity ratio does change. The broad environment becomes more abundant upon lowering the temperature. For example at -5 ^{o}C this becomes 0.46:0.54 broad:narrow and at -20 ^{o}C the ratio becomes 0.71:0.29. The broad environment has 3 times the FWHM compared to the narrow deshielded environment due to motional narrowing.

In the dry-nano-SCE lithium ions are more isolated at room temperature, observable by a central chemical shift in the ^{7}Li MAS NMR spectrum from -0.86 ppm to -1.04 ppm after extended drying (SI **Figure S13**), indicating a more isolated ionic charge (SI **Figure S13**, left). Two peaks can already be identified at room temperature of which the difference in chemical shift is only 0.039 ppm. The peak ratio is 0.58:0.42 more shielded:less shielded at room temperature. Trends in FWHM as function of temperature follow that of nano-SCE (SI **Figure S13** and **Figure S17**). Both peaks are broadened compared to nano-SCE indicating lower mobility. The lower shielding, similar to the central protons in the EMI group indicate an overall more polar interaction with the TFSI group.

Similar to nano-SCE for dry nano-SCE there is a shift of ^{7}Li signal to a chemically shielded environment, indicating surface interactions become more abundant at low temperatures. However, for dry-nano-SCE only two environments can be deconvoluted and the signal already shifts to a more shielded state at higher temperatures compared to nano-SCE. At 20 ^{o}C almost all of the signal is in the chemically shielded region (SI **Figure S17**) where in nano-SCE in this temperature range at least three lithium environments coexist (SI **Figure S14**). This confirms that the volatile molecules extend the temperature range in which lithium remains in its mobile state.

Discussion and conclusions

Nano-SCE shows promising characteristics by combining high conductivity with non-flammability and an elegant processing method. To date however, no nano-SCE has been prepared which outcompetes commercial available liquid electrolyte conductivities.[8] In this work the dry-nano-SCE shows a remarkable stable performance indicating that the SEI is stabilized at the gel/anode interface, an important characteristic for applicability. The dry-nano-SCE shows lower overpotentials compared to the semi-dry-nano-SCE. The cause of this originates from lower interfacial resistance while at the same time a good intrinsic conductivity is maintained. Limited

SEI formation by the stabilizing structure of the silica backbone, combined with good contacting due to the flexible gel is thought to be the origin of the lowered interfacial resistance. For semi-dry nano-SCE a sharp increase in charge transfer resistance at elevated temperatures is shown to be in concert with lower bulk conductivities through temperature dependent EIS, indicating an increased rate of volatiles migration to the (reactive) lithium interface. The charge transfer resistance in dry nano-SCE is found to be stable after prolonged cycling, indicating formation of a stable SEI.

The mechanism of enhanced conduction is discussed in this work. We find that a lower solvation of lithium ions by the TFSI ions in samples containing volatiles is observed in line with Chen et. Al.[10] The amount of volatiles could be quantified by using the deuterium signal from deuterated water as reference with MAS NMR. Using NMR techniques we find however that an increased bulk mobility, rather than transfer of lithium ions from local sites by means of temporal dissociation from its counter ion is the dominant source of the increased lithium ion conduction. The latter process would involve a more dramatic change in activation energy which is not observed in this study (observable by for example varying the ILE/backbone ratio).[30] We show that desolvating groups enable lithium ion mobility at lower temperatures. Fast transfer processes probed using T_1 relaxation show a good fit with electrochemical impedance spectroscopy. With the combinatory approach of relaxometry and MAS NMR this work provides a complementary analysis of the structural and electrochemical features of this promising material.

REFERENCES

(1) Le Bideau, J.; Ducros, J.-B.; Soudan, P.; Guyomard, D. Solid-State Electrode Materials with Ionic-Liquid Properties for Energy Storage: The Lithium Solid-State Ionic-Liquid Concept. *Adv. Funct. Mater.* **2011**, *21* (21), 4073–4078. https://doi.org/10.1002/adfm.201100774.

(2) Chen, X.; Vereecken, P. M. Solid and Solid-Like Composite Electrolyte for Lithium Ion Batteries: Engineering the Ion Conductivity at Interfaces. *Adv. Mater. Interfaces* **2019**, *6* (1), 1800899. https://doi.org/10.1002/admi.201800899.

(3) Li, S.; Li, N.; Sun, C. A Flexible Three-Dimensional Composite Nanofiber Enhanced Quasi-Solid Electrolyte for High-Performance Lithium Metal Batteries. *Inorg. Chem. Front.* **2021**, *8* (2), 361–367. https://doi.org/10.1039/D0QI01159B.

(4) Yi, Q.; Zhang, W.; Wang, T.; Han, J.; Sun, C. A High-performance Lithium Metal Battery with a Multilayer Hybrid Electrolyte. *ENERGY Environ. Mater.* **2022**, eem2.12289. https://doi.org/10.1002/eem2.12289.

(5) Wang, T.; Zhang, X.; Yuan, N.; Sun, C. Molecular Design of a Metal–Organic Framework Material Rich in Fluorine as an Interface Layer for High-Performance Solid-State Li Metal Batteries. *Chem. Eng. J.* **2023**, *451*, 138819. https://doi.org/10.1016/j.cej.2022.138819.

(6) Qiu, G.; Sun, C. A Quasi-Solid Composite Electrolyte with Dual Salts for Dendrite-Free Lithium Metal Batteries. *New J. Chem.* **2020**, *44* (5), 1817–1824. https://doi.org/10.1039/C9NJ04897A.

(7) Sun, C.; Liu, J.; Gong, Y.; Wilkinson, D. P.; Zhang, J. Recent Advances in All-Solid-State Rechargeable Lithium Batteries. *Nano Energy* **2017**, *33*, 363–386. https://doi.org/10.1016/j.nanoen.2017.01.028.

(8) Sagara, A.; Chen, X.; Gandrud, K. B.; Murata, M.; Mees, M.; Kaneko, Y.; Arase, H.; Vereecken, P. M. High-Rate Performance Solid-State Lithium Batteries with Silica-Gel Solid Nanocomposite Electrolytes Using Bis(Fluorosulfonyl)Imide-Based Ionic Liquid. *J. Electrochem. Soc.* **2020**, *167* (7), 070549. https://doi.org/10.1149/1945-7111/ab80d0.

(9) Sagara, A.; Yabe, H.; Chen, X.; Vereecken, P. M.; Uedono, A. Pore Structure Analysis of Ionic Liquid-Templated Porous Silica Using Positron Annihilation Lifetime Spectroscopy. *Microporous Mesoporous Mater.* **2020**, *295*, 109964. https://doi.org/10.1016/j.micromeso.2019.109964.

(10) Chen, X.; Put, B.; Sagara, A.; Gandrud, K.; Murata, M.; Steele, J. A.; Yabe, H.; Hantschel, T.; Roeffaers, M.; Tomiyama, M.; Arase, H.; Kaneko, Y.; Shimada, M.; Mees, M.; Vereecken, P. M. Silica Gel Solid Nanocomposite Electrolytes with Interfacial Conductivity Promotion Exceeding the Bulk Li-Ion Conductivity of the Ionic Liquid Electrolyte Filler. *Sci. Adv.* **2020**, *6* (2), eaav3400. https://doi.org/10.1126/sciadv.aav3400.

(11) Guyomard-Lack, A.; Delannoy, P.-E.; Dupré, N.; Cerclier, C. V.; Humbert, B.; Le Bideau, J. Destructuring Ionic Liquids in Ionogels: Enhanced Fragility for Solid Devices. *Phys Chem Chem Phys* **2014**, *16* (43), 23639–23645. https://doi.org/10.1039/C4CP03187C.

(12) Jayakody, N. K.; Fraenza, C. C.; Greenbaum, S. G.; Ashby, D.; Dunn, B. S. NMR Relaxometry and Diffusometry Analysis of Dynamics in Ionic Liquids and Ionogels for Use in Lithium-Ion Batteries. *J. Phys. Chem. B* **2020**, *124* (31), 6843–6856. https://doi.org/10.1021/acs.jpcb.0c02755.

(13) Uitz, M.; Epp, V.; Bottke, P.; Wilkening, M. Ion Dynamics in Solid Electrolytes for Lithium Batteries: Probing Jump Rates and Activation Energies through Time-Domain Li NMR. *J. Electroceramics* **2017**, *38* (2–4), 142–156. https://doi.org/10.1007/s10832-017-0071-4.

(14) McDowell, A. F.; Adolphi, N. L.; Sholl, C. A. Site and Barrier Energy Distributions That Govern the Rate of Hydrogen Motion in Quasicrystalline $Ti_{45}Zr_{38}Ni_{17}H_x$. *J. Phys. Condens. Matter* **2001**, *13* (43), 9799–9812. https://doi.org/10.1088/0953-8984/13/43/310.

(15) Bloembergen, N.; Purcell, E. M.; Pound, R. V. Relaxation Effects in Nuclear Magnetic Resonance Absorption. *Phys. Rev.* **1948**, *73* (7), 679–712. https://doi.org/10.1103/PhysRev.73.679.

(16) Assink, R. A.; Kay, B. D. Sol-Gel Kinetics I. Functional Group Kinetics. *J. Non-Cryst. Solids* **1988**, *99* (2–3), 359–370. https://doi.org/10.1016/0022-3093(88)90441-3.

(17) Issa, A.; Luyt, A. Kinetics of Alkoxysilanes and Organoalkoxysilanes Polymerization: A Review. *Polymers* **2019**, *11* (3), 537. https://doi.org/10.3390/polym11030537.

(18) Cihlář, J. Hydrolysis and Polycondensation of Ethyl Silicates. 1. Effect of PH and Catalyst on the Hydrolysis and Polycondensation of Tetraethoxysilane (TEOS). *Colloids Surf. Physicochem. Eng. Asp.* **1993**, *70* (3), 239–251. https://doi.org/10.1016/0927-7757(93)80298-S.

(19) Buckley, A. M.; Greenblatt, M. The Sol-Gel Preparation of Silica Gels. *J. Chem. Educ.* **1994**, *71* (7), 599. https://doi.org/10.1021/ed071p599.

(20) Moškon, J.; Žuntar, J.; Drvarič Talian, S.; Dominko, R.; Gaberšček, M. A Powerful Transmission Line Model for Analysis of Impedance of Insertion Battery Cells: A Case Study on the NMC-Li System. *J. Electrochem. Soc.* **2020**, *167* (14), 140539. https://doi.org/10.1149/1945-7111/abc769.

(21) Manuel Stephan, A. Review on Gel Polymer Electrolytes for Lithium Batteries. *Eur. Polym. J.* **2006**, *42* (1), 21–42. https://doi.org/10.1016/j.eurpolymj.2005.09.017.

(22) Rachocki, A.; Andrzejewska, E.; Dembna, A.; Tritt-Goc, J. Translational Dynamics of Ionic Liquid Imidazolium Cations at Solid/Liquid Interface in Gel Polymer Electrolyte. *Eur. Polym. J.* **2015**, *71*, 210–220. https://doi.org/10.1016/j.eurpolymj.2015.08.001.

(23) Guyomard-Lack, A.; Said, B.; Dupré, N.; Galarneau, A.; Le Bideau, J. Enhancement of Lithium Transport by Controlling the Mesoporosity of Silica Monoliths Filled by Ionic Liquids. *New J. Chem.* **2016**, *40* (5), 4269–4276. https://doi.org/10.1039/C5NJ03318G.

(24) Chintapalli, M.; Timachova, K.; Olson, K. R.; Mecham, S. J.; Devaux, D.; DeSimone, J. M.; Balsara, N. P. Relationship between Conductivity, Ion Diffusion, and Transference Number in Perfluoropolyether Electrolytes. *Macromolecules* **2016**, *49* (9), 3508–3515. https://doi.org/10.1021/acs.macromol.6b00412.

(25) D'Agostino, C.; Mantle, M. D.; Mullan, C. L.; Hardacre, C.; Gladden, L. F. Diffusion, Ion Pairing and Aggregation in 1-Ethyl-3-Methylimidazolium-Based Ionic Liquids Studied by ^{1}H and ^{19}F PFG NMR: Effect of Temperature, Anion and Glucose Dissolution. *ChemPhysChem* **2018**, *19* (9), 1081–1088. https://doi.org/10.1002/cphc.201701354.

(26) Fujii, K.; Soejima, Y.; Kyoshoin, Y.; Fukuda, S.; Kanzaki, R.; Umebayashi, Y.; Yamaguchi, T.; Ishiguro, S.; Takamuku, T. Liquid Structure of Room-Temperature Ionic Liquid, 1-Ethyl-3-Methylimidazolium Bis-(Trifluoromethanesulfonyl) Imide. *J. Phys. Chem. B* **2008**, *112* (14), 4329–4336. https://doi.org/10.1021/jp7105499.

(27) Saruwatari, H.; Kuboki, T.; Kishi, T.; Mikoshiba, S.; Takami, N. Imidazolium Ionic Liquids Containing LiBOB Electrolyte for Lithium Battery. *J. Power Sources* **2010**, *195* (5), 1495–1499. https://doi.org/10.1016/j.jpowsour.2009.08.081.

(28) Ober, C. A.; Gupta, R. B. PH Control of Ionic Liquids with Carbon Dioxide and Water: 1-Ethyl-3-Methylimidazolium Acetate. *Ind. Eng. Chem. Res.* **2012**, *51* (6), 2524–2530. https://doi.org/10.1021/ie201529d.

(29) Protsak, I. S.; Morozov, Y. M.; Dong, W.; Le, Z.; Zhang, D.; Henderson, I. M. A 29Si, 1H, and 13C Solid-State NMR Study on the Surface Species of Various Depolymerized Organosiloxanes at Silica Surface. *Nanoscale Res. Lett.* **2019**, *14* (1), 160. https://doi.org/10.1186/s11671-019-2982-2.

(30) Tsao, C.-H.; Su, H.-M.; Huang, H.-T.; Kuo, P.-L.; Teng, H. Immobilized Cation Functional Gel Polymer Electrolytes with High Lithium Transference Number for Lithium Ion Batteries. *J. Membr. Sci.* **2019**, *572*, 382–389. https://doi.org/10.1016/j.memsci.2018.11.033.

(31) Delgado, A.; García-Sánchez, M. F.; M'Peko, J.-C.; Ruiz-Salvador, A. R.; Rodríguez-Gattorno, G.; Echevarría, Y.; Fernández-Gutierrez, F. An Elementary Picture of Dielectric Spectroscopy in Solids: Physical Basis. *J. Chem. Educ.* **2003**, *80* (9), 1062. https://doi.org/10.1021/ed080p1062.

Elucidation of Enhanced Lithium Conductivity in Nanoporous Ionogel Using Solid State NMR

SUPPORTING INFORMATION

1. *BACKGROUND OF RELAXOMETRY STUDY*

In short, the exponential decay of magnetic moment after a pulse sequence in the T_1 (spin-lattice), T_2 (spin-spin) or $T_{1\rho}$ (spin-lattice rotational plane) is described with a correlation function. The correlation function is a simplified description of the relative change of magnetic environment as the atom travels through a volume. The time at which the relaxation is fastest corresponds to a characteristic time at which the ion travels from one environment to another. In a stable system, the characteristic time changes as function of temperature according to the Arrhenius law, which correlates the rate change of a process as a function of temperature.

A downside of the relaxometry method compared to for example PFG for diffusion estimation is that only at a specific range of frequencies (the specific spin relaxation frequencies) the characteristic step time can be found. The activation energy however can be found at the high temperature side of the relaxation as function of temperature. The shortest relaxation time evolves around the characteristic step time which is described by **Equation S3**. Here the change in characteristic step time τ_C can be described by a derivative of the Arrhenius **Equation S4**.

$$\frac{1}{T_1} \propto G(0)\frac{2\tau_c}{1+(\omega_0\tau_C)^2}$$

S3)

$$\tau_C = \tau_0 exp\,(\frac{E_A}{k_B T})$$

S4)

The relaxation time is correlated to the characteristic step time in Equation S3. Equation S4 gives an estimation of the characteristic step. The formal solution of the correlation between relaxation time and the characteristic step is given in the BPP model as **Equation S5 and S6**.[14]

$$\frac{1}{T_1} = \frac{2}{3} M_2 \left(\frac{\tau_c}{1 + {\omega_0}^2 {\tau_c}^2} + \frac{4\tau_c}{1 + 4{\omega_0}^2 {\tau_c}^2} \right)$$

S5)

$$\frac{1}{T_{1\rho}} = \frac{1}{3} M_2 \left(\frac{3\tau_c}{1 + 4{\omega_1}^2 {\tau_c}^2} + \frac{5\tau_c}{1 + {\omega_0}^2 {\tau_c}^2} + \frac{2\tau_c}{1 + 4{\omega_0}^2 {\tau_c}^2} \right)$$

S6)

Table S1 Activation energies and pre exponential step times derived from fitting relaxation rate data using varying probing frequencies.

	Activation energy E_A $(1/T_1)$ (eV)	Activation energy E_A $(1/T_{1\rho})$ (eV) (ω_1= 12.5 kHz)	Activation energy E_A $(1/T_{1\rho})$ (eV) (ω_1= 30 kHz)	Pre exponential Step time $\tau_{0,\,T1}$ (s)	Pre exponential Step time $\tau_{0,\,T1\rho}$ (s)
Nano-SCE	0.251 ± 0.005	0.50 ± 0.02		$10^{-13.2 \pm 0.1}$	$10^{-16.69 \pm 0.48}$
Semi-dry nano-SCE	0.262 ± 0.004			$10^{-13.2 \pm 0.1}$	
Dry nano-SCE	0.206 ± 0.005	0.58 ± 0.02	0.54 eV ± 0.02	$10^{-11.6 \pm 0.1}$	$10^{-17.05 \pm 0.51}$, $10^{-16.34 \pm 0.36}$

The resulting activation energies differ slightly and the accuracy of the fit improves when using Equation S5 and S6 instead of Equation S3. Comparing equations from Uitz et. Al. with McDowell et. Al.:

Method Uitz	R_1 (194 MHz) eV $E_{A,Low\text{-}E}$	$R_{1\rho}$ (12.5 kHz) eV $E_{A,High\text{-}E}$	$R_{1\rho}$ (30 kHz)
Nano-SCE	0.24 ± 0.03 eV	0.48± 0.06 eV	
Semidry nano-SCE	0.25 ± 0.03 eV		
Dry nano-SCE	0.201 ± 0.04 eV	0.57± 0.06	0.53± 0.06

Table S 1 Activation energy of lithium hop using Equation S3

Method McDowell	E_A $(1/T_1)$ eV	E_A $(1/T_{1\rho})$ eV (ω_1= 12.5 kHz)	E_A $(1/T_{1\rho})$ eV (ω_1= 30 kHz)
Nano-SCE	0.251 ± 0.005	0.50 ± 0.02	
3.5 h HVT nano-SCE	0.262 ± 0.004		
Dry nano-SCE	0.206 ± 0.009	0.58 ± 0.02	0.54 ± 0.02

Table S 2 Activation energy of lithium hop using Equation S5 and S6

2. *Cycling behavior of 3.5 hour vacuum dried nano-SCE*

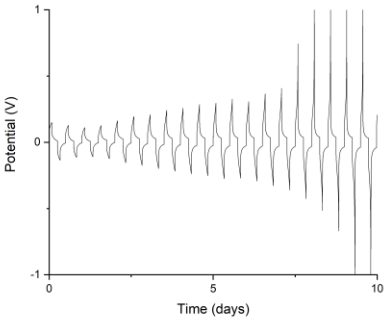

Figure S7 Galvanostatic cycling of a Li|semi-dry nano-SCE|Li symmetric cell at 0.1 mA/cm².

3. EIS SPECTRA OF NANO-SCE BEFORE AND AFTER POLARIZATION

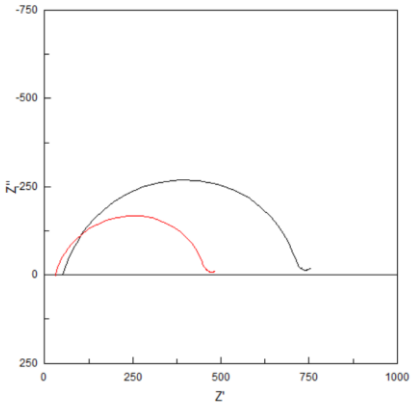

Figure S8 Nano-SCE in the pristine form (Red) shows lower resistances compared to the same material after some potentiostatic testing (Black).

4. ELECTROCHEMICAL IMPEDANCE SPECTROSCOPY BEFORE AND AFTER GALVANOSTATIC POLARIZATION

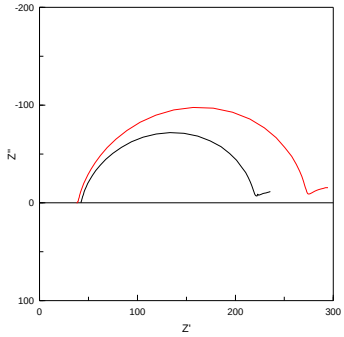

Figure S9 EIS spectrum of Dry nano-SCE before polarization (red) and after polarization (black).

5. *EIS SPECTRA OF SEMI-DRY NANO-SCE AT VARIOUS TEMPERATURES*

Obtained nyquist plots typically show three regions in the high- (1 MHz to 100 kHz) mid- (100 kHz to 1 kHz) and low frequency regime (1 kHz to 1 Hz), (**Figure S10**). The high frequency regime at low temperatures (-6 ^{o}C and lower) shows capacitance originating from the bulk nano-SCE in line with the expected capacitance for bulk materials of 10^{-10} F.[31] At higher temperatures this capacitance becomes a pure resistive component. The mid frequency range shows an imperfect semicircle, the constant phase element placed in parallel with a resistor needs phase correction of 0.87 to 0.95 (low to high temperature) and a capacitance of 10^{-5} to 10^{-7} F is found, typical for interface capacitance. Only the -40 ^{o}C measurement shows a unique low frequency capacitance regime.

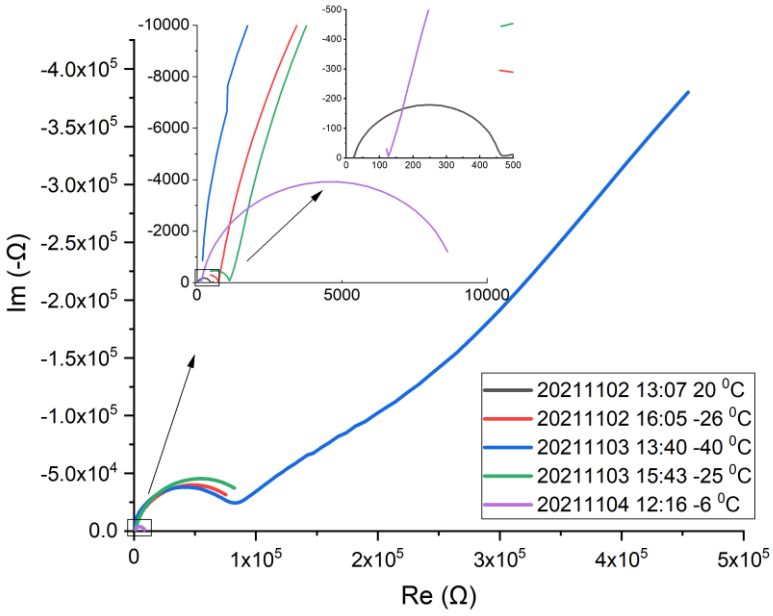

Figure S10 Nyquist plot showing EIS spectra between 1MHz and 1 Hz of semi-dry nano-SCE in symmetric lithium cell. Sample is measured in chronological order at 20 ^{o}C (black), -26 ^{o}C (red), -6^{o}C (blue), -40 ^{o}C (green) and -25 ^{o}C (purple).

The log plating/stripping transfer resistance as function of reciprocal temperature gives an activation energy of 0.71 eV for interfacial transfer (**Figure S11**, appendix). This activation energy is similar to the activation energy of 0.61 eV found for ILE indicating good contacting of the nano-SCE with the lithium metal.

6. *Interface resistance as function of temperature during EIS*

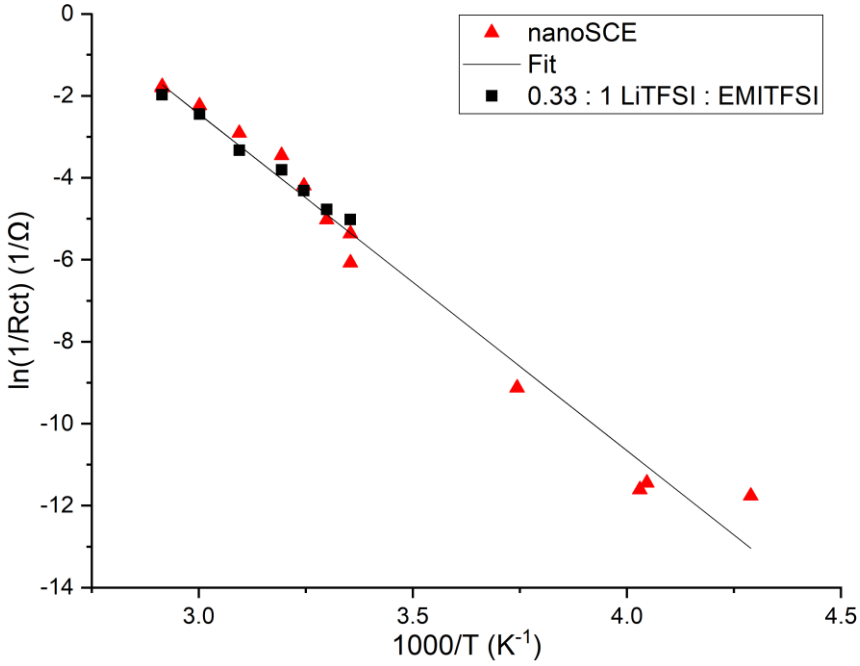

Figure S11 Interface resistance of semidry nano-SCE (red triangle) and ILE (black square) as function of temperature derived from the Mid and low frequencies in the EIS spectrum.

7. *Spinning ^{7}Li MAS NMC spectral deconvolution*

Nano-SCE at 1.5 kHz spinning rate

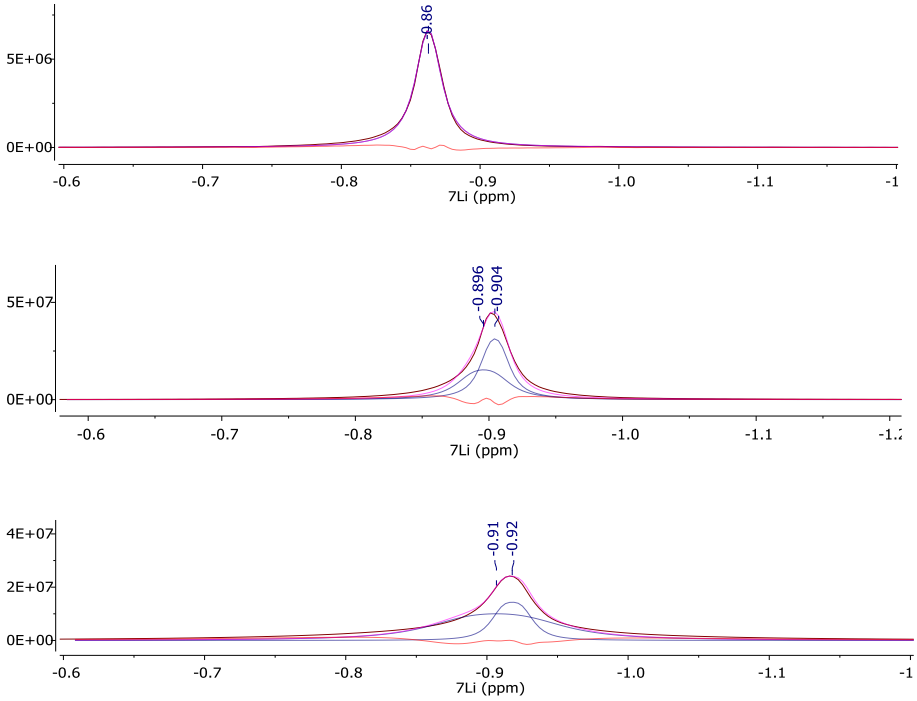

Figure S12 7Li NMR spectrum of nano-SCE at 1.5 kHz MAS at RT (top), 5 ^{o}C (middle) and -20 ^{o}C (bottom).

DRY NANO-SCE AT 1.5 KHZ SPINNING RATE

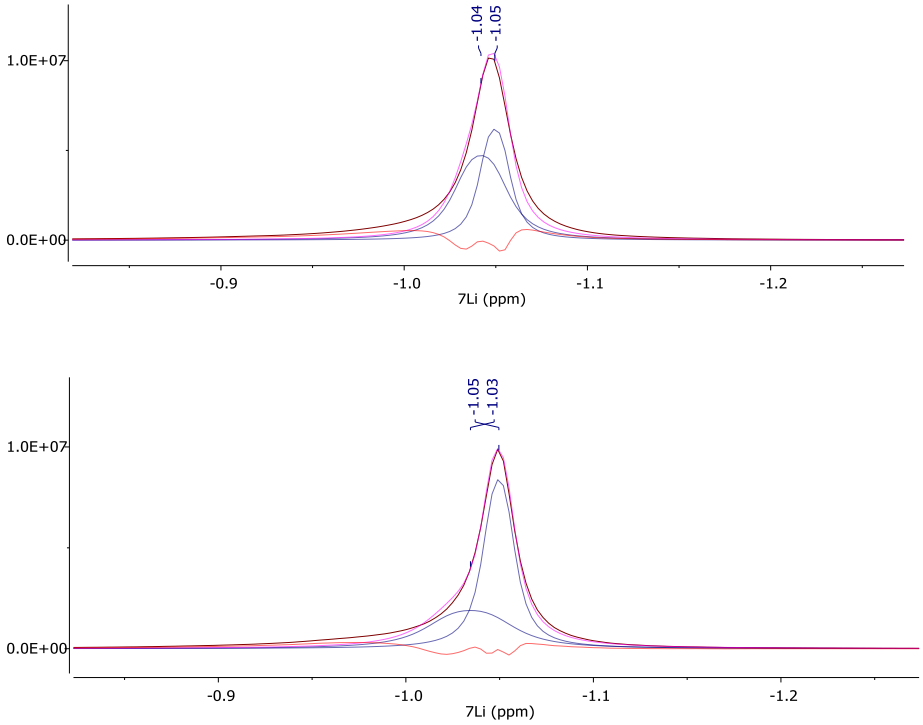

Figure S13 7Li MAS NMR spectrum of dry nanoSCE at 1.5 kHz MAS. A signal distribution change is observable during heating. At room temperature (top) the deshielded environment is less abundant compared to 40 °C (bottom).

8. STATIC ^{7}LI NMR AND DECONVOLUTION

The static ^{7}Li spectrum of nano-SCE deconvolution (Figure S14, Figure S15, Figure S16) from the original spectra show examples of the deconvolution fit of an asymmetric peak which suggest multiple environments exist. At 16 ^{o}C the broad peak shows its peak maximum at -0.74 ppm which corresponds to a more shielded environment compared to the sharp peak maximum located at -1.22 ppm. A middle region at -1.07 ppm is most abundant. At -6 ^{o}C the intermediate region becomes less abundant, the shoulder peak their relative abundance barely change. At -33 ^{o}C the environment with the lower chemical shift has become most abundant, both environments have broadened and signal from the environment with the high chemical shift has almost faded completely.

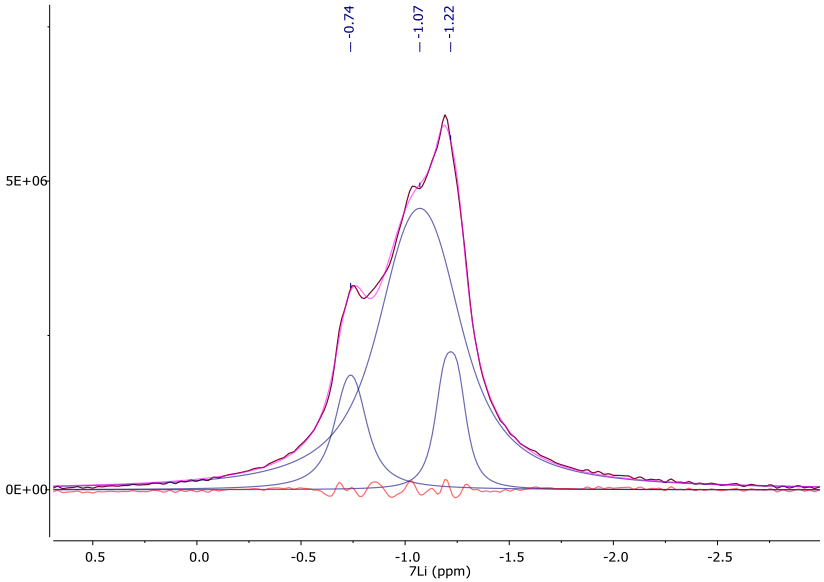

Figure S14 Example of a three peak fit 7Li spectrum. Static ^{7}Li spectrum of nano-SCE is obtained at 16 degrees Celsius. Peak signal is deconvoluted.

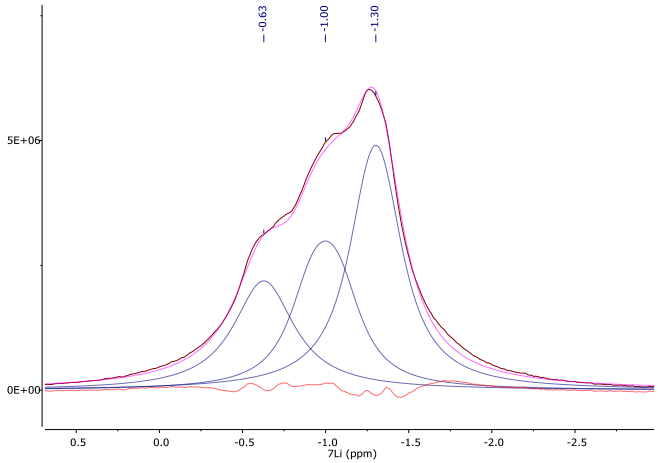

Figure S15 Example of a two peak fit 7Li spectrum. Static ^{7}Li spectrum of nano-SCE is obtained at -6 ^{o}C. Peak signal is deconvoluted.

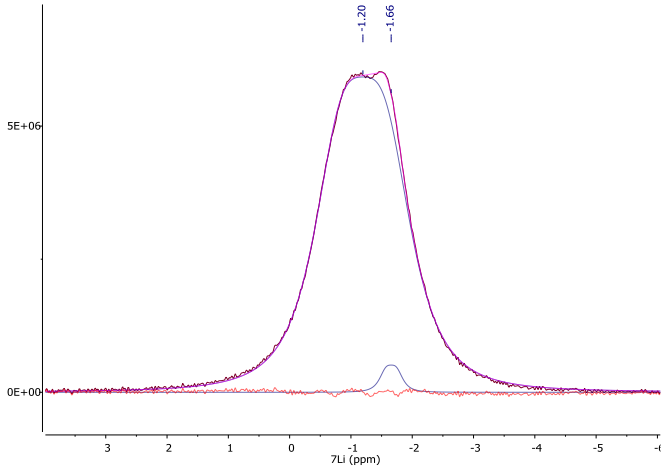

Figure S16 Example of a two peak fit 7Li spectrum. Static ^{7}Li spectrum of nano-SCE is obtained at -33 ^{o}C. Peak signal is deconvoluted.

9. *Dry nanoSCE ^{7}Li static spectrum as function of Temperature*

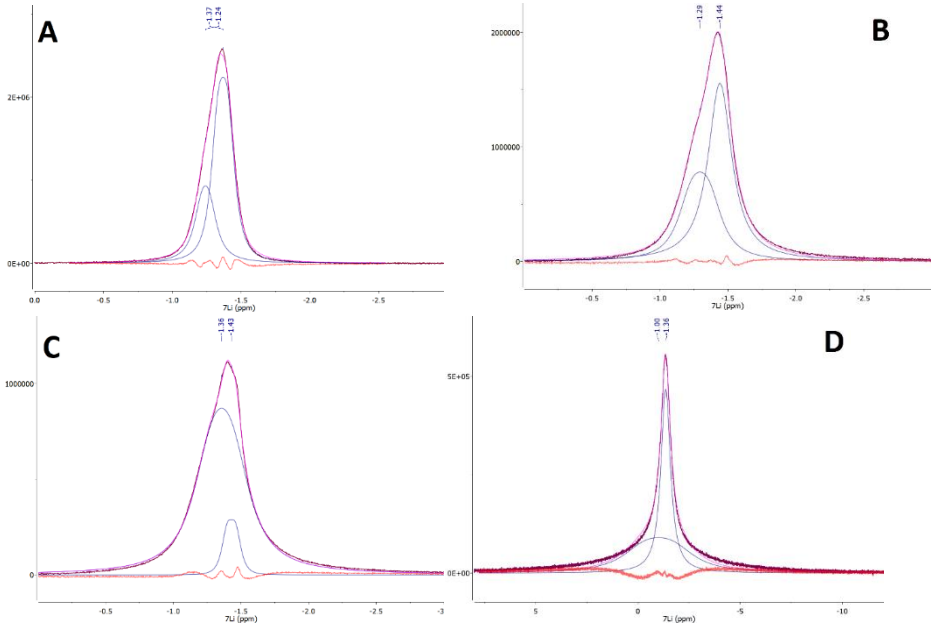

Figure S17 7Li static spectra of dry nano-SCE at four temperatures A) 70 ^{o}C, B) 40 ^{o}C, C) 20 ^{o}C, D) -30 ^{o}C.

Note that all X-axis range from 0 to -3 ppm except D ranging from 8 to -12 ppm.

10. Comparison of proton spectra of nano-SCE and dry-nano-SCE

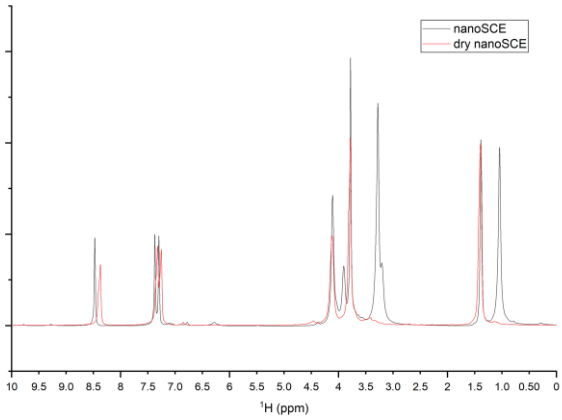

Figure S18 ^{1}H spectrum of nano-SCE (red) compared to dry-nano-SCE (blue)

11. Proton spectrum of cycled nano-SCE

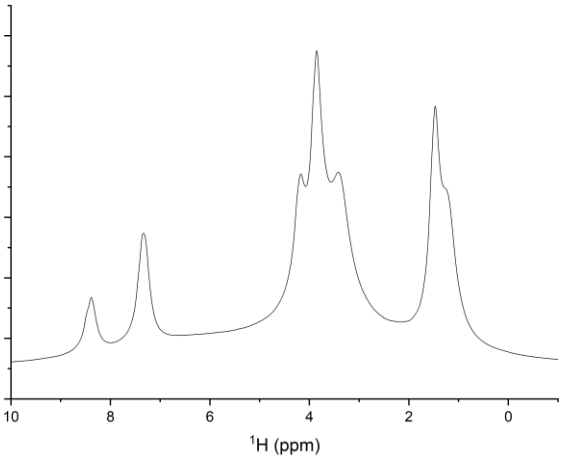

Figure S19 ^{1}H spectrum of cycled nano-SCE at 5 kHz. Sample was prepared with Al_2O_3 filler.

12. SAMPLE NAMES AND TREATMENT

Table 2 Sample treatment overview

Sample name	Treatment
Nano-SCE	Polymerization for >14 days until gel. Drying for 4 days at 800 mBarA RT. Drying for for 3 days at 200 mBarA RT.
Semi-dry nano-SCE	Nano-SCE + Drying for 3.5 hours in absolute vacuum at 60 ^{o}C.
Dry nanoSCE	Semi-dry nano-SCE + Drying overnight in absolute vacuum at 60 ^{o}C.

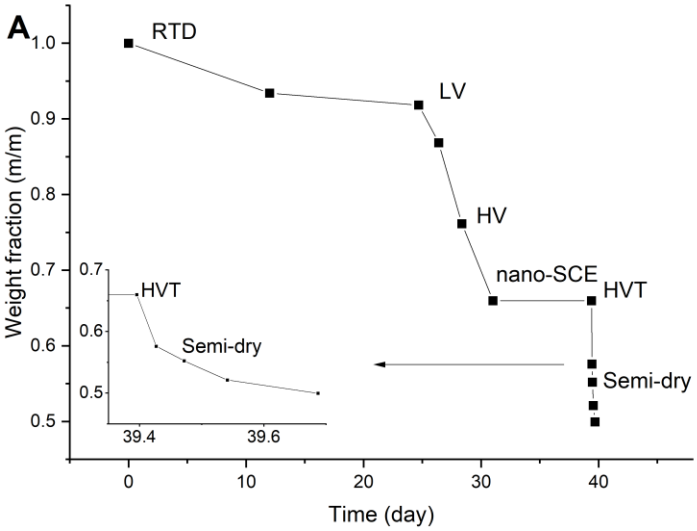

Figure S20 A) Weight of sample during formation of nano-SCE. Sample was exposed to: Room temperature drying (RTD) followed by 0.8 BarA vacuum (LV) and 0.2 BarA vacuum (HV) drying steps. Sample nano-SCE was obtained after HV and subsequently a high vacuum at elevated temperature (HVT) dried the sample to approximately its theoretical minimum (~50%).

The extent of drying is calculated by weighing the fractional weight loss and dividing this by the fractional weights of the volatile precursors, assuming only the H_2O, ethanol and PGME can evaporate under these conditions.

5. Lithium Diffusivity and Transference in High Lithium Concentration Ternary Polymer Ionic Liquids

The content of this chapter has been published in Solid State Ionics in 2025, Volume 424, 116854 in which Mark Weijers is first author.

https://doi.org/10.1016/j.ssi.2025.116854

Lithium Diffusivity and Transference in High Lithium Concentration Ternary Polymer Ionic Liquids

Abstract

For battery architectures that need a solid ion conductor with good contacting performance and high stability against electrochemical oxidation, polymerized ionic liquids (PIL) pose a valuable class of materials. The low conductivity of the binary PIL/ lithium salt system can be increased using a ternary ionic liquid acting as plasticiser. The conductive mechanism of the ternary system is however not fully understood. This work shows the shift in conduction mechanism for the ternary Li-/[1,3]PYR-/PDADMA-FSI system by increasing the lithium salt concentration and comparing the transfer mechanism to binary ionic liquid (IL) electrolyte analogues using pulsed field gradient (PFG) nuclear magnetic resonance (NMR), NMR relaxometry, Raman spectroscopy and electrochemical techniques. Two conducting regimes were found which show a strong trade-off between conductivity and transference number. In the low lithium salt regime (≤35wt% LiFSI), cluster diffusion of aggregated lithium is the dominating mechanism leading to low transference numbers (0.04 – 0.15 at room temperature (RT)). The high salt regime (≥50wt% LiFSI) shows diffusion through free lithium ion hopping transfer, which has a stronger dependence on temperature and yields higher transference numbers (0.31 at RT). Increasing lithium salt concentration shows an inverse linear correlation with conductivity. The electrochemical characteristics of ternary IL/PIL/lithium salt are shown to be highly tuneable by varying the lithium salt fraction, while it maintains excellent characteristics like processability, stability and mechanical function.

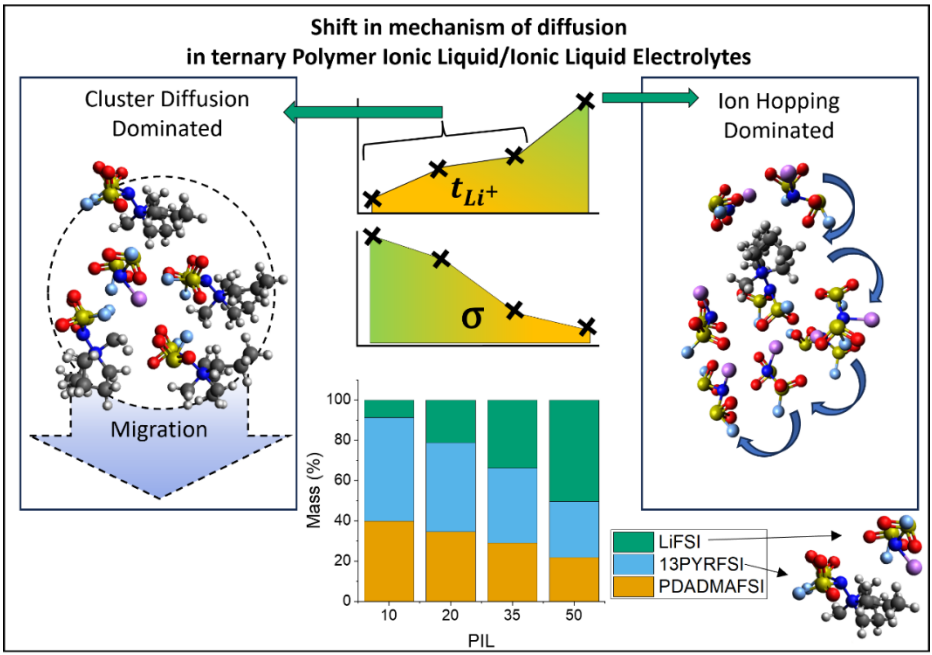

INTRODUCTION

In the search for flexible ionic conducting materials, polymerized ionic liquids (PIL) are a class of solid state electrolytes which have garnered considerable attention in terms of innovation and potential use in lithium ion batteries.[1–3] The advantage of PIL is that one of the ions is incorporated into the polymer chain, resulting in a solid material with conducting properties. To function as a lithium conductor the addition of a lithium salt is needed for cationic PIL, a class of PIL in which the cation is immobilized. Binary PIL/lithium salt show relatively low ionic conductivity (<mS/cm) with a high lithium transference number. For the poly(diallyldimethyl)ammonium fluorosulfonylimide (PDADMAFSI)/lithium fluorosulfonylimide (LiFSI) system, a conductivity of 0.078 mS/cm with a t_{Li+} of 0.56 was reported at 80 °C.[4] A secondary ionic liquid (IL) can be added as plasticiser, making it a ternary (PIL:IL:lithium salt, called IL-PIL throughout this work) system. As such, IL-PIL typically offer good ionic conductivity and a high stability against oxidation, good surface contact with electrodes at mild pressures and excellent cycling performance, as shown by Fu et al.[5] They used N-propyl-N-methylpyrrolidinium bis(trifluoromethylsulfonyl) imide ([1,3]PYRFSI) as IL, which cycled for 600 and 300 cycles in lithium metal NMC811 and LNMO full cells,

respectively. Pyrrolidinium based PILs therefore form an excellent candidate as the ion-conducting constituent of battery separators and coatings. Recently, Homann et al. showed increased lithium salt concentrations allow improved electrochemical performance in lithium metal NMC811 full cells.[6] In this work we investigate the mechanism behind the increased lithium conduction of the IL-PIL used in these works by probing molecular motions in a wide range of time scales and lithium salt concentrations.

The system investigated possesses three positively charged ions. The system contains lithium and [1,3]PYR cations and PDADMA cationic polymer. As counterion only one negatively charged ion, being FSI is used. Studies have been conducted on similar systems, optimizing for example Li(T)FSI/[x,y]PYR(T)FSI ILE systems in which x and y depict the alkyl chain length,[7,8] or including various polymers focussing on changes in molecular interactions using a fixed ratio of lithium salt to ionic polymer.[9] On a similar, PDADMA(T)FSI based IL-PIL, spin relaxation is studied to investigate local interactions.[10] Here they conclude cationic polymers mechanically stabilize liquid electrolytes with a lower net decrease in lithium motion compared to neutral polymers.[10] Also, comparison between FSI and TFSI combinatory effects[11],the effect of polymer concentration in the IL-PIL TFSI system[12] and the effect of stack pressure[13] have been studied before. Finally, the effect of the [x,y]PYR concentration[14] and the effect of the ratio between IL and PIL have also been studied to find the balance between an increase in diffusivity and the lower transference.[15] One general observation is that increasing the lithium salt in ionic liquids has shown to have a beneficial effect on the transference number and therefore net charge transfer in lithium ion conducting systems.[16] This observation has been exploited to some degree by making high salt PDADMAFSI IL-PIL using phosphonium ionic liquid instead of [1,3]PYRFSI.[17] In this study the concentration of lithium salt is varied to assess the change in effective lithium conduction to find a similar optimum and to understand the underlying mechanism of change in transference number observed between binary and ternary PIL and IL-PIL respectively.

An ideal ionic conductor would only transfer the redox active ion (giving a transference number of 1). Such a material would not suffer from problems arising from concentration depletion, which typically lead to unwanted side reactions at interfaces. Of the solid-state electrolytes, polymers show transference numbers lower than unity

due to correlated ionic motion and polymer segmental motion.[18] Adding ionic liquids reduces the transference number further, albeit with the benefit of increased conductivity. By adding a plasticising agent several additional factors can be influencing the PILs transfer numbers and conductivity:

- The lithium ions in IL, PIL, and IL-PIL are surrounded by negative counterions in a solvation shell, affecting its diffusivity.[19] Such a solvation shell may act as clusters which migrate in an electric field to one of the poles depending on the polarity of the cluster.[20]
- Ions either present as ionic liquid constituents or part of the polymer chain may affect the formation/dissolution rate of the solvation shell by formation of stable aggregates.[21]
- The counter-ion may disturb the inertia of the conducting ion by momentum conservation, which leads to a strong anticorrelated motion and very low transference numbers reported in systems with high lithium salt concentrations.[3]
- Segmental motion of the polymer affects ionic migration as well.[22]

The mobile cations are able to migrate in the electric field, leading to concentration polarization effects.[23] The role of the polymer in lithium transfer mechanisms has no clear theoretical basis in ternary systems. Analysing the mobilities at different time scales with NMR, compared to electrochemical measurements and Raman spectroscopy (Figure 1) can elucidate whether the root cause of sluggish transfer lies in the movement of lithium ions as individuals, which potentially allow a transference number of 1 (when the anions are immobilized), or if there is coupled migration.

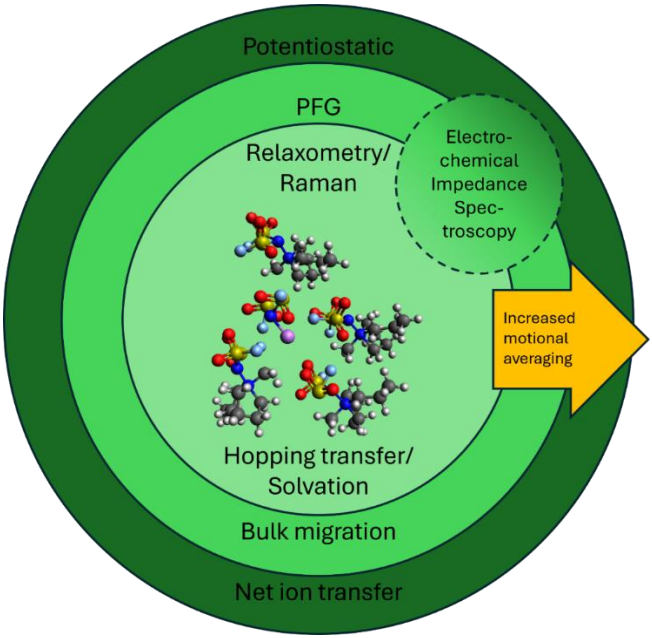

Figure 1 Description of the correlation between the measurement techniques and the information on molecular motion the technique is able to acquire. The longest time scales shows the net ion transfer originating from the various different types of diffusion phenomena in an electric field. The shortest time scale show the relative molecular motions. In between the intermediate time scale shows the tracer diffusion of specific molecular species. Together the three time scales shows which diffusion mechanism is dominating: cluster diffusion dominated (relatively high diffusion coefficient with respect to molecular hopping frequency and a high degree of concentration polarization) or ion hopping dominated (relatively low diffusion coefficient with respect to molecular hopping frequency and a low degree of concentration polarization).

Local kinetic effects like making/breaking of aggregates, defined by the degree of association, is estimated using NMR relaxometry. The aggregate cluster size is observed by Raman spectroscopy. Long range diffusion effects of aggregates, causing concentration polarization is analysed by comparing electrochemical diffusion coefficients with diffusivities measured through PFG NMR. Finally, this paper correlates the observations to a quantitative theoretical framework proposed by Wohde et. Al. [24] to increase the understanding of ion mobilities in ternary IL-PIL.

METHODS

ELECTROLYTE SYNTHESIS

IL-PIL electrolyte separators were made using the procedure of Homann et al.[6]: a 25 μm thick porous polypropylene separator (Celgard 2500) was punched into a disc with a diameter of 18 mm, dried in vacuum (< 10^{-3} mbar) for 12 h, and soaked in a solution containing 1 M LiFSI in [1,3]PYRFSI (60 wt%) and PDADMAFSI (40 wt%) in acetonitrile (ACN, Solvionic, 1:1 wt ratio) for 1 h, dried passively in a polytetrafluoroethylene (PTFE) dish and subsequently soaked again.[25] This procedure was repeated for the other samples after adding LiFSI (99.99%, Solvionic) to the solution, to increase the salt concentrations summarized in Table 1. In a previous study Yoon et. al. found an optimum lithium salt concentration for lithium charge transfer around 3M LiFSI in [1,3]PYRFSI for the ILE system without polymer.[16] The optimum concentration for maximum lithium conductivity in IL-PIL can be similar to the previously found optimum of the ILE analogue.[25] Therefore, for the IL-PIL system a concentration of 20 wt%, LiFSI (called 20 IL-PIL) was selected, which contain a similar LiFSI/IL ratio to 3 M LiFSI in [1,3]PYRFSI. Similarly, an optimized lithium IL:PIL ratio was used, previously found to be 51:40 wt%, with 9 wt% lithium salt.[5,6] Concentrations of 9 wt%, 34 wt% and 50 wt% LiFSI (called 10, 35 and 50 IL-PIL respectively) were tested to determine trends as function of lithium salt concentration.

Table 1 Materials used in this study

Abbreviation based on roundoff % LiFSI	***m/m% Polymer PDADMA FSI***	***m/m% Ionic Liquid [1,3]PYR FSI***	***m/m% Salt Li FSI***	***Molarity LiFSI in PIL***
10	40%	51%	9%	0.56
20	35%	44%	21%	1.27
35	29%	37%	34%	1.88
50	22%	28%	50%	2.56

The infiltrated Celgard separator is then dried at 20 °C in vacuum (<10^{-3} mbar) for 24 h, and transferred into an argon-filled glovebox (see Fig. 1b). Separators (Celgard 3501) were dipped in 1M and 3M LiFSI in [1,3]PYR FSI solutions. Separators were fit in between two 12 mm lithium discs in a C2032 coin cell.

Electrochemical measurements

Electrochemical (EC) measurements were conducted using a PARSTAT MC200 module (Ametek) and a climate chamber. The cells were conditioned at setpoint temperature in a climate chamber (Memmert) for at least two hours and measured in duplo. Materials were tested in symmetric Lithium coin cell configuration. Electrochemical impedance spectroscopy (EIS) measurements were conducted in a range between 0.1 Hz and 100 kHz with 10 mV amplitude. After a resting period a potentiostatic measurement at 10 mV is conducted for at least 0.5 hour (dt=1 s, 10 ms during first 10 seconds). The steady state current of the potentiostatic measurement is taken as low frequency point (<0.5 mHz) to obtain steady state resistance R_{SS} calculated from steady state current I_{SS}. The potential relaxation after this period is measured during an hour (dt=1 s, 10 ms during first 10 seconds). A second EIS measurement is conducted to check if the cell resistances changed during the period (see example Figure S 2).

Pulse field gradient NMR

For Pulsed field gradient NMR, a Bruker Ascend 600 (B_0= 14.1 T) magnet equipped with a NEO console was used. A 5 mm NMR sample tube was filled with precursor solution described above. Drying was conducted at room temperature in an argon filled glovebox until the majority of acetonitrile was evaporated. To prevent flash boil-up, samples were subjected to stepwise vacuum of 200 mbar intervals with regular intervals of 30 minutes until full vacuum was reached. After 24 hours of drying samples were measured using stimulated echo pulse field gradient procedure on ^{7}Li for Li* tracer diffusivity ($\pi/2$ pulse length of 16.8 µs, 45 W and B_1=10-500 Gauss/cm for 2 ms), ^{19}F for FSI* tracer diffusivity ($\pi/2$ pulse length of 23 µs, 15.5 B_1=10-250 Gauss/cm for 2 ms) and ^{1}H for [1,3]PYR* tracer diffusivity ($\pi/2$ pulse length of 18 µs, 20.3 W, B_1=64 - 1280 Gauss/cm for 2 ms) using a linear gradient of 8 slices with typical diffusion times of 10-50 µs. Data was fit using the Stejskal-tanner equation.[26]

NMR relaxometry

For NMR relaxometry a Bruker Ascend 500 (B_0 =11.7 T) magnet equipped with a NEO console was used. The sample was filled in an airtight 4 mm rotor zirconia rotor with a vespel cap and inserted in a 4 mm triple resonance MAS NMR probe (Bruker). For ^{7}Li (194.37 MHz), $\pi/2$ pulse lengths of 3.5-4.5 µs (143.88 W) corresponding to RF field

strengths of 71.8-55.5 kHz were utilized. T_1 saturation recovery measurements were performed under static conditions in the temperature range of -40 to 85 °C. Low temperature measurements were conducted by cooling the variable temperature gas flow through liquid nitrogen as coolant and subsequent heating to the appropriate temperature. Relaxation measurement fitting was performed using the Dynamics Center module from Bruker. Temperature dependent relaxation rate fitting was conducted using the OriginPro 2019 software after deconvolution of the spectra.

In order to estimate the rate of lithium complexation and transfer, spin-lattice (T_1) relaxation measurements can be used to determine the hopping rate and energetics of lithium transfer from one position to another. Similarly, fluorine relaxation can be correlated to the transfer of FSI ions with respect to its surroundings. The change in relaxation rate correlates to the effectiveness at which the nucleus is able to lose its excited state and return to equilibrium. In our case, the Larmor frequency of lithium (ω_0=194.37 MHz) and fluorine (ω_0=470.592 MHz) in the magnetic field (500 MHz ^{1}H) which we use, determine the characteristic rate $1/\tau_c$ at a certain temperature T_C, at which the nucleus relaxes fastest in its surroundings. The nuclear relaxation rate at this temperature is most efficient, and generally correlates to the average transfer period of the nucleus from one surrounding to another. When the movement of ions is uncorrelated, this results in a symmetric exponential shape which can be fit using the Bloembergen-Purcell-Pound[27] formulation (Eq. 1) to obtain the activation energy of the transfer.[28] Here the relaxation period T_1 is fit as function of the hopping time τ and second moment, or interaction strength M_2.

$$\frac{1}{T_1} = \frac{2}{3} M_2 \left(\frac{\tau}{1 + {\omega_0}^2 \tau^2} + \frac{4\tau}{1 + 4{\omega_0}^2 \tau^2} \right)$$

Eq. 1

The hopping period at other temperatures is subsequently estimated using the Arrhenius equation (Eq. 2), solving τ_0 and E_A. The characteristic hopping period τ_c, having the duration of the inversed larmor frequency, is measured as the fastest relaxation at temperature T_c.

Eq. 2

$$\tau = \tau_0 e^{\frac{-E_A}{k_b T}}$$

The relaxometry method yields information on the energetic environment at a specific (relatively high) frequency (short time scale), which combined with PFG can show the correlation of complexation time, diffusivity and transference.

Raman Spectroscopy

Raman spectroscopy was performed on a Horiba Jobin Yvon LabRAM HR800 Raman Spectroscopy system, using an excitation wavelength of 515 nm (Cobolt Fandango™ 50) and a 50x objective lens. Raman measurements were recorded between 100 and 2000 cm^{-1} and an acquisition time of 20 s and accumulation of 5 using the maximum slit and hole opening (1000) with a grating of 1800. To avoid air exposure, the specimens were transferred (in an Ar glovebox) to an airtight homemade optical sample holder.

Derivation of transference and conductivity

The transference number during anion blocking condition (t_{Li+}^{abc}, Eq. 3) is a useful measure to quantify net effective current for lithium ion battery applications in concentrated solutions.[29] The anion blocking transference definition from Vargas-Barbosa and Roling[29] is used which is the ratio of lithium conductivity σ_{Li+} to total conductivity σ_{tot} which is defined as the sum of lithium and other, residual conductivity σ_{res}. The anion blocking transference compensates for initial current contribution and solid electrolyte interface (SEI) layer resistances, R_{SEI} which varies between interface layer composition, salt concentrations and temperatures. The ratio of lithium conductance in the bulk to the total conductance is calculated using resistances R_{ele} and R_{SEI} obtained from high frequency and inflection point in the EIS spectrum respectively. Steady state resistance R_{ss} is obtained from current j_{ss} under potential U from PITT (Figure S 1). Electrolyte resistance R_{ele} is measured using the high frequency impedance resistance in the EIS spectra. The SEI resistance R_{SEI} is taken as the real resistance readout at the tipping point of the first semicircle (10 – 50 Hz) in the EIS spectra, minus the electrolyte resistance. Steady state current j_{ss} is taken as the current readout after 12 hours of polarization at potential U.

Eq. 3

$$t_{Li^+}{}^{abc} = \frac{\sigma_{Li^+}}{\sigma_{Li^+} + \sigma_{res}} = \frac{\sigma_{Li^+}}{\sigma_{tot}} = \frac{1/(\frac{U}{j_{ss}} - R_{SEI})}{1/R_{ele}}$$

This transference number is compared with the transference determined from diffusivities obtained by PFG (Eq. 4).[29] Here the charge is not indicated, as in PFG this cannot be discerned.

Eq. 4

$$t_{Li+}^{PFG} = \frac{\sigma^*{}_{Li}}{\sigma^*{}_{Li} + \sigma^*{}_{FSI} + \sigma^*{}_{13PYR}}$$

The tracer conductance (σ*) is calculated using the Nernst Einstein equation.

$$\sigma^*{}_x = \frac{c_x F^2}{RT} D_x^{PFG}$$

The tracer conductance may be split in an associated (1- α) and dissociated fraction α following Vargas-Barbosa and Roling [29], yielding the lithium ion conductance σ_{Li+} :

$$\sigma^*{}_{Li} = \alpha\sigma_{Li^+} + (1-\alpha)\sigma_{LiFSI}$$

In analogy to [29] this can be done with FSI^- and counter ions $13PYR^+$ and $PDADMA^+$ using dissociated fractions β and γ respectively. Since PDADMA is immobile, $\sigma_{PDADMA+}$ remains practically zero. The PFG transference becomes Eq. 5.

Eq. 5

$$t_{Li+}^{PFG} = \frac{\alpha\sigma_{Li^+} + (1-\alpha)\sigma_{LiFSI}}{\alpha\sigma_{Li^+} + \beta\sigma_{13PYR^+} + (\alpha+\beta+\gamma)\sigma_{FSI^-} + 2(1-\alpha)\sigma_{LiFSI} + (1-\beta)\sigma_{13PYRFSI}}$$

$$= \frac{\sigma_{Li^+} + s}{\sigma_{Li^+} + \left(1 + \frac{(\beta+\gamma)}{\alpha}\right)\sigma_{FSI^-} + \frac{\sigma^*{}_{13PYR}}{\alpha} + 2s}$$

With the variable s indicating the associated fraction to LiFSI as $s = \frac{1-\alpha}{\alpha}\sigma_{LiFSI}$

Lithium Diffusivity and Transference in High Lithium Concentration Ternary Polymer Ionic Liquids

Two ionic transfer mechanisms contribute to the lithium transference number in anion-blocking conditions. The first being through free lithium (cation) migration and the second through neutral pair diffusion with anion migration.[29] Similarly the anion blocking transference is defined as Eq. 6. [29]

Eq. 1

$$t_{Li+}^{abc} = \frac{\sigma_{Li^+} + \frac{s\sigma_{FSI^-}}{(\sigma_{FSI^-} + s)}}{\sigma_{Li^+} + \left(1 + \frac{(\beta + \gamma)}{\alpha}\right)\sigma_{FSI^-} + \frac{\sigma^*_{13PYR}}{\alpha}}$$

Free lithium cation migration requires the lithium ion to hop from site to site in order to balance the ion transfer happening at the electrode interfaces. For neutral pair diffusion with anion migration there is a dependence on FSI ions hopping to do the same.

Comparison of t_{Li+}^{abc} and t_{Li+}^{PFG} in Eq. 5 and Eq. 6 highlights two differences between the techniques. First, the conductivity in t_{Li+}^{abc} originating from anion migration is not appropriately accounted for in the PFG transference estimation. This mode of conductivity is determined by the degree of association with lithium(s) and motion of free anions σ_{FSI^-}. Second, the degree of association lowering the PFG transference, giving t_{Li+}^{PFG} =0.5 at high degrees of association $s >> \sigma_{ion}$ diverges from the physical behavior of electrolytes in anion blocking conditions. In this work the two values are reported as function of salt concentration to observe which type of migration dominates the mode of transference.

A comparison of tracer diffusivity and effective diffusivity is conducted using PFG and the potential relaxation rate after PITT. For electrochemical diffusivity from potential relaxation generally two approaches are used.[30] Long term relaxation yields diffusivity estimations near concentration equilibrium. Short term relaxation yield diffusivity estimations which may need concentration correction. Short term relaxation is suitable here due to the relatively short depolarization period over separator thickness L (30 µm) and limited concentration polarization with PITT (5 – 9 mV dU, where ~46 mV/mol was measured in a concentration cell). In the estimation of short relaxation diffusivity $D_{+,eff}$ the slope m of a linear fit of potential readout U versus squared time (Eq. 7) from t= 0.5 to 8 seconds is used in Eq. 8.[30]

Eq. 7

$$U = mt^{1/2} + U_0$$

Eq. 8

$$D_{Li^+,eff} = \frac{\pi L^2}{16}\left(\frac{m}{U_0}\right)^2$$

The slow potential relaxation (6 s > t > 10 s) which does not include activity coefficients does not show linearity upon plotting log(U(t)) and are two orders below the expected diffusivities (Figure S 5). The low values obtained using long potential relaxation may origin from the almost complete relaxation of short range polarization, either due to the short pathway (low resolution) or by larger secondary effects like SEI equilibration in the symmetric lithium metal cell after 12 hours of potentiostatic measurement.

RESULTS

After acetonitrile evaporation, a transparent Celgard sheet was obtained which was infiltrated with a non-sticky gel for concentrations lower than 50 IL-PIL. The conductivity and transference of the systems are measured in symmetric Li:Li cells through EIS and potentiostatic measurements at various temperatures as is shown in Figure 2. Similar to the ILE analogue the lithium conduction is the highest in the 20 IL-PIL system (Figure 2). The t_{Li+}^{abc} increases with increasing salt concentration to a more typical lithium-salt-in-polymer value of t_{Li+}^{abc}= 0.26. However, for the 35 IL-PIL and 50 IL-PIL material the total conductivity drops severely. Strikingly the transference number of the 10 IL-PIL and 20 IL-PIL systems are not that different compared to the 1 M and 3 M ILE systems (Figure S 3). Based on these observations, the role of the polymer seems to have a minimal effect on the transference number at these concentrations.

Increasing the temperature does typically increase the total conductivity and may cause divergence of the transference number when the mobilities of the constituents have a different temperature dependence. The total conductivity σ_{tot} of 20 IL-PIL is in the same order compared to 10 IL-PIL as function of temperature (Figure 2B). With increasing salt concentrations, the σ_{tot} becomes generally lower. The observed optimum of $\sigma_{Li,RT}$ for 20 wt% LiFSI concentration in 20 IL-PIL remains. However σ_{Li+} shows a different temperature dependence between the different salt concentrations.

At 333 K, the 50 IL-PIL σ_{Li} even exceeds the 35 IL-PIL σ_{Li} due to its high transference number.

Elevated temperatures generally show a positive effect on the transference number (Figure 2A, EC lines). This positive influence is stronger for higher salt concentrations. The activation energy for lithium transfer generally appears to be higher compared to the other conducting constituents, which translates to an increasing transference as function of temperature for all materials tested. The plasticising effect of 1,3PYRFSI increases the mobility of all constituents, yielding a higher conductivity σ_{res} for lower LiFSI fraction IL-PILs. Immobilization of the FSI anion, which may yield transference numbers above 0.5 are not observed.

A comparison of the transferences measured electrochemically and derived from PFG NMR provides insight into the mode of transport and utilization of ion mobility in the material (Figure 2A, PFG lines). Only for 35 IL-PIL the t_{Li+}^{PFG} shows a negative trend as a function of temperature. In this system the FSI* tracer conductance is increasing more at higher temperatures compared to the other tracer conductivities in this material. The anion blocking transference t_{Li+}^{abc} is generally found to be lower compared to t_{Li+}^{PFG} (Figure 2A) for all materials tested and both values are below 0.5. This behavior is expected to originate from a high mobility of ion pairs compared to dissociated ions (SI Figure S 4). A $t_{PFG} < 0.5$ is expected only with a relatively high mobility of secondary cations, like $[1,3]PYR^{+}$. An exception to the comparatively lower t_{Li+}^{abc} is the 50 IL-PIL, which shows a t_{Li+}^{abc} which is equal or higher than t_{Li+}^{PFG}. Based on Eq. 5 and Eq. 6, an increasing t_{Li+}^{PFG} can be explained by a lower conductivity of [1,3]PYR* or if the transfer mechanism of free lithium starts to dominate. The tracer diffusivities of Li* and FSI* as a function of temperature remain the same order of magnitude for all LiFSI concentrations tested (Figure 3A). Also the ratio of [1,3]PYR*/Li* diffusivity remains similar (0.76 for 10 IL-PIL and 0.56 for 50 IL-PIL, Figure S 11), indicating a small decrease in the specific [1,3]PYR* diffusivity. The total conductivity σ_{tot} does however drop, indicating less mobility of conducting ions while the specific lithium conductivity σ_{Li} does not show much difference (Figure 2B). Therefore in this case, conduction through free lithium ions appears to become a significant part of the charge transfer mechanism in anion blocking condition.

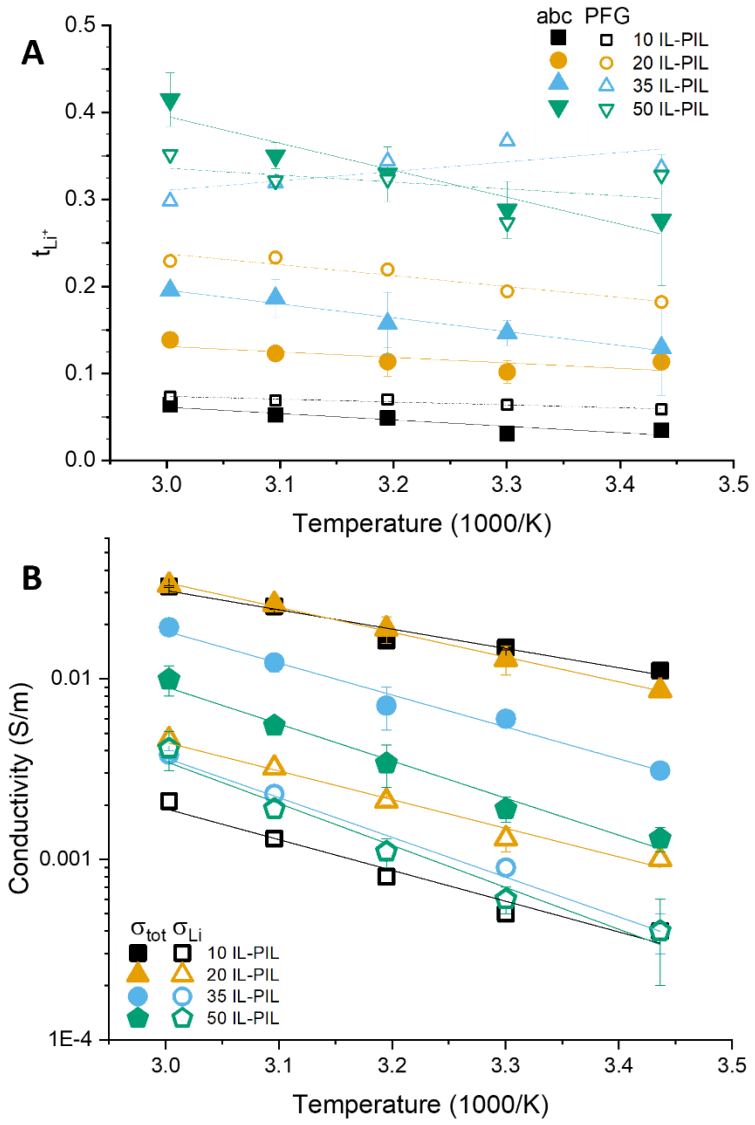

Figure 2 (A) Transference number obtained electrochemical under anion blocking condition t_{Li+}^{abc} compared to transference number t_{Li+}^{PFG} obtained from PFG NMR and (B) total ionic conductivity σ_{tot} and lithium-ion conductivity σ_{Li} of IL-PILs with varying LiFSI concentration as a function of temperature. With higher lithium salt concentration the contribution of lithium conductivity increases. Error bars indicate difference between duplic measurement.

Lithium Diffusivity and Transference in High Lithium Concentration Ternary Polymer Ionic Liquids

Differences between tracer diffusivity D_{PFG} and effective diffusivity D_{EC} obtained through electrochemical potential relaxation show the degree of correlated motions of ions by e.g. association/solvation or repulsion. For IL-PIL the tracer diffusivity of Li* and FSI* has a strong dependence on temperature and are in the same order of magnitude in the complete temperature range (Figure 3A). However, D_{EC} (Figure 3B) is an order of magnitude lower and shows only a weak dependence on temperature. A temperature dependence similar to D_{PFG} with increasing salt concentrations is not observed in the potential relaxation method. This indicates that D_{PFG} does not adequately represent the ion motion during depolarization of the electrolyte. PFG measurements do not probe association as it directly traces the bulk migration of the NMR sensitive nucleus in the applied magnetic field gradient only. Therefore the observed difference between tracer and effective diffusivities may originate from a high degree of association of lithium to the FSI counterion.

The temperature dependence of D_{PFG} (Figure 3A/B, ^{7}Li for Li* and ^{19}F for FSI*) and conductivities σ_{Li} and σ_{tot} (Figure 2) were fitted using the Arrhenius equation yielding the activation energy $E_{A,diff}$ and $E_{A,EC}$ respectively (Figure 3C). Activation energies of the total conductivity $E_{A,EC,tot}$ and FSI* tracer diffusivity $E_{A,diff,FSI}$ show a similar temperature dependence for both processes. The activation energies show a trend that is in line with viscous behavior. Upon the addition of polymers or kosmotropic (order-making, interaction enhancing) salts in polyelectrolyte solutions, an increase in the viscosity is observed due to higher constrained mobility and lowered electrostatic repulsion.[31] Such constraints cause an increased dependence on temperature, which is observed in the IL-PIL series as well. The change in activation energy of FSI* tracer diffusivities $E_{A,diff,FSI}$ are smaller compared to the change in $E_{A,EC,tot}$ but show a similar trend. Upon addition of the polymer the FSI diffusion activation energy $E_{A,diff,FSI}$ shows a significant decrease, which is not translated to a decrease of $E_{A,EC,tot}$ (Figure 3C, ^{19}F of 1M ILE versus 10 IL-PIL). This indicates that the FSI^- anion becomes less dependent on changes of ordering when the polymer is introduced.

The temperature dependence of lithium diffusion and conduction point to multiple modes of lithium transfer. Similar to lithium diffusion $D_{diff,Li}$ the temperature dependence of lithium conduction σ_{Li} decreases when the polymer is introduced ($E_{A,Diff,Li}$ and $E_{A,EC,Li}$ Figure 3C between 1M ILE versus 10 IL-PIL). However, the temperature dependence of lithium conductivity $E_{A,EC,Li}$ seems to follow the trend of

$E_{A,EC,tot}$ above 10 IL-PIL concentration rather than $E_{A,diff,Li}$, which hints the conduction mechanism at these concentrations is not solely dependent on lithium ion diffusion. For ILE this trend in activation energy is similar: a higher LiFSI concentration results in a lower temperature dependence of lithium diffusivity while it shows an increased temperature dependence for lithium conductivity (following the total conductivity). In figure 3C the activation energies for lithium conductivity $E_{A,EC,Li}$ of 20 IL-PIL shows a lower temperature dependence compared to both lower and higher salt concentrations 10 IL-PIL and 35 IL-PIL respectively. A second observation is that the lower temperature dependence of lithium diffusion $E_{A,diff,Li}$ in 50 IL-PIL compared to 35 IL-PIL does not translate to a lower temperature dependence of lithium conductivity $E_{A,EC,Li}$. This highlights PFG NMR measurements are not sufficient to predict the mode of conduction in ternary systems as lithium association plays a strong role in the conduction mechanism.

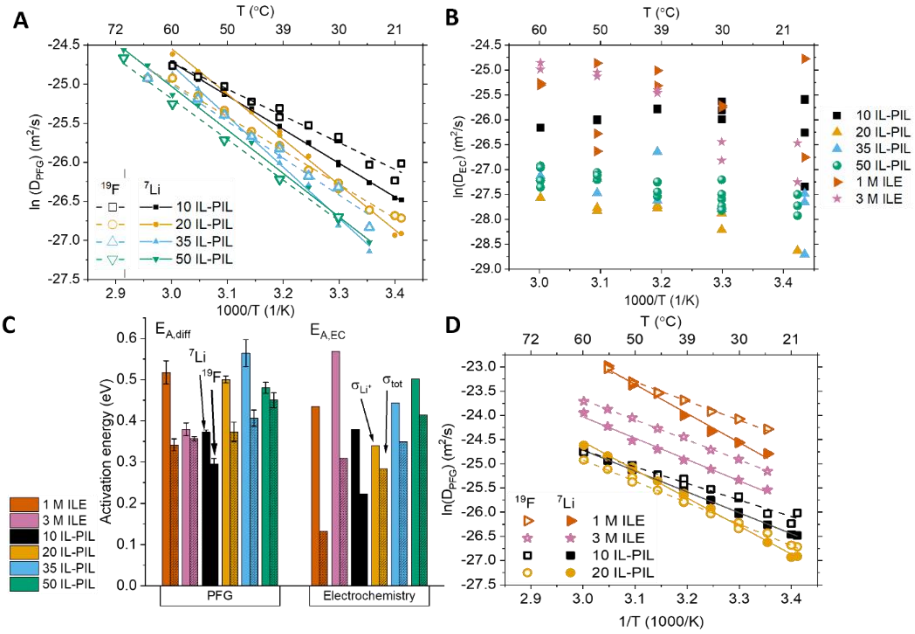

Figure 3 Temperature dependence of Lithium and FSI Diffusivities of IL-PILs and ILE from 20 to 60 °C. A) Lithium (^{7}Li) and FSI (^{19}F) tracer diffusivity in PILs obtained through PFG NMR. B) Effective electrochemical diffusivity $D_{Li+,eff}$ obtained by fast potential relaxation measurements. C) Activation energies obtained by fitting Arrhenius equation on tracer diffusivities (left), lithium and total conductivities (right). D) Lithium (^{7}Li) and FSI (^{19}F) tracer diffusivity of PILs compared to their ILE analogue.

Solvation and Raman

Raman spectroscopy is used to study the solvation environment of lithium ions in the IL-PIL system when the LiFSI concentrations are increased. The S-N-S symmetric stretching vibration of FSI is often used to obtain information about the Li^+ - FSI^- coordination modes. These modes are typically categorised as solvent-separated ion pairs (SSIP at 720 cm^{-1}), contact ion pairs (CIP at 730 cm^{-1}) and aggregates (AGG I at 739 cm^{-1} and AGG II at 752 cm^{-1}).[32–34] According to the literature, diluted LiFSI based electrolytes (< 0.25 LiFSI/solvent ratio) result in predominantly SSIP and CIP Raman bands, while the peaks associated with Li^+ - FSI^- aggregates become more present at moderate-to-higher salt concentrations.[32] A similar trend is observed in our Raman spectra in Figure 4. The lowest LiFSI concentration at 10 IL-PIL shows a signal at lower Raman shifts, matching well with SSIP and CIP coordination modes. Peak broadening was observed at 20 IL-PIL, indicating the coexistence of different types of ionic – solvent interactions, which did not change when the LiFSI concentration is increased to 35 IL-PIL. This result is not surprising since the transference number barely changed (Figure 2A) between 20 and 35 IL-PIL. At 50 IL-PIL, the Li^+ - FSI^- environments are mostly in their aggregated states. The 50 IL-PIL shows phase transitions at -16.3 (2.03 J/g) and -0.9 °C (1.77 J/g) with DSC (Figure S 7, using a heating rate of 10 °C/min), where lower concentrations only show a change in specific heat below -15 °C, but show no clear phase transition between -35 and 100 °C. The phase transition of 50 IL-PIL, together with the low aggregation indicates LiFSI is near its glass transition state.

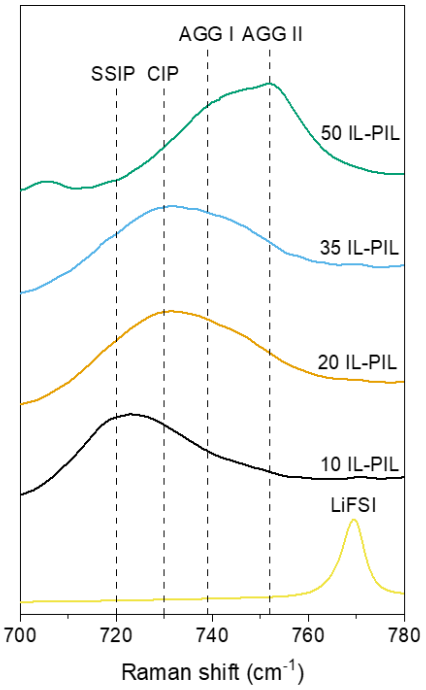

Figure 4 Raman spectra of the S-N-S stretching vibration between 700 and 780 cm^{-1} for various LiFSI concentrations (given in wt%) in IL-PIL at room temperature. Different Li^+ - FSI^- ion pairing modes, such as solvent-separated ion pairs (SSIP, 720 cm^{-1}), contact ion pairs (CIP, 730 cm^{-1}) and aggregates (AGG I at 739 cm^{-1} and AGG II at 752 cm^{-1}) are identifiable with an increase in the LiFSI concentration and match well with ref [33,34].

Spin lattice relaxation

The duration of lithium association to its counterion is probed by measuring the differences in relaxation rate in NMR relaxometry for the Li and the counterion. This yields the Li^+ and FSI^- hopping frequency which is the inverse of the complexation time (Figure 5A and B respectively). The peak maxima (drop down lines) indicate the temperature at which the hopping frequency is equal to the Larmor frequency of the nucleus probed. The fluorine spectrum (Figure 5B) highlights that this characteristic frequency occurs at higher temperatures with increasing salt concentration. This indicates a lowered mobility within the solvation complex when the LiFSI salt

concentration is increased. The ILE indicate increased hopping frequency compared to the IL-PIL analogues (Figure 5B, dashed drop down lines).

The characteristic lithium hopping rate does not follow the same trend compared to fluorine, when increasing the salt concentration: above 20 wt% LiFSI with increasing LiFSI mass fraction the characteristic rate does not change significantly (Figure 5A, drop down lines). The relaxation rate increases (Figure 5A, peak height), but that illustrates an increasing dipolar interaction strength, not the timescale of the mobility itself. As the FSI^- hopping frequency decreases as a function of salt concentration, this results in a net increase in the lithium hopping rate. This may explain the higher transference numbers at increasing lithium salt concentrations. Lithium mobility in ionic liquids show generally a higher characteristic rate compared to the IL-PIL analogues (Figure 5A). The BPP model for NMR spin-lattice relaxation shows a good fit with a single uncorrelated hopping transfer process (Figure 5, fitting lines). The peak symmetry indicates that lithium transfers occurs via a single transfer process between equal (or indistinguishable) states of aggregation during nanosecond intervals. The model fit results in the activation energy for transfer $E_{A,trans}$ (Figure 5C) which allow extrapolation of the characteristic hopping rate at temperatures other than T_C using the Arrhenius equation.

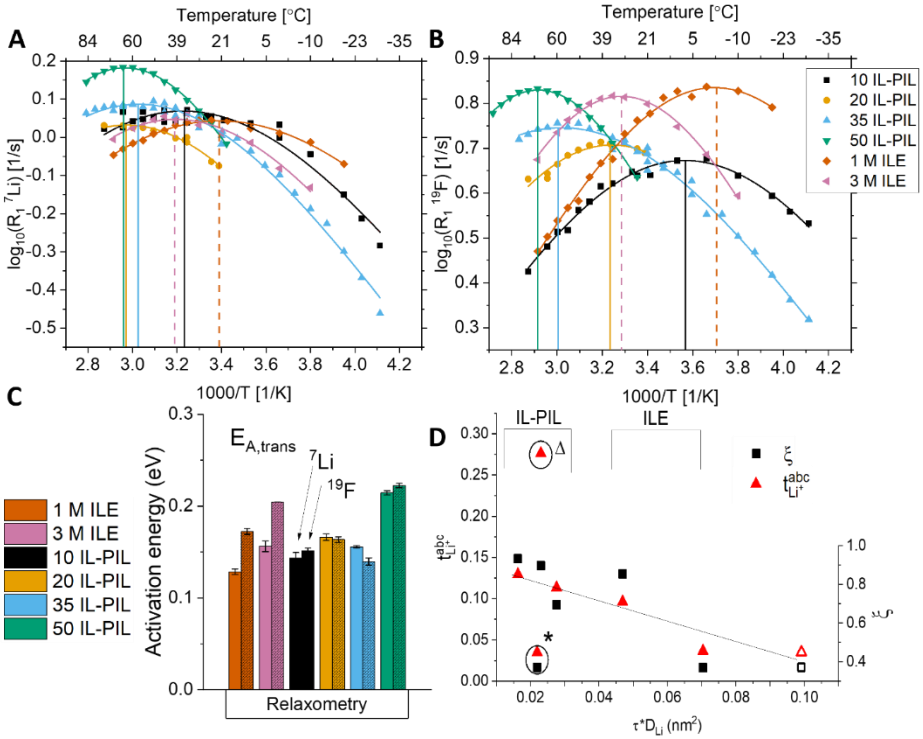

Figure 5 ^{7}Li (A) and ^{19}F (B) NMR Relaxometry on IL-PIL and ILE. The change in relaxation rate R_1 as function of temperature indicate the change in spin-lattice motion of the nucleus at its larmor frequency. Line indicates the fit of the BPP model. Activation energies obtained by the BPP model fit (C) and correlation between transference and RMS displacement estimation using PFG diffusivity and characteristic hopping time at 30°C (D). Line is added in (D) to guide the eye. Open triangle/square indicates implied RMS displacement of 10 IL-PIL (encircled with asterisk), when similar τ_c as 20 IL-PIL is assumed as phase changes occurred at temperatures above 70 °C during relaxometry. 50 IL-PIL is second outlier indcated with Δ symbol.

To test if the mode of conduction is through neutral pair displacement, the anion blocking transference can be correlated to the displacement of lithium in a complex. The duration of a complex can be estimated by taking the inverse of the lithium hopping frequency, which yields characteristic duration of a complex τ. When τ is multiplied by the tracer diffusivity of lithium D_{Li}^{PFG} this yields the neutral displacement τD_{Li} (Figure 5D).

Lithium Diffusivity and Transference in High Lithium Concentration Ternary Polymer Ionic Liquids

To increase the mechanistic understanding, Wohde et. Al [24] proposed a quantitative method to distinguish correlated movement of lithium originating from counterions (by associative movements) and cation-cation and/or anion-anion interactions. This approach relates the anion blocking transference to the complex duration using parameter ξ as the degree of correlated movement via Eq. 9.[24] Here ϕ is defined as the degree of non-ideality originating from cation-cation correlations, and (1- ϕ) as the degree of non-ideality from anion-anion correlations. Here the case of equal contributions of cation-cation and anion-anion non-idealities is tested which result in $\phi=t_{Li+}^{PFG}$.

Eq. 9

$$t_{Li^+}^{abc} = \frac{\xi^2 - 4\phi + 4\phi^2}{4(1-\phi)(1-\xi)}$$

As expected a negative correlation appears between lithium complex displacement τ^*D_{Li} and transference (Figure 5D). Two outliers are observed. The 50 IL-PIL (Figure 5D, indicated with Δ) indicates lithium complex displacement is not dictating the mode of transference $t_{Li^+}^{abc}$ as it does not follow the trend of lithium complex displacement found for other IL-PIL concentrations (Figure 5D, line). A change in mode of conductance by free lithium ions when LiFSI becomes the major mass fraction of the material is expected. This could result in strong cation-cation (anti)correlations in which case Eq. 9 would not be applicable. In concordance, the solvation of lithium (Figure 4) and hopping transfer energy $E_{A,trans}$ (Figure 5C) increases significantly for the 50 IL-PIL compared to lower LiFSI weight fractions. This indicates a higher energy is needed for breaking up the more strongly bound aggregates observed with Raman (Figure 4). In contrast, the change in $E_{A,trans}$ for PILs does not change significantly for concentrations below 50 %wt LiFSI.

The second outlier is at 10 IL-PIL (Figure 5C, circle with asterisk) which shows a poor correlation between complexation, transference and the degree of association . It must be noted that during relaxometry acquisition of 10 IL-PIL, samples which were held above approximately 70 °C repeatedly showed an increasing instead of a decreasing Li relaxation rate during ramping down of the temperature (Figure S 7). The

relaxation time becomes similar to ionic liquids with a maximum relaxation rate at a lower temperature. This may indicate that a (local) phase separation occurred, which is not visible in differential scanning calorimetry (DSC) measurements (Figure S 8). Phase separation of 10 IL-PIL at high temperatures may have influenced determination of the τ_c, implying longer complexation times, as T_C was never reached during heating. When a similar characteristic temperature T_C as 20, 35 and 50 IL-PIL are assumed the correct correlation between τ^*D_{Li} and $t_{Li^+}^{abc}$ becomes apparent (Figure 5D, open triangle/square).

DISCUSSION

The conduction mechanism of salts dissolved in polymers can be understood by correlating the polymer's rheologic behavior and carrier concentration to the conductive performance of the solvated ions.[35] Ternary polymer ionic liquids show different behavior as the ionic liquid cation lowers the effective transference but increases the mobility of all constituents to a great extent. In this work a range of lithium salt concentrations are tested to understand the role of the ionic liquid cation in constructive and anticorrelated motion of the lithium ion.

The energetics of the ionic lithium complex formation, as observed by relaxometry, remain unchanged with increasing lithium salt concentration until the lithium salt becomes the dominant fraction in 50 PIL. Below this concentration a contribution from the presence of the polymer in the gel is not apparent in the lithium transfer process, as the activation energy of transfer is not altered. Tracer diffusivity of FSI, being the counterion of all cation constituents, forms a good indicator for the change in mobility by viscosity changes in the polymer gel. The activation energy of conduction shows a strong correlation to the FSI diffusivity. The conduction mechanism can therefore be described as 'cluster diffusion dominated'. Positive correlations of transference to the degree of association ξ imply a significant contribution of neutral carriers' mobility. A dramatic shift in both relaxation behavior and solvation of lithium is observed in 50 IL-PIL, indicating a strong shift in lithium transfer mechanism. The transfer may be described as 'hopping transfer dominated' originating from free lithium ion conduction at these concentrations, as AGG II aggregation state dominates for this concentration.

The high temperature dependence of mobility in 'dilute' lithium-ion concentrations in ionic liquids as observed in PFG NMR becomes smaller when the polymer is introduced. Increasing the lithium salt concentration in the ternary systems reverses

this effect. The activation energy of lithium diffusivity in the 20 IL-PIL shows a local minimum between this trade-off, and electrochemical measurements show a local optimum of lithium conductivity at room temperature for this material. The increased net lithium conductivity of 20 IL-PIL indicates an optimal balance between the carrier concentration, correlated motion and viscosity below 60 °C. Generally the diffusivity of lithium in IL-PILs are lower compared to the ILE, which may be explained by the severe change in material viscosity.

IL-PILs can be deposited on (electrode) substrates using wet processing techniques and therefore pose a valuable material for use as lithium conductor in solid state batteries. This work shows that depending on the desired transference number and conductivity one can select the lithium salt concentration to have the desired conduction mechanism. At high temperatures the lithium conductivity consistently increases with higher weight fractions of the conducting salt. At lower temperatures there exists an optimum which balances the mobility and lithium concentration. For high temperature lithium battery applications (40-60 °C) IL-PIL with high conducting salt concentrations have the benefit of showing high transference numbers as well.

REFERENCES

(1) Shaplov, A. S.; Marcilla, R.; Mecerreyes, D. Recent Advances in Innovative Polymer Electrolytes Based on Poly(Ionic Liquid)s. *Electrochimica Acta* **2015**, *175*, 18–34. https://doi.org/10.1016/j.electacta.2015.03.038.

(2) Eshetu, G. G.; Mecerreyes, D.; Forsyth, M.; Zhang, H.; Armand, M. Polymeric Ionic Liquids for Lithium-Based Rechargeable Batteries. *Mol. Syst. Des. Eng.* **2019**, *4* (2), 294–309. https://doi.org/10.1039/C8ME00103K.

(3) Barbosa, J. C.; Correia, D. M.; Gonçalves, R.; de Zea Bermudez, V.; Lanceros-Mendez, S.; Costa, C. M. Ionic Liquids in the Scope of Lithium-Ion Batteries: From Current Separator Membranes to next Generation Sustainable Solid Polymer Electrolytes. *Mater. Chem. Front.* **2023**, *7* (21), 5046–5062. https://doi.org/10.1039/D3QM00852E.

(4) Makhlooghiazad, F.; Miguel Guerrero Mejía, L.; Rollo-Walker, G.; Kourati, D.; Galceran, M.; Chen, F.; Deschamps, M.; Howlett, P.; O'Dell, L. A.; Forsyth, M. Understanding Polymerized Ionic Liquids as Solid Polymer Electrolytes for Sodium Batteries. *J. Am. Chem. Soc.* **2024**, *146* (3), 1992–2004. https://doi.org/10.1021/jacs.3c10510.

(5) Fu, C.; Homann, G.; Grissa, R.; Rentsch, D.; Zhao, W.; Gouveia, T.; Falgayrat, A.; Lin, R.; Fantini, S.; Battaglia, C. A Polymerized-Ionic-Liquid-Based Polymer

Electrolyte with High Oxidative Stability for 4 and 5 V Class Solid-State Lithium Metal Batteries. *Advanced Energy Materials* **2022**, *12* (27), 2200412. https://doi.org/10.1002/aenm.202200412.

(6) Homann, G.; Wang, Q.; Liu, S.; Devincenti, A.; Karanth, P.; Weijers, M.; Mulder, F. M.; Piesins, M.; Gouveia, T.; Ladam, A.; Fantini, S.; Battaglia, C. A Quasi-Solid-State Polymer Lithium–Metal Battery with Minimal Excess Lithium, Ultrathin Separator, and High-Mass Loading NMC811 Cathode. *ACS Appl. Energy Mater.* **2024**, *7* (21), 10037–10043. https://doi.org/10.1021/acsaem.4c02099.

(7) Nicotera, I.; Oliviero, C.; Henderson, W. A.; Appetecchi, G. B.; Passerini, S. NMR Investigation of Ionic Liquid−LiX Mixtures: Pyrrolidinium Cations and TFSI $^{-}$ Anions. *J. Phys. Chem. B* **2005**, *109* (48), 22814–22819. https://doi.org/10.1021/jp053799f.

(8) Moreno, M.; Simonetti, E.; Appetecchi, G. B.; Carewska, M.; Montanino, M.; Kim, G.-T.; Loeffler, N.; Passerini, S. Ionic Liquid Electrolytes for Safer Lithium Batteries: I. Investigation around Optimal Formulation. *J. Electrochem. Soc.* **2017**, *164* (1), A6026–A6031. https://doi.org/10.1149/2.0051701jes.

(9) Brinkkötter, M.; Lozinskaya, E. I.; Ponkratov, D. O.; Vlasov, P. S.; Rosenwinkel, M. P.; Malyshkina, I. A.; Vygodskii, Y.; Shaplov, A. S.; Schönhoff, M. Influence of Anion Structure on Ion Dynamics in Polymer Gel Electrolytes Composed of Poly(Ionic Liquid), Ionic Liquid and Li Salt. *Electrochimica Acta* **2017**, *237*, 237–247. https://doi.org/10.1016/j.electacta.2017.03.219.

(10) Brinkkötter, M.; Gouverneur, M.; Sebastião, P. J.; Vaca Chávez, F.; Schönhoff, M. Spin Relaxation Studies of Li $^{+}$ Ion Dynamics in Polymer Gel Electrolytes. *Phys. Chem. Chem. Phys.* **2017**, *19* (10), 7390–7398. https://doi.org/10.1039/C6CP08756F.

(11) Martinez-Ibañez, M.; Boaretto, N.; Meabe, L.; Wang, X.; Zhu, H.; Santiago, A.; Zugazua, O.; Forsyth, M.; Armand, M.; Zhang, H. Revealing the Anion Chemistry Effect on Transport Properties of Ternary Gel Polymer Electrolytes. *Chem. Mater.* **2022**, *34* (16), 7493–7502. https://doi.org/10.1021/acs.chemmater.2c00260.

(12) Gouverneur, M.; Jeremias, S.; Schönhoff, M. 7Li Nuclear Magnetic Resonance Studies of Dynamics in a Ternary Gel Polymer Electrolyte Based on Polymeric Ionic Liquids. *Electrochimica Acta* **2015**, *175*, 35–41. https://doi.org/10.1016/j.electacta.2015.03.026.

(13) Agrawal, A.; Yari, S.; Hamed, H.; Gouveia, T.; Lin, R.; Safari, M. Synergistic Interactions between the Charge-transport and Mechanical Properties of the Ionic-liquid-based Solid Polymer Electrolytes for Solid-state Lithium Batteries. *Carbon Energy* **2023**, *5* (11), e355. https://doi.org/10.1002/cey2.355.

(14) Pont, A.-L.; Marcilla, R.; De Meatza, I.; Grande, H.; Mecerreyes, D. Pyrrolidinium-Based Polymeric Ionic Liquids as Mechanically and

Electrochemically Stable Polymer Electrolytes. *Journal of Power Sources* **2009**, *188* (2), 558–563. https://doi.org/10.1016/j.jpowsour.2008.11.115.

(15) Appetecchi, G. B.; Kim, G.-T.; Montanino, M.; Carewska, M.; Marcilla, R.; Mecerreyes, D.; De Meatza, I. Ternary Polymer Electrolytes Containing Pyrrolidinium-Based Polymeric Ionic Liquids for Lithium Batteries. *Journal of Power Sources* **2010**, *195* (11), 3668–3675. https://doi.org/10.1016/j.jpowsour.2009.11.146.

(16) Yoon, H.; Howlett, P. C.; Best, A. S.; Forsyth, M.; MacFarlane, D. R. Fast Charge/Discharge of Li Metal Batteries Using an Ionic Liquid Electrolyte. *J. Electrochem. Soc.* **2013**, *160* (10), A1629–A1637. https://doi.org/10.1149/2.022310jes.

(17) Wang, X.; Zhu, H.; Girard, G. M. A.; Yunis, R.; MacFarlane, D. R.; Mecerreyes, D.; Bhattacharyya, A. J.; Howlett, P. C.; Forsyth, M. Preparation and Characterization of Gel Polymer Electrolytes Using Poly(Ionic Liquids) and High Lithium Salt Concentration Ionic Liquids. *J. Mater. Chem. A* **2017**, *5* (45), 23844–23852. https://doi.org/10.1039/C7TA08233A.

(18) Rosenwinkel, M. P.; Schönhoff, M. Lithium Transference Numbers in PEO/LiTFSA Electrolytes Determined by Electrophoretic NMR. *J. Electrochem. Soc.* **2019**, *166* (10), A1977–A1983. https://doi.org/10.1149/2.0831910jes.

(19) Martínez-Crespo, P.; Otero-Lema, M.; Cabeza, O.; Montes-Campos, H.; Varela, L. M. Structure, Dynamics and Ionic Conductivities of Ternary Ionic Liquid/Lithium Salt/DMSO Mixtures. *Journal of Molecular Liquids* **2022**, *359*, 119188. https://doi.org/10.1016/j.molliq.2022.119188.

(20) Pesko, D. M.; Timachova, K.; Bhattacharya, R.; Smith, M. C.; Villaluenga, I.; Newman, J.; Balsara, N. P. Negative Transference Numbers in Poly(Ethylene Oxide)-Based Electrolytes. *J. Electrochem. Soc.* **2017**, *164* (11), E3569–E3575. https://doi.org/10.1149/2.0581711jes.

(21) Chen, S.; Zhang, S.; Liu, X.; Wang, J.; Wang, J.; Dong, K.; Sun, J.; Xu, B. Ionic Liquid Clusters: Structure, Formation Mechanism, and Effect on the Behavior of Ionic Liquids. *Phys. Chem. Chem. Phys.* **2014**, *16* (13), 5893–5906. https://doi.org/10.1039/C3CP53116C.

(22) Diederichsen, K. M.; McShane, E. J.; McCloskey, B. D. Promising Routes to a High Li^+ Transference Number Electrolyte for Lithium Ion Batteries. *ACS Energy Lett.* **2017**, *2* (11), 2563–2575. https://doi.org/10.1021/acsenergylett.7b00792.

(23) Gao, T.; Itliong, J.; Kumar, S. P.; Hjorth, Z.; Nakamura, I. Polarization of Ionic Liquid and Polymer and Its Implications for Polymerized Ionic Liquids: An Overview towards a New Theory and Simulation. *Journal of Polymer Science* **2021**, *59* (21), 2434–2457. https://doi.org/10.1002/pol.20210330.

(24) Wohde, F.; Balabajew, M.; Roling, B. Li $^{+}$ Transference Numbers in Liquid Electrolytes Obtained by Very-Low-Frequency Impedance Spectroscopy at Variable Electrode Distances. *J. Electrochem. Soc.* **2016**, *163* (5), A714–A721. https://doi.org/10.1149/2.0811605jes.

(25) Homann, G.; Wang, Q.; Liu, S. A Solid-State Polymer Lithium-Metal Battery with Minimal Excess Lithium, Ultrathin Separator, and High-Mass Loading NMC811 Cathode. *Adv. Energy Sustainability Res.* **2024**.

(26) Stejskal, E. O.; Tanner, J. E. Spin Diffusion Measurements: Spin Echoes in the Presence of a Time-Dependent Field Gradient. *The Journal of Chemical Physics* **1965**, *42* (1), 288–292. https://doi.org/10.1063/1.1695690.

(27) Bloembergen, N.; Purcell, E. M.; Pound, R. V. Relaxation Effects in Nuclear Magnetic Resonance Absorption. *Phys. Rev.* **1948**, *73* (7), 679–712. https://doi.org/10.1103/PhysRev.73.679.

(28) McDowell, A. F.; Adolphi, N. L.; Sholl, C. A. Site and Barrier Energy Distributions That Govern the Rate of Hydrogen Motion in Quasicrystalline $Ti_{45}Zr_{38}Ni_{17}H_{x}$. *J. Phys.: Condens. Matter* **2001**, *13* (43), 9799–9812. https://doi.org/10.1088/0953-8984/13/43/310.

(29) Vargas-Barbosa, N. M.; Roling, B. Dynamic Ion Correlations in Solid and Liquid Electrolytes: How Do They Affect Charge and Mass Transport? *ChemElectroChem* **2020**, *7* (2), 367–385. https://doi.org/10.1002/celc.201901627.

(30) Ehrl, A.; Landesfeind, J.; Wall, W. A.; Gasteiger, H. A. Erratum: Determination of Transport Parameters in Liquid Binary Lithium Ion Battery Electrolytes: I. Diffusion Coefficient [*J. Electrochem. Soc.* , 164, A826 (2017)]. *J. Electrochem. Soc.* **2018**, *165* (11), X12–X12. https://doi.org/10.1149/2.1171811jes.

(31) Wyatt, N. B.; Gunther, C. M.; Liberatore, M. W. Increasing Viscosity in Entangled Polyelectrolyte Solutions by the Addition of Salt. *Polymer* **2011**, *52* (11), 2437–2444. https://doi.org/10.1016/j.polymer.2011.03.053.

(32) Han, S.-D.; Borodin, O.; Seo, D. M.; Zhou, Z.-B.; Henderson, W. A. Electrolyte Solvation and Ionic Association: V. Acetonitrile-Lithium Bis(Fluorosulfonyl)Imide (LiFSI) Mixtures. *J. Electrochem. Soc.* **2014**, *161* (14), A2042–A2053. https://doi.org/10.1149/2.0101414jes.

(33) Iriawan, H.; Herzog, A.; Yu, S.; Ceribelli, N.; Shao-Horn, Y. Upshifting Lithium Plating Potential To Enhance Electrochemical Lithium Mediated Ammonia Synthesis. *ACS Energy Lett.* **2024**, *9* (10), 4883–4891. https://doi.org/10.1021/acsenergylett.4c02149.

(34) Pham, T. D.; Bin Faheem, A.; Lee, K. Design of a LiF-Rich Solid Electrolyte Interphase Layer through Highly Concentrated LiFSI–THF Electrolyte for Stable Lithium Metal Batteries. *Small* **2021**, *17* (46), 2103375. https://doi.org/10.1002/smll.202103375.

(35) Sekhon, S. S. Conductivity Behaviour of Polymer Gel Electrolytes: Role of Polymer. *Bull Mater Sci* **2003**, *26* (3), 321–328. https://doi.org/10.1007/BF02707454.

(36) Hanwell, M. D.; Curtis, D. E.; Lonie, D. C.; Vandermeersch, T.; Zurek, E.; Hutchison, G. R. Avogadro: An Advanced Semantic Chemical Editor, Visualization, and Analysis Platform. *J Cheminform* **2012**, *4* (1), 17. https://doi.org/10.1186/1758-2946-4-17.

SUPPORTING INFORMATION

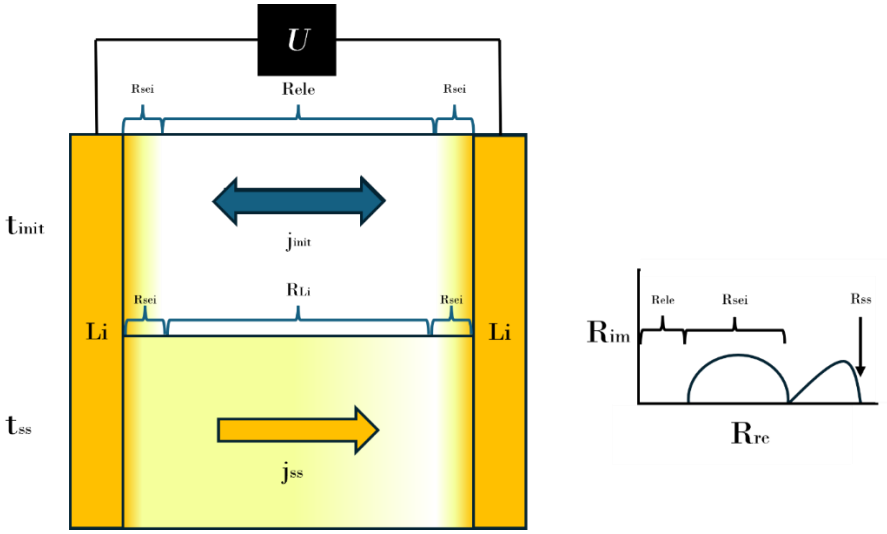

Figure S 1 Graphical depiction of electrochemical test procedure. Left: Potentiostatic Intermittent Titration probes under a small potential U (e.g. 10 mV) the initial j_{init} and steady state current j_{ss} through the electrolyte. The test is performed in anion blocking conditions by using a symmetric lithium/lithium cell to obtain steady state resistance R_{ss}. Gradient color depict the presence of concentration gradients of conducting species, which reduce the net current of lithium ions in the steady state. Right: Nyquist plot from electrochemical impedance spectroscopy obtained from the same cell setup gives insight in the contribution of electrolyte resistances (typically in the high frequency domain on the left side of the Nyquist plot), SEI resistance buildup (middle frequency region, semicircle) and polarization and/or diffusive resistances (low frequency region, right side of Nyquist plot). The two techniques together give insight in the total and specific lithium conductivity.

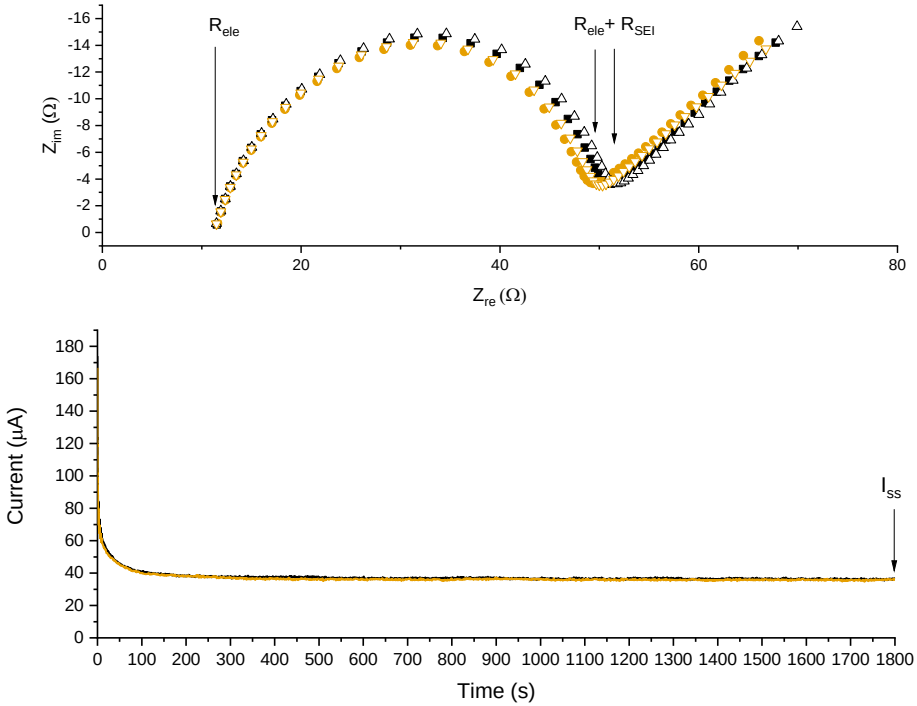

Figure S 2 Electrolyte conductivity and transference measurement through EIS and potentiostatic measurements in symmetric Lithium cells in duplo. After equillibration in a climate chamber EIS is conducted to obtain electrolyte and SEI resistivity (top, closed symbols). Subsequently potentiostatic measurement at 10 mV is conducted to obtain I_{ss} (bottom) after which SEI resistivity is measured again (top, open symbols).

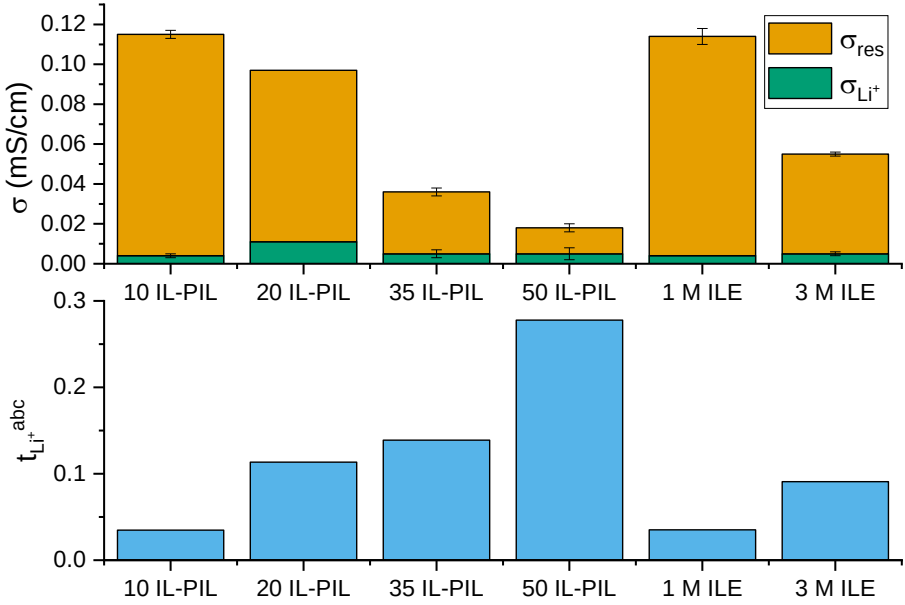

Figure S 3 Ionic conductivity (top) and anion blocking transference number (bottom) of IL-PIL and IL electrolyte at 20 °C. Total conductivity σ_{tot} obtained by high frequency impedance spectroscopy can be separated in conductivity attributed to lithium σ_{Li+} obtained by potentiostatic measurements and the residual conductivity σ_{res}. The 20 IL-PIL shows similar conductivities to the 10 IL-PIL but the net lithium conductivity increases, similar to 1M and 3M ILE. Error bars indicate difference between duplic measurement.

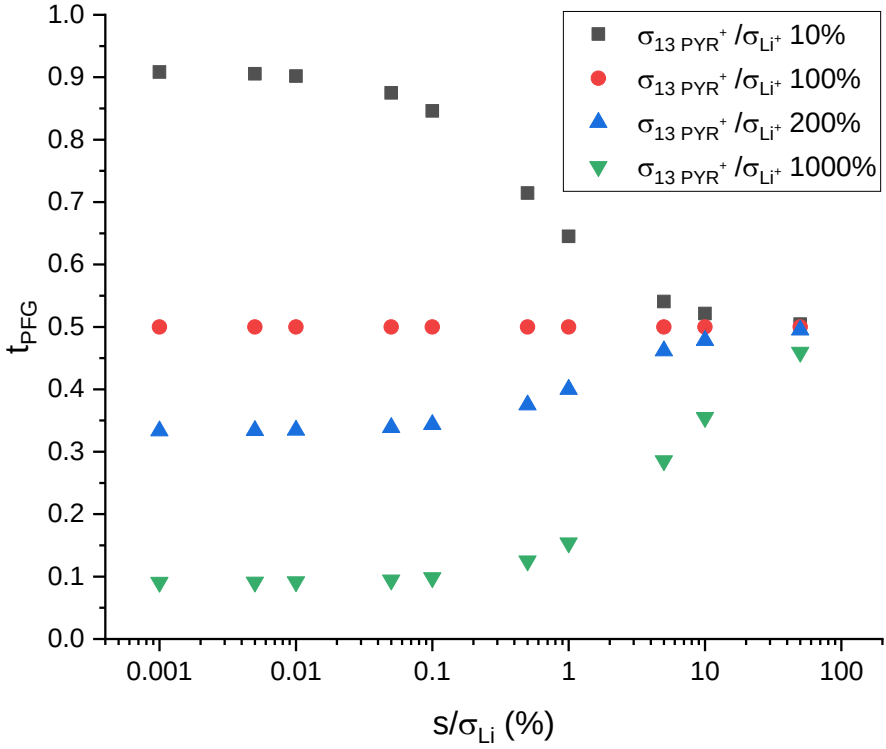

Figure S 4 Effect of degree of lithium association s to the observed transference with PFG. The relative conductivity of mobile cations cause a net negative or positive change in transference as the degree of association increases. The utmost left side of the graph indicates the $t_{Li^+}^{abc}$ with only Li^+ transport (the degree of association s does not contribute in Li^+ transport).

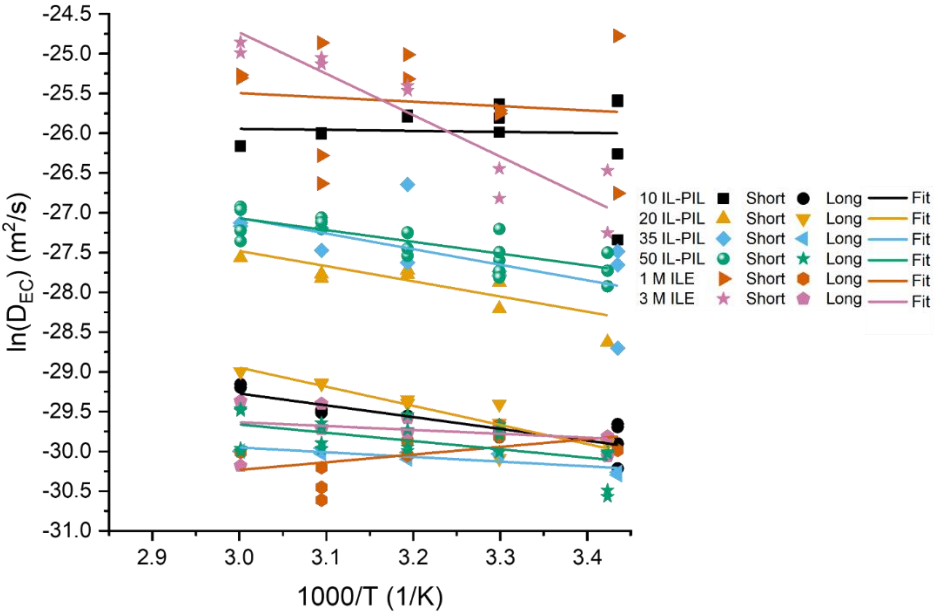

Figure S 5 Diffusivities of IL-PILs and ILEs obtained from Short and Long term PITT relaxation fitting. Long term relaxation shows three orders of magnitude lower diffusivities

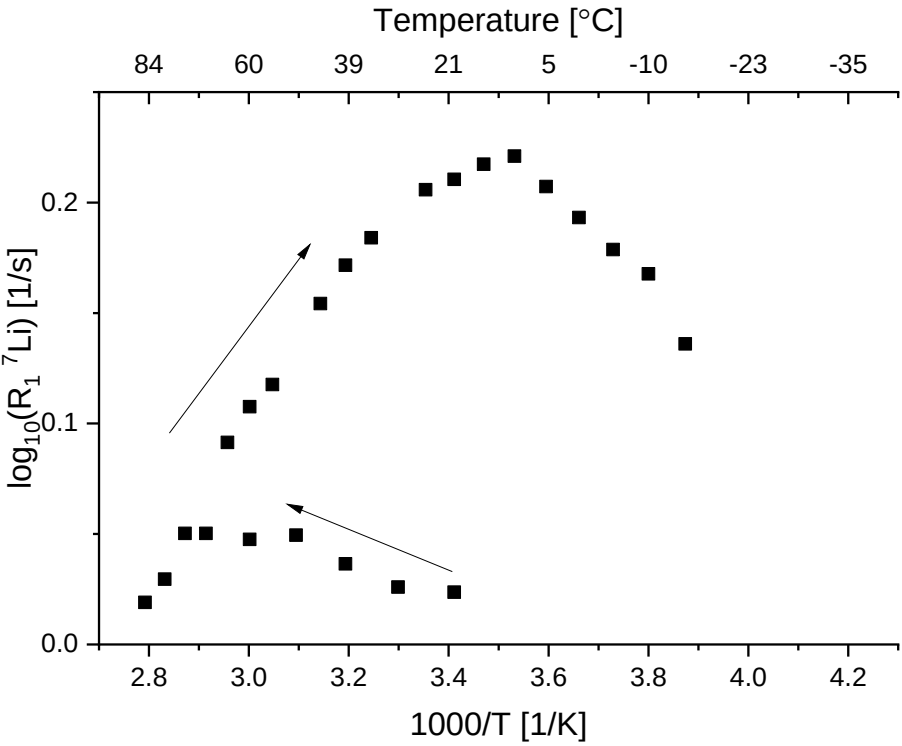

Figure S 6 The T1 relaxation rate R_1 in NMR relaxometry of 10 IL-PIL sample shows an increasing relaxation rate after heating to 85 °C. The relaxation rates observed are in line with ionic liquid analogs, which indicates phase separation occurs above a threshold temperature around 70 °C.

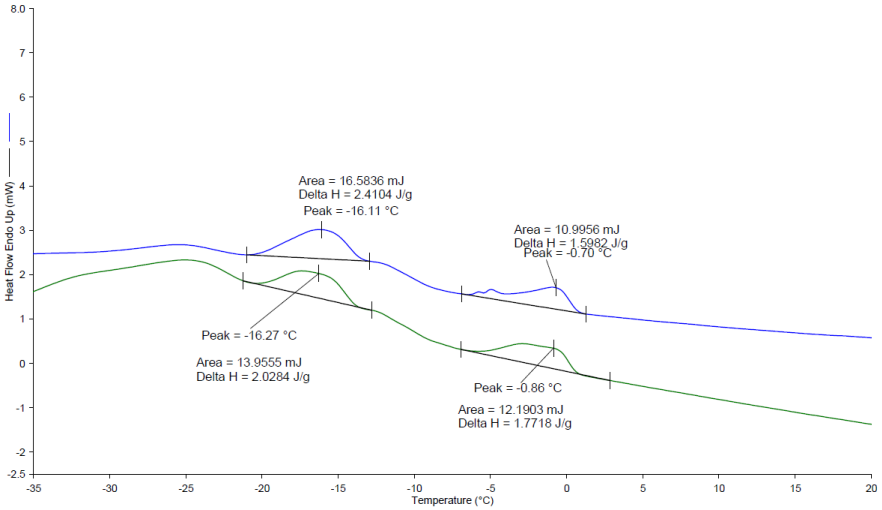

Figure S 7 DSC thermograph of 50 IL-PIL indicating two reversible endothermic processes around -16.2 and -0.8 °C.

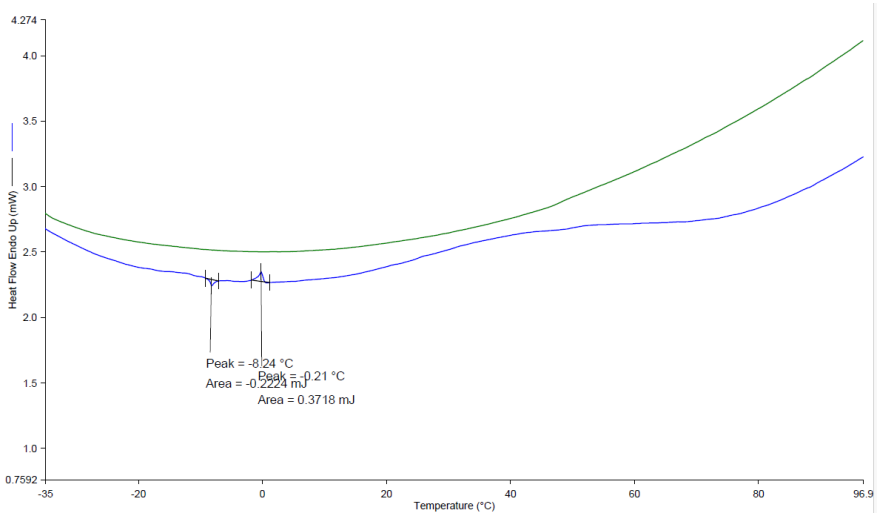

Figure S 8 DSC thermograph of 10 IL-PIL indicating two processes around -8.2 and -0.2 °C during initial heating (blue), not apparent during the second cycle (green).

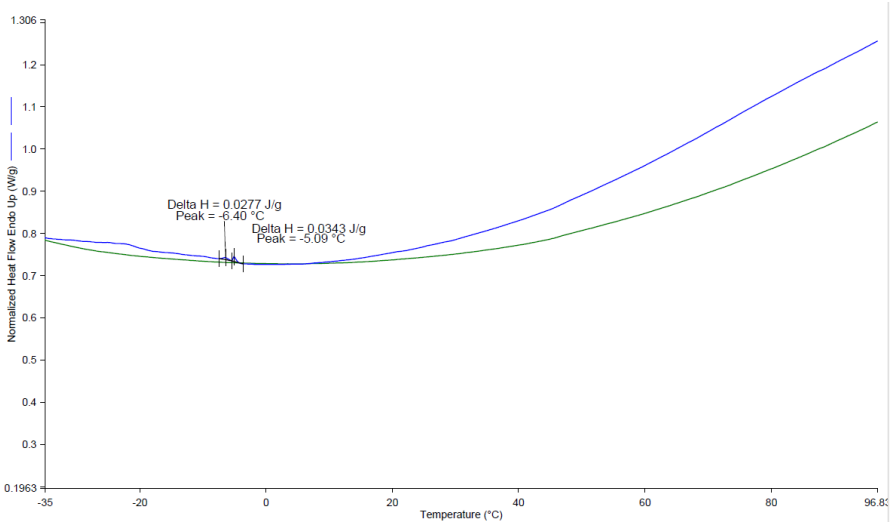

Figure S 9 DSC thermograph of 20 IL-PIL indicating two processes around -6.4 and -5.1 °C during initial heating (blue), not apparent during the second cycle (green).

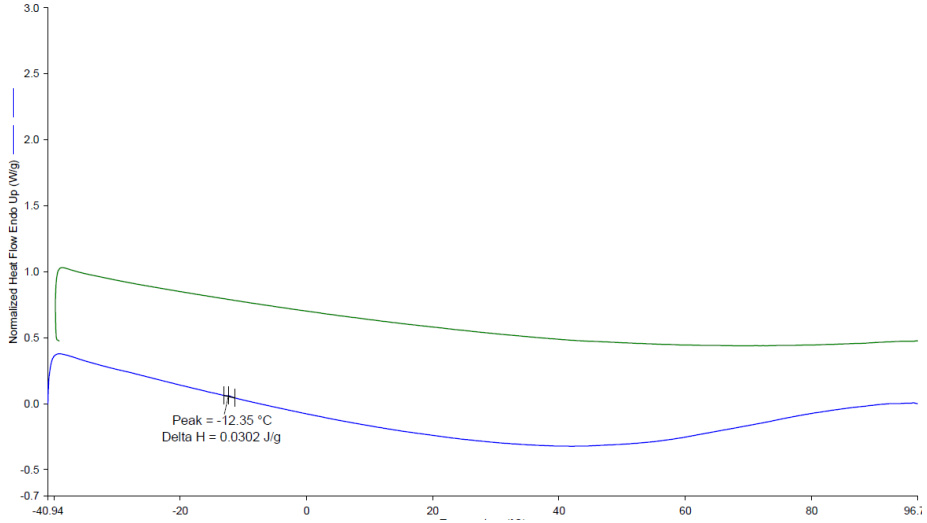

Figure S 10 DSC thermograph of 35 IL-PIL indicating one non-reversible process around -12.35 °C during heating (blue), not apparent during the second cycle (green).

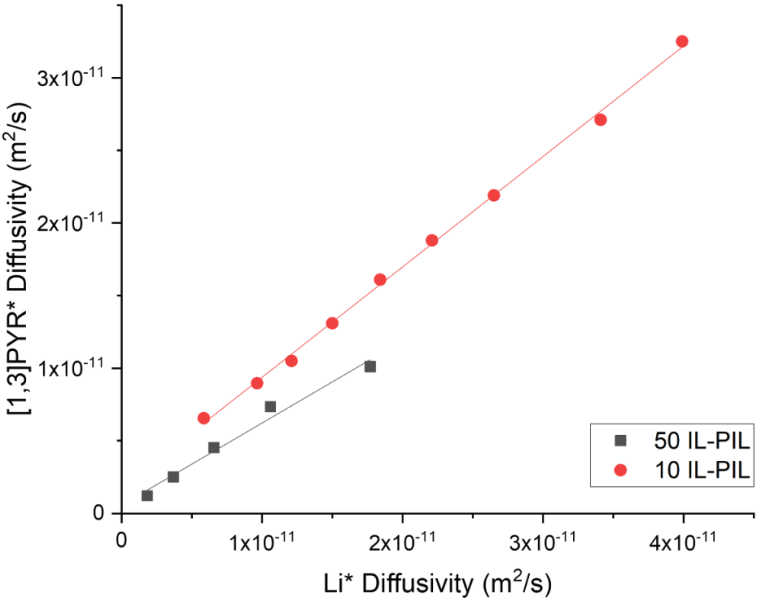

Figure S 11 Relative PFG tracer diffusivity of [1,3]PYR* to Li* for the lowest and highest LiFSI wt% IL-PILs. The ratio of diffusivity changes only slightly, indicating no dramatic change is observed between relative motion of the two constituents.

6. Surfactants Supporting Liquid Electrolyte with Homogeneous Anodeless Lithium Plating

The content of this chapter is in the process of submission to a scientific journal.

ABSTRACT

The use of lithium metal as anode maximizes the gravimetric capacity possible for lithium ion batteries. Processing lithium metal is challenging because of its high reactivity, leading to high manufacturing costs. Therefore approaches to circumvent lithium metal processing are sought. An anodeless battery assembly, in which the copper current collector serves as initial plating surface, offers a potential solution. However, uncontrolled lithium growth during plating is a major challenge as plating on copper is less energetically favourable compared to plating on lithium. Here the use of different surfactants as surface modifier during plating onset is investigated as a means to homogenize the onset lithium plating on copper. From the selected surfactants, the plating efficiency of initial plating on copper has been found to increase from 25 to 67% upon adding BTAB surfactant to conventional electrolyte. The use of BTAB surfactant shows an increased lithium plating density *in operando* using Neutron Depth Profiling (NDP) with an oxygen and fluorine rich SEI as found by XPS . A net plating efficiency of 97.6% is shown by cycling 3.2 mAh/cm^2 capacity in Cu:NMC811 cells with BTAB surfactant in conventional $LiPF_6$ in EC:DMC:EMC electrolyte. Upon replacing the BTA^+ counterion with $TFSI^-$ a coulombic efficiency of 99.6% is reached in similar experiments.

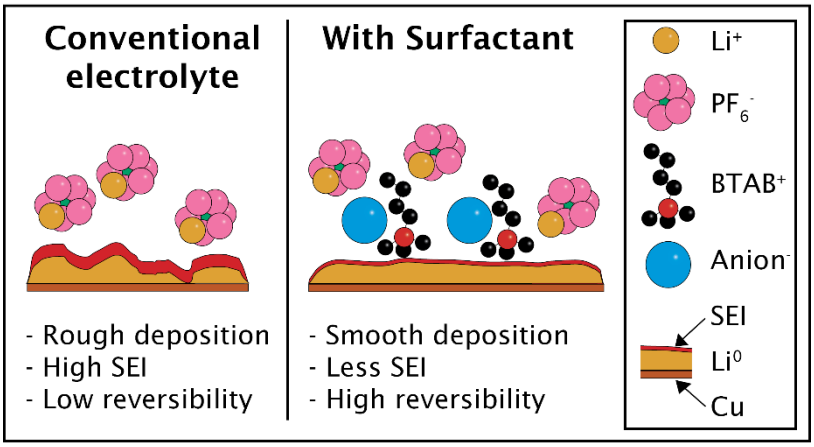

INTRODUCTION

The use of lithium metal anodes is considered to have a key role in the upcoming high energy density battery generation. Studies of both liquid and solid electrolytes which stabilize the solid lithium metal/electrolyte interface (SEI) have intensified, with recent successes in both solid and liquid classes.[1] Lithium metal is however highly reactive and therefore challenging for manufacturing processes, which make it also expensive.[2] Although projections are still quite uncertain, the cost of lithium metal use during manufacturing could amount to as much as one third of the total battery.[3] An approach to refrain from usage of lithium metal during manufacturing is to host lithium deposition on an initially bare lithium-less current collector layer. In this way during manufacturing such a layer can be stacked in between the separator and cathode sheets, and upon first charging the lithium metal forms on the host layer. Anodeless battery designs would therefore combine high energy density anode type in the form of lithium metal with a relatively cheap manufacturing process.

One major challenge of the anodeless approach is the irreversible loss of lithium during the initial electrode plating reactions. As all lithium originates from the (overlithiated) cathode material, loss of lithium participating in the redox processes translates to a severe loss in gravimetric capacity. During lithium plating the lithium should be dense to prevent contact loss during subsequent stripping and to minimize buildup of the solid electrolyte interface (SEI) on the lithium – electrolyte interfaces, which also comes at the cost of electrolyte loss. The morphology of lithium metal upon plating layer growth is influenced by the surface structure and chemistry, deposition rate, deposition time and electrolyte characteristics.[4] Passivating and/or templating the host surface are common approaches to increase the coulombic efficiency of the initial plating step.[5,6]

Lithiation modifiers are explored by e.g. modifying the local dielectric distribution leading to a change in preferred lithium deposition.[7,8] Changing the dielectric distribution during plating by adding a mobile dielectric modifier is not much explored, however. Previously Dai et al. reported that addition of surfactant CTAC (positive head group, 16 carbon alkane tail) homogenizes the lithium on lithium deposition.[9] Using optical microscopy structural differences were shown between CTAC containing electrolyte (smooth plating) and non-CTAC containing electrolyte (whiskered growth). Another work by Xiao et. al. show addition of TAHP (positive head group, 1 carbon

alkane tail) shows a positive effect in lithium sulfur batteries.[10] Here a combination of homogenization and reduction of sulfur anion mobility was thought to be the origin of improved performance.

In this work the effectiveness of using surfactants BTA^+ (4 carbon alkane tail) as lithium plating mediator on pristine copper surfaces is shown. The BTA^+ additive is explored previously for electrochemical conversion in aqueous systems[11] but to our knowledge never in lithium batteries. A shorter alkane tail lowers the hydrophobic interactions but alters the migration mobility and dramatically increases the solubility in liquid electrolyte.[12] A lowered double layer capacitance is observed for additives with low hydrophobic tail lengths, which effectively would yield a lower plating overpotential.[11] The role of the surfactant positive head group would be oriented towards the negative Cu or Li, forming a small barrier towards the electrolyte with the hydrophobic tail. In this way it can act as interface with electrolyte and SEI layer, that can be self-repairing as it remains mobile on the electrode surface. To verify the function of the polar head group, also a negatively charged surfactant is tested. During lithium plating the copper surface is negatively charged which would cause this surfactant to have little effect, as it is not expected to orient towards the Cu/Li surface. By combining these surfactants as surface interaction modifiers during lithiation, combined with SEI stabilizers in other works[13,14], one would possibly enable the development of methods for the use of affordable lithium metal anodes in rechargeable batteries with liquid electrolytes.

METHODS

CELL ASSEMBLY

The electrolyte is produced by dissolving (1-Butyl)Trimethylammonium bromide (BTAB), (1-Hexadecyl)Trimethylammonium chloride (Cetrimoniumchloride or CTAC), lithium stearate (LiSt) or (1-Butyl)Trimethylammonium bis(trifluoromethylsulfonyl)imide (BTATFSI) in Standard 1 M $LiPF_6$ in 1:1:1 EC:DMC:DEC v/v/v% electrolyte (Sigma). Concentrations were varied between no additive (0 mM or NA), 12, 30, 120 mM BTAB, 100 mM BTATFSI, or saturated solutions (CTAC and LiSt) made by rigorous mixing for 30 minutes at ambient temperature. Lithium:copper test cells were made in C2032 coin cells, KF40 lab cells, in-house developed 3 point KF40 lab cells (**Figure S 1**), and pouch cells, depending on the experiment. Coin and lab cells were using 14-16 mm diameter copper sheet as working electrode and lithium foil as counter electrode. Prior to assembly the copper foil was cleaned with 0.1 M HCl,

ethanol and subsequently vacuum dried. Celgard 2400 is used as separator. For operando Neutron Depth Profiling (NDP) an in-house developed 'windowed' pouch cell was made. The pouch consists of a 36x36 mm copper current collector with nickel tab, on which a 15 mm diameter ^{6}Li disc is placed. A 40x40 Celgard 2400 sheet is used as separator and a 34x34 mm copper sheet with nickel tab is used as working electrode. Prior to assembly the current collector is heat glued to the pouch outer casing, which contains a 18 mm hole, called the window. In this way the back side of the current collector is bare, facilitating tritium particles to exit the core of the pouch, necessary for the neutron depth profiling measurement.

The full cell battery is made using a NMC811 cathode consisting of active material $LiNi_{0.8}Mn_{0.1}Co_{0.1}O_2$, carbon black (C45, Timrex), conductive additive (KS4 graphite, Timrex), and PVDF binder (Solef 5130). NMP solvent is used for casting the slurry using the phase inversion method [15] . The cathode weight ratio is 92%AM:3%CB:1%KS4:4%PVDF m/m% with a very high final loading of 5.9 ± 0.5 mAh/cm^2 (BTAB and reference full cell tests) and 14.1 mAh/cm^2 (BTATFSI full cell test). To prevent Cu/stainless steel side reactivity a polyethylene foil is added around the 12.7 mm diameter NMC811 electrode. A central 12 mm diameter hole is punched in the foil to ensure electrical contact of the stub with the current collector.

ELECTROCHEMICAL CHARACTERISATION

Half cells were cycled in a MACCOR-4000 cell cycler using galvanostatic cycling for 24 hours at 0.1, 0.2 and 0.5 mA/cm^2 current densities. The stripping potential limit was set to – 1 V. Impedance spectroscopy is conducted after 24 hours initial plating using a PARSTAT MC200 module (Ametek) between 0.1 Hz and 100 kHz with 10 mV amplitude. Full cell cycling is performed between 3 V and 4.3 V at 0.1C. For restricted cycling tests the initial plating is performed at 0.5 mA/cm^2 current density until cutoff voltage is reached. Stripping duration during subsequent cycling at 0.1C was limited to 6 hours. The BTATFSI full cell tests were performed with 0.15 mA/cm^2 current density for plating and stripping using the same potential and duration cutoff. NDP cells were tested with a SP-300 (Biologic) or PGSTAT (Autolab) galvanostat/potentiostat at 0.1 mA/cm^2 current density. Cyclic voltammetry is conducted using a lithium reference with an electrolyte immersed celgard separator between two stainless steel surfaces, at a scanning rate of 0.1 V/s.

NEUTRON DEPTH PROFILING

Neutron depth profiling is used to monitor the lithium plating density in situ.[16,17] Lithium plating density was monitored by subjecting the battery to a neutron beam, and measuring the residual energies of the $^{6}Li+^{1}n\rightarrow{}^{3}H+^{4}He$ neutron absorption reaction products coming out of the battery. The particle residual energy is obtained after the particles travelled from the position where lithium absorbed a neutron and produced the ^{3}H and ^{4}He inside the battery cell, towards the PIPS detector (Passivated Implanted Planar Silicon Detectors, a solid state particle detector, Mirion). The tritium particles lose energy as they travel through matter. The rate of tritium energy loss, called the stopping power is different for various materials and can be accurately calculated.[18] The trajectory of tritium passing from the point of annihilation through electrolyte, deposited lithium, 15 µm copper sheet, helium gas to the detector thus yields only a limited set of possible trajectories with a set of possible detected energies (**Note S 1**). During analysis, lower detector energies are cut off as they may also originate from X-rays (Bremsstralung). For this study the tritium particles energy and counts are collected during intervals of 1 minutes. The energy loss in the trajectory from the pouch to the detector is minimized by flushing helium gas in an in-house made pouch holder with PIPS detector mount, as He has low stopping power.[19] The annihilation rate of lithium (and thus the formation rate of tritium particles) from the neutron beam flux is normalized using a secondary detector monitoring annihilation rate from a pure ^{6}Lithium source simultaneously. Due to aperture and detector gain adjustments between measurements, relating the absolute detector count rate to lithium concentration was not possible with high accuracy. Instead, the increase in particle count during initial plating on the copper window during the first 5 minutes is used as direct reference. This is possible as initial plating occurs completely inside the depth detection limits at the copper surface of the window, which allows relating the increase in count rate directly to the net added lithium concentration.

SEM AND XPS ANALYSIS

Scanning electron microscopy (SEM) pictures were taken using a JEOL JSM-IT700HR FE-SEM setup in scattering electron imaging (Acceleration Voltage: 3 kV). Energy Dispersive X-ray mapping is performed in Backscattered electron imaging mode (Acceleration voltage: 15 kV).

Surface composition was measured with X-ray photoelectron spectroscopy (XPS) using a K-alpha spectrometer (Thermo Fisher Scientific) with a Al K_α source with a spot size of 400 µm. Argon etching is performed using 3 kEv acceleration voltage, 10 s/slice for 10 slices and 30 s/slice for 20 slices consecutively.

RESULTS

LITHIUM PLATING PERFORMANCE

The initial plating efficiency on copper is tested in Cu:Li half cells for 24 hours at low current density (0.1 mA/cm^2). Upon disassembling a clear macroscopic change in morphology was observed (**Figure 1**). The 120 mM BTAB shows complete coverage of the copper anode with smooth lithium. The 30 mM BTAB clearly show improved lithium coverage compared to the NA control cell, but in this cell still some bare copper can still be observed. The control cell shows preferential plating sites in the middle section in which the lithium forms a dense area, leading to less complete coverage and contact loss at the edge. LiST and CTAC show plating performance similar to 30 mM BTAB (**Figure S 2**).

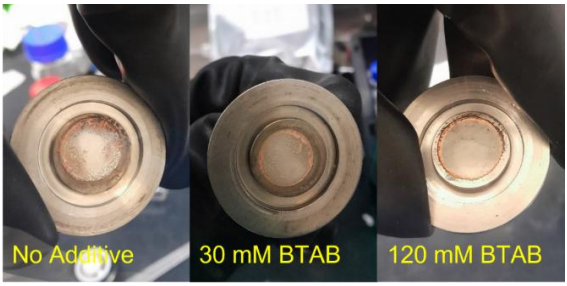

Figure 1 Lithium plating morphology after 24 hours plating on Copper at 0.1 mA/cm^2. Plating in standard electrolyte (left) shows unequally distributed lithium compared to 30 mM (middle) and 120 mM BTAB (right).

The potential trace during onset of plating show variation in potential induced by SEI and/or morphology differences between cells with different surfactant additives and concentrations (**Figure 2**A). The initial plating causes a resistive barrier relevant for the energy efficiency which is reflected by the overpotentials during stable plating (**Figure 2**B). EIS before disassembly shows a semi-circle diameter which is smaller in the same order as the smaller overpotential losses in Figure 2B; smaller circle diameter

corresponds to smaller overpotential. The impedance spectroscopy was performed after 24 hours of plating at 0.1 mA/cm^2 (**Figure 2**A,B,C). With lithium stearate and CTAC additive a secondary sloping potential is observed during onset plating starting at 500 and 900 mV vs Li/Li$^+$ respectively, causing an increased duration of SEI formation (**Figure 2**A). For these cells in EIS a wider semicircle can be observed which is generally assigned to SEI and double layer resistances (**Figure 2**C). Generally the observed semicircles height exceeds the width, indicating multiple simultaneous capacitive processes occur at slightly differing frequencies. Remarkably, for the 120 mM BTAB cell an almost truly circularly symmetric semi-circle with the smallest radius is observed which may indicate both high lithium plating homogeneity with a single well defined SEI resistance and lower net transfer resistance. In the low frequency range (10 mHz – 800 mHz), for surfactant containing cells, a secondary capacitive feature is observed which is indicated by the start of a second semicircle. The plating potential during the 24th hour of plating at 0.1 mA/cm^2 follows the trend in EIS showing total resistance buildup in the order R_{NA}>R_{LiSt}>$R_{30\ mM\ BTAB}$ >R_{CTAC}>$R_{120\ mM\ BTAB}$.

The plating efficiency is tested by stripping the cells at 0.1 mA/cm^2 for 24 hours (**Figure 2**D). Lithium stearate, a surfactant with a negatively charged head group shows the lowest CE% (5.5%). Without an additive 27% of the lithium could be stripped. Surfactants with a positively charged head group show positive influence on the plating efficiency. CTAC, 30 mM BTAB, 120 mM BTAB and BTATFSI show 32%, 39%, 65% and 72% coulombic efficiency respectively. BTATFSI was not part of the original selection and specific results on BTATFSI is discussed in a separate paragraph. An image of the lithium deposition on copper during onset plating after 2 hours is shown in (**Figure S 8**). Originally 120 mM BTAB formulation is selected for further investigation as it both shows a lower overpotential and a high stripping efficiency.

Step amperometry is used to verify the coulombic efficiency of plating lithium on copper with and without BTAB in the case of repeated complete stripping. A 24 hour plating step followed by a 24 hour stripping step at a current density of 0.1, 0.2 and 0.5 mA/cm^2, repeated 10 times per current density (**Figure 2**F). Generally the plating efficiency varies due to SEI buildup and contact loss of lithium during stripping. The 120 mM BTAB cells show consistently less spread in efficiency (less contact loss) and a higher average plating efficiency (less SEI buildup) indicating this surfactant has a positive influence on the lithium morphology and SEI respectively.

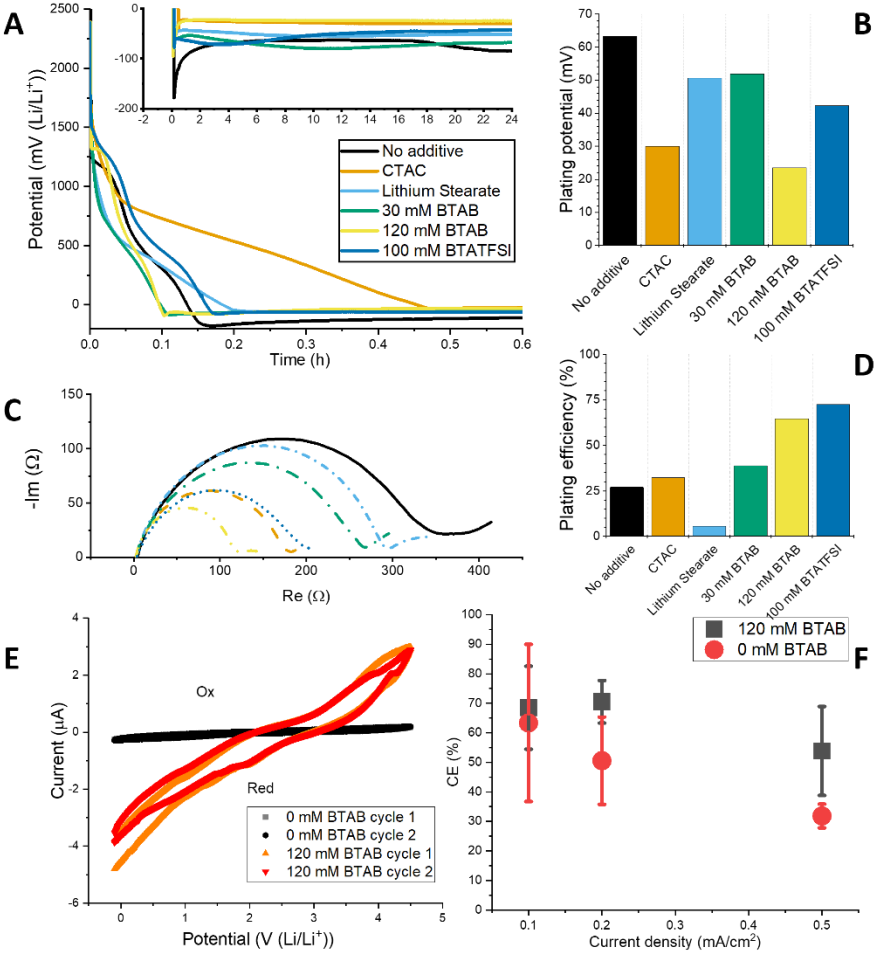

Figure 2 A: Potential during the first 10 hours of lithium plating on copper using 1M LiPF6 in EC:DMC:EMC electrolyte containing surfactant additives. B: Stable plating potential of lithium on copper after 24 h at 0.1 mA/cm². C: Subsequent EIS after 24 h of lithium plating on Copper in Cu:Li cells with various surfactants. D: Plating coulombic efficiency on copper after 24 hours of plating of lithium on copper at 0.1 mA/cm². E: Potential stability and electrical conductivity analysis using cyclic voltammetry of electrolytes in symmetric stainless steel configuration with lithium reference electrode. F: Coulombic efficiency (CE) of plating on copper at various consecutive increasing current densities in Cu:Li cells with 1M $LiPF_6$ in EC:EMC with and without 120 mM BTAB. Average CE of BTAB containing cells show an increase compared to non-BTAB cells.

Surfactants Supporting Liquid Electrolyte with Homogeneous Anodeless Lithium Plating

Changes in lithium morphology

The lithium surface morphology is expected to show a large difference. Surfactants are surface active species anticipated to leave a different morphology of the plated structure. On a microscopic scale the lithium surface of the 120 mM BTAB cells show a more even distribution with lower roughness compared to the negative control (**Figure 3**B and A respectively). Also lesser variation across the complete plating surface as shown in Figure 1 is apparent (**Figure 2**D and C respectively).

Measurement of the plating density during the onset of anodeless plating *in situ* is conducted using neutron depth profiling. Here the lithium density of the first few micrometer depth near the copper current collector in the battery are monitored. This is done by obtaining the flux of the lithium/neutron capture product tritium $^{3}H^{+}$ together with its specific energy.[19] During the first two hours of galvanostatic plating

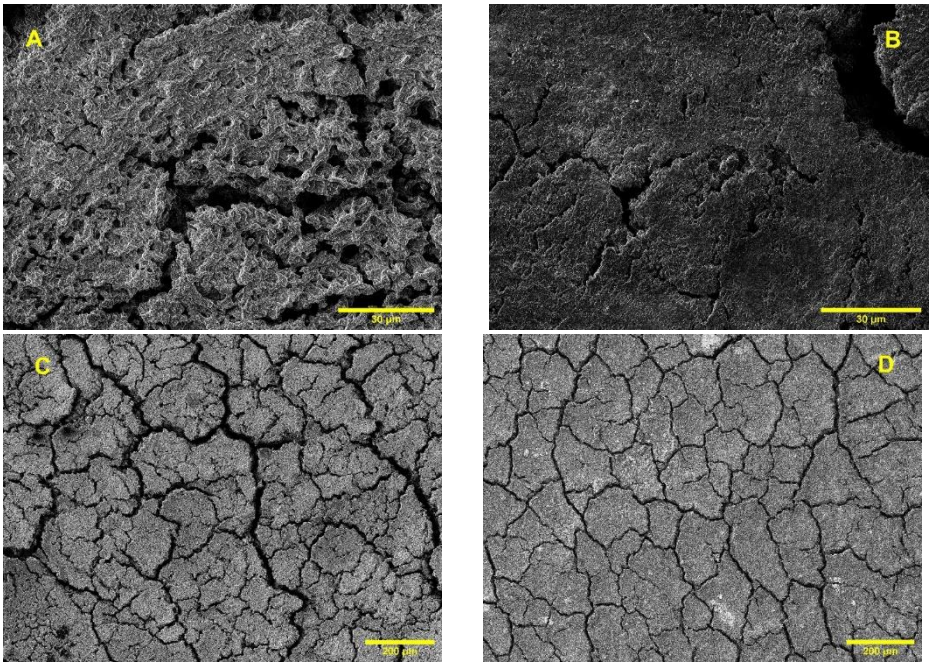

Figure 3 SEM images of lithium morphology plated on Copper of 0 mM (A,C) and 120 mM BTAB (B,D) versus NMC811 full cells. The lithium morphology shows lower porosity for the 120 mM BTAB indicating surfactant allows denser plating.

at 0.1 mA/cm^2 (with respect to the ^{6}Li metal disc), depth profiles of 0 mM and 120 mM BTAB containing half cells were taken. The energy spectrum was obtained after the neutron flux is normalized and the detector background is subtracted (**Figure 4**D,E). A derivation to depth profiling and its results are added in **Note S 1** and **Figure S 3**.

The lithium density features near the current collector compared to the bulk can be reviewed by comparing the particle flux and energy distribution. The high energy (500 – 800 kEv) tritium detections originate from ^{6}Li near the current collector, where lower energy (250 – 400 kEv) incidents originate from deeper regions, leading to more tritium energy loss. The energy profile of the 120 mM BTAB containing cell shows a peak shape at high ^{3}H energy particle detection (~700 kEv), translating to denser lithium plating near the current collector (**Figure 4**E, 65 minutes) compared to the 0 mM BTAB containing cell (**Figure 4**D, 65 minutes). The depth profile of the 0 mM BTAB containing cell shows an increase in counts distributed along the complete horizontal axis of the energy spectrum (**Figure 4**D, 65 and 95 minutes). This implies the lithium growth extends to the deeper regions of the sample, out of the detection window of the NDP. The detector count rate indicates this as well (**Figure 4**C). An increase in count rate is a direct measure of an increase in lithium amount in the detection window. A change in the slope during galvanostatic plating, as observed for 0 mM BTAB (starting from t=50 minutes) indicates the lithium is plated out of the window deeper into the cell towards the separator. For the 120 mM BTAB containing cell the change in slope is less pronounced indicating a longer period of plating near the copper surface. The energy profile and count rate of the NDP measurement therefore show that BTAB causes the onset lithium plating on copper to be denser compared to the same setup without BTAB additive.

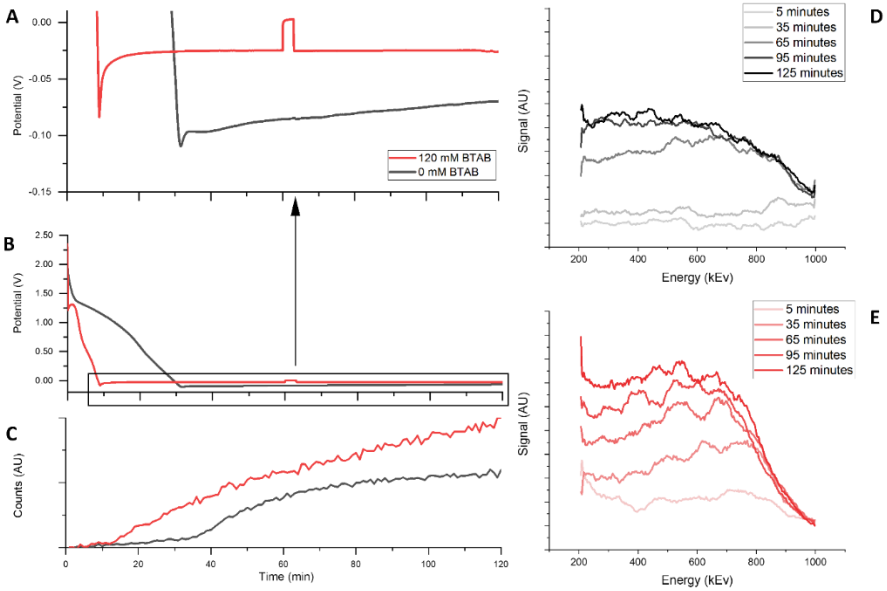

Figure 4 Neutron Depth profiles indicating Lithium density observed from the copper current collector during first 2 hours of plating at 0.1 mA/cm^2 on bare copper. Here the potential trace (A, B) and the tritium detection rate (C) of cells containing 120 mM BTAB and 0 mM BTAB in 1 M $LiPF_6$ in 1:1:1 EC:DMC:DEC v/v/v% is shown. As long as the potential measured is still positive a slight increase in particle count can be observed, about linear in time. This will corespond with initial SEI formation, having a lower Li density. After the potential becomes negative the change of the slope of particle count indicates dense Li detection within the tritium energy window. The reduction of the slope later on indicates that more of the lithium is plated out of the detection window as well for the 0mM BTAB, while for the 120 mM BTAB it is still within the window. The particle energy profile of several time intervals during plating of 0 mM BTAB (D) and 120 mM BTAB cells (E) are shown. The increased signal intensity at higher detection energies (~700 kEv) for the 120 mM BTAB represents preferential plating near the copper current collector window side. A 5 minute rest period to probe OCP (16 mV) after 60 minutes was introduced for the BTAB containing cell.

Cycling performance in full cell

The compatibility of BTAB additive with NMC811 cathodes is explored in Cu:NMC811 cells. The lithium inventory retention during cycling Cu:NMC811 batteries with 120 mM BTAB in the electrolyte are compared to cells in which no surfactant was added.[20] Two procedures are tested. One which fully utilizes the lithium of the active material and one which adjusts the discharge procedure to account for the initial plating

efficiency (LIM procedure). With full stripping procedure an initial coulombic efficiency (ICE) of 67.5% is observed (**Figure S 4**). During the second and third cycle the coulombic efficiency is higher compared to the first (92%), which indicates possibly two different nucleation processes are occurring: starting from bare copper (resulting in a lower CE) and subsequently starting with copper containing SEI (resulting in a higher CE).

The LIM procedure limits the lithium stripping by setting the discharge time to 60% of the complete discharge period at that C-rate. The potential trace of cycling the surfactant containing cells with the LIM procedure is shown in **Figure 5**A. Limiting discharge to 60% would be a safe margin considering the expected ICE observed in the FULL procedure. Indeed limiting the discharge time increases the amount of cycles in which lithium is fully utilized to 22 and 37 cycle in a duplicate experiment (**Figure 5**B). This test shows that the total lithium inventory of 6.58 mAh shows 2.63 mAh lithium inventory loss after a net plating of 86.86 and 146.08 mAh of lithium capacity during repeated plating and stripping for the duplicate cells. The average plating efficiency of the complete test becomes 97.6±0.6%. In contrast to this, a cell cycled with the LIM procedure without surfactant shows only 2 cycles with full lithium utilization (33% plating efficiency). Addition of BTAB shows therefore a great positive influence on the plating efficiency in full cell anodeless batteries.

The large difference between the duplicate cells containing the surfactant may have several causes. The battery containing surfactant shows an extended charge period during the first and second cycle (**Figure 5**B, black and brown respectively). The duration of this period varies between the duplicate cells. This difference therefore cannot be accounted for by the ICE originating from the lithium nucleation reaction on bare copper. The origin of the charge capacity may be found to be side reactivity of the BTAB Bromide ions with the stainless steel casing (**Figure S 5**). Apparently the side reactivity does not result in a severe loss of lithium inventory, but would lower the net lithium plating rate extending the charge duration, as a fraction of the current is consumed by side reactions. As a result, the lowered plating current density yields a higher plating efficiency, as shown by the half-cell cycling test (**Figure 2**F) which possibly explains the improved cycling behavior compared to its duplicate in the long run.

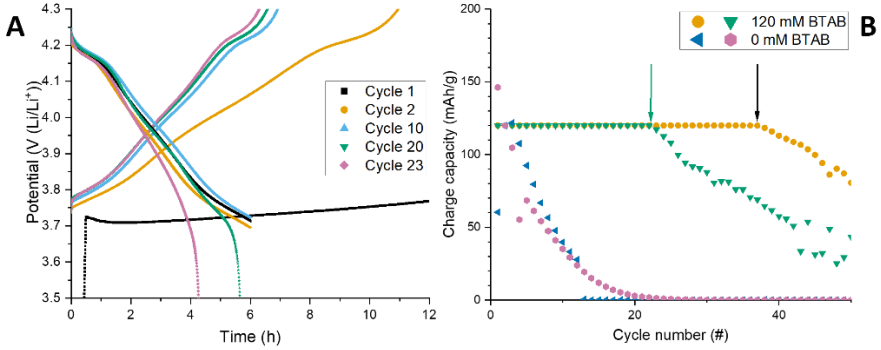

Figure 5 Capacity limited stripping performance Cu:NMC811 cells. A) Potential trace during formation of a 5.4 mAh/cm² a NMC811:Cu cell with 120 mM BTAB in 1 M $LiPF_6$ in 1:1:1 EC:DMC:DEC v/v/v% electrolyte, cycled at 0.1C. First plating performed at 0.5 mA/cm². Discharge was limited to 60% of 5.4 mAh/cm². B) Cycling performance of limited stripping cycling with Cu:NMC811 with and without 120 mM BTAB for two different cells each. Cells without BTAB show a fast decline in retained charge capacity. Arrows from left to right indicate the last cycle at which 60% of the lithium inventory could be used (green, black).

Surface characterization

The initial plating homogeneity and efficiency show a great effect in the full cell performance during subsequent cycling. A successful initial plating shows lowered polarization and higher subsequent stripping efficiency. However, generally the coulombic efficiency continues to be low after the first few cycles, possibly due to the noted steel corrosion (CE of 89±2% from cycle 11 to point of loss of inventory). The SEI composition at the anode with and without BTAB is investigated by using XPS (**Figure 6**). Surface analysis of the plated lithium through XPS shows the BTAB containing cell has a higher organic SEI relative to the lithium signal, containing 33±3%atm O and 12±3%atm C compared to 10±1%atm O and 2.0±0.5% atm C for the non-BTAB containing cell. Trace amounts of bromine (1.2±1.2%atm Br) and nitrogen (0.2±0.2 %atm N) of the BTAB molecule were detected after argon etching exposing subsurface layers as well. This indicates presence of surfactant in the SEI. The electrochemical stability of BTAB is therefore tested using CV. Here 120 mM BTAB electrolyte is measured in a symmetric stainless steel configuration (i.e. only stainless steel in contact with the electrolyte, **Figure 2**E). The electrolyte with 120 mM BTAB shows initially oxidative redox activity around 3.5 to 4 V vs Li/Li^+ and a subsequent reduction at 2 V during the first cycles. The currents are very small and the current balance (total

oxidation – total reduction) between cycles 1 and 2 shows negligible difference (0.11 and 0.13 µAh net oxidation respectively). After repeated cycling oxidation and reduction peaks emerge following redox activity expected from Br^-/Br_2 closely (**Figure S 6**: at 2 V and 4.2 V vs Li/Li^+). The net oxidation balances to 2.4 µAh which indicate the additional features observed in the first CV are amplified. A retarded current response may be observed as well: an increased oxidation current during de reduction sweep from 4.5 to 3V is sometimes observed. This might be caused by a gas/liquid equilibrium as Br_2 is observed at the gas liquid interface (**Figure S 6**, right).

As the Br^-/Br_2 electrochemical side reaction is undesirable in the cell, instead of Br^- as BTA counterion, $TFSI^-$ is used in full cells to test if it shows similar high plating efficiencies without risking the bromine redox couple. 100 mM BTATFSI is mixed with

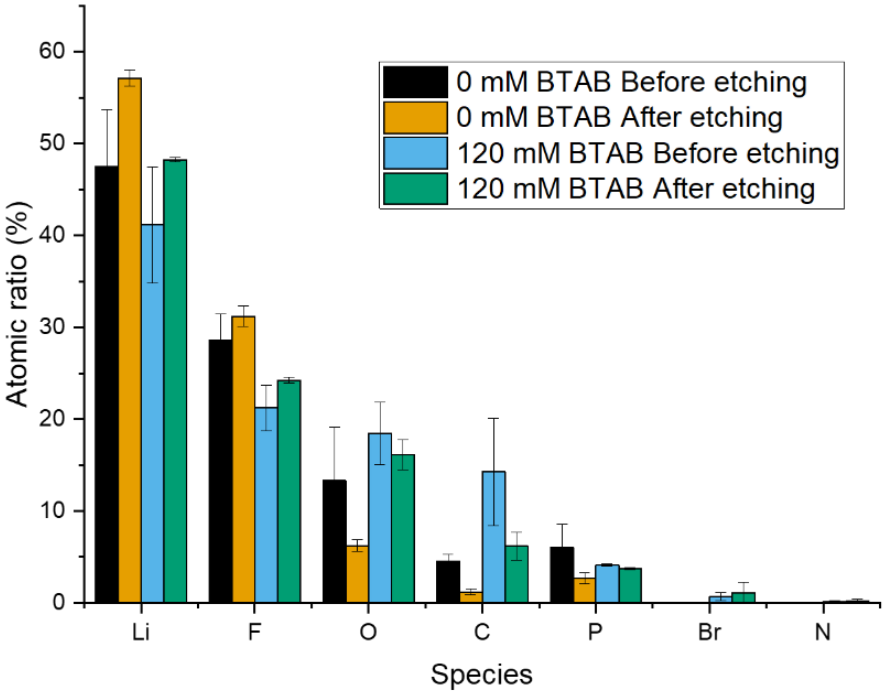

Figure 6 SEI composition of cells after cycling, measured by an XPS. Argon etching is used to etch surface oxygen from the sample. A slight decrease of F species and a prominent increase in C and O is observed in the SEI of the BTAB cell.

Surfactants Supporting Liquid Electrolyte with Homogeneous Anodeless Lithium Plating

1 M $LiPF_6$ in EC:DMC:DEC and tested in NMC811:Copper cells. Repeated plating/stripping shows a similar efficiency of 71.4% at 0.1 mA/cm^2 compared to BTAB containing electrolyte and 24 hour experiment (**Figure 7**A). However, at higher currents the plating efficiency lowers to 59% and 46% with 0.2 and 0.5 mA/cm^2 which is significantly lower compared to BTAB containing electrolyte, but higher compared to electrolyte containing no additive.

To show cycling performance capabilities extremely thick NMC811 cathodes with 66.5 mg/cm^2 loading are used versus Cu in anodeless coin cells. Initial plating shows 14.1 mAh/cm^2 plated capacity. Limited plating/stripping is repeated at a current density of 0.15 mA/cm^2 until 4.3 V with discharge duration of 6 hours per cycle, giving a net capacity of 0.9 mAh/cm^2 giving 3.8 mWh/cm^2 per cycle during the first 30 cycles. This approach naturally results in a low CE% during the first cycle (6%, Figure 7B), as the stripping is limited in capacity. The additional capacity necessary to reach the limiting upper voltage can be used to estimate the efficiency of stripping/plating and continued presence of additional side reactions. This amounts to a CE% of 99.3%±0.6% for the first 14 cycles. Each consecutive cycle is showing an increased CE% toward 99.6% (Figure 7B). To project the cell failure the average CE% of the last 5 cycles is taken as reference for the following cycles. The high CE% observed illustrates BTATFSI can stabilize the lithium plating process as sole additive to standard electrolyte to a great degree.

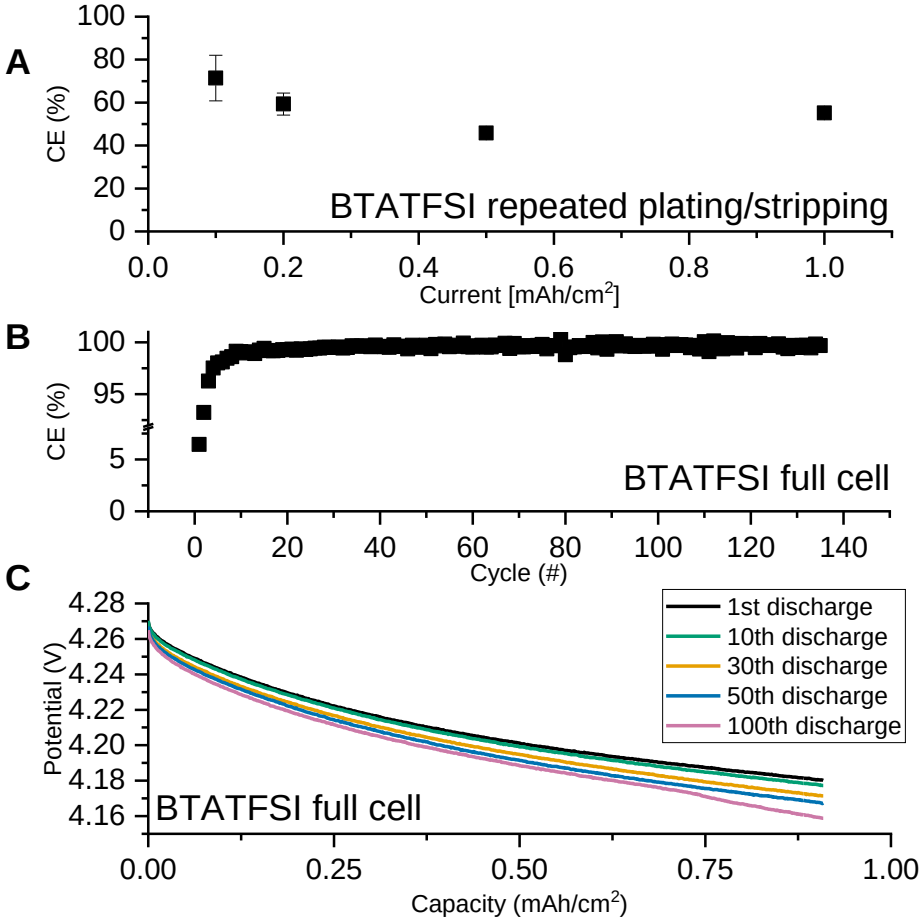

Figure 7 Performance of 100 mM BTATFSI, 1 M $LiPF_6$ in 1:1:1 EC:DMC:DEC v/v/v%. A) Repeated plating and stripping (5 times per cycle) testing the lithiation efficiency on copper at various (subsequently applied) currents in a Li:Cu cell. B) and C): full cell cycling in Cu:NMC811 cell with plating until 4.3 V potential limit and limited stripping duration of 0.15 mA/cm² for 6 hours. CE% is taken as capacity difference of consecutive plating step to reach limiting potential divided by the stripped capacity. CE% (B) and potential drift during discharge (C) is shown.

The cell is opened and the lithium morphology and composition is inspected using SEM at the position where the Li plating is present after the long cycling (**Figure 8**). A homogeneous surface is observed with a low porous deposition morphology **(Figure 8**A and B respectively). The SEI composition is obtained by XPS using argon etching

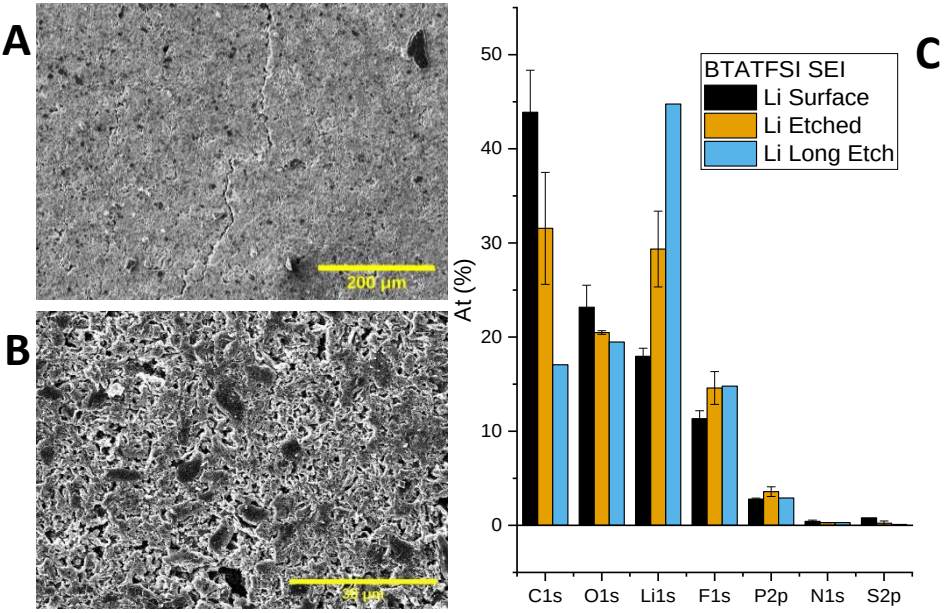

Figure 8. Lithium metal on copper surface of 100 mM BTATFSI, 1 M $LiPF_6$ in 1:1:1 EC:DMC:DEC v/v/v% Cu:NMC811 cell after cycling as observed by SEM (A and B with 200 and 30 µm scale bars). C. Shows XPS results of the surface and the etched surface using an argon beam for 30 s (orange) and 300 s (blue).

(**Figure 8**C), showing a fluorine and oxygen rich composition containing some phosphorous as well. There is relatively more oxygen in the SEI compared to the SEI composition of the 0 mM cell shown in **Figure 6**, which is known to be beneficial for SEI stabilization.[14]

Discussion and Conclusions

The use of BTA^+ surfactant as additive for liquid electrolytes helps the formation of equally distributed lithium coverage during initial plating, as can be observed from the resistive behavior in the EIS and from the SEM images. Migration of surface active BTA^+ molecules to the surface of the negative electrode including negative surface active sites during plating apparently forms a relatively thin but homogeneous layer and in that way prevents preferred plating at a few nucleation sites with lowest barrier only. The nucleation process, supported by BTAB presence, yields a denser lithium formation over the complete surface near the current collector, as shown by NDP.

Using electrochemical cycling we show that BTAB and BTATFSI additives yield a higher average coulombic efficiency during plating/complete stripping cycles compared to the pure standard electrolyte. The lithium morphology in the BTAB cell shows both macroscopic and microscopic changes. On the macroscale a visually smooth lithium sheet is obtained after initial plating. Also with SEM a more smooth, dense lithium structure is found, indicating effective plating homogenization. The BTAB surfactant, however, does not prevent SEI buildup during subsequent cycling. The instable SEI leads to continuous loss of lithium which led to eventual capacity fade during extended cycling. The additive also has been found to show side reactivity during cycling when in contact with stainless steel.

Full cell batteries with surfactant modifiers may have a benefit in a combined approach of homogenization by the action of the surfactant, after which a SEI stabilization agent from such electrolytes forms a stable SEI layer. By comparing the additive with standard electrolyte in full cells we show convincingly surfactant addition is a facile method to provide a higher lithium metal density during initial plating on copper in anodeless battery configurations. Formation of a highly stable SEI to achieve a CE% of 99.6% during cycling indicates the additive BTATFSI could be explored in future research in representative cell types for commercial applications. Moreover, compatibility testing with other liquid electrolytes remains necessary, to further stabilize the SEI, to minimize the lithium inventory loss during onset and subsequent plating/stripping and to increase the allowable current density. Only then achieving coulombic efficiencies near 100% can be achieved, necessary for well performing lithium metal batteries. This work shows that addition of cationic surfactants to electrolytes provide a facile and viable approach to enable anodeless lithium metal battery designs with otherwise conventional carbonate liquid electrolytes.

REFERENCES

(1) Wang, Q.; Zhao, C.; Wang, J.; Yao, Z.; Wang, S.; Kumar, S. G. H.; Ganapathy, S.; Eustace, S.; Bai, X.; Li, B.; Wagemaker, M. High Entropy Liquid Electrolytes for Lithium Batteries. *Nat Commun* **2023**, *14* (1), 440. https://doi.org/10.1038/s41467-023-36075-1.

(2) Acebedo, B.; Morant-Miñana, M. C.; Gonzalo, E.; Ruiz de Larramendi, I.; Villaverde, A.; Rikarte, J.; Fallarino, L. Current Status and Future Perspective on Lithium Metal Anode Production Methods. *Advanced Energy Materials* **2023**, *13* (13), 2203744. https://doi.org/10.1002/aenm.202203744.

(3) Wang, Z.; Cao, Y.; Zhou, J.; Liu, J.; Shen, X.; Ji, H.; Yan, C.; Qian, T. Processing Robust Lithium Metal Anode for High-Security Batteries: A Minireview. *Energy Storage Materials* **2022**, *47*, 122–133. https://doi.org/10.1016/j.ensm.2022.01.049.

(4) Wang, Q.; Zhao, C.; Wang, S.; Wang, J.; Liu, M.; Ganapathy, S.; Bai, X.; Li, B.; Wagemaker, M. Clarifying the Relationship between the Lithium Deposition Coverage and Microstructure in Lithium Metal Batteries. *J. Am. Chem. Soc.* **2022**, *144* (48), 21961–21971. https://doi.org/10.1021/jacs.2c08849.

(5) Zhao, P.; Pan, J.; Zhang, D.; Tang, Y.; Tai, Z.; Liu, Y.; Gao, H.; Huang, F. Designs of Anode-Free Lithium-Ion Batteries. *Batteries* **2023**, *9* (7), 381. https://doi.org/10.3390/batteries9070381.

(6) Liu, B.; Zhang, L.; Xu, S.; McOwen, D. W.; Gong, Y.; Yang, C.; Pastel, G. R.; Xie, H.; Fu, K.; Dai, J.; Chen, C.; Wachsman, E. D.; Hu, L. 3D Lithium Metal Anodes Hosted in Asymmetric Garnet Frameworks toward High Energy Density Batteries. *Energy Storage Materials* **2018**, *14*, 376–382. https://doi.org/10.1016/j.ensm.2018.04.015.

(7) Wang, C.; Liu, M.; Thijs, M.; Ooms, F. G. B.; Ganapathy, S.; Wagemaker, M. High Dielectric Barium Titanate Porous Scaffold for Efficient Li Metal Cycling in Anode-Free Cells. *Nat Commun* **2021**, *12* (1), 6536. https://doi.org/10.1038/s41467-021-26859-8.

(8) Xu, Y.; Menon, A. S.; Harks, P. P. R. M. L.; Hermes, D. C.; Haverkate, L. A.; Unnikrishnan, S.; Mulder, F. M. Honeycomb-like Porous 3D Nickel Electrodeposition for Stable Li and Na Metal Anodes. *Energy Storage Materials* **2018**, *12*, 69–78. https://doi.org/10.1016/j.ensm.2017.11.011.

(9) Dai, H.; Xi, K.; Liu, X.; Lai, C.; Zhang, S. Cationic Surfactant-Based Electrolyte Additives for Uniform Lithium Deposition via Lithiophobic Repulsion Mechanisms. *J. Am. Chem. Soc.* **2018**, *140* (50), 17515–17521. https://doi.org/10.1021/jacs.8b08963.

(10) Xiao, Y.; Liu, Z.; Wu, J.; Liu, C.; Peng, Y.; Fan, Y.; Chang, J.; Zheng, Z.; Huang, W.; Chen, G.; Deng, Y. Cationic Surfactant for Lithium-Sulfur Batteries Enables

Efficient Use of Sulfur and Limits Lithium Dendrite Formation. *Cell Reports Physical Science* **2023**, *4* (11), 101658. https://doi.org/10.1016/j.xcrp.2023.101658.

(11) Ge, W.; Chen, Y.; Fan, Y.; Zhu, Y.; Liu, H.; Song, L.; Liu, Z.; Lian, C.; Jiang, H.; Li, C. Dynamically Formed Surfactant Assembly at the Electrified Electrode–Electrolyte Interface Boosting CO_2 Electroreduction. *J. Am. Chem. Soc.* **2022**, *144* (14), 6613–6622. https://doi.org/10.1021/jacs.2c02486.

(12) Cho, J.; Yoon, S.; Min Sim, K.; Jin Jeong, Y.; Eon Park, C.; Kwon, S.-K.; Kim, Y.-H.; Chung, D. S. Universal Selection Rule for Surfactants Used in Miniemulsion Processes for Eco-Friendly and High Performance Polymer Semiconductors. *Energy Environ. Sci.* **2017**, *10* (11), 2324–2333. https://doi.org/10.1039/C7EE01943B.

(13) Qian, J.; Adams, B. D.; Zheng, J.; Xu, W.; Henderson, W. A.; Wang, J.; Bowden, M. E.; Xu, S.; Hu, J.; Zhang, J. Anode-Free Rechargeable Lithium Metal Batteries. *Adv Funct Materials* **2016**, *26* (39), 7094–7102. https://doi.org/10.1002/adfm.201602353.

(14) Hobold, G. M.; Lopez, J.; Guo, R.; Minafra, N.; Banerjee, A.; Shirley Meng, Y.; Shao-Horn, Y.; Gallant, B. M. Moving beyond 99.9% Coulombic Efficiency for Lithium Anodes in Liquid Electrolytes. *Nat Energy* **2021**, *6* (10), 951–960. https://doi.org/10.1038/s41560-021-00910-w.

(15) Karanth, P.; Weijers, M.; Ombrini, P.; Ripepi, D.; Ooms, F.; Mulder, F. M. A Phase Inversion Strategy for Low-Tortuosity and Ultrahigh-Mass-Loading Nickel-Rich Layered Oxide Electrodes. *Cell Reports Physical Science* **2024**, 101972. https://doi.org/10.1016/j.xcrp.2024.101972.

(16) Chen, C.; Oudenhoven, J. F. M.; Danilov, D. L.; Vezhlev, E.; Gao, L.; Li, N.; Mulder, F. M.; Eichel, R.; Notten, P. H. L. Origin of Degradation in Si-Based All-Solid-State Li-Ion Microbatteries. *Advanced Energy Materials* **2018**, *8* (30), 1801430. https://doi.org/10.1002/aenm.201801430.

(17) Oudenhoven, J. F. M.; Labohm, F.; Mulder, M.; Niessen, R. A. H.; Mulder, F. M.; Notten, P. H. L. In Situ Neutron Depth Profiling: A Powerful Method to Probe Lithium Transport in Micro-Batteries. *Advanced Materials* **2011**, *23* (35), 4103–4106. https://doi.org/10.1002/adma.201101819.

(18) Ziegler, J. F.; Biersack, J. P. The Stopping and Range of Ions in Matter. In *Treatise on Heavy-Ion Science*; Bromley, D. A., Ed.; Springer US: Boston, MA, 1985; pp 93–129. https://doi.org/10.1007/978-1-4615-8103-1_3.

(19) Verhallen, T. W. *Neutron Depth Profiling: Following the Lithium Distribution in Rechargeable Batteries*; 2019.

(20) Nanda, S.; Gupta, A.; Manthiram, A. Anode-Free Full Cells: A Pathway to High-Energy Density Lithium-Metal Batteries. *Advanced Energy Materials* **2021**, *11* (2), 2000804. https://doi.org/10.1002/aenm.202000804.

Surfactants Supporting Liquid Electrolyte with Homogeneous Anodeless Lithium Plating

SUPPORTING INFORMATION

3 POINT CELL ARCHITECTURE

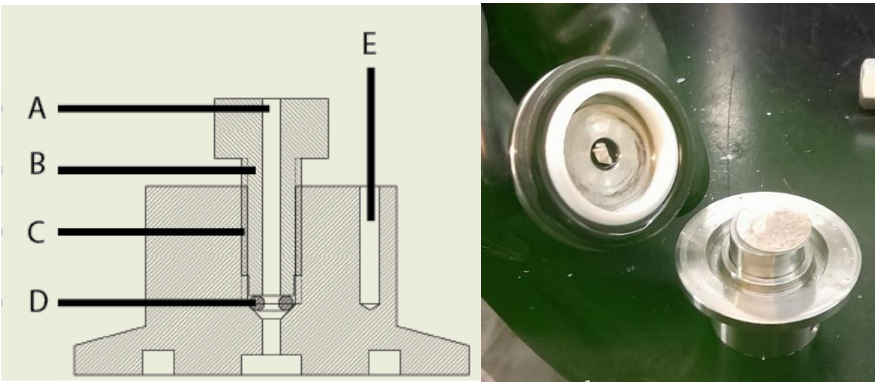

Figure S 1 Three point electrode assembly. Left: drawing of cross section with: A) Feed through of copper wire, B) Ferrule feed through, C) BSPP Thread, D) O-ring fixing of wire, E) insert for banana plug of working electrode. Right: photo of the three point cell assembly. The reference electrode is a flint of lithium mounted on electrically insulating padding. A lithium counter electrode is placed on a cylindrical stube mounted on a spring. The cell is closed using a teflon inner ring and an EPDM O-ring. The flange is closed using a non conductive belt.

PLATING PERFORMANCE SURFACTANTS

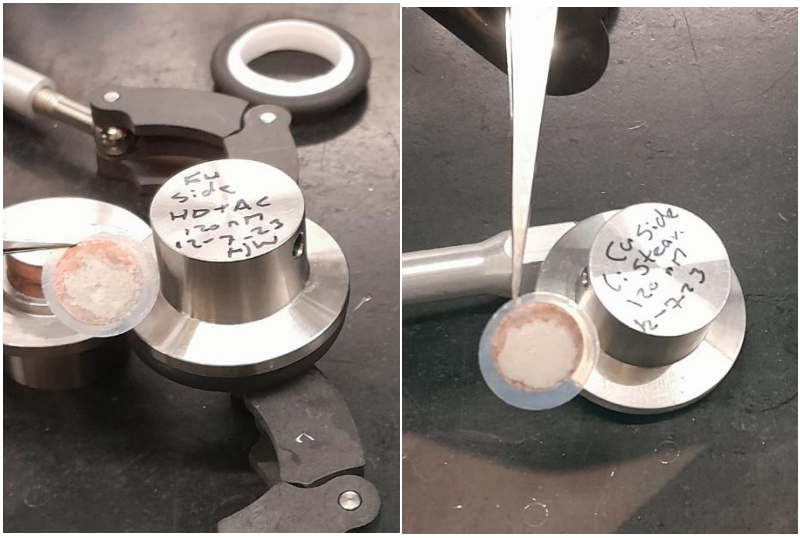

Figure S 2 Lithium plating morphology after 24 hours plating on Copper at 0.1 mA/cm2. Plating performance of HDTAC and Lithium Stearate containing electrolyte. 120 mM indication cell body is the original weighed amount of surfactant solution, the surfactant did not fully dissolve (saturated solution).

NOTE S 1 DERIVATION DEPTH PROFILING

The logarithmic nature of stopping powers and the dependance on the material obscures the plating density difference. Therefore a mathematical derivation is made to approximate the depth. Above a threshold ion kinetic energy (typically 180 kEv) the stopping power follows the power law. An equation in the form of (Eq. 1 is therefore used to fit the stopping powers of pure compounds Lithium and EC and a 50/50% mixture of Lithium and EC which by the stochastic nature of ion stopping equals a trajectory of 50% lithium and 50% EC.

$$\frac{dE}{dx} = -\frac{1}{a}E^{-b}$$

$$\int_{E_0}^{E} -a * E^b dE = \int_0^x dx$$

(Eq. 1)

Here a and b are fitting constant where a is positive and b is between 0 and 1. The value E_0 is 2727 kEv, the energy of annihilation product ^3H. Distance x in µm and energy E are derived. A formula in the form of Eq. 2 is obtained.

$$x = \frac{a}{b+1}({E_0}^{b+1} - E^{b+1})$$

Eq. 2

For the part of the battery which has an unchanging geometry from sample to sample the energy loss from the constant trajectory can be obtained by rewriting Eq. 2.

$$E_0 = (-a(b+1) * x + E^{b+1})^{1/(b+1)}$$

Eq. 3

The approach above yields good approximations for ions with high energies in any material. However for low energies the strong non-linearity of stopping power (through copper) yields a large error. As the current collector is the final trajectory of the particle coming out of the battery, typically the tritium particle contains low kinetic energy. Therefore a riemann table is made solving Eq. 4, which gives the approximation of energy E_1 entering the current collector as function of the particle energy at the exit side E_2.

$$E = \sum_{x=0}^{10\mu m} E_x + \frac{dE_x}{dx}\Delta x$$

Eq. 4

The final particle trajectory through helium is performed similar to copper.

Phase	**a**	**b**	**Limits**
Lithium	1/1578.8	0.605	1400<E<3000 kEv
Ethylene Carbonate	1/2449.9	0.569	1400<E<3000 kEv

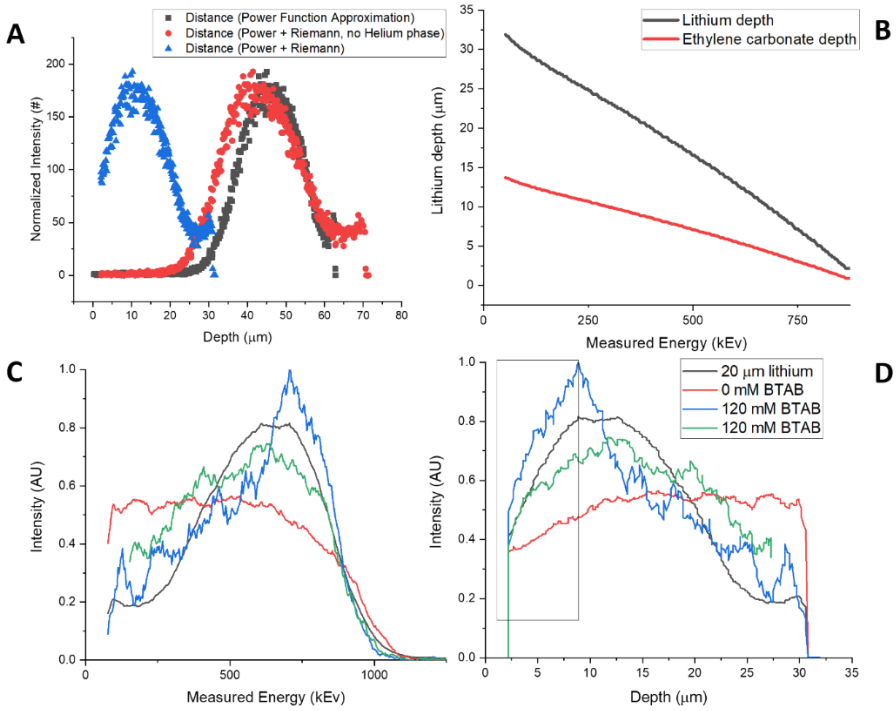

Figure S 3 A) Approximation of lithium depth profile of a 20 micron thick lithium sheet on Copper using power function approximation eq. 2 (red), incorporating Riemann approximation of stopping power loos in copper trajectory (black), incorporating Riemann approximation of stopping power in helium trajectory (blue). B) detection limit of lithium depth assuming pure lithium phase (black) or pure electrolyte phase (red). C) NDP energy profile peak shape comparison after 2 hours of galvanostatic plating at 0.1 mA/cm². D) NDP depth profile converted to depth from data of C. Pure lithium stopping trajectory is assumed for energy to depth conversion. Rectangle indicates region in which stopping power assumption holds for 120 mM BTAB. To compensate for signal intensity differences, peak shape is obtained by 10 channel averaging and normalization of total lithium count. Note that the signal intensity is normalized, obscuring the tenfold intensity of lithium metal signal.

XPS

Table S 1 Atomic ratio obtained by survey spectrum of Lithium SEI as measured by XPS.

	0 mM BTAB (%atm)	120 mM BTAB (%atm)
O	19.17 / 7.44	21.83 / 15.06
C	5.3 / 3.75	20.10 / 8.41
N	0 / 0.03	0.04 / 0.22
Br	0 / 0	0.24 / 1.10
P	8.52 / 3.54	4.22 / 4.02
B		
Li	41.27 / 53.72	34.83 / 47.46
F	25.73 / 31.50	18.73 / 23.73

FULL CELL CYCLING WITH COMPLETE STRIPPING

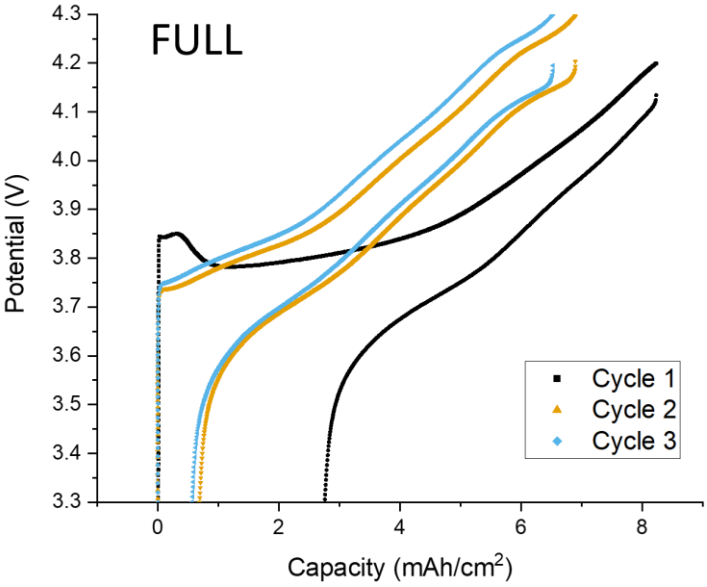

Figure S 4 Full cell complete stripping performance. Potential versus areal capacity during formation of a NMC811:Cu cell with 120 mM BTAB in 1 M $LiPF_6$ in 1:1:1 EC:DMC:DEC v/v/v% electrolyte, cycled at 0.1C. Plating efficiency is used to set the stripping limit of the limited stripping procedure shown in the main text.

EDS ON COPPER OF FULL CELLS WITH STAINLESS STEEL SURROUNDING

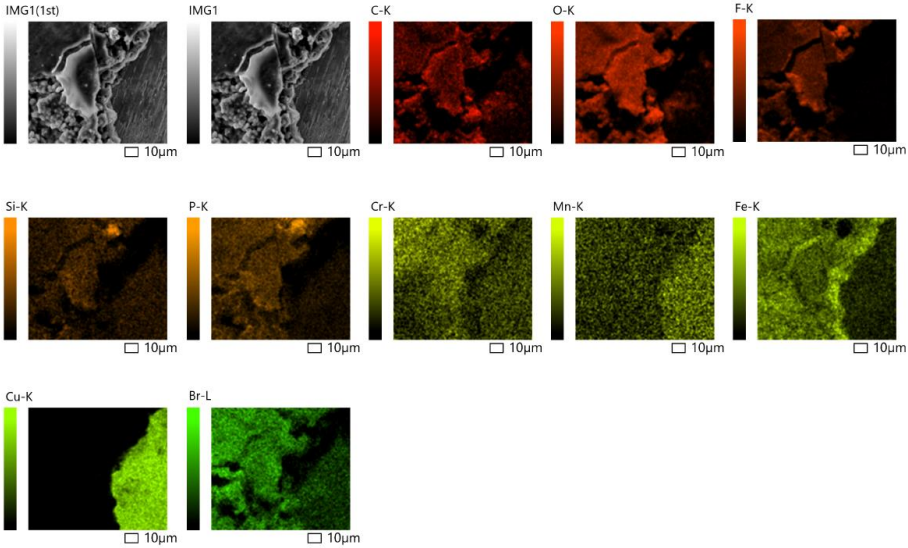

Figure S 5 Analysis of atomic composition on copper of a shorting Cu:NMC811 full cell. Dissolution and subsequent electroplating of stainless steel from the cell body was found to be the origin of observed side reactivity.

BROMIDE REDOX DURING CV

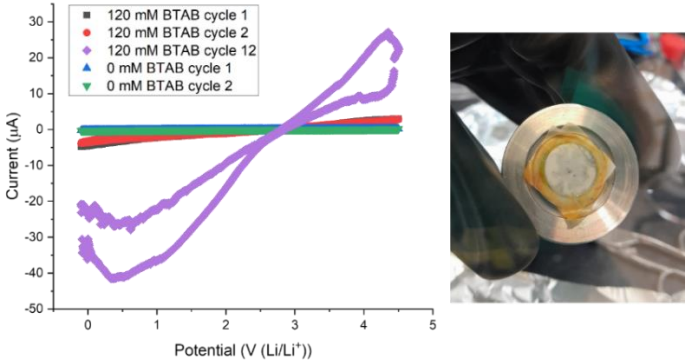

Figure S 6 Bromide redox during CV tests vs stainless steel. Left: Br2 to Br- redox is becomes apparent after repeated cycles of CV (purple, peaks at 4V vs Li/Li+ and below 2V vs Li/Li+. Right: dissolved bromine shows a distinct orange color after cycling. Inner circle (white) indicates position of counter electrode.

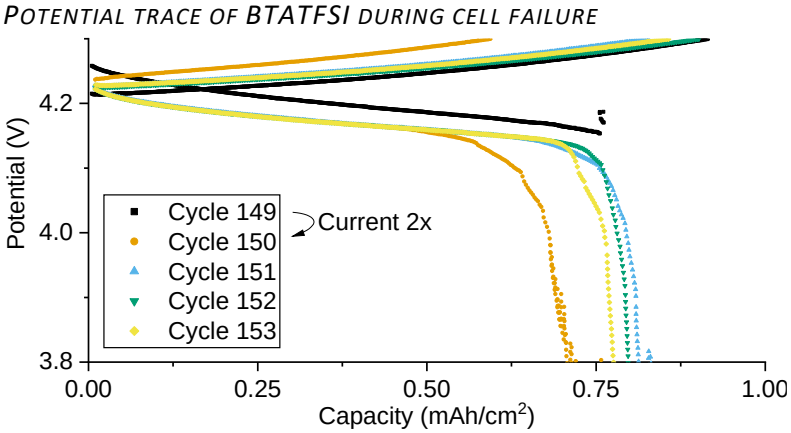

Figure S 7. Cell performance after circuit brake during discharge of cycle 149. Potential versus areal capacity in NMC811:Cu cell with 100 mM BTATFSI in 1 M $LiPF_6$ in 1:1:1 EC:DMC:DEC v/v/v% electrolyte. Initially the current is set at 0.2 mA/cm², which is doubled from cycle 150 onward.

ONSET PLATING OF 100 MM BTATFSI IN 1 M $LiPF_6$ IN 1:1:1 EC:DMC:DEC

Figure S 9. Onset plating of lithium after 2 hours of plating at 0.1 mA/cm² with 100mM BTATFSI in 1 M $LiPF_6$ in 1:1:1 EC:DMC:DEC in a Li:Cu cell.

7. Fluorine Free Lithium Ion Batteries: A Working Alternative

The content of this chapter is in the process of submission to a scientific journal.

Fluorine Free Lithium Ion Batteries: A Working Alternative

ABSTRACT

Current commercial battery designs contain fluorinated materials as binders and electrolyte salts to ensure high electrochemical and thermal stability. Upcoming regulations in Europe and the US restrict the manufacturing of such materials, as their persistence in drinking water and soil can cause long term ecological harm. In this perspective, we showcase a completely fluorine-free battery design which has similar performance compared to commercial standards, while using aqueous processed LiNi0.8Mn0.1Co0.1O2 (NMC811) and graphite as cathode and anode active materials respectively. The cell shows 98% retained capacity after 600 cycles at room temperature, indicating good stability of active material with non-fluorinated binders. The charge rate performance (69% retained capacity at 1C, 1.5 mAh/cm2) could be improved by combining two fluorine-free salts (67% retained capacity at 1C with 2.5 times the loading, 3.3 mAh/cm2). This work illustrates that fluorine-free cell designs show good battery performance over a wide potential window.

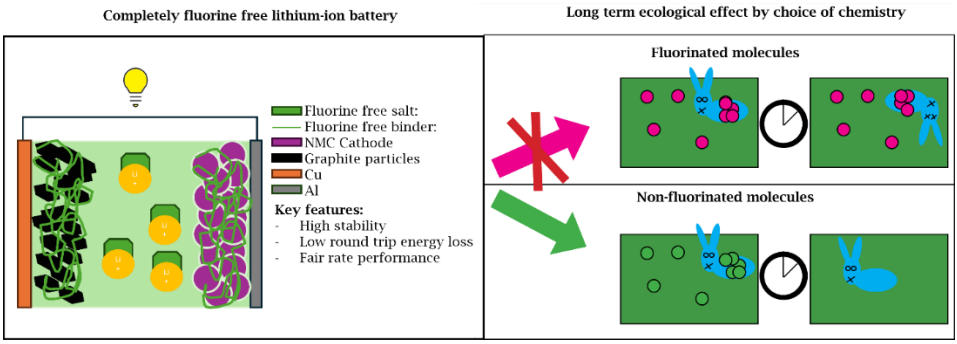

INTRODUCTION

Current commercial battery designs contain highly fluorinated molecules to ensure high electrochemical and thermal stability. Binders such as polyvinylene difluoride (PVDF), polytetrafluorethylene (PTFE), electrolytes containing lithium salts in the form of lithium hexafluorophosphate ($LiPF_6$) and additives like fluoroethylene carbonate (FEC) have become the state-of-the-art in cathode and electrolyte manufacturing respectively.[1–4] The beneficial (electro)chemical stability features of these materials when confined inside of a battery cell are, however, proving to be harmful outside of their application area, i.e. during manufacturing, recycling and end-of life demolition. Fluorinated alkanes and HF-producing substances are indicated to be harmful, as they induce long-term health and environmental hazards. Their persistence causes accumulation over time at so-called 'hot spots', locations with continuous increased concentrations of organic fluorine containing compounds. Intensive purification and regeneration of the land after exposure remains the only option.[5] Also, bioaccumulation occurs during exposure to PFAS, as nature has not developed a system that addresses the rejection or the digestion of fluorinated carbons.[6] The stability that enhances battery lifetime is preventing natural routes to degrade to environmentally harmless substances. Therefore, the public opinion and legal standpoint on fluorinated compounds, especially the fluorinated polymers (Poly/PerFluorinatedAlkyl Substances or PFAS) has shifted from 'highly appreciable' to 'not preferable unless necessary' at best.[7] Within the EU, there is the intention under review to have a restriction on 'the manufacture, placing on the market and use of PFASs'.[8] In the US, similar developments were announced.[9] However, some applications such as lithium batteries, currently need PFAS for its high performance. If other options exist, they are preferred and should be chosen. Showing alternative chemistries with similar performance during operation is, therefore, instrumental to be able to enforce a PFAS ban in battery applications. Moreover, from a recycling perspective banning PFAS binders from battery chemistry would enhance the electrode recyclability.[10] Also, the presence of fluorine during recycling, specifically the pyro- and hydrometallurgic processing, complicates the recycling process as well due to the formation of highly corrosive HF.[11] In this context, this perspective focusses on showing a completely fluorine-free battery composition that may replace the current fluorinated ones. The fluorine-free battery shows high rate performance over a large

potential window (2.7-4.3 V) and can cycle more than 500 times with high capacity retention.

Various approaches for fluorine free battery designs[12], electrolytes[13,14] and binders[15,16] have been proposed. The intrinsic advantage of lithium-ion batteries is the high cell potential which stems from the large potential window between anodes at a reduction potentials down to the extreme of Li/Li^+ at -3.04V vs SHE, and cathode at an oxidation potential which can be as high as +1.46V vs SHE (+4.5V vs Li/Li^+) for nickel rich layered oxides. The high oxidation potential at the battery cathode limits the applicability of several polymer binders, especially if potentially oxygen-releasing cathode materials are used; organic binders consisting of unprotected carbon chains may be subject to oxidation from instabilities occurring at the active material interfaces.[17] Degradation and potential contact loss of binder to active material lead to a fade in capacity, which would reduce the battery's lifetime. At the anode, this problem is less prominent as it resides at highly reducing potentials around -3.04 V vs SHE. For this reason, F-free organic binders have already been used commercially at the anode.

The second concern is the processability of the binder and active material. For a fluorinated binder like PVDF, organic solvents such as N-methylpyrrolidone (NMP) is used, although they are toxic. Such organic solvents are also used because of the limited compatibility of cathode active materials with more benign solvents like water: In their discharged state, nickel-rich layered oxides are typically prone to exchange of lithium and hydrogen when exposed to water.[18] The effect results in a higher lithium hydroxide concentration and, thereby, a higher alkalinity (higher pH) of the solution. Many studies, however, have addressed this issue, proposing processing methods, which include extensive drying, limited contact times and/or addition of acids and base components to the solvent.[19–22] As a result, the degradation of cathode active material by water-based processing has been minimized to a marginal difference.[22] The fluorine-free organic binders, which are -unlike many fluorinated ones- soluble in water, thus become available. Therefore, an additional advantage beyond the potential phasing out of PFAS is the less harmful processing of these binders in water as a solvent as well.

A list of organic binders, highlighting their applicability and their advantages and disadvantages, is shown in Table S1. The most promising options for fluorine-free binders have been polyacrylic acid (PAA) and carboxy methyl cellulose combined with styrene butadiene rubbers (CMC/SBR).[21,23,24] Here, the Graphite anode and the

NMC811 cathode are produced using PAA and CMC/SBR respectively. Advantages for using PAA in graphite anodes are its thermal stability and maintained electrolyte accessability at low porosity, resulting in improved energy densities.[25] For anodes which incorporate silicon in future fluorine free batteries, to increase the energy density further, PAA or PAA/CMC are the most suitable options as it offers higher cycling stability.[26] Silicon anodes in fluorine free systems also do not suffer from fluorine containing decomposition reactions creating HF when combined the PAA acidic groups, which otherwise would cause silicon dissolution of SiO_x in the SEI.[27] The choice of CMC/SBR as binder in NMC811 cathodes is based on comparable performances to conventional PVDF binder reported for similar NMC cathodes[23] and the possibility of functionalization to passivate the SEI further.[28,29] This paper highlights that combining such organic binders with specifically fluorine free electrolytes offers advantages considering the SEI stability, leading to a high cycling life.

To ensure the electrolyte function, the Li^+ conducting salt needs to have high stability in oxidative and reductive environments to prevent degradation at the cathode and anode respectively. Further, the conductive ion in the salt needs to have limited solvation and binding strength to its counterion to reduce the energy cost of transferring the ion from the bulk electrolyte phase, through the electric double layer to the active material at the electrode interfaces.[30] These combined demands have proved to be challenging.[31] Electrochemical stability often goes hand in hand with the high energy cost of ionic transfer. The development of fluorine-free salts that cover both aspects has been a field of research, which has yielded only a few feasible options so far, as treated by Hernandez et al in [31]. An asymmetric, charge delocalized counterion with moderate to high ionic strength seems pivotal in generating both charge dissociation in conventional electrolyte solvents, while maintaining low lithium ion solvation by solvent molecules surrounding the ion pair in the electric double layer of the anode. [31–33] The latter is necessary to reduce side reactions of solvent molecules. Generating a stable solid electrolyte interface (SEI) composition, with additives or solvent should then finally minimize side reactivity at the active sites.

One of the most promising options for fluorine-free salts is Lithium bis(oxalato)borate (LiBOB).[34,35] LiBOB synthesis is performed using a benign route of wet processing HBO_3 with lithium hydroxide and dioxalic acid.[36] It contains a quarternary oxygenated boron ion of which the oxygen atoms are linked to ethene to prevent reduction. The ion is

fairly large and has shown to support limited ionic conductivity and has limited solubility in carbonate electrolytes[37]. It is, however, fairly stable at both cathode and anode interfaces after initial interphase formation. LiBOB is also used as an additive, as it decomposes at the anode and cathode resulting in a conducting SEI[38], CEI[39] and a passivated aluminium current collector,[40] which may be stabilized together with polymerizing additives like vinylene carbonate (VC) or 1,3,2-Dioxathiolane 2,2 Dioxide (DTD).[41,42]

Another commonly used salt is $LiNO_3$, which most often functions as sacrificial salt to increase conductivity in the SEI layer. The potential stability of $LiNO_3$ is not suitable to act as conducting lithium salt in carbonate electrolytes, as the molecule is preferably reduced.[48] However, by modifying the solvation shell stable cycling has been demonstrated in LNO:Graphite and LFP:graphite cells.[49] The $LiNO_3$ salt shows extraordinary performance in CEI formation for applications in wide temperature ranges,[50] showing conductivity between -60 and 80 °C. Also, in combination with $LiClO_4$ a stable SEI in lithium metal can be formed using $LiNO_3$[51]. In this work, instead of $LiNO_3$ as sacrificial salt we demonstrate the combination of the passivating behavior of LiBOB combined with VC and DTD as it is known to passivate the aluminium current collector.

Lithium perchlorate, $LiClO_4$ has been another candidate with widespread attention in the past due to its high ionic conductivity.[43] However, $LiClO_4$ is a strong oxidizing agent, which has a tendency to create oxygen radicals and has shown reactivity with the aluminium current collector above 3.2 - 3.5 V vs Li/Li^+.[44,45] However, LiBOB is known to passivate the aluminium surface.[46] The use of $LiClO_4$ has caused concerns considering safety and is currently restricted to limited use for practical lithium ion batteries. The electrolyte solvents used in conventional liquid state Li-ion batteries are usually flammable, which is also the case here. As these solvents are normally non-fluorinated this is similar flammability as for conventional liquid state Li-ion batteries. Nevertheless, its use has been compared to $LiPF_6$ by Marom et al.[47] arguing previous safety experiments were conducted using solely lithium metal anodes, while for graphite, the main conclusion is that 'in terms of onset temperatures for thermal runaway, the two electrolytes are equivalent'. Therefore, here LiBOB is used without and combined with $LiClO_4$ to show 1) the high (electro)chemical stability of fluorine-free battery cells, 2) an increased lithium conductivity by combining the two salts, which would further bring forward the usage of electrolytes like LiBOB for batteries that need high rate performances. Compared to pure LiBOB, we propose that a salt

addition similar to $LiClO_4$ would be necessary to increase the bulk mobility, while LiBOB, VC, and DTD adequately stabilize the interfaces with the electrodes.

For the full fluorine-free battery design, we report the performance of a battery containing state-of-the-art Graphite anodes and NMC-811 cathodes in which PAA and SBR/CMC binders are utilized for anode and cathode respectively.

METHODS

Graphite anodes were made using 90/5/5 m/m% Timrex E-SLS 30 graphite (Imerys)/PAA binder (3000K, Aldrich)/carbon Super P C45 (MSE). The powder mixture was suspended in three steps using a top stirrer (IKA). First 18:1 water to powder mass was added to a container and after initially suspending for 15 minutes a 2:1 water to powder mass ratio was added. This was repeated a second time until a castable slurry was obtained. A coating was made using a 200 and 300 µm doctor blade casting on copper foil, after which the coating was dried in a vacuum oven at 60 °C for at least 16 hours.

NMC-811 cathodes were made using 94/3/1/1 m/m% NMC-811 (Gelon, polycrystalline)/carbon Super P C45 (MSE)/KS4 (Timcal)/SBR (15wt% stabilized suspension, Targray)/CMC (Sigma). Powders were suspended in 12:1 water to powder ratio. An ink was obtained after 60 minutes. A coating was made using a 150 and 250 µm doctor blade casting on aluminium foil, after which the coating was dried in a vacuum oven at 60 °C for at least 16 hours and subsequently for 16 hours at 80 °C.

Dried anode and cathodes were punched into 14 and 15 mm diameter circles respectively and subsequently assembled in CR2032 coin cell using a Celgard 2400 separator with 90 µl electrolyte. The base LiBOB electrolyte used is 0.6 M LiBOB in 2/49/49 v/v% Vinylene carbonate/Ethylene carbonate/dimethyl carbonate (VC/EC/DMC, E-lyte). A second electrolyte with increased conductivity and stabilizing agent DTD (Merck Sigma) was formulated as 0.3/0.3 M LiBOB/$LiClO_4$ in 1/2/48.5/48.5 v/v% DTD/VC/EC/DMC, called LiBOB/$LiClO_4$. A reference electrolyte of 1 M $LiPF_6$ in 1/1/1 v/v/v% EC/DMC/DEC (Merck Sigma) is used during the chemical stability tests.

Galvanostatic cycling was performed after a 24 hour rest period on a MACCOR-4000 cell cycler between 2.7 and 4.3 V. Fast discharging was tested initially at C/10 charge rate and C/10, C/5, C/2 and 1C discharge rate for 5 discharge cycles each. After rate

performance for cycling again a period of 40-42 cycles at C/10 charge and discharge rate was used. After this period 1C charge and discharge rates cycling was initiated. For LiBOB/$LiClO_4$ cells, initially the same current density for the same set period was used to compare electrolyte aging, meaning the tests were performed at 0.4 times the C-rate indicated above, after which the full potential window and appropriate C-rate was used to test the cell performance further. Electrochemical impedance (EIS), cyclic voltammetry (CV), potentiostatic intermittent titration (PITT) and step amperometry was measured on a Parstat MC200 Module. EIS was measured at 2.7 V between 100 kHz and 10 mHz AC frequencies at 10 mV amplitude. Chemical stability was measured using CV at a scan rate of 0.1 V/s from OCP in the potential range of 0 – 5 V in Li/Al cells, using a glass fibre separator immersed with electrolyte. Electrolyte conductivity was measured using two stainless steel plates with a PP spacer of 47 µm with a 10 mm diameter hole filled with electrolyte using EIS. Step amperometry and PITT (dU=0.01V) was measured in symmetric lithium metal cells with Celgard 2400 as separator in C2032 coin cells. Conductivity values were calculated by using eq. 1 taking PITT steady state current I_{ss}, charge transfer resistance R_{ct} and electrolyte resistance R_{ele} (Table S2). The cell area A, if applicable Celgard porosity ε (40%) and thickness (25 µm) was used.

$$\sigma = \frac{d}{A * \varepsilon * (R_{ss} - R_{ct})}$$

eq. 1

To perform post-mortem analyses, graphite electrodes were retrieved from coin cells after cycling. The samples were washed with DMC to remove salt traces and dried. Scanning electron microscopy (SEM) pictures were taken using a JSM-IT700HR FE-SEM setup (JEOL) in scattering electron imaging (Acc. Voltage: 1 kV - 5 kV). Energy dispersive X-ray spectroscopy was performed in Backscattered electron composition (Acc. voltage: 20 kV) mode. Surface composition was measured with X-ray photoelectron spectroscopy (XPS) using a K-alpha spectrometer (Thermo Fisher Scientific) with a Al Kα source with a spot size of 400 µm. Charge correction was performed by calibrating the adventitious carbon peak (285 eV).

RESULTS

The fluorine-free electrolytes show lower conductivities than generally reported for liquid electrolytes. The ionic conductivity of 0.6 M LiBOB and 0.6 M $LiClO_4$ in EC:DMC in blocking conditions in a stainless steel cell configuration shows $\sigma_{SS,RT}$ =1.6 ± 0.3

mS/cm and 1.5 ± 0.3 mS/cm respectively. The conductivity decreases to $\sigma_{ele,RT}$ = 0.12 and 0.07 mS/cm and $\sigma_{Li,RT}$ = 0.06 and / 0.04 mS/cm respectively when measured in wetted Celgard 2400 separators in symmetric lithium cells. Such steep decrease in conductivity when wetted on the separator can be the result of poor compatibility with the separator.[52] Practical conductivity of 0.3 M/0.3 M LiBOB/$LiClO_4$ in symmetric lithium cell however increases to $\sigma_{ele,RT}$ = 0.65 mS/cm, $\sigma_{Li,RT}$ = 0.13 mS/cm.

The chemical stability of $LiClO_4$ is a second concern, as reduction of $LiClO_4$ occurs (Figure 1C, arrow at 0.7 V), probably to LiCl and Li_2O.[53] LiBOB however only shows mild oxidation during the initial sweep (Figure 1B, arrow) after which no additional side reactivity is observed. $LiPF_6$ shows only minor side reactivity above 4.2 V indicating mild EC oxidation, becoming larger every sweep (Figure 1A, arrow).

To test the buildup of SEI resistance electronic impedance spectroscopy (EIS) is carried out before and after a galvanostatic test at 0.1 mA/cm^2 in symmetric lithium cells for 1 hour. An increase in charge transfer resistance can be observed for 0.6 M $LiClO_4$, while for the electrolytes containing LiBOB this effect remains marginal (Figure 1D, increase in first semicircle). The EIS fitting indicates two semicircles for all fits (fitting results can be found in Table S2). Typically the SEI and Charge transfer have different characteristic frequencies. Charge transfer resistance, of which the double layer capacitance in parallel is fitted typically in the microfarad order, shows small resistances for LiBOB containing species before and after the galvanostatic cycling period. $LiClO_4$ cells however show an increase of charge transfer resistance, indicating slight passivation of the lithium interface may have occurred. SEI resistance shows an increase for the LiBOB containing cells. The LiClO4 cell here shows a lowered SEI resistance, which indicate the passivation layer is not stable and renewing constantly. A combination of both salts in an electrolyte may effectively show lower polarization due to elevated ion conductivity, while maintaining a stable interface at the electrode interfaces. This is illustrated by the step amperometry results in Figure 1E. Here $LiClO_4$ electrolyte initially shows similar polarization compared to LiBOB, after which it starts to show a buildup of additional polarization after a few hours of galvanostatic current while the polarization of LiBOB and LiBOB/ $LiClO_4$ electrolytes maintains fairly Tafel like behaviour (Figure 1F), with at most a small Ohmic contribution: the DC potential grows much less than linearly with current, indicating that an activated Buttler Volmer type behaviour is still dominating the observed overpotential. The deviation from Tafel

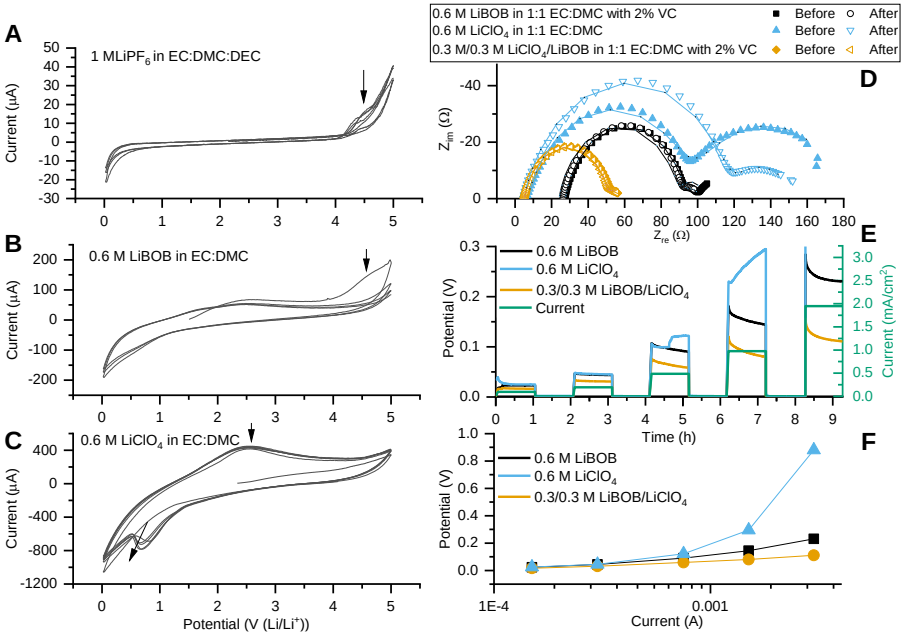

Figure 1. Chemical stability of $LiPF_6$ (A), LiBOB (B) and $LiClO_4$ (C) lithium salts in carbonate solvents measured using cyclic voltammetry at 0.1 V/s in Lithium/Aluminium half cells for three sweeps. $LiClO_4$ shows an additional reduction reaction at 1 V (red arrow). Nyquist plot of symmetric lithium cells (D) show increasing SEI resistance with $LiClO_4$ electrolyte, which is reduced when introducing LiBOB salt. Step amperometry (E) and Tafel plot of end point potentials during step amperometry (F) in symmetric lithium cells shows a lower overpotential for the 0.3 M / 0.3 M $LiClO_4$ electrolyte as a result.

behavior becomes large, however, for pure $LiClO_4$ electrolyte, indicating strongly current dependent resistance term.

Using the combined salt configuration we report excellent cycling stability and fair rate capabilities at room temperature (RT, 18 °C). We show, however, that there remains a trade-off between stability and rate performance. On one hand, LiBOB shows very high cycling stability, which comes at the cost of limited round-trip energy efficiency due to high overpotentials. On the other hand, the combined LiBOB/$LiClO_4$ salt shows excellent rate performance with a slightly lower cycling stability as a trade-off. In Figure 2A, the potential trace during galvanostatic cycling of a LiBOB full cell is shown. At relatively low C/10 (dis)charge rates, already a significant potential difference

between charging and discharging is observed at 50% depth of (dis)charge. This mainly originates from the potential drop in the electrolyte caused by its sluggish bulk diffusivity. The LiBOB cell shows 99 mV potential difference between charge and discharge at C/10 or 0.15 mA/cm^2. The energy efficiency of the cell is 95%. A higher current density of 1.5 mA/cm^2 (1C) shows 460 mV potential difference yielding 87.4% energy efficiency. At this cycling rate, the capacity retention is reduced to 70.5%. The low electrolyte conductivity contributes heavily to the overpotential and, therefore, capacity fade at higher charge rates. This performance difference in conductivity affects the energy efficiency and allowable electrode loading for achieving fair rate performanes. Therefore, a LiBOB/$LiClO_4$ cell is shown with 2.5 times the mass loading to illustrate the beneficial performance of the mixed ion electrolyte.

Upon long-duration cycling, initially, the current density of LiBOB and LiBOB/$LiClO_4$ cells are kept at 0.15 mA/cm^2 to compare cell overpotentials (Figure S 2) ignoring the contributions of the relatively low double layer resistances at these currents. Then the C-rate definition is utilized for a longer cycling period (Figure 1C/D). The LiBOB/$LiClO_4$ cell shows a reduced 70 mV potential difference at 0.15 mA/cm^2 (Figure 1B) with an energy efficiency of 98%. This is 3% more compared to LiBOB and is acceptable for lithium ion batteries at cell level.[54] At 1C, the overpotential (483 mV) and capacity retention (66%) is similar to the 1C performance of the LiBOB cell which contained 2.5 times lower loading. The lower overpotential of LiBOB/$LiClO_4$ allows a higher current, yielding 86.1% energy efficiency at 1C with 7.14 mWh/cm^2 (and 2.05 mAh/cm^2) energy density (which was 3.05 mWh/cm^2, 0.9 mAh/cm^2 for LiBOB at the same C-rate). The difference in rate performance illustrates a route to lower the overpotentials in the electrolyte by the addition of the $LiClO_4$ salt.

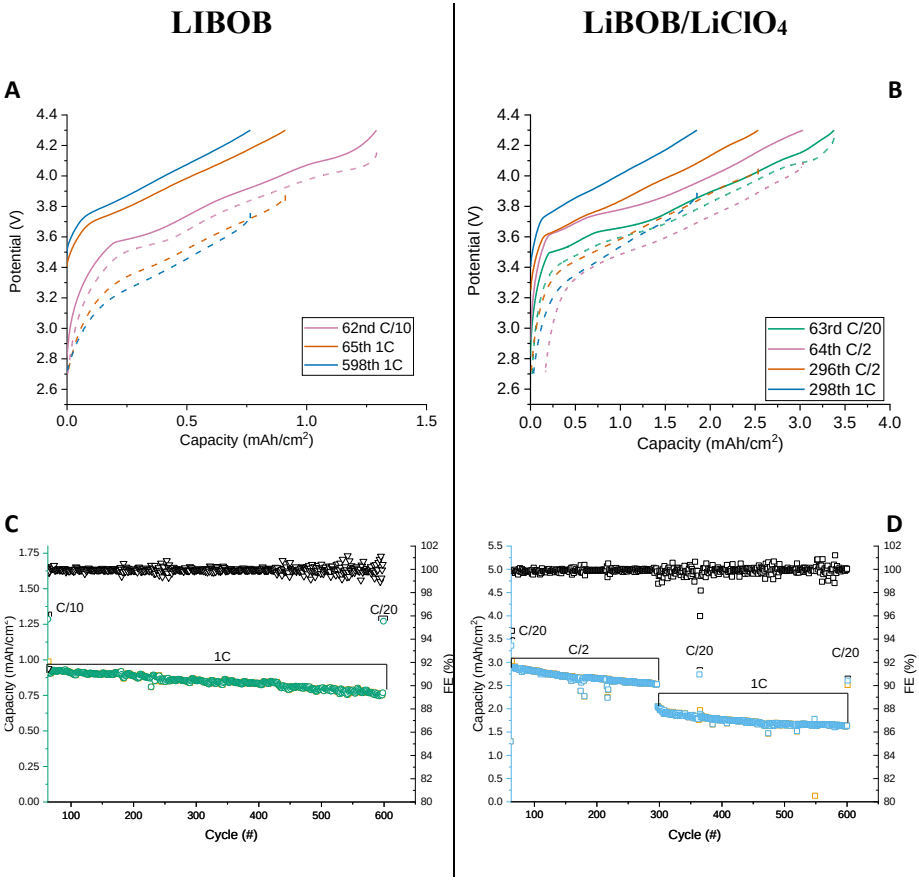

Figure 2. Potential trace (A,B solid charge, dotted discharge), cycling performance (C,D) of NMC811/Graphite full cells. A/C: cell with theoretical areal cathode loading of 1.3 mAh/cm² with 0.6 M LiBOB in 2/49/49 v/v% VC/EC/DMC electrolyte. B/D: same electrode materials but with theoretical areal cathode loading of 3.3 mAh/cm² illustrating the enhanced conductivity of the electrolyte with 0.3/0.3 M LiBOB/LiClO4 in 1/2/48.5/48.5 v/v% DTD/VC/EC/DMC.

In Figure 2C, the cycling results of a LiBOB NMC811/Graphite full cell is shown. The LiBOB cell shows 98% retained capacity in the 600th cycle at C/20 (Figure 2C).This shows that the LiBOB cell is able to obtain both anodic and cathodic stability. In contrast, the LiBOB/$LiClO_4$ cell retained 74.8% of its capacity after 600 cycles (Figure 2). In terms of performance loss at 1 C the difference is smaller. During the last 300 1C cycles the LiBOB/$LiClO_4$ cell loses 18% capacity at 1C, compared to 12% for the LiBOB cell. The apparent stability of the LiBOB cell does not mean there is no change observed when comparing resistances due to electrolyte degradation and SEI buildup,

as shown by EIS (Figure 3 top, fitting results shown in Table S4). Charge transfer resistances through the SEI and double layer capacitance typically occur between 10 and 1000 Hz[55] and show several Ohms difference (100 Hz arrow). The electrolyte resistances R_{ele} at 100 kHz show only marginal increase (pristine: 10.7 Ω, cycled: 13.0 Ω). Although these changes occur, they only imply that at higher rates, the voltage cut-off is reached earlier. At C/20, the capacity is still accessible, meaning limited Li inventory loss in irreversible SEI formation and/or lithium plating at high charge rates, and thus limited capacity loss is observed. For the $LiClO_4$ containing electrolyte, it is observed that R_{ele} remains lower after cycling (9.7 Ω) compared to the pristine LiBOB cell (13.0 Ω) (Figure 3, bottom). A large change in capacitive response is observed in the low-frequency impedance range (100 Hz - 100 mHz) which may originate from the limited lithium loss in NMC, which makes that the electrode in the fully discharged state (OCP=2.7 V) is nevertheless different; non-blocking diffusional resistances deeper in the crystallites can extend the low frequency and more resistive response.[56]

After cycling, cells were opened and graphite electrodes were retrieved. The electrode integrity seems unaltered and a smooth film layer is formed on both LiBOB and LiBOB/$LiClO_4$ cells (SI Figure S5). The surface composition of the cell containing LiBOB/$LiClO_4$ shows a slightly lower binding energy for Li1s compared to the LiBOB cell (0.5 eV, Figure 4B and A respectively), which may originate from a higher abundance of $LiBO_2$ species. The abundance of boron on graphite electrodes after cycling were higher for LiBOB (5.0 +/- 0.5 %at) compared to LiBOB/$LiClO_4$ (3.4 +/- 0.3 at%) cells, as measured with XPS (SI Table S5).

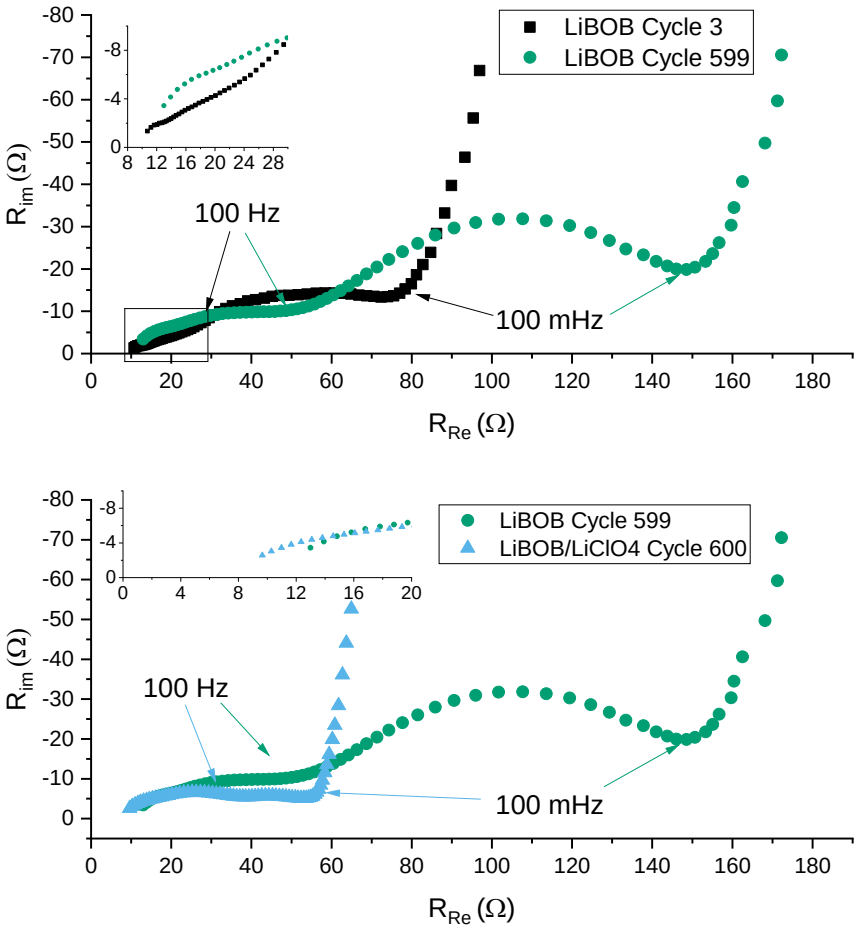

Figure 3 Top) Electrochemical Impedance spectroscopy (EIS) of fluorine-free NMC-811/Graphite full LiBOB cells at OCP=2.7 V after formation and extensive cycling. Bottom) EIS spectra of fluorine-free NMC811/Graphite full LiBOB and $LiClO_4$ cells after cycling, at 2.7 V OCP. Loading and electrolyte composition between cells differed. LiBOB: 1.3 mAh/cm² with 0.6 M LiBOB in 2/49/49 v/v% VC/EC/DMC, LiBOB/$LiClO_4$: 3.3 mAh/cm² with 0.3/0.3 M LiBOB/LiClO4 in 1/2/48.5/48.5 v/v% DTD/VC/EC/DMC. High frequency impedance shows electrolyte resistance R_{ele} (7.8 Ω, 100 kHz) of LiBOB/$LiClO_4$ remains lower compared to LiBOB (pristine: 10.7 Ω, cycled: 13.0 Ω). Lower frequencies are not directly comparable due to differences in cathode and anode loading.

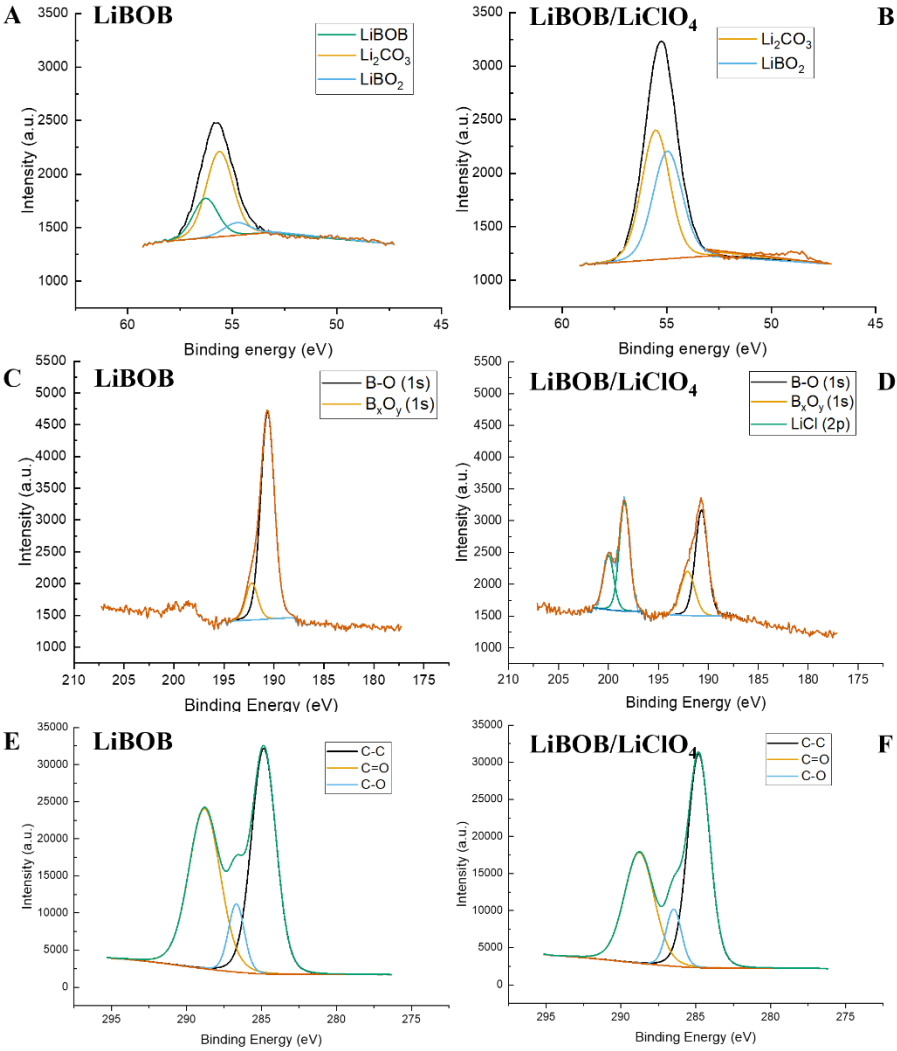

Figure 4 XPS Profile of graphite electrode after cycling. Li1s scan of A) LiBOB and B) LiBOB/$LiClO_4$ indicates slightly lowered oxidation state of lithium in the SEI upon presence of $LiClO_4$ in the electrolyte. Allocation of environments according to [57]. Boron B1s and Chloride Cl2p spectrum of C) LiBOB and D) LiBOB/$LiClO_4$ showing a change in oxidation state of boron, which is increased compared to LiBOB. Carbon C1s spectrum of D) LiBOB and E) LiBOB/$LiClO_4$ indicating graphite/hydrocarbon C-C, semi carbonate-like C=O and polyether/carbon C-O species.[38]

Two clear chemical environments of boron could be identified of which the LiBOB/$LiClO_4$ cell shows an increased fraction of boron with higher binding energy (32.6 % B1s(1)/$B1s_{total}$ in Figure 4C) compared to LiBOB cells (13.5 % B1s(1)/$B1s_{total}$ Figure 4D). DTD in the LiBOB/$LiClO_4$ resulted in 1.2 at% sulfur present on the surface. A low amount of chlorine (0.3 at%) is observed, indicating a low amount of LiCl or other degradation products from $LiClO_4$ is formed. The LiBOB/$LiClO_4$ shows a higher amount of (semi)carbonate compared to polyether/C-O in the C1s spectrum (Figure 4E and F), which is characteristic of LiBOB degradation products in the SEI and in line with the abundance of the Li1s carbonate environment.[38] Polyethers are more typical from polymerization originating from radical reactions forming CO_2 during EC degradation.[38] The SEI composition thus is dominated by carbonates (38 at% and 34 at% C for LiBOB and LiBOB/$LiClO_4$), with boron containing degradation products from LiBOB (both cells) and sulfur from DTD (LiBOB/$LiClO_4$ cell). Both are known for their good SEI stabilization performance. Although the oxidation state of boron species shows a slightly higher abundance for LiBOB/$LiClO_4$, no major change in organic/inorganic SEI composition is observed between LiBOB and LiBOB/$LiClO_4$ cells.

DISCUSSION AND CONCLUSIONS

The fluorine-free LiBOB/PAA/SBR/CMC based battery shows outstanding capacity retention, while not using a fluorine-based materials inventory. $LiClO_4$ addition to the electrolyte yields improved rate performances at higher areal capacities, at the cost of increased capacity fade during long-term cycling. For higher areal capacity batteries, the addition of $LiClO_4$ may be considered, as it increases the ionic conductivity, and with respect to safety, the thermal instability onset is reported to be similar to that of $LiPF_6$.[47] The graphite electrode structure after cycling is unaltered, as observed by SEM. Also, the SEI composition for LiBOB/$LiClO_4$ seems to be improved when compared to LiBOB. The LiBOB cell contains a lower abundance of (stable) LiBOB degradation products compared to LiBOB/$LiClO_4$. The abundance of chlorine (from $LiClO_4$) on the surface is relatively low, indicating low amounts of LiCl formed. These results highlight that fluorine-free lithium-ion batteries are achievable in batteries with realistic areal capacities using the appropriate fluorine-free binders and a fluorine-free electrolyte salt. Acceptable (dis)charge rates and durability are observed, compatible with typical applications where (dis)charge rates of C/2 – 1C with active mass loadings greater than 1.5 to 3 mAh/cm^2 are required. Such applications include general mobile battery-powered applications like laptops, power tools, and electric vehicles.[58,59]

REFERENCES

(1) Piątek, J.; Afyon, S.; Budnyak, T. M.; Budnyk, S.; Sipponen, M. H.; Slabon, A. Sustainable Li-Ion Batteries: Chemistry and Recycling. *Advanced Energy Materials* **2021**, *11* (43), 2003456. https://doi.org/10.1002/aenm.202003456.

(2) Li, M.; Lu, J.; Chen, Z.; Amine, K. 30 Years of Lithium-Ion Batteries. *Advanced Materials* **2018**, *30* (33), 1800561. https://doi.org/10.1002/adma.201800561.

(3) Xu, N.; Shi, J.; Liu, G.; Yang, X.; Zheng, J.; Zhang, Z.; Yang, Y. Research Progress of Fluorine-Containing Electrolyte Additives for Lithium Ion Batteries. *Journal of Power Sources Advances* **2021**, *7*, 100043. https://doi.org/10.1016/j.powera.2020.100043.

(4) Wang, Y.; Wu, Z.; Azad, F. M.; Zhu, Y.; Wang, L.; Hawker, C. J.; Whittaker, A. K.; Forsyth, M.; Zhang, C. Fluorination in Advanced Battery Design. *Nat Rev Mater* **2023**, *9* (2), 119–133. https://doi.org/10.1038/s41578-023-00623-4.

(5) Wang, P.; Wang, T.; Giesy, J. P.; Lu, Y. Perfluorinated Compounds in Soils from Liaodong Bay with Concentrated Fluorine Industry Parks in China. *Chemosphere* **2013**, *91* (6), 751–757. https://doi.org/10.1016/j.chemosphere.2013.02.017.

(6) Lewis, A. J.; Yun, X.; Spooner, D. E.; Kurz, M. J.; McKenzie, E. R.; Sales, C. M. Exposure Pathways and Bioaccumulation of Per- and Polyfluoroalkyl Substances in Freshwater Aquatic Ecosystems: Key Considerations. *Science of The Total Environment* **2022**, *822*, 153561. https://doi.org/10.1016/j.scitotenv.2022.153561.

(7) Dorrance, L. R.; Kellogg, S.; Love, A. H. What You Should Know About Per- and Polyfluoroalkyl Substances (PFAS) for Environmental Claims. *Environmental Claims Journal* **2017**, *29* (4), 290–304. https://doi.org/10.1080/10406026.2017.1377015.

(8) *Per- and Polyfluoroalkyl Substances (PFAS)*. https://echa.europa.eu/registry-of-restriction-intentions/-/dislist/details/0b0236e18663449b.

(9) EPA, press office. Biden-Harris Administration Finalizes First-Ever National Drinking Water Standard to Protect 100M People from PFAS Pollution. *EPA*.

(10) Wolf, A.; Nagler, F.; Daubinger, P.; Neef, C.; Mandel, K.; Flegler, A.; Giffin, G. A. Circular Battery Design: Investing in Sustainability and Profitability. *Energy Environ. Sci.* **2024**, 10.1039.D4EE03418J. https://doi.org/10.1039/D4EE03418J.

(11) Wang, M.; Liu, K.; Yu, J.; Zhang, Q.; Zhang, Y.; Valix, M.; Tsang, D. C. W. Challenges in Recycling Spent Lithium-Ion Batteries: Spotlight on Polyvinylidene Fluoride Removal. *Global Challenges* **2023**, *7* (3), 2200237. https://doi.org/10.1002/gch2.202200237.

(12) Savvidou, E. K.; Rensmo, A.; Benskin, J. P.; Schellenberger, S.; Hu, X.; Weil, M.; Cousins, I. T. PFAS-Free Energy Storage: Investigating Alternatives for Lithium-Ion Batteries. *Environ. Sci. Technol.* **2024**, *58* (50), 21908–21917. https://doi.org/10.1021/acs.est.4c06083.

(13) Nam, S.; Seong, H.; Kim, Y.; Kim, K.; Kim, C.; Kwon, S.; Park, S. All Fluorine-Free Lithium-Ion Batteries with High-Rate Capability. *Chemical Engineering Journal* **2024**, *497*, 154790. https://doi.org/10.1016/j.cej.2024.154790.

(14) Ramesh, S. L.; Lopez, J. Fluorine-Free Electrolytes for Lithium Metal Batteries: Challenges and Opportunities in Solvation Structure and Interphase Design. *ACS Energy Lett.* **2025**, *10* (4), 1671–1679. https://doi.org/10.1021/acsenergylett.5c00319.

(15) Jang, J.; Ahn, J.; Ahn, J.; Jeong, U.; Yoon, J.; Park, J. K.; Shin, W.; Kang, M. J.; Cho, M.; Kang, D. J.; Kim, J.; Yoo, J.; Im, H. A Fluorine-Free Binder with Organic–Inorganic Crosslinked Networks Enabling Structural Stability of Ni-Rich Layered Cathodes in Lithium-Ion Batteries. *Adv Funct Materials* **2024**, *34* (42), 2410866. https://doi.org/10.1002/adfm.202410866.

(16) Leibetseder, F.; Xie, J.; Leeb, E.; Hesser, G.; Pettinger, K.; Bretterbauer, K. Recyclable Fluorine-Free Water-Borne Binders for High-Energy Lithium-Ion Battery Cathodes. *Advanced Energy Materials* **2024**, *14* (27), 2401074. https://doi.org/10.1002/aenm.202401074.

(17) Dong, T.; Mu, P.; Zhang, S.; Zhang, H.; Liu, W.; Cui, G. How Do Polymer Binders Assist Transition Metal Oxide Cathodes to Address the Challenge of High-Voltage Lithium Battery Applications? *Electrochem. Energ. Rev.* **2021**, *4* (3), 545–565. https://doi.org/10.1007/s41918-021-00102-w.

(18) Bresser, D.; Buchholz, D.; Moretti, A.; Varzi, A.; Passerini, S. Alternative Binders for Sustainable Electrochemical Energy Storage – the Transition to Aqueous Electrode Processing and Bio-Derived Polymers. *Energy Environ. Sci.* **2018**, *11* (11), 3096–3127. https://doi.org/10.1039/C8EE00640G.

(19) Kuo, J.-H.; Li, C.-C. Water-Based Process to the Preparation of Nickel-Rich Li(Ni $_{0.8}$ Co $_{0.1}$ Mn $_{0.1}$)O $_{2}$ Cathode. *J. Electrochem. Soc.* **2020**, *167* (10), 100504. https://doi.org/10.1149/1945-7111/ab95c5.

(20) Pedaballi, S.; Li, C.-C. Effects of Surface Modification and Organic Binder Type on Cell Performance of Water-Processed Ni-Rich Li(Ni0.8Co0.1Mn0.1)O2 Cathodes. *Journal of Power Sources* **2020**, *472*, 228552. https://doi.org/10.1016/j.jpowsour.2020.228552.

(21) Radloff, S.; Scurtu, R.-G.; Hölzle, M.; Wohlfahrt-Mehrens, M. Applying Established Water-Based Binders to Aqueous Processing of LiNi $_{0.83}$ Co $_{0.12}$ Mn $_{0.05}$ O $_{2}$ Positive Electrodes. *J. Electrochem. Soc.* **2021**, *168* (10), 100506. https://doi.org/10.1149/1945-7111/ac2861.

(22) Bauer, W.; Çetinel, F. A.; Müller, M.; Kaufmann, U. Effects of pH Control by Acid Addition at the Aqueous Processing of Cathodes for Lithium Ion Batteries. *Electrochimica Acta* **2019**, *317*, 112–119. https://doi.org/10.1016/j.electacta.2019.05.141.

(23) Demiryürek, R.; Gürbüz, N.; Hatipoglu, G.; Er, M.; Malkoc, H.; Guleryuz, O.; Uyar, G.; Uzun, D.; Ateş, M. N. Roll-to-roll Manufacturing Method of Aqueous-processed Thick LiNi $_{0.5}$ Mn $_{0.3}$ Co $_{0.2}$ O $_{2}$ Electrodes for Lithium-ion Batteries. *Intl J of Energy Research* **2021**, *45* (15), 21182–21194. https://doi.org/10.1002/er.7171.

(24) Boz, B.; Vuksanovic, M.; Neidhart, L.; Höchtl, M.; Fröhlich, K.; Jahn, M. Aqueous Manufacturing of Ni-Rich Cathodes Using Polyacrylic Acid As Binder for Lithium-Ion Batteries. *Meet. Abstr.* **2022**, *MA2022-02* (7), 2542–2542. https://doi.org/10.1149/MA2022-0272542mtgabs.

(25) Park, Y.-S.; Oh, E.-S.; Lee, S.-M. Effect of Polymeric Binder Type on the Thermal Stability and Tolerance to Roll-Pressing of Spherical Natural Graphite Anodes for Li-Ion

Batteries. *Journal of Power Sources* **2014**, *248*, 1191–1196. https://doi.org/10.1016/j.jpowsour.2013.10.076.

(26) Parikh, P.; Sina, M.; Banerjee, A.; Wang, X.; D'Souza, M. S.; Doux, J.-M.; Wu, E. A.; Trieu, O. Y.; Gong, Y.; Zhou, Q.; Snyder, K.; Meng, Y. S. Role of Polyacrylic Acid (PAA) Binder on the Solid Electrolyte Interphase in Silicon Anodes. *Chem. Mater.* **2019**, *31* (7), 2535–2544. https://doi.org/10.1021/acs.chemmater.8b05020.

(27) Nguyen, C. C.; Yoon, T.; Seo, D. M.; Guduru, P.; Lucht, B. L. Systematic Investigation of Binders for Silicon Anodes: Interactions of Binder with Silicon Particles and Electrolytes and Effects of Binders on Solid Electrolyte Interphase Formation. *ACS Appl. Mater. Interfaces* **2016**, *8* (19), 12211–12220. https://doi.org/10.1021/acsami.6b03357.

(28) Isozumi, H.; Kubota, K.; Tatara, R.; Horiba, T.; Hida, K.; Matsuyama, T.; Yasuno, S.; Komaba, S. Impact of Newly Developed Styrene–Butadiene–Rubber Binder on the Electrode Performance of High-Voltage $LiNi_{0.5}Mn_{1.5}O_4$ Electrode. *ACS Appl. Energy Mater.* **2020**, *3* (8), 7978–7987. https://doi.org/10.1021/acsaem.0c01334.

(29) Rolandi, A. C.; Barquero, A.; Pozo-Gonzalo, C.; De Meatza, I.; Casado, N.; Forsyth, M.; Leiza, J. R.; Mecerreyes, D. Biobased Acrylic Latexes/Sodium Carboxymethyl Cellulose Aqueous Binders for Lithium-Ion NMC 811 Cathodes. *ACS Appl. Polym. Mater.* **2024**, *6* (2), 1236–1244. https://doi.org/10.1021/acsapm.3c02167.

(30) Chen, X.; Zhang, Q. Atomic Insights into the Fundamental Interactions in Lithium Battery Electrolytes. *Acc. Chem. Res.* **2020**, *53* (9), 1992–2002. https://doi.org/10.1021/acs.accounts.0c00412.

(31) Hernández, G.; Mogensen, R.; Younesi, R.; Mindemark, J. Fluorine-Free Electrolytes for Lithium and Sodium Batteries. *Batteries & Supercaps* **2022**, *5* (6), e202100373. https://doi.org/10.1002/batt.202100373.

(32) Borodin, O. Challenges with Prediction of Battery Electrolyte Electrochemical Stability Window and Guiding the Electrode – Electrolyte Stabilization. *Current Opinion in Electrochemistry* **2019**, *13*, 86–93. https://doi.org/10.1016/j.coelec.2018.10.015.

(33) Guerrero-García, G. I. Size and/or Charge Asymmetry Effects in Coulombic Fluids in the Presence of External Fields: From Simple Electrolytes to Molten Salts. *Biophysical Chemistry* **2022**, *282*, 106747. https://doi.org/10.1016/j.bpc.2021.106747.

(34) Song, W.; Harlow, J.; Logan, E.; Hebecker, H.; Coon, M.; Molino, L.; Johnson, M.; Dahn, J.; Metzger, M. A Systematic Study of Electrolyte Additives in Single Crystal and Bimodal $LiNi_{0.8}Mn_{0.1}Co_{0.1}O_2$ /Graphite Pouch Cells. *J. Electrochem. Soc.* **2021**, *168* (9), 090503. https://doi.org/10.1149/1945-7111/ac1e55.

(35) Xu, K.; Zhang, S.; Lee, U.; Allen, J.; Joww, R. LiBOB: Is It an Alternative Salt for Lithium Ion Chemistry? *J. Power Sources* **2005**, *146* (1–2), 79–85. https://doi.org/10.1016/j.jpowsour.2005.03.153.

(36) Lestariningsih, T.; Sabrina, Q.; Nuroniah, I.; Prihandoko, B.; Marti Wigayati, E.; Rina Ratri, C. Study the Synthesis of LiBOB Compounds Using Lithium Sources from Sea Water. *J. Phys.: Conf. Ser.* **2019**, *1282* (1), 012044. https://doi.org/10.1088/1742-6596/1282/1/012044.

(37) Xu, K. Tailoring Electrolyte Composition for LiBOB. *J. Electrochem. Soc.* **2008**, *155* (10), A733. https://doi.org/10.1149/1.2961055.

(38) Xu, K.; Lee, U.; Zhang, S.; Wood, M.; Jow, T. R. Chemical Analysis of Graphite/Electrolyte Interface Formed in LiBOB-Based Electrolytes. *Electrochem. Solid-State Lett.* **2003**, *6* (7), A144. https://doi.org/10.1149/1.1576049.

(39) Dong, Y.; Young, B. T.; Zhang, Y.; Yoon, T.; Heskett, D. R.; Hu, Y.; Lucht, B. L. Effect of Lithium Borate Additives on Cathode Film Formation in $LiNi_{0.5}Mn_{1.5}O_4$ /Li Cells. *ACS Appl. Mater. Interfaces* **2017**, *9* (24), 20467–20475. https://doi.org/10.1021/acsami.7b01481.

(40) Xu, K.; Zhang, S.; Jow, T. R.; Xu, W.; Angell, C. A. LiBOB as Salt for Lithium-Ion Batteries:A Possible Solution for High Temperature Operation. *Electrochem. Solid-State Lett.* **2002**, *5* (1), A26. https://doi.org/10.1149/1.1426042.

(41) Harlow, J. E.; Ma, X.; Li, J.; Logan, E.; Liu, Y.; Zhang, N.; Ma, L.; Glazier, S. L.; Cormier, M. M. E.; Genovese, M.; Buteau, S.; Cameron, A.; Stark, J. E.; Dahn, J. R. A Wide Range of Testing Results on an Excellent Lithium-Ion Cell Chemistry to Be Used

as Benchmarks for New Battery Technologies. *J. Electrochem. Soc.* **2019**, *166* (13), A3031–A3044. https://doi.org/10.1149/2.0981913jes.

(42) Li, J.; Li, H.; Stone, W.; Glazier, S.; Dahn, J. R. Development of Electrolytes for Single Crystal NMC532/Artificial Graphite Cells with Long Lifetime. *J. Electrochem. Soc.* **2018**, *165* (3), A626–A635. https://doi.org/10.1149/2.0971803jes.

(43) Aravindan, V.; Gnanaraj, J.; Madhavi, S.; Liu, H. Lithium-Ion Conducting Electrolyte Salts for Lithium Batteries. *Chemistry A European J* **2011**, *17* (51), 14326–14346. https://doi.org/10.1002/chem.201101486.

(44) Suresh, P.; Shukla, A. K.; Shivashankar, S. A.; Munichandraiah, N. Electrochemical Behaviour of Aluminium in Non-Aqueous Electrolytes over a Wide Potential Range. *Journal of Power Sources* **2002**, *110* (1), 11–18. https://doi.org/10.1016/S0378-7753(02)00166-0.

(45) Zhang, S. S.; Jow, T. R. Aluminum Corrosion in Electrolyte of Li-Ion Battery. *Journal of Power Sources* **2002**, *109* (2), 458–464. https://doi.org/10.1016/S0378-7753(02)00110-6.

(46) Hofmann, A.; Schulz, M.; Winkler, V.; Hanemann, T. Anodic Aluminum Dissolution in Conducting Salt Containing Electrolytes for Lithium-Ion Batteries. *J. Electrochem. Soc.* **2014**, *161* (3), A431–A438. https://doi.org/10.1149/2.094403jes.

(47) Marom, R.; Haik, O.; Aurbach, D.; Halalay, I. C. Revisiting LiClO[Sub 4] as an Electrolyte for Rechargeable Lithium-Ion Batteries. *J. Electrochem. Soc.* **2010**, *157* (8), A972. https://doi.org/10.1149/1.3447750.

(48) Quan, Y.; Cui, X.; Hu, L.; Kong, Y.; Zhang, X.; Liang, H.; Zhu, Y.; Wang, C.; Zhang, N.; Li, S. Enhancing Li^+ Transportation at Graphite-Low Concentration Electrolyte Interface Via Interphase Modulation of $LiNO_3$ and Vinylene Carbonate. *Carbon Neutralization* **2025**, *4* (1), e184. https://doi.org/10.1002/cnl2.184.

(49) Chen, H.; Chen, K.; Luo, L.; Liu, X.; Wang, Z.; Zhao, A.; Li, H.; Ai, X.; Fang, Y.; Cao, Y. $LiNO_3$ -Based Electrolytes via Electron-Donation Modulation for Sustainable Nonaqueous Lithium Rechargeable Batteries. *Angew Chem Int Ed* **2024**, *63* (10), e202316966. https://doi.org/10.1002/anie.202316966.

(50) Yuan, S.; Cao, S.; Chen, X.; Wei, J.; Lv, Z.; Xia, H.; Chen, L.; Ng, R. B. F.; Tan, F. L.; Li, H.; Loh, X. J.; Li, S.; Feng, X.; Chen, X. Anion-Modulated Solvation Sheath and Electric Double Layer Enabling Lithium-Ion Storage From −60 to 80 °C. *J. Am. Chem. Soc.* **2025**, *147* (5), 4089–4099. https://doi.org/10.1021/jacs.4c13011.

(51) Xu, S.; Xu, S.; Guo, X.; Xiong, J.; Wei, Z.; Zhu, S.; Xu, J.; Gong, S.; Shi, P.; Guo, S.; Min, Y. Construction of a Fluoride-Free and High-Voltage Lithium Metal Battery with a Li_3N/Li_2O Heterostructure Solid Electrolyte Interface. *Adv Funct Materials* **2025**, 2500335. https://doi.org/10.1002/adfm.202500335.

(52) Yang, H.; Shi, X.; Chu, S.; Shao, Z.; Wang, Y. Design of Block-Copolymer Nanoporous Membranes for Robust and Safer Lithium-Ion Battery Separators. *Advanced Science* **2021**, *8* (7), 2003096. https://doi.org/10.1002/advs.202003096.

(53) Fu, X.; Deng, X.; Deng, Y.; Xiong, X.; Zheng, Y.; Zhang, Z.; Dang, D.; Wang, G. Lithium Perchlorate Additive for Dendritic-Free and Long-Life Li Metal Batteries. *Energy Fuels* **2022**, *36* (18), 11219–11226. https://doi.org/10.1021/acs.energyfuels.2c02242.

(54) Meister, P.; Jia, H.; Li, J.; Kloepsch, R.; Winter, M.; Placke, T. Best Practice: Performance and Cost Evaluation of Lithium Ion Battery Active Materials with Special Emphasis on Energy Efficiency. *Chem. Mater.* **2016**, *28* (20), 7203–7217. https://doi.org/10.1021/acs.chemmater.6b02895.

(55) Atebamba, J.-M.; Moskon, J.; Pejovnik, S.; Gaberscek, M. On the Interpretation of Measured Impedance Spectra of Insertion Cathodes for Lithium-Ion Batteries. *J. Electrochem. Soc.* **2010**, *157* (11), A1218. https://doi.org/10.1149/1.3489353.

(56) Xiao, H.; Tao, Z.; Bai, H.; Wang, H.; Fu, Y.; Si, N.; Bai, H. State of Charge Effects on the Parameters of Electrochemical Impedance Spectroscopy Equivalent Circuit Model for Lithium Ion Batteries. *IOP Conf. Ser.: Earth Environ. Sci.* **2020**, *474* (5), 052038. https://doi.org/10.1088/1755-1315/474/5/052038.

(57) Justin Gorham. NIST X-Ray Photoelectron Spectroscopy Database - SRD 20, 2012. https://doi.org/10.18434/T4T88K.

(58) Liu, Y.; Zhu, Y.; Cui, Y. Challenges and Opportunities towards Fast-Charging Battery Materials. *Nat Energy* **2019**, *4* (7), 540–550. https://doi.org/10.1038/s41560-019-0405-3.

(59) Hernández, G.; Naylor, A. J.; Chien, Y.-C.; Brandell, D.; Mindemark, J.; Edström, K. Elimination of Fluorination: The Influence of Fluorine-Free Electrolytes on the Performance of $LiNi_{1/3}Mn_{1/3}Co_{1/3}O_2$/Silicon–Graphite Li-Ion Battery Cells. *ACS Sustainable Chem. Eng.* **2020**, *8* (27), 10041–10052. https://doi.org/10.1021/acssuschemeng.0c01733.

SUPPORTING INFORMATION

Table S1 A set of promising organic binders reported in literature

Binder	Pro's	Cons	References
Polyacrylic acid (PAA)	Aqueous binder, helps protection from aluminium corrosion, good dispersant and adhesive properties due to hydrogen bonding	Lower adhesion to graphite compared to PVDF, surfaces may need pretreatment to improve adhesion	[1, 2, 3, 4, 5]
Carboxylic methyl cellulose (CMC)	Aqueous binder, good dispersant, good adhesive and mechanical properties, inexpensive	Brittle and stiff	[1, 2, 3, 4, 5, 6]
Styrene butadiene rubber (SBR)	Good mechanical properties	Prone to oxidation at higher voltage, Ratio with CMC important for current collector adhesion, emulsion in water	[1, 3, 5]
Polyethersulfone (PES)	High mechanical strength, good wetting performance	Organic solvent processing	[7]
Alginate-based binder	Aqueous binder, high binding strength, crosslinking properties, good mechanical properties	Varying performance reported	[1, 3, 6]
Guar gum	Ability to promote Li^+ transfer, mechanical tolerance to dramatic volume expansion		[1]
Chitosan	Good adhesion, able to copolymerise	Lower performance for anodes, low amount of research	[1]

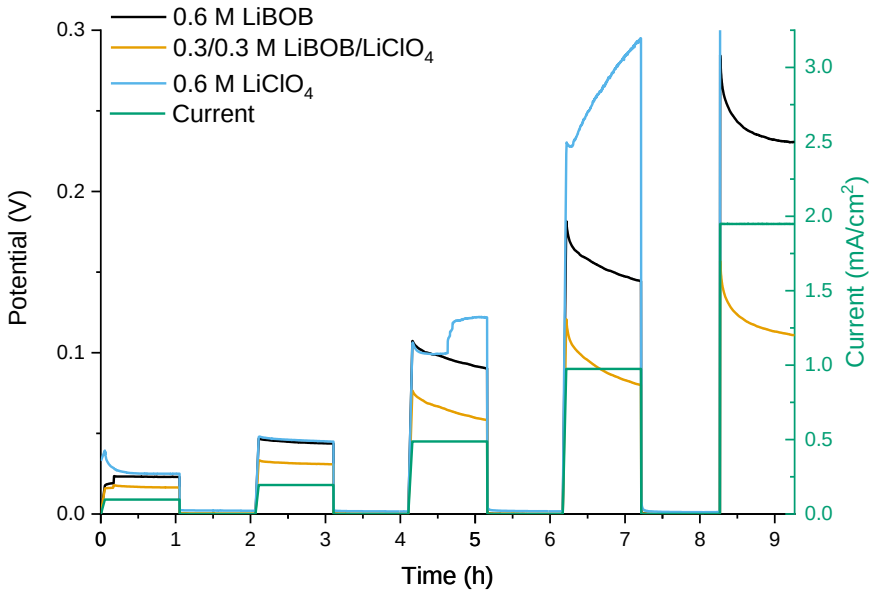

Figure S1 Step amperometry of symmetric lithium metal cell with celgard separator infiltrated with 0.6 M LiBOB in 2/49/49 v/v% VC/EC/DMC or 0.3/0.3 M LiBOB/$LiClO_4$ in 1/2/48.5/48.5 v/v% DTD/VC/EC/DMC electrolyte.

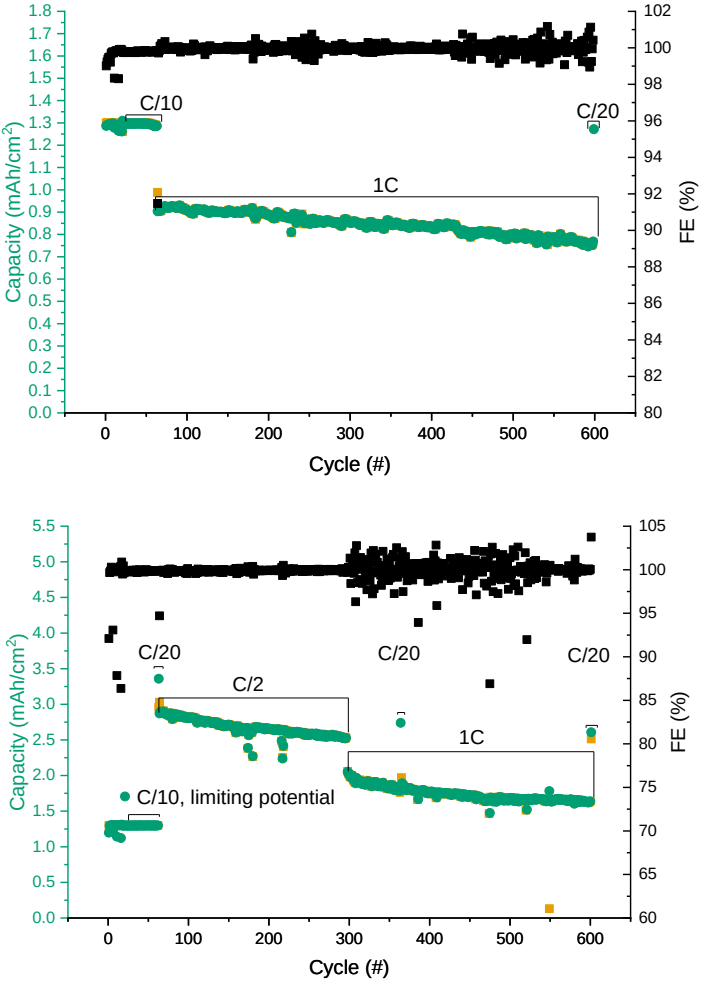

Figure S2 Full cycling history of NMC811/Graphite full cell with 0.6 M LiBOB in 2/49/49 v/v%VC/EC/DMC electrolyte (left) and 0.3/0.3 M LiBOB/LiClO4 in 1/2/48.5/48.5 v/v% DTD/VC/EC/DMC electrolyte (right).

Table S2 Fitted EIS resistance and capacitance of symmetric lithium cells before a 1 hour period of galvanostatic current of 0.1 mA/cm², shown in Figure 1D of the main text.

	R1(+)	R_SEI (+)	R_CT (+)	CPE1_SEI-T(+)	CPE1_SEI-P(+)	CPE_CT-T(+)	CPE_CT-P(+)
0.3 M LiBOB 0.3 M $LiClO_4$ before	5.199	7.306	45.8	0.0302	0.616	2.52E-05	0.849
0.3 M LiBOB 0.3 M $LiClO_4$ after	5.088	6.107	46.08	0.0196	0.841	2.64E-05	0.844
0.6 M $LiClO_4$ before	6.634	87.11	88.96	0.0025	0.667	1.39E-05	0.764
0.6 M $LiClO_4$ after	4.54	34.04	114.1	0.0059	0.696	9.45E-06	0.787
0.6 M LiBOB before	27.51	8.163	65.67	0.0232	0.773	2.18E-05	0.841
0.6 M LiBOB after	23.99	13.76	65.96	0.0139	0.845	2.30E-05	0.834

Table S3 Parameter estimation for constrained circuit model fit of full cell

	LiBOB	LiBOB/$LiClO_4$	Formula
Active material area (cm^2)	2.9 / 3.66 (NMC/graphite)	7.2 / 9.1 (NMC/graphite)	BET (cm^2/g) * Q (mAh) / q_{AM} (mAh/cm^2) * A_{el} (cm^2)
C_{SEI} expected	4.6 e^{-5} F (1 nm SEI)	1.2 e^{-4} F (1 nm SEI)	ε ε_0 (F/m) * A (m^2) / L (m, 1 nm taken) =
C_{DL} expected	6.5 e^{-5}	1.6 e^{-4}	A_{AM} (m^2) * 10^{-5} (F/m^2)
R_{ct} expected	3.9	1.6	R * T / n / F / i_0 (0.001 A/cm^2) / A_{AM}

Figure S4 Circuit model fit of full cells with table of fitting results and circuit model fit of LiBOB after cycling. Circuit elements used are W_{diff}: diffusional migration through porous electrode, R_{ele}: electrolyte resistance, R_{CT}/CPE_{dl}: Charge transfer resistance/ Double layer capacitance at interface, R/CPE_{SEI}: SEI resistance/capacitance.

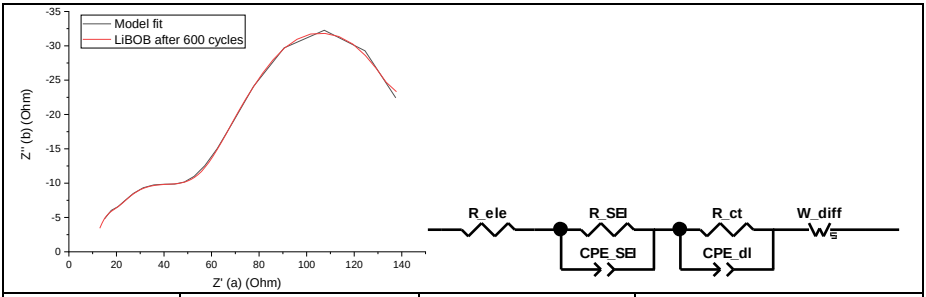

	LiBOB after formation	LiBOB after cycling	LiBOB/$LiClO_4$ after cycling
R1	8.16	10.83	3.937
R_SEI	2.625	30.96	15.33
R_SEI expected	negligible	20 - 200	
C_SEI	0.000373	0.00019015	0.000239
C_SEI expected	2.9E-05	2.89639E-05	0.000116
SEI_Peak_freq expected		177.4850697	
R_CT	NA	2.648	1.763
R_CT_exp	3.92054	3.920540056	1.568216
C_CT	NA	1.4642E-07	5.09E-07
C_CT_expected	6.55E-05	6.54552E-05	0.000164
R_diff	79.55	110.2	49.41
C_diff	0.65588	0.55119	1.777

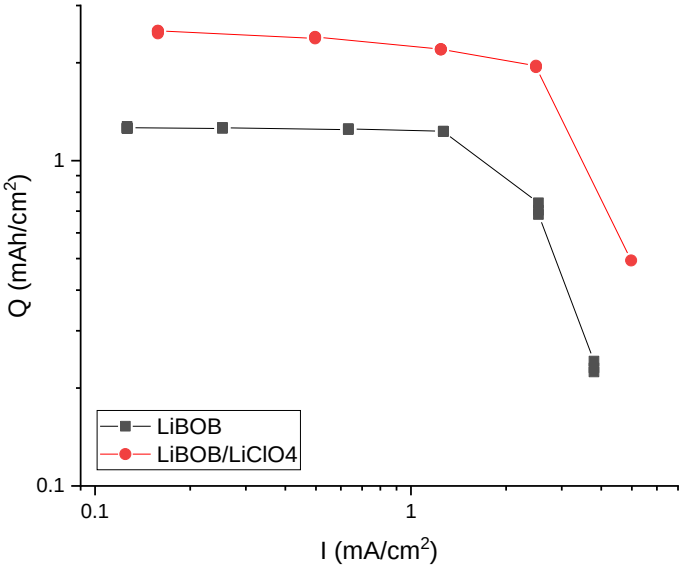

Figure S4 Rate capability of NMC811/Graphite full cells with LiBOB: 1.3 mAh/cm² with 0.6 M LiBOB in 2/49/49 v/v% EC/DMC, LiBOB/$LiClO_4$: 2.46 mAh/cm² with 0.3/0.3 M LiBOB/LiClO4 in 1/2/48.5/48.5 v/v% DTD/VC/EC/DMC.

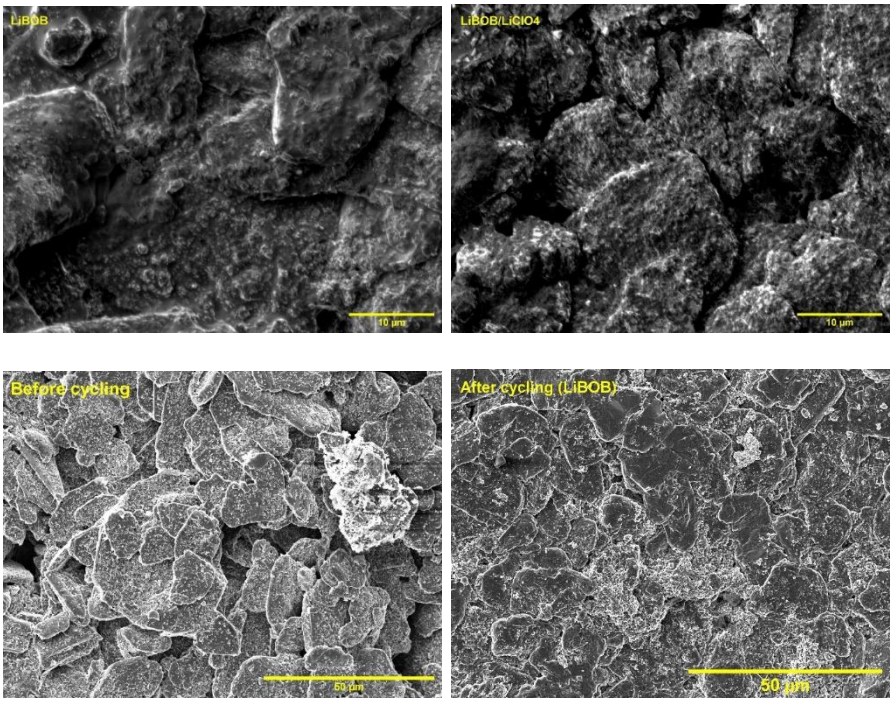

Figure S5. SEM image of graphite electrode. Top Left: after cycling, from LiBOB cell (1 kEv). Top Right: after cycling, from LiBOB/$LiClO_4$ (1 kEv). Bottom Left: pristine electrode (5 kEv). Bottom right: cycled LiBOB (5 kEv). Low accelaration voltages (1 kEv) show surface coverage of SEI and binder (top). Higher accelaration voltages show particle morphology and an overview of electrode structure before and after cycling (bottom left and right respectively).

Table S5 Composition of graphite surface (XPS, few nanometers) and subsurface (EDS, few micrometers) after cycling of LiBOB and LiBOB/$LiClO_4$ cells. Compositional survey is average of two spots.

	LiBOB		LiBOB/$LiClO_4$	
At%	EDS	XPS	EDS	XPS
C	77.2 +/- 2.2	37.8 +/- 1.0	73.9 +/- 0.2	34.1 +/- 1.9
O	17.6 +/- 2.3	36.6 +/- 0.1	20.8 +/- 0.1	31.9 +/- 0.4
B	5.0 +/- 0.2	5.1 +/- 0.5	5.1 +/- 0.1	3.4 +/- 0.3
Li	NA	20.5 +/- 1.4	NA	29.1 +/- 1.7
Cl	0.0 +/- 0.0	0.0 +/- 0.0	0.0 +/- 0.0	0.3 +/- 0.1
S	0.0 +/- 0.0	0.0 +/- 0.0	0.1 +/- 0.0	1.2 +/- 0.2

SI REFERENCES

(1) Lingappan, N.; Kong, L.; Pecht, M. The Significance of Aqueous Binders in Lithium-Ion Batteries. *Renewable and Sustainable Energy Reviews* **2021**, *147*, 111227. https://doi.org/10.1016/j.rser.2021.111227.

(2) Li, J.; Fleetwood, J.; Hawley, W. B.; Kays, W. From Materials to Cell: State-of-the-Art and Prospective Technologies for Lithium-Ion Battery Electrode Processing. *Chem. Rev.* **2022**, *122* (1), 903–956. https://doi.org/10.1021/acs.chemrev.1c00565.

(3) Cholewinski, A.; Si, P.; Uceda, M.; Pope, M.; Zhao, B. Polymer Binders: Characterization and Development toward Aqueous Electrode Fabrication for Sustainability. *Polymers* **2021**, *13* (4), 631. https://doi.org/10.3390/polym13040631.

(4) Park, Y.-S.; Oh, E.-S.; Lee, S.-M. Effect of Polymeric Binder Type on the Thermal Stability and Tolerance to Roll-Pressing of Spherical Natural Graphite Anodes for Li-Ion Batteries. *Journal of Power Sources* **2014**, *248*, 1191–1196. https://doi.org/10.1016/j.jpowsour.2013.10.076.

(5) Radloff, S.; Scurtu, R.-G.; Hölzle, M.; Wohlfahrt-Mehrens, M. Applying Established Water-Based Binders to Aqueous Processing of $LiNi_{0.83}Co_{0.12}Mn_{0.05}O_2$ Positive Electrodes. *J. Electrochem. Soc.* **2021**, *168* (10), 100506. https://doi.org/10.1149/1945-7111/ac2861.

(6) Soeda, K.; Yamagata, M.; Ishikawa, M. Alginic Acid as a New Aqueous Slurry-Based Binder for Cathode Materials of LIB. *ECS Trans.* **2015**, *64* (18), 13–22. https://doi.org/10.1149/06418.0013ecst.

(7) Wahyudi, W.; Cao, Z.; Kumar, P.; Li, M.; Wu, Y.; Hedhili, M. N.; Anthopoulos, T. D.; Cavallo, L.; Li, L.; Ming, J. Phase Inversion Strategy to Flexible Freestanding Electrode: Critical Coupling of Binders and Electrolytes for High Performance Li–S Battery. *Adv Funct Materials* **2018**, *28* (34), 1802244. https://doi.org/10.1002/adfm.201802244.

8. ANALYSIS OF GASIFICATION BIOCHAR FROM LIGNOCELLULOSIC WASTE FOR HIGH PERFORMANCE BIOGRAPHITE ANODE

The content of this chapter is in the process of submission to a scientific journal.

Analysis of gasification biochar from lignocellulosic waste for high performance biographite anode

ABSTRACT

Renewable graphite from low-grade waste is an alternative for fossil-derived graphite for anodes in lithium-ion batteries. There are various thermochemical processes available for producing battery grade biographite. The biochar coming from gasifiers is currently considered to have limited usefulness, despite its carbon-rich composition. In this study we focus on the biochar by-product of gasification from a novel 50 kWth Indirectly Heated Bubbling Fluidized Bed Steam Reformer (IHBFBSR) design, which is treated with a graphitization step. The high crystallinity and good initial performance make it a mature candidate for use as raw material in lithium ion batteries. The resulting graphitized biochar (biographite) is characterized by using X-ray crystallography, scanning electron microscopy, X-ray photoelectron spectroscopy and energy dispersive X-ray spectroscopy to assess its crystallinity, morphology, surface composition and subsurface composition respectively. The material is tested in half cell batteries for use in lithium-ion batteries. The graphite has a high crystallinity which is necessary for good lithium diffusivity in the lattice structure. Also 96% of the theoretical graphite capacity in lithium-ion batteries is found. The biographite flakes are however non homogeneous in size. Also in battery half cells the material shows capacity fade linked to exfoliation of the material. The initial coulombic efficiency (ICE) during charging is lower than conventional graphites due to surface reactivity. Size distribution, exfoliation and ICE must therefor be addressed to make the IHBFBSR biographite fit for battery utility.

INTRODUCTION

Nowadays, renewable sourcing of materials is becoming increasingly important in view of concerns regarding the availability and sustainability[1] of conventional resources which are required for large scale electric vehicle (EV) manufacturing. Up to now, conventional resources for lithium battery anode grade graphites include non-renewable mineral graphite and synthetic graphite which are either mined or produced from petroleum coke at extreme temperatures (≅ 3000°C) respectively.[2] Furthermore, the uneven global distribution of graphite means that some countries may face supply chain disruptions, which could impact the manufacturing of EVs that depend on these materials. Therefore graphite is identified as 'strategic material' by the European Commission.[3]

In the battery industry, mineral or synthetic graphite are of high interest as anode active material in lithium ion batteries. These graphites are highly ordered, have moderate gravimetric capacity, long cycle life and a low working potential for lithium intercalation.[4,5] [6,7] Ordered graphite sheets allows a high degree of lithium intercalation with low resistance.[6] For sodium ion batteries often additional processing is needed to expand the sheet distancing to allow pore filling.[8,9] Alternative anode materials in the form of silicon/graphite,[10] silicon[11] and lithium metal[12,13] are currently emerging. These alternative materials face a high standard as the stability of graphite anodes is unprecedented.[14] For applications which need long term stability rather than high volumetric capacity, graphite still remains the first choice. The cost of graphite anodes compared to alternatives stated above are a second incentive to use this anode material. In a typical battery chemistry, 7% of the cost is associated with the raw material.[15] For example, the cost associated with silicon is sixfold compared to graphite (assuming SiO).[16] With the cost competitiveness and performance of graphite in the lithium ion battery field the development of a sustainable alternative, such as using biochar to graphite, remains a good investment in the near future.

Biochar is a product or by-product of thermochemical conversion of biomass by torrefaction, pyrolysis, gasification, hydrothermal carbonization (HTC) and hydrothermal liquefaction (HTL). Biochar produced from biomass resources offers an advantage due to their low embodied carbon and renewable nature which would relief the usage of fossil-based graphite. To ensure good EV battery performance while using biochar as a precursor of anode active material, the biochar must have similar

characteristics as the state-of-the art materials. Key performance indicators of such characteristics are showing negligible coulombic inefficiencies and high capacity retention in lithium batteries[17].

In biomass gasification the majority of attention has been focused on producing and upgrading the syngas from the gasification process. The gasification biochar is still considered a byproduct in this process as it is only a few percent of the carbon balance. Hence biochar valorisation from gasifiers is still limited. Up to now the majority of research has focused on the use of biochar as adsorbent materials and soil amendment.[18,19] Nevertheless, the majority of these solutions are still at lab or prototype scale. This is because the properties of biochar are highly influenced by the type of feedstock, thermochemical technology, reactor type and scale. Meanwhile, the biofuel industry is rapidly expanding. Focusing on the utility of biochar from gasifiers is critical because companies that require large amounts of biochar may face a risk or an opportunity, depending on whether or not they can find a profitable use for this material.

The main challenges regarding the use of biochar as a precursor for anode materials for lithium ion batteries directly are its poor pore features, its surface functionalization and to maintain biomass conversion efficiency of the syngas formation process while not affecting biochar properties. Also impurities present in the biochar will make downstream purification more difficult.[20] Some of these challenges could be solved by combining a thermochemical process followed by a graphitization process to produce an ordered and high-performance graphite for lithium battery anodes. Thus, recent studies evaluate the use of a thermochemical process to create the biochar, which is then graphitized to turn the amorphous carbon structure of biochar into crystalline graphitic carbon, known as biographite.[4,5,21,22] Biographite has gained attention as material for lithium ion batteries due to its low surface area after carbon coating, reduced coulombic losses, and good packing efficiency which increases volumetric and areal capacity when used in lithium ion batteries.[5] Biographite, which is derived typically from slow pyrolysis (400°C - 600°C) has been successfully obtained from a variety of feedstocks (wood flour, corncobs, medium-density fiberboard derived from recycled wood biomass, softwood, among others), providing good performance in terms of reversible capacity (307 mAh/g – 353 mAh/g).[4,5,21]

According to one study[23] gasification, torrefaction, and HTC are rarely chosen since they do not frequently match the definition of biochar as defined in the European Biochar Certificate standards (EBC)[24]. Nonetheless, it is known that biochars coming from gasification are known to have higher stability, high specific surface area (SA), lower content of poly-aromatic hydrocarbons (PAH) and are more porous than alternative technologies such as pyrolysis.[25] This is mainly attributed to the gasification temperature (600°C - 750°C) which is relatively higher than slow pyrolysis (400°C - 600°C).[18,25] Still biochar from gasification has been limited explored for valuable applications like lithium ion battery anodes.[26] Moreover, recent developments in reactor design may change this outlook even more, since a recent study suggests[18] that indirectly heated biomass gasification can produce a carbon-rich biochar (> 92%) with increased porosity (89–198 cm3/g) and high heating value (28–31 MJ/kg a.r.) from a-quality secondary forest wood pellets. This is achieved by converting wood pellets into syngas in a novel Indirectly Heated Bubbling Fluidized Bed Steam Reformer (IHBFBSR) design.[18] The IHBFBSR gasifier has been built and commissioned by the Dutch company Petrogas - Gas Systems in collaboration with the Process & Energy Department of the Delft University of Technology[27]. The reactor is made of 310S (AISI) steel and stands at a height of approximately 3 meters[27].

In this study we report the electrochemical performance of biographite produced from gasification biochar obtained from an atmospheric pressure 50 kWth IHBFBSR located at the Delft University of Technology followed by a graphitization process. The biochar used for this work was produced at 836°C, $\lambda = 0.20$ and SB = 0.80 and has a high carbon content (96 wt%) and low ash content (< 5 wt%) [18] . Therefore, this biochar has the potential to produce high quality biographite, reduce pre-treatment steps (e.g., ash or heavy metal removal) and ease the intensity of the graphitization process. Obtaining such highly graphitic carbon is key for providing adequate renewable alternatives for battery anode active material.

Tests are conducted to evaluate the most important performance characteristics for usage in a lithium ion battery. The performance was assessed using key performance indicators (KPI) such as gravimetric capacity, stability and rate capability using electrochemical techniques. We compare the gravimetric capacity of lithiation combined with XRD to assess accessibility and the crystallinity/intersheet distancing respectively. In addition, galvanostatic intermittent titration technique (GITT)

estimates the effective diffusivity in biographite during lithium intercalation. The feasibility for using this material is shown, combined with characterization experiments which explain the performance. Furthermore, from this data, it is possible to gain information regarding whether the gasification biochar requires post-treatment actions to avoid undesirable characteristics in the biographite. Examples for such post-treatment actions are expanding the graphite sheets enabling higher rates and/or other ions species,[28] applying coatings or surface functionalization to tune the solid electrolyte interface (SEI) formation[29] or perform mechanical treatments like milling or sieving to optimize the particle size and shape.[30]

METHODS

MATERIAL SYNTHESIS AND CHARACTERIZATION

The biochar was obtained from experiments performed at the IHBFBSR unit located at Delft University of Technology (TU Delft). The studied biochar was produced at 836°C, λ = 0.20, SB = 0.80 using corundum as bed material with main diameter 490 µm. Detailed characterization of this type of biochar can be found in ref [[18]] by del Grosso et. Al. The IHBFBSR biochar was mixed with iron nitrate [$Fe(NO_3)_3$] with a weight ratio of pure iron to biochar of 20 wt%. This mixture was graphitized in a horizontal tube furnace with a heating rate of 10°C/min to 1000°C for 3h. After the graphitization process, iron was removed from the biographite by washing with 0.1 M hydrochloric acid (HCl) followed by ethanol in an ultrasonic bath. The gasifier biographite was subsequently filtered and dried at 105°C for 24h. An iron catalyst was chosen as it has been reported an effective catalyst for the graphitization of waste at relatively low temperatures.[1]

XRD measurements of the biographite were performed with a Bruker D8 Advance diffractometer Bragg-Brentano geometry and Lynxeye position sensitive detector with a radiation source of Cu Kα. The divergence slit is V12, the scatter screen height is 5 mm, and the X-ray machine is operated at 45 kV and 40 mA. The Debye–Scherrer equation was used to determine the crystallite size of the biographite. The surface area of the biochar was estimated using N_2 adsorption-desorption isotherms measured at 77 K with an autosorb iQ equipment. The surface area was determined by applying the Brunauer-Emmett-Teller (BET) method. A multi-point BET was carried out. The samples were degassed (N_2; 150°C; 6 h) before proceeding with BET analysis.

ELECTRODE SYNTHESIS AND CHARACTERIZATION

Gasifier biographite powder was vigorously mixed with polyvinylidene fluoride (PVDF) binder (Solef 5130, Solvay), conductive additive (Carbon Super C45, Timcal) in a 90:5:5%m ratio. Solvent N-Methyl-2-pyrrolidone (NMP,anhydrous 99.5%, Sigma Aldrich) was added in 1:20 m/m ratio with PVDF and thoroughly mixed for an hour using a top stirrer at 1 kRPM (IKA). The anode was cast on copper foil using a doctor blade with a 200 µm blading thickness. The electrode sheet is dried at 60^{o}C at < 30 mBarA for at least 24 hours to remove residual solvent.

Surface analysis of the electrode material is carried out using X-ray Photoelectron Spectroscopy (XPS). A K-alpha Thermo Fisher Scientific (USA) spectrometer with a monochromatic Al K-alpha source was used with a spot size of 400 um. Elemental analysis and high energy spectra of Carbon (C 1s) and Oxygen (O 1s) were obtained. Electrode images and Energy dispersive X-ray spectroscopy (EDS) were obtained with Scanning electron microscopy (SEM) using a JEOL JSM-IT700HR FE-SEM setup. EDS using 15 kV acceleration voltage is used to verify the XPS elemental analysis in depth (penetration depth ~micrometer). The elemental composition of biomass, biochar and biographite comprises: major (>1%at.), minor (1–0.1%at.), and trace (<0.1%at.) elements.

ELECTROCHEMICAL CHARACTERIZATION

Half cell (HC) batteries were made versus Lithium and Sodium metal in coin cells and an in-house made 3-point cell (see the SI for the cell design). The electrode was punched using a 12.7 mm diameter coin cell electrode punch. For coin cells, CR2032 coins were assembled with Celgard 2400 separator and 15 mm metal discs as counter electrode. As electrolyte 100 µl 1 M $LiPF_6$ in 3:7 EC:EMC v/v + 2% VC solution was used. For sodium metal HC batteries $LiPF_6$ was exchanged with $NaPF_6$. The 3 point cell was made using a KF40 flange stub fitted with a teflon ring and EPDM gasket, sealed using a polymer chain clamp (**SI Figure 8**). One stub was fitted with a 15 mm diameter copper cylinder and spring containing a 15 mm lithium metal disc. The other stub contained the reference wire feed through, which was insulated by kapton cladding. The reference wire was fixed at the feed through with a ferrule fitting fixing an O-ring from the outside. The working electrode with a 6 mm centre hole was placed on the stub and a flint of lithium metal was placed in the centre of the hole on the reference wire, in plane with the electrode. To ensure the flint of lithium remained in place during

closing, a 6 mm diameter non-conductive padding with wire feedthrough was used. The same electrolyte and celgard separator as the coin cell assembly are used.

Galvanostatic charge/discharge cycling tests were performed between 0 and 1.5 V vs Li/Li^+. The cells were cycled in a MACCOR-4000 multichannel battery cell cycler in a climate controlled room at 18°C. Theoretical gravimetric capacity of graphite is assumed (372 mAh/g, 2.43 mAh/cm^2 , 1C = 372 mA/g).[6] Cells were cycled 16 times at 0.1C to compare with typical graphite intercalation potential curves after which cells were cycled at C/2 in CCCV mode. A slow C/50 cycle was performed to assess the available gravimetric capacity after 168 cycles. The 3 point cell was cycled at C/2 for 100 cycles. Before and after the 100 cycles, two cycles at 0.1C were performed.

Particle diffusivity was probed by combining galvanostatic intermittent titration (GITT) and electrochemical impedance spectroscopy (EIS) during intercalation and deintercalation in a Parstat MC equipped with a PMC200 potentiostat (Ametek). The GITT pulse interval was 30 minutes at 0.1C with open circuit intervals of 5 minutes. EIS is used to assess the internal resistances after extended cycling.

RESULTS

IHBFBSR BIOGRAPHITE STRUCTURE AND COMPOSITION

The conversion of biomass to biographite is followed by measuring the materials crystallinity with XRD. **Figure 1** presents the XRD results obtained for the raw biomass, gasifier biochar and gasifier biographite from the IHBFBSR gasifier. For raw biomass, there are two wide peaks at 2θ = 17° and 23°, which are credited to cellulose and turbostratic crystalline C, respectively.[18] After gasification, the flattening of the biochar peak at 2θ = 17° and 23°, as well as low intensity peak at 2θ = 43.4°, indicates the conversion of amorphous cellulose to biochar with poor crystallinity. Additionally, following graphitization, the biographite shows a high degree of crystallinity with a characteristic peak at 2θ=26.5° and 44.6°. A d-spacing of 3.4 Å and a crystalline size of 34.29 nm was obtained using Bragg and Debye–Scherrer equations respectively. The d-spacing and crystalline size are in line with precarbonized Fe-catalyzed graphitized woody materials.[1]

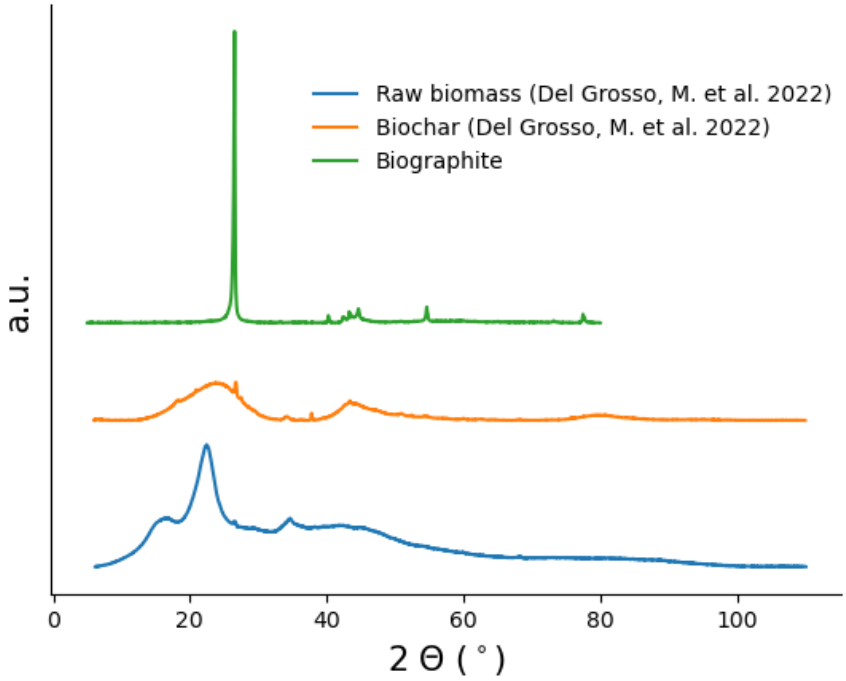

Figure 1 XRD pattern of raw biomass, biochar and biographite respectively. A sharp peak is observed in the biographite spectrum indicating highly crystalline graphite is obtained after graphitization of IHBFBSR gasifier char.

The size of crystallites of the gasifier biographite is comparable with results reported for other graphitic carbons produced from pyrolysis of iron-impregnated cellulose (21-31 nm, produced at 1000, 1400, and 1800°C)[21,31] as well as commercial graphite (47.1 nm).[32] The benefit of the IHBFBSR gasifier biographite compared to slow pyrolysis is that the biographite exhibits larger crystalline size. The material was also manufactured at a lower temperature of 1000 °C. Furthermore, this demonstrates the advantage of employing biochar from gasification as a precursor because high-value syngas is created concurrently, as opposed to using slow pyrolysis just for biographite production. The BET surface area of the biographite is 126.91 m^2/g, 58% lower than the original biochar (300 m^2/g[18]). The results indicate that the graphitization process contributed significantly to the closure of the pores, which is consistent with previous

research[33]. Nonetheless, the measured surface area is significantly higher than that of Shi et al.,[33] (42-93 m^2/g) and commercial graphite (5-20 m^2/g[34]).

The biographite electrodes have 6.52 +/- 0.07 mg/cm^2 active material loading and a thickness of 76 µm. The structure of the biographite electrode is shown in **Figure 2** using SEM. The electrode structure shows a homogeneous distribution of particles between 1 and 20 µm (**Figure 2**A). The larger flakes contain traces of Fe (1.6%m), as indicated from EDS line scan results (SI **Figure 6**). Furthermore, the EDS composition (**Table 1**) indicates minor elements such as Si (0.97%m), Cl (0.56%m), Al (0.15 %m) and Ti (0.12 %m). Furthermore, acid washing was successful in eliminating iron impurities, with a surface concentration of 1.6% (Table 1), which is comparable to other studies that used iron as a catalyst in graphitizing biomass for graphite production[35,36]. Si, Al and Ti were already contained in the biochar as reported by Del Grosso et al.[18] With respect to Cl, this is the result of the acid washing process. There is also a fairly high oxygen amount (6.14%m) with respect to the carbon (82.86%m). Also Cu (4.3%m) is observed, originating from the current collector.

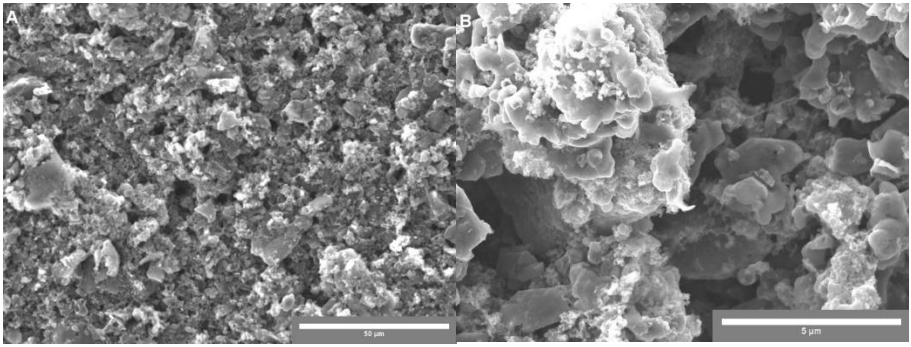

Figure 2 SEM image of Biographite electrode structure. A) A wide particle size distribution on the surface is observed. B) Micrometer sized biographite flakes are covered with (nm sized) carbon black conductive additive particles.

Table 1 Elemental analysis on biographite electrode. EDS is used to obtain elemental composition of micrometer depth. XPS is used to analyze the surface composition.

Element	EDS Mass%	XPS Mass%
C	82.9	77.2
O	6.1	6.6
F	3.3	12.8
Fe	1.6	NA
Cu	4.3	0.1
Si	1.0	1.8
Cl	0.6	NA
Al	0.2	1
Ti	0.1	NA
O/C	7.4	8.5

Results from XPS indicate that the biographite near-surface (nm depth) has high carbon purity level (**Table 1**). Aside from C, O, F and Si no further elements were detected in the XPS survey spectra. The O/C ratio is higher than EDS (micron depth), indicating the oxygenated compounds on the surface of the graphite. Higher magnification SEM image (**Figure 2**B) shows that the IHBFBSR biographite exhibits rounder features, which is consistent with biographites derived from iron-catalysed graphitization of lignocellulosic biomass.[37] Furthermore, the graphite (flakes) and carbon black are well dispersed (**Figure** *2*B).

IHBFBSR BIOGRAPHITE ANODE PERFORMANCE IN LITHIUM BATTERIES

The potential trace of graphite formation versus lithium metal provides valuable information about the presence and extent of side reactivity and/or graphite exfoliation (**Figure 3**B). The potential profile shows an irreversible capacity of 1.67 mAh/cm^2, which is 74% of the reversible capacity during discharge, yielding an initial coulombic efficiency (ICE) of 46% (**Figure 3**B, black). This performance is similar to previous studies for biographites from iron-catalyzed graphitization.[1] The majority of the irreversible capacity can be assigned to an additional voltage plateau above 0.8 V versus Li/Li$^+$. The initial irreversible lithiation at such potential can be attributed to Solid-Electrolyte Interface (SEI) formation by EC decomposition on the graphite active material.[29,38] Compared to typical graphite (76% ICE)[39], the irreversible capacity is high (46% ICE) and may be attributed to the (i) high surface area (126.91 m^2/g) containing

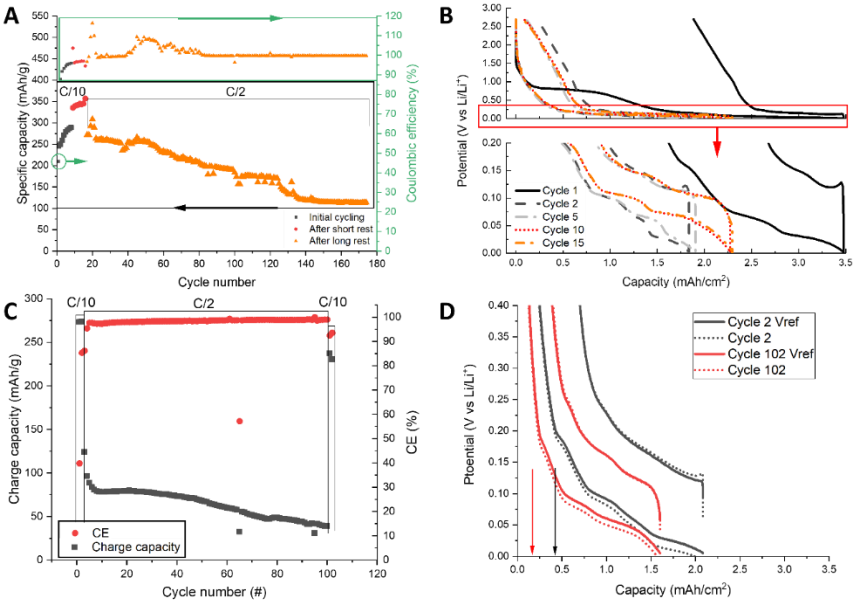

Figure 3 Top: (Dis)charge capacity and coulombic efficiency (A/C) and potential traces (B/D) of biographite:Li HC during long duration cycling (A/B) and in a 3 point electrode cell test (C/D). In the 3 point electrode reference potential Vref shows local potential at the biographite side. Arrows indicate the capacity at which the potential limit was reached during deintercalation.

imperfections/impurities (**Figure 2**)[14] and (ii) presence of high roughness on the surface which can extend the decomposition of EC-like components. Previous studies[33,34,40] have suggested that large surface areas may have a negative impact on graphite's electrochemical performance, as there is an almost linear relationship between irreversible capacity and BET specific surface area.

As can be seen from **Figure 3**A, the biographite improves in terms of gravimetric capacity during the first 16 cycles. The intercalation potential and coulombic efficiency after the first two formation cycles improves gradually indicating small losses due to continued side reactivity. The graphite lithiation plateau at 150 - 100 mV initially shows a steep sloping plateau (**Figure 3**B, black) which extends after cycling to the three characteristic intercalation plateaus which are expected of lithium intercalation in graphite (**Figure 3**B, dark gray and grey). Also the overpotential for intercalation lowers

(**Figure 3**B, cycle 2 dark grey, 1.45 to 1.7 mAh/cm^2 and cycle 5 light grey, 1.44 to 2.25 mAh/cm^2). One potential explanation is that the graphite interlayer distance expands over time during initial cycling creating a higher surface area availability resulting in the extension of the second intercalation plateau (**Figure 3**B, comparison of potential plateau cycle 2 to 5). At the same time, the overpotential during initial intercalation below 0.75 mAh/cm^2 shows negligible change. To determine if the material performance improvement is due to electrochemical activity, a short rest period was introduced in the deintercalated state. After four weeks, the initial gravimetric capacity during cycling was enhanced by 16% (from 289 mAh/g to 335 mAh/g) in cycle 10 (**Figure 3**B red), after which further capacity improvement shows a maximum of 357 mAh/g in cycle 16 (**Figure 3**A). An improved wetting and/or further expansion of the graphite may be causing such improvement during the rest period leading to almost full utilization of the graphitic carbon in the 16th cycle. It is worth noting that following the short rest, the overpotential decreases -it costs less energy to lithiate the graphite- but the third plateaus is barely observable (**Figure 3**B, red compared to grey).

A prolonged rest period lasting 6 months was implemented following cycle 16 to assess electrode stability (**Figure 3**B, orange). After this period, the half cell initially shows a lowered capacity during intercalation at C/10 (293 mAh/g), after which during C/2 cycling hysterisis and a steep drop in gravimetric capacity compared to the cycle before the extended rest starts to occur. The specific capacity of 357 mAh/g could not be recovered after prolonged shelf life. From cycle 16 onward buildup of internal resistances cause a steep potential drop during the CC step and current fade during the CV step. A high overpotential during deintercalation is observed as well (SI **Figure 3**). A gradual capacity fade is measured till 100 mAh/g in the 160th cycle (**Figure 3**A). The half cell testing suffers from continued side reactions at the lithium metal counter electrode side as shown by EIS (SI **Figure 4**). The EIS spectrum demonstrates that the bulk conductivity is decreased, which has a significant impact on rate performance. Thus, an extended intercalation/deintercalation cycle at 0.02C was performed after prolonged cycling to examine the (de)intercalation performance of the biographite itself. The result shows that the biographite still has a capacity of 265 mAh/g after 168 cycles, which is 98% of the capacity during the initial cycle and 73 % of the maximum capacity the graphite anode showed before the long rest period.

In order to exclude the possibility of SEI buildup at the counter electrode to be the cause of capacity fade, a repeated test was conducted using a three-point cell with a

lithium metal reference near the graphite electrode (shown in SI **Figure 8**). The three-point cell was cycled at a (dis)charge rate of 0.5C (**Figure 3**C). Results indicate that during graphite intercalation, the potential difference between the lithium counter electrode and the reference lithium amounts to 11 mV. The formation was halted to observe the OCP after formation period at cutoff potential of 0.6 V. The open cell potential of 1.2 V indicated negligible intercalation (SI **Figure 7**). In SI **Figure 7**, between 0.6 and 0.2 V additional side reactivity can be observed which is linked to exfolation of the graphite.[41] During the second cycle a capacity of 274 mAh/g was found after which immediately C/2 cycling was started. Without the rest period an improvement in gravimetric capacity was not observed. After 100 cycles, the cell shows 237 mAh/g capacity, 87% of the original capacity, which is higher compared to the duration tests but lower compared to commercial analogs (e.g. Yan et al.[42] reporting 98% after 40 cycles with a similar electrolyte and commercial graphite, which would extrapolate to 95% after 100 cycles). The exfoliation of graphite flakes leading to active material contact loss over time may therefore be the dominant capacity fading mechanism during extended cycling.

To facilitate high charge rates, graphite should be highly ordered to allow lithium to diffuse between the sheets. Indeed, GITT measurements (SI **Figure 5**) shows expected diffusion coefficients during deintercalation of the graphite, following the trend in diffusion coefficient progression in commercial graphite materials.[43] The wide particle size distribution becomes apparent during intercalation. Here, a higher apparent diffusion coefficient is observed. Smaller particles with a larger surface-to-molar volume ratio may operate as a capacitor, temporarily holding a higher fraction of lithium and redistributing it during the rest phase of the GITT process. The heterogeneous particle distribution and presence of impurities in the biographite would cause additional wear on smaller particles during fast charging and charging at lower temperatures.[44] As such, particle heterogeneity should be resolved in a subsequent upgrading step.

DISCUSSION AND CONCLUSIONS

The gravimetric capacity of the IHBFBSR biographite found during electrochemical testing support findings from XRD, demonstrating that the majority of the material is highly graphitic yielding a high gravimetric capacity (357 mAh/g, where commercial graphites are nearing 360 mAh/g, e.g. MSE natural graphite). The reversible

gravimetric specific capacity cannot be retained towards the 169th cycle, which shows 265 mAh/g capacity remains available. The highest observed capacity is however near the theoretical capacity of graphite intercalation (372 mAh/g), showing excellent promise of this material. The characteristic voltage plateaus around 150 mV and 100 mV show high ordering of the graphene layers, characteristic of thermally treated carbons.[6]

There are three characteristics of the IHBFBSR biographite which need improvement to meet with the high lithium ion battery anode standard. First, the initial coulombic efficiency is too low to directly use graphitized biochar as anode material. Some initial capacity is typically necessary to form a stable SEI.[45] The low ICE found for biographite would lead to a loss of lithium inventory in full cell batteries, making the total gravimetric battery capacity low. There are several pretreatment steps to mitigate a low ICE caused by the high amount of surface defects. One approach is reduction of the oxygen content and roughness of the pristine material by chemical treatment or coating.[14,46,47] In order to stabilize the CE during subsequent cycles the use of electrolyte additives to form a completely stable SEI layer is already well known in literature.[17] A second concern is excessive wear on a fraction of graphite as shown in GITT. Such wear is originating from the particle heterogeneity causing uneven intercalation rates. Here a sieving and milling approach would offer a viable solution. A final concern is the capacity gain and subsequent fade observed after prolonged cycling, which may be attributed to expanding and possibly exfoliation of the graphite. Here formation of a strong surface layer using electrolyte additives and/or usage of a protective coating may lead to increased performances, as observed with pyrolysis derived biographites.

To make an estimate of the potential use of graphites during future studies, the experiments can be shortened to obtain the key performance parameters using only ICE (SEI formation, potential lithium inventory loss), GITT (particle heterogeneity and rate performance) and a < 20 day cycling test at C/2 combined with a 'formation – rest – cycle method' to assess wear, capacity fade mechanisms like contact loss, wetting and/or exfoliation. Shortening such initial study is necessary as there is a wide variety of possible substrates and processing parameters possible. With this testing approach it takes less time to investigate the feasibility of using the graphite and the result of subsequent processing strategies for valorization.

REFERENCES

(1) Vook, T.; Dey, S. C.; Yang, J.; Nimlos, M.; Park, S.; Han, S.-D.; Sagues, W. J. Sustainable Li-Ion Anode Material from Fe-Catalyzed Graphitization of Paper Waste. *Journal of Energy Storage* **2023**, *73*, 109242. https://doi.org/10.1016/j.est.2023.109242.

(2) Ragan, S.; Marsh, H. Science and Technology of Graphite Manufacture. *J Mater Sci* **1983**, *18* (11), 3161–3176. https://doi.org/10.1007/BF00544139.

(3) European Commission. Directorate General for Internal Market, Industry, Entrepreneurship and SMEs. *Study on the Critical Raw Materials for the EU 2023: Final Report.*; Publications Office: LU, 2023.

(4) Gomez-Martin, A.; Martinez-Fernandez, J.; Ruttert, M.; Heckmann, A.; Winter, M.; Placke, T.; Ramirez-Rico, J. Iron-Catalyzed Graphitic Carbon Materials from Biomass Resources as Anodes for Lithium-Ion Batteries. *ChemSusChem* **2018**, *11* (16), 2776–2787. https://doi.org/10.1002/cssc.201800831.

(5) Banek, N. A.; Abele, D. T.; McKenzie, K. R. Jr.; Wagner, M. J. Sustainable Conversion of Lignocellulose to High-Purity, Highly Crystalline Flake Potato Graphite. *ACS Sustainable Chem. Eng.* **2018**, *6* (10), 13199–13207. https://doi.org/10.1021/acssuschemeng.8b02799.

(6) *Advanced Batteries*; Springer US: Boston, MA, 2009. https://doi.org/10.1007/978-0-387-76424-5.

(7) Shi, Z.; Wang, S.; Jin, Y.; Zhao, L.; Chen, S.; Yang, H.; Cui, Y.; Svanberg, R.; Tang, C.; Jiang, J.; Yang, W.; Jönsson, P. G.; Han, T. Establishment of Green Graphite Industry: Graphite from Biomass and Its Various Applications. *SusMat* **2023**, *3* (3), 402–415. https://doi.org/10.1002/sus2.139.

(8) Yu, P.; Tang, W.; Wu, F.-F.; Zhang, C.; Luo, H.-Y.; Liu, H.; Wang, Z.-G. Recent Progress in Plant-Derived Hard Carbon Anode Materials for Sodium-Ion Batteries: A Review. *Rare Met.* **2020**, *39* (9), 1019–1033. https://doi.org/10.1007/s12598-020-01443-z.

(9) Li, Y.; Vasileiadis, A.; Zhou, Q.; Lu, Y.; Meng, Q.; Li, Y.; Ombrini, P.; Zhao, J.; Chen, Z.; Niu, Y.; Qi, X.; Xie, F.; van der Jagt, R.; Ganapathy, S.; Titirici, M.-M.; Li, H.; Chen, L.; Wagemaker, M.; Hu, Y.-S. Origin of Fast Charging in Hard Carbon Anodes. *Nat Energy* **2024**. https://doi.org/10.1038/s41560-023-01414-5.

(10) Li, P.; Kim, H.; Myung, S.-T.; Sun, Y.-K. Diverting Exploration of Silicon Anode into Practical Way: A Review Focused on Silicon-Graphite Composite for Lithium Ion Batteries. *Energy Storage Materials* **2021**, *35*, 550–576. https://doi.org/10.1016/j.ensm.2020.11.028.

(11) Tan, D. H. S.; Chen, Y.-T.; Yang, H.; Bao, W.; Sreenarayanan, B.; Doux, J.-M.; Li, W.; Lu, B.; Ham, S.-Y.; Sayahpour, B.; Scharf, J.; Wu, E. A.; Deysher, G.; Han, H. E.; Hah, H. J.; Jeong, H.; Lee, J. B.; Chen, Z.; Meng, Y. S. Carbon-Free High-

Loading Silicon Anodes Enabled by Sulfide Solid Electrolytes. *Science* **2021**, *373* (6562), 1494–1499. https://doi.org/10.1126/science.abg7217.

(12) Fang, C.; Wang, X.; Meng, Y. S. Key Issues Hindering a Practical Lithium-Metal Anode. *Trends in Chemistry* **2019**, *1* (2), 152–158. https://doi.org/10.1016/j.trechm.2019.02.015.

(13) Hobold, G. M.; Lopez, J.; Guo, R.; Minafra, N.; Banerjee, A.; Shirley Meng, Y.; Shao-Horn, Y.; Gallant, B. M. Moving beyond 99.9% Coulombic Efficiency for Lithium Anodes in Liquid Electrolytes. *Nat Energy* **2021**, *6* (10), 951–960. https://doi.org/10.1038/s41560-021-00910-w.

(14) Wu, Y. P.; Jiang, C.; Wan, C.; Holze, R. Effects of Pretreatment of Natural Graphite by Oxidative Solutions on Its Electrochemical Performance as Anode Material. *Electrochimica Acta* **2003**, *48* (7), 867–874. https://doi.org/10.1016/S0013-4686(02)00780-6.

(15) Wood, D. L.; Li, J.; Daniel, C. Prospects for Reducing the Processing Cost of Lithium Ion Batteries. *Journal of Power Sources* **2015**, *275*, 234–242. https://doi.org/10.1016/j.jpowsour.2014.11.019.

(16) Greenwood, M.; Wentker, M.; Leker, J. A Bottom-up Performance and Cost Assessment of Lithium-Ion Battery Pouch Cells Utilizing Nickel-Rich Cathode Active Materials and Silicon-Graphite Composite Anodes. *Journal of Power Sources Advances* **2021**, *9*, 100055. https://doi.org/10.1016/j.powera.2021.100055.

(17) Eldesoky, A.; Logan, E. R.; Louli, A. J.; Song, W.; Weber, R.; Hy, S.; Petibon, R.; Harlow, J. E.; Azam, S.; Zsoldos, E.; Dahn, J. R. Impact of Graphite Materials on the Lifetime of NMC811/Graphite Pouch Cells: Part II. Long-Term Cycling, Stack Pressure Growth, Isothermal Microcalorimetry, and Lifetime Projection. *J. Electrochem. Soc.* **2022**, *169* (1), 010501. https://doi.org/10.1149/1945-7111/ac42f1.

(18) Del Grosso, M.; Cutz, L.; Tiringer, U.; Tsekos, C.; Taheri, P.; de Jong, W. Influence of Indirectly Heated Steam-Blown Gasification Process Conditions on Biochar Physico-Chemical Properties. *Fuel Processing Technology* **2022**, *235*, 107347. https://doi.org/10.1016/j.fuproc.2022.107347.

(19) Yi, S. C.; Heijbroek, A.; Cutz, L.; Pillay, S.; de Jong, W.; Abeel, T.; Gebert, J. Effects of Fir-Wood Biochar on CH4 Oxidation Rates and Methanotrophs in Landfill Cover Soils Packed at Three Different Proctor Compaction Levels. *Science of The Total Environment* **2024**, *907*, 167951. https://doi.org/10.1016/j.scitotenv.2023.167951.

(20) Liu, W.-J.; Jiang, H.; Yu, H.-Q. Emerging Applications of Biochar-Based Materials for Energy Storage and Conversion. *Energy Environ. Sci.* **2019**, *12* (6), 1751–1779. https://doi.org/10.1039/C9EE00206E.

(21) Sagues, W. J.; Yang, J.; Monroe, N.; Han, S.-D.; Vinzant, T.; Yung, M.; Jameel, H.; Nimlos, M.; Park, S. A Simple Method for Producing Bio-Based Anode Materials for Lithium-Ion Batteries. *Green Chem.* **2020**, *22* (20), 7093–7108. https://doi.org/10.1039/D0GC02286A.

(22) Yap, Y. W.; Mahmed, N.; Norizan, M. N.; Abd Rahim, S. Z.; Ahmad Salimi, M. N.; Abdul Razak, K.; Mohamad, I. S.; Abdullah, M. M. A.-B.; Mohamad Yunus, M. Y. Recent Advances in Synthesis of Graphite from Agricultural Bio-Waste Material: A Review. *Materials* **2023**, *16* (9), 3601. https://doi.org/10.3390/ma16093601.

(23) Enaime, G.; Baçaoui, A.; Yaacoubi, A.; Lübken, M. Biochar for Wastewater Treatment—Conversion Technologies and Applications. *Applied Sciences* **2020**, *10* (10), 3492. https://doi.org/10.3390/app10103492.

(24) EBC. European Biochar Certificate - Guidelines for a Sustainable Production of Biochar., 2022.

(25) Fryda, L.; Visser, R. Biochar for Soil Improvement: Evaluation of Biochar from Gasification and Slow Pyrolysis. *Agriculture* **2015**, *5* (4), 1076–1115. https://doi.org/10.3390/agriculture5041076.

(26) Lower, L.; Dey, S. C.; Vook, T.; Nimlos, M.; Park, S.; Sagues, W. J. Catalytic Graphitization of Biocarbon for Lithium-Ion Anodes: A Minireview. *ChemSusChem* **2023**, *16* (24), e202300729. https://doi.org/10.1002/cssc.202300729.

(27) Tsekos, C.; del Grosso, M.; de Jong, W. Gasification of Woody Biomass in a Novel Indirectly Heated Bubbling Fluidized Bed Steam Reformer. *Fuel Processing Technology* **2021**, *224*, 107003. https://doi.org/10.1016/j.fuproc.2021.107003.

(28) Buqa, H.; Goers, D.; Holzapfel, M.; Spahr, M. E.; Novák, P. High Rate Capability of Graphite Negative Electrodes for Lithium-Ion Batteries. *J. Electrochem. Soc.* **2005**, *152* (2), A474. https://doi.org/10.1149/1.1851055.

(29) Bernardo, Ph.; Dentzer, J.; Gadiou, R.; Märkle, W.; Goers, D.; Novák, P.; Spahr, M. E.; Vix-Guterl, C. Influence of Graphite Surface Properties on the First Electrochemical Lithium Intercalation. *Carbon* **2011**, *49* (14), 4867–4876. https://doi.org/10.1016/j.carbon.2011.07.007.

(30) Röder, F.; Sonntag, S.; Schröder, D.; Krewer, U. Simulating the Impact of Particle Size Distribution on the Performance of Graphite Electrodes in Lithium-Ion Batteries. *Energy Tech* **2016**, *4* (12), 1588–1597. https://doi.org/10.1002/ente.201600232.

(31) Ghogia, A. C.; Romero Millán, L. M.; White, C. E.; Nzihou, A. Synthesis and Growth of Green Graphene from Biochar Revealed by Magnetic Properties of Iron Catalyst. *ChemSusChem* **2023**, *16* (3), e202201864. https://doi.org/10.1002/cssc.202201864.

(32) Lopez quintela, M. A. Method for obtaining graphene sheets, 2014.

(33) Shi, Z.; Jin, Y.; Han, T.; Yang, H.; Gond, R.; Subasi, Y.; Asfaw, H. D.; Younesi, R.; Jönsson, P. G.; Yang, W. Bio-Based Anode Material Production for Lithium–Ion Batteries through Catalytic Graphitization of Biochar: The Deployment of Hybrid Catalysts. *Sci Rep* **2024**, *14* (1), 3966. https://doi.org/10.1038/s41598-024-54509-8.

(34) Winter, M.; Novák, P.; Monnier, A. Graphites for Lithium-Ion Cells: The Correlation of the First-Cycle Charge Loss with the Brunauer-Emmett-Teller Surface Area. *J. Electrochem. Soc.* **1998**, *145* (2), 428. https://doi.org/10.1149/1.1838281.

(35) Gai, L.; Li, J.; Wang, Q.; Tian, R.; Li, K. Evolution of Biomass to Porous Graphite Carbon by Catalytic Graphitization. *Journal of Environmental Chemical Engineering* **2021**, *9* (6), 106678. https://doi.org/10.1016/j.jece.2021.106678.

(36) Thompson, E.; E. Danks, A.; Bourgeois, L.; Schnepp, Z. Iron-Catalyzed Graphitization of Biomass. *Green Chemistry* **2015**, *17* (1), 551–556. https://doi.org/10.1039/C4GC01673D.

(37) Hunter, R. D.; Davies, J.; Hérou, S. J. A.; Kulak, A.; Schnepp, Z. Milling as a Route to Porous Graphitic Carbons from Biomass. *Philos Trans A Math Phys Eng Sci* **2021**, *379* (2209), 20200336. https://doi.org/10.1098/rsta.2020.0336.

(38) Novák, P.; Joho, F.; Lanz, M.; Rykart, B.; Panitz, J.-C.; Alliata, D.; Kötz, R.; Haas, O. The Complex Electrochemistry of Graphite Electrodes in Lithium-Ion Batteries. *Journal of Power Sources* **2001**, *97–98*, 39–46. https://doi.org/10.1016/S0378-7753(01)00586-9.

(39) Li, X.; Sun, X.; Hu, X.; Fan, F.; Cai, S.; Zheng, C.; Stucky, G. D. Review on Comprehending and Enhancing the Initial Coulombic Efficiency of Anode Materials in Lithium-Ion/Sodium-Ion Batteries. *Nano Energy* **2020**, *77*, 105143. https://doi.org/10.1016/j.nanoen.2020.105143.

(40) Placke, T.; Siozios, V.; Rothermel, S.; Meister, P.; Colle, C.; Winter, M. Assessment of Surface Heterogeneity: A Route to Correlate and Quantify the 1st Cycle Irreversible Capacity Caused by SEI Formation to the Various Surfaces of Graphite Anodes for Lithium Ion Cells. *Zeitschrift für Physikalische Chemie* **2015**, *229* (9), 1451–1469. https://doi.org/10.1515/zpch-2015-0584.

(41) Goers, D.; Spahr, M. E.; Leone, A.; Märkle, W.; Novák, P. The Influence of the Local Current Density on the Electrochemical Exfoliation of Graphite in Lithium-Ion Battery Negative Electrodes. *Electrochimica Acta* **2011**, *56* (11), 3799–3808. https://doi.org/10.1016/j.electacta.2011.02.046.

(42) Yan, Z.; Obrovac, M. N. Electrolyte Reactivity on Graphite and Copper as Measured in Lithium Double Half Cells. *J. Electrochem. Soc.* **2017**, *164* (13), A2977–A2986. https://doi.org/10.1149/2.0431713jes.

(43) Park, J. H.; Yoon, H.; Cho, Y.; Yoo, C.-Y. Investigation of Lithium Ion Diffusion of Graphite Anode by the Galvanostatic Intermittent Titration Technique. *Materials* **2021**, *14* (16), 4683. https://doi.org/10.3390/ma14164683.

(44) Kim, M.; Kim, I.; Kim, J.; Choi, J. W. Lifetime Prediction of Lithium Ion Batteries by Using the Heterogeneity of Graphite Anodes. *ACS Energy Lett.* **2023**, *8* (7), 2946–2953. https://doi.org/10.1021/acsenergylett.3c00695.

(45) An, S. J.; Li, J.; Daniel, C.; Mohanty, D.; Nagpure, S.; Wood, D. L. The State of Understanding of the Lithium-Ion-Battery Graphite Solid Electrolyte Interphase (SEI) and Its Relationship to Formation Cycling. *Carbon* **2016**, *105*, 52–76. https://doi.org/10.1016/j.carbon.2016.04.008.

(46) Cui, X.; Tang, F.; Li, C.; Zhang, Y.; Wang, P.; Li, S.; Ye, X. Pretreatment of Graphite Anodes with Lithium Sulfate to Improve the Cycle Performance of Lithium-Ion Batteries. *Energy Technol.* **2017**, *5* (4), 549–556. https://doi.org/10.1002/ente.201600360.

(47) Gaberscek, M. Improved Carbon Anode for Lithium Batteries Pretreatment of Carbon Particles in a Polyelectrolyte Solution. *Electrochem. Solid-State Lett.* **1999**, *3* (4), 171. https://doi.org/10.1149/1.1390992.

SUPPORTING INFORMATION

XPS SURVEY OF ELECTRODE

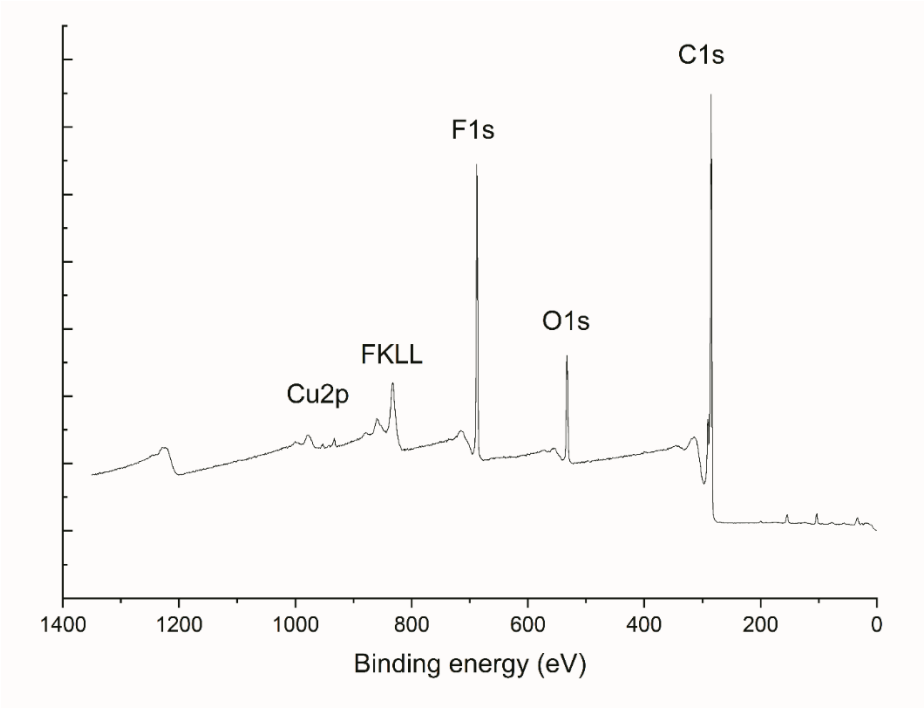

Figure 4 XPS survey of biographite electrode. Carbon, Fluorine and oxygen have significant atomic fractions (table below).

Name	Position (eV)	FWHM	Raw Area	%At Conc
C 1s	285.08	2.65	2294870	77.17
F 1s	688.08	2.65	1332570	12.77
O 1s	533.08	2.8	508554	6.6
Si 2p	103.08	2.73	45825.6	1.77
Al 2p	77.08	5.56	17160.6	1
Ni 2p	860.08	8.55	200335	0.46
N 1s	400.08	2.31	7152.5	0.14
Cu 2p	933.08	3.54	41061	0.09

Electrochemical performance with sodium

Similarly to lithium half cells, the biographite was tested for its performance as a sodium-ion battery anode (SI **Figure 5**). The potential trace during cell formation shows an irreversible sodiation plateau at 0.5 V versus Na/Na^+ with a capacity of 1.28 mAh/cm^2 similar to lithium formation. Both irreversible lithium and sodium processes occur at -2.5 V versus hydrogen evolution reaction, showing a common electrochemical reaction process. These results indicate that the IHBFBSR biographite needs additional treatment to be used in SIB. This is due to compact graphites (3.4 Å) are typically known as poor sodium storage materials.[38] The material surprisingly shows 0.2 mAh/cm^2 reversible capacity which is 21% of theoretical intercalation capacity based on expanded natural graphite (150 mAh/g).[8] The difference between observed and theoretical capacity shows the inaccessibility of intercalation sites in the material. Expansion of the biographite interlayers is therefore necessary to enable sodium intercalation to relevant gravimetric capacities.

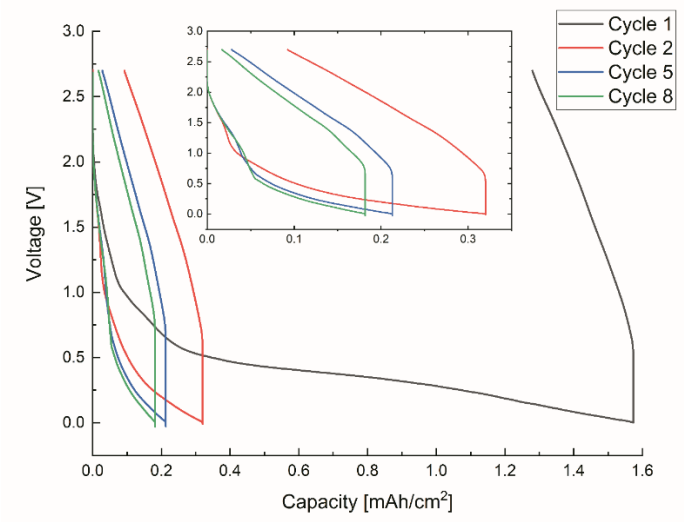

Figure 5 Electrochemical performance of biographite versus sodium metal in a half cell configuration during 0.1C cycling.

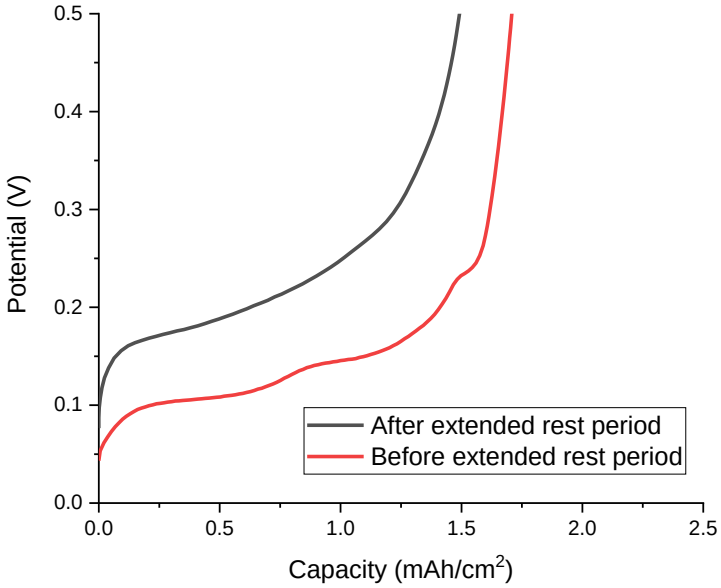

Figure 6 Potential versus specific capacity during deintercalation of biographite in cycle 16 (red) and 17 (black). The increase in potential is caused by internal resistance buildup on the surfaces as observed by EIS (Figure 7).

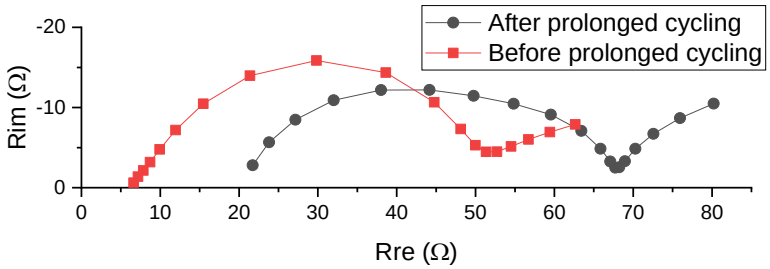

Figure 7 EIS spectrum of Biographite:Li half cells just before cycle 17 and after cycle 160 at 75 mV OCP. Internal resistance buildup shows by increasing high frequency resistance (start semicircle, left) and charge transfer resistances (semicircle).

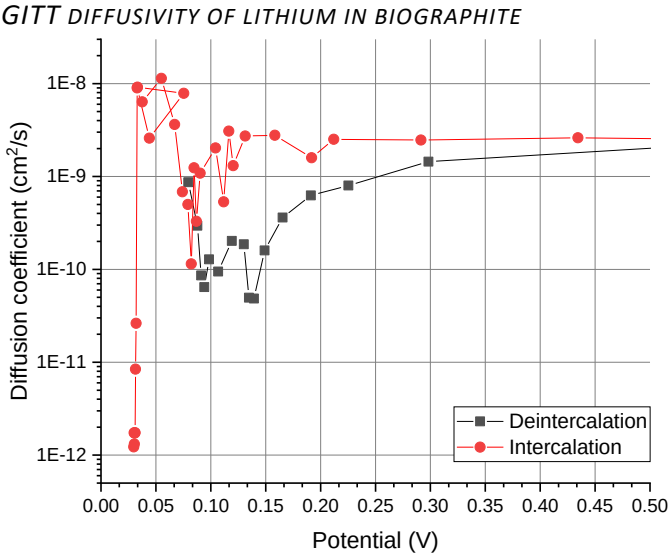

Figure 8 GITT of biographite:lithium half cell after the 16th cycle. Characteristic lower diffusion coefficient between 0.1 and 0.2 V during deintercalation is found.[1] A slightly higher diffusion coefficient is observed around full lithiation before a stagnation of lithiation happens around LiC_6 saturation at 30 mV. The mixed particle size distribution shows a more homogenized (higher) diffusion coefficient during intercalation.

EDS LINE ANALYSIS ON BIOGRAPHITE ELECTRODE

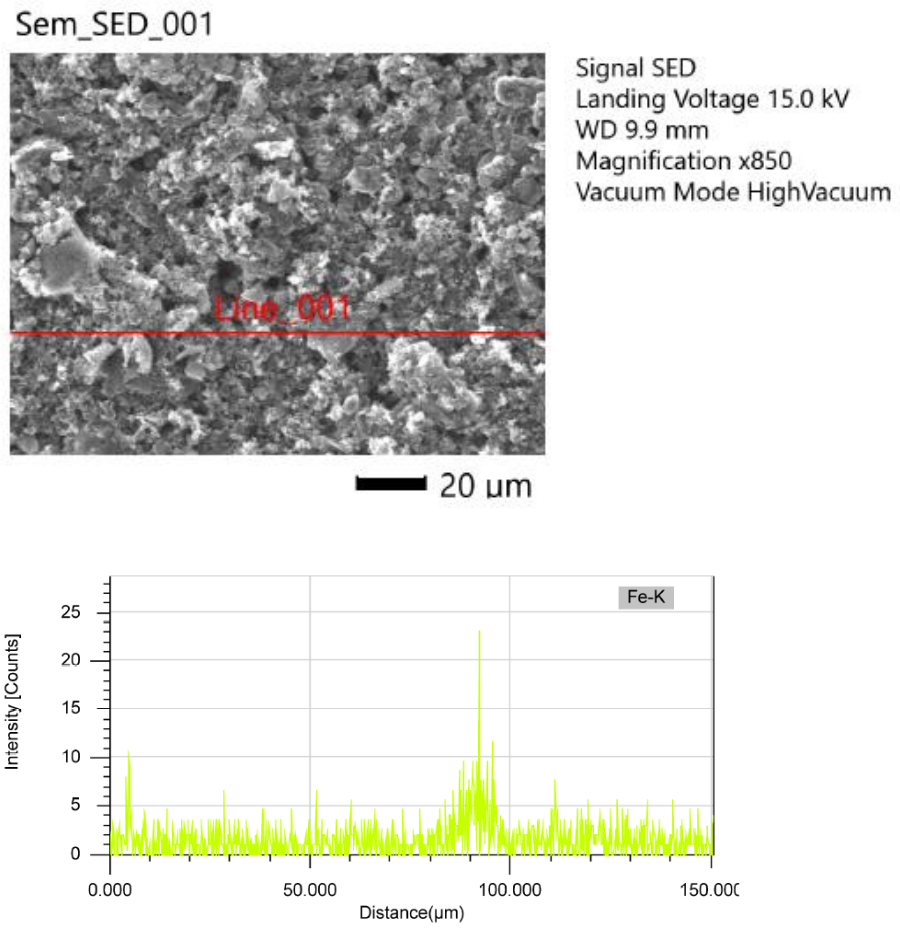

Figure 9 EDS line analysis on biographite electrode highlighting the Fe content resides in the large graphite flakes.

DIFFERENTIAL CAPACITY OF BIOGRAPHITE DURING FORMATION

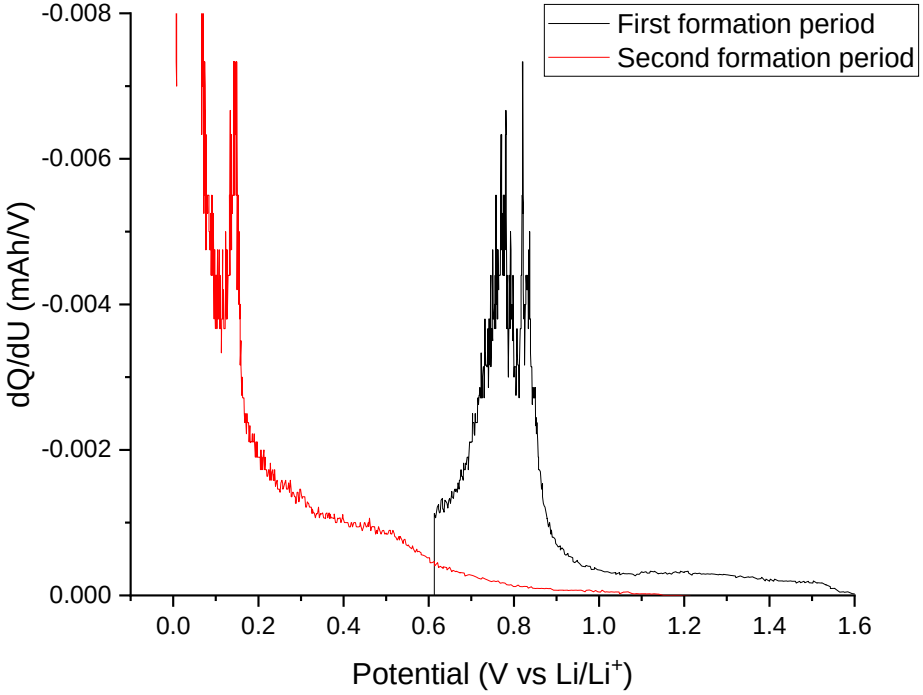

Figure 10 Differential capacity plot as function of potential on the formation cycle of gasifier biographite. The formation was performed in two stages. Initial graphite loading (black) shows high degree of SEI formation from 1.0 to 0.6 V. After a rest period the open cell potential went to 1.22 V indicating negligible intercalation. During the second stage the capacity from 0.6 V till 0.2 V is more pronounced. Disordered lithiation and exfoliation of the graphite are known reaction occurring in this potential window.[2]

Vacuum flange 3 point electrode cell design

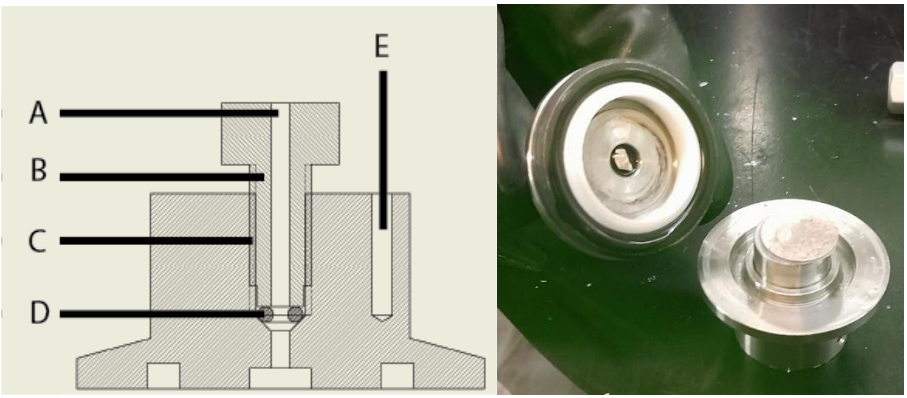

Figure 11 Three point electrode assembly. Left: drawing of cross section with: A) Feed through of copper wire, B) Ferrule feed through, C) BSPP Thread, D) O-ring fixing of wire, E) insert for banana plug of working electrode. Right: photo of the three point cell assembly. The reference electrode is a flint of lithium mounted on electrically insulating padding. The lithium counter electrode is placed on a cylindrical stube mounted on a spring. The cell is closed using a teflon inner ring and an EPDM O-ring. The flange is closed using a non conductive belt.

Supplementary Information Bibliography

1. Park, J. H., Yoon, H., Cho, Y. & Yoo, C.-Y. Investigation of Lithium Ion Diffusion of Graphite Anode by the Galvanostatic Intermittent Titration Technique. *Materials* **14**, 4683 (2021).
2. Goers, D., Spahr, M. E., Leone, A., Märkle, W. & Novák, P. The influence of the local current density on the electrochemical exfoliation of graphite in lithium-ion battery negative electrodes. *Electrochimica Acta* **56**, 3799–3808 (2011).

General Conclusion

The first chapter of this thesis treats a model which is able to describe economical alternative European energy systems based on hypothesized completely renewable energy only. Cost estimations are made for the different models that vary with regards to the input assumptions. In this way first a renewable energy harvest model is used which does not constrain the installed wind power and solar power as main sources for renewable energy. In subsequent models different restrictions are introduced where an important restriction is the limit to useable surface area limits the installed capacity for wind power. Other assumptions are chosen to highlight the impact of chemicals production ('irreplaceables') on the total energy demand and infrastructural choices in this society which does not have a fossil source of carbon anymore. It is shown that the effect of the intermittent renewable electricity from sun and wind results in low capacity factors for electricity to chemicals conversions, which can be addressed in different ways. One of the ways that appears relatively promising is to select the conversion of mainly relatively low cost solar power into hydrogen and store that subsequently as ammonia. The ammonia can then provide baseload hydrogen feedstock and also function as energy carrier for power generation when there is lack of renewable power. Wind power and energy storage using battery technology would play a significant role as well. When in addition a learning curve is assumed for cost reduction by scaling up the ammonia storage technology one arrives at relatively the lowest costs, using more sun PV, increased curtailment, next to the scaled ammonia storage overtaking part of the battery short term electricity storage as well. As the input parameters clearly define which model turns up the more a promising cost levels while still being socially acceptable, more scientific research may refine these possible future models further.

The subsequent chapters present lithium-ion battery research. A constant in current and alternative energy systems is the use of battery storage for mobility, (wearable) appliances and storage on the electric grid. The choice of chemistry we use has an impact for safety, applicability, price and our ecology. Safety needs to be considered as conventional battery chemistries are quite flammable. Less flammable are solid state electrolytes, but they may be less conductive. This work shows the change in diffusivity of lithium in two gel type electrolytes (polymer ionic liquid ternary gels and sol-gels in chapters 4 and 5 respectively) when modifying the amount of mobile carriers and salt concentrations. This knowledge is useful when these materials are

applied possibly as thin film separators in next generation batteries. The application of batteries in the transport sector can be enlarged when such batteries have a high charge density, to allow long driving ranges for electric vehicles. In chapter 3 we show that low tortuosity structured cathodes can be produced using phase inversion that reach high (60 mg/cm^2) electrode mass loadings. At the conclusion of this work these electrodes were selected for the demonstrators of the EU H2020 project Solidify over other options from the research consortium. These high capacity electrodes can pair with lithium metal anodes. Such a design using high cathode loadings and lithium metal anodes will minimize the amount of inactive parts in the battery, maximizing its volumetric energy density. An additional step towards the use of rechargeable lithium metal batteries may be provided by the research in chapter 6, indicating that specific surfactant molecules in liquid electrolytes act as plating modifier, allowing more homogenueous plating during battery charging. Coulombic efficiencies up to 99.6% can be achieved after initial plating. Finally, the selection of benign chemicals would benefit the ecological imprint of batteries, which also pertains to the use of fluorine and PFAS free chemicals. In this thesis chapter 7 concludes that all-fluorine free batteries are within reach, using a combination of alternative lithium salts and fluorine free binders, showing good performance for 600 charge-discharge cycles. Here a combination of a passivating lithium salt (LiBOB) and highly conductive salt ($LiClO_4$) allow similar performance to a conventional lithium salt ($LiPF_6$). Also, the use of biographite obtained from woody biomass char residues is shown to be a suitable alternative from mineral coal derived graphites in chapter 8.

Some of the battery technologies in this thesis are competing options, requiring a different component design. However, the research provides the understanding to make these battery technology aspects more applicable, green and/or affordable.

SUMMARY

There is an urge for rapid change in our energy system as several deadlines for agreements on climate change mitigation goals are near, with the final deadline being 2050 to achieve the formidable task of realization of a CO_2 neutral society. There are viable solutions to redesign our energy system through renewables, but the cost of such a redesign will only be more steep if carried out short before the deadline. From 2025 every year 4% of our energy system needs to be replaced using a simple linear approach, a percentage that will grow if we postpone it.

There are viable solutions for redesigning our energy system. In chapter 2 a wide number of possibilities is compared in models for a future energy system, and their basic features and feasibilities are compared. For a completely renewable system liquid fuels with low investment cost and high conversion efficiencies are necessary to provide sufficient energy during our winter periods, while being generated in the spring and summer from solar energy. One of the viable solutions is ammonia production, a proven technology which can be upscaled rapidly. Short term storage solutions in batteries need to be cheap and scalable to aggregated TWh capacities. Availability of sufficient minerals pose problems for many battery chemistry types in this respect.

Electrification of our transport sector seems necessary to prevent a steep price increase for carbon based fuels, but also to migrate away from the low energy efficiency of combustion engines. Battery storage technology plays a central role in electrification of vehicles. Improving battery performance is an ongoing process, in which currently lithium type of technology shows the best fit between consumer demands (high energy density, cycle life and charge rate), the availability of materials, and the behavior of the chemistry involved. In this work lithium ion transport problems in electrolyte and high mass-loading cathodes of lithium ion batteries is addressed. Enhancing the lithium conductivity of the materials through optimization of the lithium salt concentration and modification of the solvation shell around the lithium ion has shown to be an effective method to increase the conductivity in ionic liquids, solgels and polymerized ionic liquids. The (dis)charge rate performance is however not only dictated by such conductivity, but also by the effective pathlength of the ions through the cathode. In this respect a processing step during manufacturing of cathodes is proposed, which introduces better accessible and less tortuous channels in the electrode structure. Such channels facilitate a shorter net pathlength for ions travelling

deeper into the electrode enabling uniform charge distribution and increased areal capacities.

Availability of sufficient minerals and renewable resources for batteries is a concern. Currently the battery anode contains mostly graphite active material. Maximizing the utilization of biomass, using graphitized char from syngas gasifiers as battery anode is shown to be an effective way to make maximum use of scarce biomass resources. Using lithium metal as anode instead of graphite would, however, be the most efficient way of utilizing materials, as the electrode would solely consist of active material. The uncoordinated growth of lithium metal during the charging process however poses a major problem. Surfactant molecules dissolved in liquid electrolytes show to have a positive effect on coordination of lithium growth to more dense lithium, which poses a possible avenue for new research to find new electrolyte formulations.

This work gives a clear insight in our current energy consumption behavior and the scale of our energy need. It provides possible improvements for specifically lithium batteries with liquid electrolytes. Currently it appears sodium battery chemistry is promising to be integrated in a completely renewable energy system. Fortunately the 'lessons learned' in this work are usable for research in sodium type of chemistry, because the fundamental mechanisms of intercalation, conductivity and redox activity are similar.

SAMENVATTING

Er is een noodzaak voor snelle verandering van ons energie systeem omdat de deadlines voor het behalen van klimaatakkoorden in zicht komen. De meest belangrijke is om CO_2 neutraal te zijn in 2050. Er zijn geschikte oplossingen om ons energiesysteem te herontwerpen door het gebruik van hernieuwbare stoffen, maar de kosten die voor zo'n herontwerp gemaakt moeten worden zullen alleen maar groter worden op het moment dat ze korter voor de deadline worden uitgevoerd. Startend vanaf 2025 moet elk jaar 4% van ons energie systeem worden vervangen, een percentage die zal groeien als we het uitstellen.

Er zijn bruikbare oplossingen voor het herontwerp van ons energie systeem. Voor een compleet hernieuwbaar systeem zijn vloeibare brandstoffen met lage investeringskosten en hoge omzettings efficienties nodig om voldoende energie gedurende de winter periodes te voorzien, welke zijn gegenereerd gedurende de lente- en zomerperiode. Een van de bruikbare oplossingen is ammoniakproductie, een bewezen technologie die snel kan worden opgeschaald. Oplossingen voor korte termijn opslag dienen goedkoop en schaalbaar te zijn naar TWh capaciteit. De verkrijgbaarheid van voldoende mineralen veroorzaakt problemen voor veel batterij types in dit opzicht.

Electrificatie van onze transport sector lijkt nodig om een sterke prijsstijging van koolstof gebaseerde brandstof te voorkomen, maar ook om af te stappen van laag efficiente verbrandingsmotoren. Batterijtechnologie speelt een belangrijke rol bij het electrificeren van voertuigen. Het verhogen van de batterij prestaties speelt een centrale rol in de electrificatie van auto's. Het verhogen van de prestatie is een continu proces waarbij momenteel lithium type batterijtechnologie het beste past bij de vraag van consumenten (een hoge energie dichtheid, een lange levensduur en hoge laadsnelheden), de verkrijgbaarheid van materialen en het gedrag van de stoffen zelf. In deze thesis wordt het transport van lithium ionen in de batterij geaddresseerd. Het verhogen van de lithium geleidbaarheid door het optimalizeren van de lithium zoutconcentratie en het aanpassen van de solvatie rondom het lithium ion is een effectieve methode om de geleidbaarheid te verhogen in ionische vloeistoffen, solgels en gepolymeriseerde ionische vloeistoffen. De (ont)laadsnelheid wordt echter niet alleen bepaald door deze geleidbaarheid, maar ook door de padlengte van het ion. In

dit opzicht wordt een extra processtap voorgesteld bij het vervaardigen van electrodes, waarbij kanaaltjes aangelegd worden in de structuur van de electrode om zo'n kortere padlengte te faciliteren. Zo'n kanaal transporteert ionen naar dieper gelegen delen in de electrode, zodat er een uniforme laaddistributie over de electrode wordt verkregen.

De verkrijgbaarheid van voldoende mineralen en hernieuwbare grondstoffen voor batterijen is een zorg. Momenteel bestaat de anode van de batterij uit grafiet. Het maximaliseren van het gebruik van biomassa, door gegrafitiseerd kool uit syngas gasificatie voor batterij anodes te gebruiken, laat een methode zien om maximaal gebruik te maken van schaarse biomassa grondstoffen. Lithium metaal anodes gebruiken als anode in plaats van grafiet zou het meest efficient zijn, omdat deze anode geheel bestaat uit actief material. Echter, ongecontroleerde groei van lithium tijdens het opladen creeërt een probleem voor oplaadbare batterijen. Het toevoegen van oppervlakte actieve stoffen, opgelost in vloeibare electrolyten laten een positief effect zien in het coördineren van de aangroei van lithium naar dichter lithium. Dit geeft een mogelijke richting aan nieuw onderzoek om lithium metaal batterijen mogelijk te maken.

Dit werk geeft een duidelijk inzicht in ons huidige energie consumptie gedrag en schaal. Het geeft inzicht in de mogelijke verbeteringen voor specifiek lithium batterijen met vloeibare electrolieten. Momenteel lijkt natrium type batterijchemie veelbelovend te zijn om te worden geïntegreerd in een volledig hernieuwbaar energie systeem. Gelukkig zijn de 'lessons learned' in dit werk een bruikbaar handvat voor onderzoek in natrium type chemie, omdat de mechanismes van intercalatie, geleidbaarheid en redox activiteit erg op elkaar lijken.

ACKNOWLEDGEMENTS

For this work I received great help from colleagues, friends and family. I would especially like to thank Fokko Mulder and Pranav Karanth for the close collaboration we had the past four years. I enjoyed many of the scientific discussions we had during the project. In the lab we would be much less effective without great help from Frans Ooms, Herman Schreuders, Joost Middelkoop, Esther Bijl, Michel Steenvoorden, Duco Bosma and Bart Boshuizen. As NMR is the technique which is most used throughout this work, Swapna Ganapathy needs to be especially thanked for her expertise and patience. In general scientific colleagues Bernard Dam, Luis Cutz and Pedro Groszewicz and co-supervisor Marnix Wagemaker, thank you for being both a peer and a joy to work with. During the past four years a lot of students have helped me research, providing insight in possible angles and avenues on how batteries could work better. Many thanks to Joep Borninkhof, Albert de Kogel, Ragib Ullah, Dik Vleer and Koen de Graaf. Also under supervision of Pranav: Jelle Prins, Nimra Mary, Marilene Taufik and Samar Vonk have contributed to parts of this thesis. In the European Consortium we have had a very good collaboration with Felix Nagler, Gerrit Homann and their supervisors Andreas Flegler and Corsin Battaglia respectively. Also the people from Powall, Solvionic, Umicore and Sidrabe were a joy to work with. The project supervision was one of the hardest tasks in the consortium. For this I would like to thank Amelia Langley, Daniele Lecce, Veroni Ballet and Philippe Vereecken which made sure everybody was on the same track during the project. At work, during stressful times, it helps to have great colleagues around. Office 'roomies' Mark Sassenberg, Diana Chaykina, Ziqing Yuan, lab 'roomies' Remco van der Jagt, Eveline van der Maas, Pierfrancesco Ombrini, Viktor Landgraf, Xavier Kouoi, Shengnan Zang, Hanan Al-Kutubi, Chaofan Chen, Boaz Izelaar, Dylan van Noordenne, Peter Jungbacker, Mark Kwakernaak and all other people from SEE and MECS research groups, the chemical engineering department and the faculty of Applied Sciences, thank you for being wonderful people. Last and not least, thanks to my wife and both my and her parents for being a stable foundation. This allowed me to make sufficient space in my head the past four years to create this thesis while a little toddler was around.

This project has received funding from the European Union's Horizon 2020 research and innovation programme SOLiDIFY under grant agreement No 875557.

LIST OF PUBLICATIONS

PUBLICATIONS RELATED TO THIS THESIS:

Transition to net zero carbon emission economy: Cost analysis of alternative scenario's in the European energy market (under review) - Lead investigator

Authors: Mark Weijers and Fokko Mulder

Phase inversion strategy enables low tortuosity, ultrahigh mass loading Ni-rich layered oxide electrodes – Lead investigator

Authors: Pranav Karanth, Mark Weijers, Pierfrancesco Ombrini, Davide Ripepi, Frans Ooms, Fokko Mulder

Elucidation of Enhanced Lithium Conductivity in Nanoporous Ionogel Using Solid State NMR – Lead investigator

Authors: Mark Weijers, Pranav Karanth, Swapna Ganapathy, Fokko Mulder

Lithium Diffusivity and Transference in high concentration ternary polymer ionic liquids - Lead investigator

Authors: Mark Weijers, Pranav Karanth, Gerrit Homann, Boaz Izelaar, Aleksandra Kondakova, Swapna Ganapathy, Ruud Kortlever, Corsin Battaglia, Fokko Mulder

Use of surfactant for homogenueous anodeless lithium plating (under review) – Lead investigator

Authors: Mark Weijers and Fokko Mulder

Fluorine Free Lithium Ion Batteries: a case study (under review) - Lead investigator

Authors: Mark Weijers, Pranav Karanth, Joep Borninkhof, Fokko Mulder

High performance graphite anode of gasifier char from lignocellulotic waste materials (under review) – Lead investigator

Authors: Mark Weijers, Fokko M. Mulder, Luis Cutz

OTHER PUBLICATIONS:

Enhancing pseudocapacitive intercalation in Ti3C2Tx MXene with molecular crowding electrolytes – Experimental work: Rheometry

Authors: Chaofan Chen, Albert de Kogel, Mark Weijers, Lars J Bannenberg and Xuehang Wang

A Quasi-Solid-State Polymer Lithium–Metal Battery with Minimal Excess Lithium, Ultrathin Separator, and High-Mass Loading NMC811 Cathode – Experimental work: XPS, NMR

Authors: Gerrit Homann**,** Qing Wang, Sufu Liu, Antoine Devincenti, Pranav Karanth, Mark Weijers, Fokko M. Mulder, Matiss Piesins, Tom Gouveia, Alix Ladam, Sebastien Fantini, Corsin Battaglia

Rational design of safe, fluorine-free dual salt electrolytes for Lithium metal batteries - Experimental works: NMR, Rheometry.

Authors: Pranav Karanth, Mark Weijers, Anastasiia Lavrinenko, Boaz Izelaar, Swapna Ganapathy, Marnix Wagemaker, Fokko Mulder

REPOSITORIES

The chapters in this thesis have individual repositories which can be found by following these DOI weblinks:

Chapter 2: www.doi.org/10.4121/20bc4390-db5b-481c-8408-7af9546b13ab

Chapter 3: www.doi.org/10.4121/d963a4b7-6879-4c1b-86ff-2596956b5e7a

Chapter 4: www.doi.org/10.4121/fd71c68f-ac6c-448a-98e7-f1017a0b4b7a

Chapter 5: www.doi.org/10.4121/0bd878cd-0d1d-420e-b424-aad2782cb616

Chapter 6: www.doi.org/10.4121/783b048d-ce34-42e8-9254-7e75324f4860

Chapter 7: www.doi.org/10.4121/4b3fd60f-242f-47f3-b5d8-cf8816759ea2

Chapter 8: www.doi.org/10.4121/a886b7df-d656-4620-8334-c834686e7ab5

CURRICULUM VITAE

Mark Weijers was born on 2 February 1990 in Noordwijkerhout, the Netherlands. He started his research and got his Master degree majored in Biochemical Engineering in 2014 at TU Delft. After that, he directly started as Researcher and later Process Development Engineer at Waste2Chemical, now Chaincraft until 2020. There he contributed to the development and engineering of the complete production process of manufacturing fatty acids from food and feed wastes.

In 2020 he started his PhD study on material and architecture optimization in lithium batteries in the group of Materials for Energy Storage and Conversion at Delft University of Technology, supervised by Prof. dr. Fokko Mulder. The position was financially supported by a European H2020 grant called SOLiDIFY, which focused on optimization of a high energy density solid electrolyte and lithium metal anode battery design to make it ready for upscaling in the market.